Geochemical processes at a seawater-freshwater interface

Andersen, Martin Søgaard

Publication date:
2001

Document Version
Publisher's PDF, also known as Version of record

Environment & Resources
Technical University of Denmark

Geochemical Processes at a Seawater-Freshwater Interface

Martin Søgaard Andersen

GEOCHEMICAL PROCESSES AT A SEAWATER-FRESHWATER INTERFACE

by
Martin Søgaard Andersen

Ph.D. Thesis
Environment and Resources DTU
Technical University of Denmark
2001

Kgs. Lyngby, November, 2001

Martin Søgaard Andersen

Geochemical Processes at a Seawater-Freshwater Interface

Cover: Birte Brejl
Printed by: DTU tryk
Environment & Resources DTU
ISBN 87-89220-89-7

The thesis will be available as a downloadable pdf-file from the department's homepage on: www.er.dtu.dk

Environment & Resources DTU
Library
Bygningstorvet, Building 115, Technical University of Denmark
DK-2800 Kgs. Lyngby

Phone:
Direct: (+45) 45 25 16 10
(+45) 45 25 16 00
Fax: (+45) 45 93 28 50
E-mail: library@er.dtu.dk

PREFACE

This report about geochemical processes at a seawater-freshwater interface is the result of a Ph.D. study carried out at Environment and Resources DTU (E&R DTU), Technical University of Denmark (DTU). The study was funded by grants from DTU and the Groundwater Research Centre at DTU. This project constitutes one third of the field investigations at Skansehage. The other two parts are focused more deeply in the redox processes and in the density depended reactive transport modelling and are carried out by Ph.D. students, Vibeke Nyvang and Flemming Damgaard Christensen. This work could never have been completed without their contributions and cooperation in the field work and the data collection.

The supervisor on the Ph.D. study has been docent Dieke Postma (E&R DTU), whom I would like to thank for enlightening discussions and keeping med on the right track. A special thanks goes to Rasmus Jakobsen (E&R DTU) for encouraging discussions during the whole project and willingness to discuss the wildest ideas at almost any hour.

During the project, a lot of people have been very helpful, and I would like to thank the following persons:

At E&R, Erik Lange and Ellen Zimmer Hansen for their enthusiastic and caring technical and practical support during construction and maintenance of the field site. Erik Lange, Ellen Zimmer Hansen, Lene Jensen, Henrik Skov, Vibeke Nyvang, Flemming Christensen, a bunch of students and some of my friends are thanked for the mostly nice and long days at Skansehage taking samples in burning sun or at -10°C. Lene Jensen, Bente Frydenlund and Henrik Skov are thanked for helping analysing a lot of samples. Hans Hansen and Denny Viholt are thanked for technical support in the workshop with last minute repair of bits and pieces before a field campaign. Frank Andreasen is thanked for his GPR-profiles, and Hector Diaz for PC-support. Birte Brejl og Torben Dolin are thanked for some figures and drawings.

At the field site, I would like to thank the neighbours – who permitted us access to their property's for wells and installations of wells and pumps. A special thank to Mr. and Mrs. Otte for their coffee and cakes, when needed. Orla is thanked for opening his guesthouse out of season when needed.

A thank to my friend Søren Frank for discussions and support and to my fellow Ph.D.-student Claus Kjøller for making the titlepage.

Finally a special thank to Dorte for her support and for holding out.

SUMMARY

This thesis presents the results from a field study of the physical and geochemical processes at a sea-/freshwater interface situated in a coastal sandy aquifer at Skansehage in the northern part of Zealand, Denmark. The study was conducted in a shallow phreatic aquifer consisting of Holocene sand and gravel deposits of marine origin. A marine peat layer of lower permeability underlies the 9 m thick aquifer. A detailed transect of more than 100 monitoring wells were constructed crossing the sea-/freshwater interface, from the beach and 120 m landward. These wells were used for 1) monitoring the movement of the interface by electrical conductivity (EC) measurements, 2) taking water samples for full hydrochemical analysis and 3) for hydraulic testing.

Natural situation

The sea-/freshwater interface (represented by the 50 % seawater contour) of the natural situation is at the coast situated 4 m below sea-level and dipping landward to reach the bottom of the aquifer 40 m from the coast at an elevation of –9 m depth. The location and geometry of the interface was found to be in reasonable equilibrium with the local hydrogeological parameters of recharge, density contrast, etc. The single most important disturbance of this equilibrium seems to be by inundation of surface seawater during winter storms. Such inundations cause seawater plumes with a higher density to migrate down through fresh regions of the aquifer at topographical lows. The plumes leave a tail of diluted seawater, which is slowly being flushed seaward by the discharging freshwater. In the seawater wedge slow seawater advection seem to be occurring.

The freshwater is chemically dominated by a Ca^{2+} and HCO_3^- and was found to be anoxic with methanogenesis being the prevailing redox-processes. Towards the coast the freshwater zone exhibits a pattern of refreshening with a chromatographic cation sequence where Ca^{2+} is displacing Mg^{2+} from the cation exchanger, which in turn displaces Na^+ and K^+ further towards the coast. The loss of Ca^{2+} due to the ion exchange lowers the saturation index for calcite possibly leading to calcite dissolution, as indicated by an observed increase in pH and alkalinity. The observed refreshening pattern in the cations is believed to be a consequence of the seaward flushing of previous inundated seawater plumes.

Within the seawater wedge sulfate reduction is an important process causing depletion of sulfate relative to chloride and accumulation of sulfide and alkalinity. The increase in alkalinity causes saturation for calcite and possibly some calcite precipitation. The water chemistry of the dispersed mixing zone between the saltwater and freshwater could to a large degree be explained by mixing of aquifer saltwater and freshwater accompanied by sulfate reduction and calcite dissolution.

In the low permeable peat layer below the seawater wedge and the mixing zone a substantial organic matter degradation is occurring leading to a high alkalinity and a high concentration of NH_4^+, PO_4^{2-} and DOC. Methane formation seems to be the dominating TEAP (terminal electron accepting process). The CO_2 production related to the methane formation drives dissolution of calcite. Ca^{2+} released by calcite dissolution and NH_4^+ from the mineralisation of organic matter displaces Na^+, Mg^{2+} and K^+ from the cation exchanger in the sediment. The high CEC of the peat layer (5-40 meq/l) serves as a sink for Ca^{2+} and therefore facilitates further dissolution of calcite. This chain of coupled processes leads to the observed simultaneous enrichment for all cations in the pore water of the peat.

A particular inundation event and subsequent vertical migration of seawater density plumes down through the fresh aquifer was recorded. The density plumes contained a high concentration of Na^+, Mg^{2+} and K^+ and displaced Ca^{2+} from the cation exchanger in the fresh part of the aquifer whereas Mg^{2+} was displaced from the cation exchanger in the brackish part. The introduction of sulfate into the aquifer by the plumes apparently shifted the redox-conditions from methanogenesis to sulfate reduction.

Seawater intrusion

For the seawater intrusion experiment seven pumps were installed 140 m from the coastline and was pumped with an average discharge of 30 m^3/h for 10 months. The advance of the seawater front into the aquifer was monitored in the transect. The intrusion velocity was about 0.33 m/d and in total the front advanced to about 85 m from the coastline during the 10 months. From being a landward dipping interface in the natural situation the interface became a vertical front during the intrusion. The reason for this is a combination of the aquifer heterogeneity such as permeability variations and leakage up through the bottom aquitard. Also the density gradient over the sea-/freshwater interface is much smaller than the head gradient caused by the pumping. A wedge shaped seawater intrusion is therefore not observed.

During the intrusion the pre-existing mixing zone, with its sulfate depletion and high concentrations of sulfide, alkalinity and higher pH is being pulled into the aquifer, ahead of the intruding surface seawater. The high seawater concentration of Na^+, Mg^{2+} and K^+ displaces Ca^{2+} from the cation exchanger. The Ca^{2+} released accumulates in a peak coinciding with the high alkalinity of the landward migrating pre-existing mixing zone. This leads to an increasing calcite supersaturation with travelled distance and possibly to the precipitation of calcite. However, a zone of subsaturation is believed to be caused by the acid production related to sulfate reduction follows the zone of calcite supersaturation, potentially re-dissolving any calcite precipitated at the front. The rapid disappearance of methane from the transect could indicate that methane is being re-oxidised by sulfate during the intrusion.

RESUMÉ

Denne afhandling beskriver de fysiske og geokemiske processer i en salt-/ferskvands grænseflade fra et feltforsøg i et kystnært sandet grundvandsmagasin både under naturlige forhold og under kunstig frembragt saltvandsintrusion. Grundvandsmagasinet er beliggende på Skansehage i Nordsjælland, Danmark, og består af Holocene sand- og grusaflejringer af marin oprindelse. Nedadtil afgrænses det 9 meter tykke grundvandsmagasin af et lavpermeabelt marint tørvelag. Et detaljeret transekt med mere end 100 observationsboringer blev konstrueret vinkelret på salt-ferskvandsgrænsefladen – fra stranden og 120 meter ind i landet. Disse boringer blev benyttet til 1) at monitere grænsefladebevægelser ved hjælp af elektriske ledningsevne (EC) målinger, 2) at udtage vandprøver til vandkemiske analyser og 3) hydrauliske test.

Naturlig situation
Grænsefladen mellem salt- og ferskvand (repræsenteret ved konturen for 50% havvand) er i den naturlige situation placeret 4 meter under havniveau ved kysten og hælder ind mod land for at nå bunden af grundvandsmagasinet 40 meter fra kysten i kote -9 m. Placeringen og geometrien af grænsefladen er i ligevægt med de lokale hydrogeologiske parametre som nedbør, densitets forskelle m.m. Den vigtigste forstyrrelse af denne ligevægt ser ud til at være havvandsoversvømmelser under vinterstorme. Oversvømmelser af topografiske lavninger medfører, at saltvandstunger med højere densitet bevæger sig ned gennem den ferske del af grundvandsmagasinet. Tungerne efterlader en hale af brakvand, som langsomt bliver fortrængt af ferskvand. På saltvandssiden af grænsefladen ser det ud til, at der foregår en langsom cirkulation af saltvand.

Det ferske grundvand er domineret af Ca^{2+} og HCO_3^+ og er anoxisk med methanogenese som den dominerende redoxproces. Kationerne i ferskvandszonen optræder i en kromatografisk sekvens, hvor Ca^{2+} skubber Mg^{2+} af ionbytteren, som derefter ionbytter med Na^+ og K^+ længere ud mod kysten. Tabet af Ca^{2+} p.g.a.ionbytningen sænker mætningsindekset for kalcit, hvilket sandsynligvis leder til kalcitopløsning, som også er indikeret ved en observeret stigning i pH og alkaliniteten. Den observerede kationfordeling i ferskvandszonen skyldes fortrængningen af saltvandstungerne fra havvandsoversvømmelserne.

I den salte del af grundvandet er sulfatreduktion en vigtig proces, som medfører en akkumulation af sulfid og alkalinitet og resulterer i et underskud af sulfat i forhold til klorid. Produktionen af alkalinitet medfører en stigende kalcitmætning og muligvis udfældning af kalcit. Vandkemien i blandingszonen mellem salt- og ferskvand kan i høj grad forklares med opblanding af saltvand og fersk grundvand samt af sulfat reduktion og kalcitopløsning.

I det lavpermeable tørvelag under den salte del af grænsefladen og opblandingszonen er en omsætning af organisk materiale årsag til en høj alkalinitet og til høje koncentrationer af NH_4^+, PO_4^{2+} og DOC. Methanogenese ser ud til at være den dominerende redox-proces. CO_2-produktionen, relateret til methanogenesen, resulterer i opløsning af kalcit. Ca^{2+}, som frigives ved kalcitopløsning, samt NH_4^+ fra mineraliseringen af organisk materiale fortrænger Na^+, Mg^{2+} og K^+ fra ionbytteren i sedimentet. Den høje CEC i tørvelaget (5-40 meq/l) holder således koncentrationen af Ca^{2+} nede og giver derfor anledning til yderligere opløsning af kalcit. Denne kæde af koblede processer leder til et samtidigt overskud af alle kationer relativt til klorid.

En havvandsoversvømmelse samt den efterfølgende udvikling af saltvandstunger ned i den ferske del af grundvandsmagasin blev registreret. Tungerne indeholdt høje koncentrationer af Na^+, Mg^{2+} og K^+, som fortrængte Ca^{2+} fra ionbytteren i den ferske del af grundvandsmagasinet, mens Mg^{2+} blev fortrængt fra ionbytteren i brakvandszonen. Tungernes høje sulfatindhold ændrede tilsyneladende omsætningen af organisk stof fra methanogenese til sulfatreduktion.

Saltvandsintrusion

Under saltvandsintrusionsforsøget blev der installeret 7 pumper 140 m fra kystlinien. De pumpede med en gennemsnitsydelse på 30 m^3/h i 10 måneder. Saltvandsindtrængningen blev fulgt ved målinger i transektet. Intrusionshastigheden var omkring 0,33 m/d og salt/ferskvandsgrænsefladen flyttede sig ca. 85 m ind i løbet af de 10 måneder. Fra at være en skrående grænseflade i den naturlige situation blev den vertikal under intrusionen. Årsagen til dette skyldes en kombination af heterogeniteter i grundvandsmagasinet så som variationer i permeabilitet og lækage op gennem bunden af grundvandsmagasinet. Desuden er de indadrettede trykgradienter forårsaget af oppumpningen af meget større betydning for transporten end densitetsgradienterne over salt-ferskvands grænsefladen.

Under intrusionen blev den eksisterende opblandingszone med høje koncentrationer af sulfid og alkalinitet samt højere pH transporteret ind i grundvandsmagasinet foran det indtrængende havvand. De høje koncentrationer af Na^+, Mg^{2+} og K^+ i havvandet fortrænger Ca^{2+} fra ionbytteren. Den frigivne Ca^{2+} akkumuleredes i en top, der transporteres indad sammen med den høje alkalinitet fra opblandingszonen. Dette medfører en øget kalcit overmætning efterhånden som intrusionen bevægger sig indad og muligvis til udfældning af kalcit. Denne zone efterfølges imidlertid af en zone med kalcitundermætning som er forårsaget af et pH-fald relateret til sulfatreduktion i den havvandspåvirkede del af grundvandsmagasinnet, Denne zone kan muligvis genopløse kalcit udfældet på fronten. Det bratte fald i methankoncentrationen i transektet indikerer, at methan muligvis bliver reoxideret af sulfat under intrusionen.

TABLE OF CONTENTS

1. INTRODUCTION

In coastal aquifers the position and shape of the interface between the fresh- and seawater is determined by a number of factors that comprise: The density contrast between the seawater and freshwater, the permeability distribution in the aquifer, the freshwater discharge to the coast and the sea-level fluctuations (Bear et al., 1999). The position of the interface is therefore subject to change if the freshwater discharge is altered due to changes in the recharge (precipitation) or by abstraction of groundwater, and if the sea level changes. On a geological time scale changes over 100 m in the relative sea-level, during the last glaciation, have had a tremendous impact on the interface between seawater and freshwater. Relict effects of these sea-level fluctuations can still be seen in some aquifers today more than several thousands of years after. Some aquifers are still subject to the flushing of seawater-derived ions (Chapelle and Knobel, 1983, Appelo 1994a). Other aquifers aquifers are known to contain fresh or brackish water in their offshore portions far from the expected present day interface position. This is believed to be remnants of previous low sea levels (Kooi et al., 2000, Kooi and Groen, 2001, Post et al., 2001).

More recently, groundwater abstraction in coastal zones has caused seawater intrusion to become an increasing problem (Todd, 1980, Reilly and Goodman, 1985, Reilly, 1993, Bear et al., 1999). One of the earliest reports of salinisation as caused by saltwater intrusion is from 1855 (Braithwaite, 1855, referenced in Todd, 1980). Saltwater intrusion has been observed in all parts of the world particularly in areas with arid and semiarid climate (Nadler et al., 1980, Calvache and Pulido-Bosch, 1997, Giménez and Morell, 1997), in areas with high irrigation demands (Howard and Mulings, 1996, Steinich et al., 1998), in areas with changed land use pattern (Beekman, 1991, Stuyfzand, 1993) and in densely populated areas such as Los Angeles (Laverty and van der Goot, 1955) and Long Island (Lusczynski and Swarzenski, 1966, Reilly, 1993). The problem may aggravate in the years to come due to various reasons. A majority of the earth's population inhabits coastal regions and an increasing portion of their water supply for domestic, industrial and agricultural purposes comes from aquifers. With the forecasted increase in population growth and of urban development in coastal areas, water supply demands will become greater. Also the issue of global climatic change with raising ocean levels and altered precipitation patterns has a potential for future problems in relation to the sea-/freshwater equilibrium.

The physics of the sea-/freshwater interface have been studied extensively, especially the aspects that concern the flow and equilibrium between miscible fluids of different densities (Bear, 1972, Todd, 1980, Reilly and Goodman, 1985 and Bear et al., 1999). Today 3-D density dependent flow and transport modeling codes are becoming standard tools for evaluating past and potential changes in the sea-/freshwater equilibrium (Voss, 1984, Kipp 1987). Less attention have so far been given to the chemical aspects of the changes in the sea-/freshwater equilibrium. In the past it has often merely been a question of determining whether salt loads will exceed some critical water quality threshold (Todd, 1980) or to determine whether salinisation is of marine origin or is caused by other sources such as deep brines and dissolution of evaporites (Howard and Mullings, 1996, Giménez and Morell, 1997, Xue et al., 2000). However, in recent years many investigations have focused ion exchange processes as the qualitative cause of changes in the water composition and as a tool to determine aquifer salinisation or flushing (Beekman, 1991, Stuyfzand, 1993, Appelo, 1994b, Appelo, 1996).

In the recent years the notion that flow and transport of seawater may be dynamically coupled to geochemical reactions has been emerging (i.e. that chemical reactions may enhance or retard the flow). Laboratory evidence and perhaps also field data from different environments indicate that transport of seawater into fresh aquifers and mixing of sea- and freshwater may lead to increased permeability in some environments and reduced permeability in others. Dramatic reduction's in hydraulic conductivity have been observed in column experiments as a consequence of changes in clay properties related to changes in salinity (Goldenberg et al., 1983, Goldenberg, 1985). Possibly this has also been observed in the field (Konikow et al., 2001). In carbonate aquifers prolonged mixing of sea- and freshwater is believed to cause calcite dissolution and increase the porosity and permeability (Back et al., 1979, Back et al., 1986, Sanford and Konikow, 1989).

The fact that different geochemical reactions are coupled, in relation to changes in the sea-/freshwater position, is well known (Beekman, 1991, Stuyfzand, 1993, Appelo, 1996). These processes have been investigated in column experiments (e.g. Beekman, 1991) and also in field investigations of systems with variable salinity such as artificial recharge of water with a differing salinity and composition compared to the aquifer (Van Breukelen et al., 1998) and contaminant plumes from landfills and waste repositories (Brun, 1996). Coupling of ion exchange processes with carbonate equilibria has been studied by Appelo (1994a), Griffioen (1992), Lefèvre et al. (1993)

and Bjerg and Christensen (1993). Also the coupling of redox-reactions and carbonate equilibrium has been studied by Smart et al. (1988) and Stoessell et al. (1993), for carbonate aquifers. But few studies has been dedicated to the coupling of all three processes at the same time. However, Beekman (1991) explained the evolution along a refreshening flow path as a coupled effect of cation exchange, calcite dissolution and organic matter degradation. Stuyfzand (1993) have compiled a huge dataset for a dune area in Holland comprising both refreshening and seawater intrusion and undertaken a chemically holistic interpretation encompassing almost every possible geochemical process.

However, it appears that so far detailed field investigations of the physical and coupled geochemical effects in relation to particular seawater intrusion events with good control and knowledge of the pre-intrusion conditions are very limited.

2. OBJECTIVES

The objective of this study is therefore to obtain a fundamental understanding of the physical and geochemical processes and their interactions at a detailed scale occurring in a seawater/freshwater system. The objective is pursued by field scale investigations of:

a) The processes occurring in a natural steady state situation at a seawater/freshwater interface.

b) The processes occurring during a forced seawater intrusion experiment

c) The processes occurring during the natural recovery of the steady state situation and the irreversibility of the processes.

The third phase is a slow process and it is still ongoing at the time of completion of this dissertation. The processes related to the natural recovery will therefore not be addressed in this project.

The structure of the report

This report is divided into two parts each with its own data presentation and discussion. The first part is dealing with the processes occurring in the natural situation at the sea-/freshwater interface while the second part describes the data from the seawater intrusion experiment.

3. BASICS OF ION EXCHANGE AND REDOX-REACTIONS

In the following the basic theory will be given to ion exchange and redox-processes in relation to seawater intrusion and the mixing of sea and freshwater.

3.1 Ion exchange processes

Ion exchange processes has for long been recognized as the cause of distinctly different water compositions in coastal aquifer systems (Foster, 1950 and Back, 1966). Groundwater enriched in both Na^+ and HCO_3^- has been attributed to aquifers formerly containing marine or brackish water and now being flushed by fresh groundwater containing Ca^{2+} and HCO_3^- (e.g. Appelo, 1994a), a process also known as refreshening. Conversely seawater intruding a fresh or brackish aquifer has been shown to lead to a water composition enriched in Ca^{2+} and depleted in Na^+ relative to Cl^- (e.g. Appelo and Geirnaert, 1991). In an overall sense both processes can be understood in terms of the following ion exchange reaction:

$$\tfrac{1}{2}Ca^{2+} + Na - X \leftrightarrow Na^+ + \tfrac{1}{2}Ca - X_2 \qquad (3.1)$$

In this equation (-X) represents a cation exchange site of constant negative charge. Going from left to right represents refreshening with loss of solute Ca^{2+} and increase in solute Na^+. The opposite direction thus represents seawater intrusion. The Gaines-Thomas convention assumes that the exchanger surface has a total constant charge. A mass action equation can be written for the exchange reaction, here according to the Gaines-Thomas convention (Gaines and Thomas, 1953), which states that the activity of an exchangeable cation can be represented by its equivalent fraction on the exchange complex. In general terms the mass action equation is:

$$\frac{[I^{z_i}]^{1/z_j}}{[I^{z_i}]^{1/z_i}} = K_{1/j} \cdot \frac{\beta_j^{1/z_j}}{\beta_i^{1/z_i}} \qquad (3.2)$$

For the calcium and sodium exchange the mass action equation is:

$$\frac{[Na^+]}{[Ca^{2+}]^{1/2}} = K_{Na/Ca} \cdot \frac{[Na-X]}{[Ca-X_2]^{1/2}} \quad \Rightarrow \quad \frac{[Na^+]}{[Ca^{2+}]^{1/2}} = K_{Na/Ca} \cdot \frac{\beta_{Na}}{\beta_{Ca}^{1/2}} \qquad (3.3)$$

Here [ ] denotes activities, z is the charge, $K_{Na/Ca}$ is the equilibrium selectivity coefficient giving the affinity of, in this case, Ca^{2+} to the cation exchanger relative to Na^+, and (β_I) is the equivalent fraction of a cation I on the exchanger given by (Appelo & Postma, 1993):

$$\beta_I = \frac{meq_{I-Xz}}{\sum_{I,J...} meq_{I-Xz}} = \frac{meq_{I-Xz}}{CEC} \qquad (3.4)$$

where I,J,... are exchangeable cations, meq_{I-Xz} indicate the number of milli-equivalent of an exchangeable cation, which is normally given in meq/100g dry sediment and the sum of exchangeable cations Σmeq_{I-Xz} is essentially equal to the CEC (cation exchange capacity). The ion exchange reactions have also been described by other conventions where the exchanger is considered to consist of a specific number of sites. The Gapon (1933) convention assumes a total number of sites and that the activities of the exchangeable cations, on an equivalent base, are proportional to the number of exchange sites (X^-). If instead molar fractions are use for the activity of the exchangeable fraction the Vanselow (1932) convention is applied. The choice of convention has largely been determined on how well a given data set is fitted. In this study the Gaines-Thomas convention will be used, which is also the convention adopted in the geochemical code PHREEQC (Parkhurst and Appelo, 1999) used in this study. The selectivity coefficients used in the PHREEQC database are average values given by Appelo and Postma (1993) partly compiled by Bruggenwert and Kamphorst (1982) in Bolt (1982). In the PHREEQC database the exchangeable cations ($I-X_z$) have been assigned the same activity corrections as the free solute cations (I^{z+}). The assumption behind this is that the major cations mainly adsorbs as hydrated outer sphere complexes and therefore have an activity as the free solute ion (Appelo, 1994a). It should be stressed here that this assumption is more a matter of convenience than due to a proven rigorous theory, and because it seem to produce reasonable results.

Apart from Na^+ and Ca^{2+} other cations may participate in the exchange reactions associated with refreshening and seawater intrusion, most noticeably magnesium (Mg^{2+}), and to some extent also

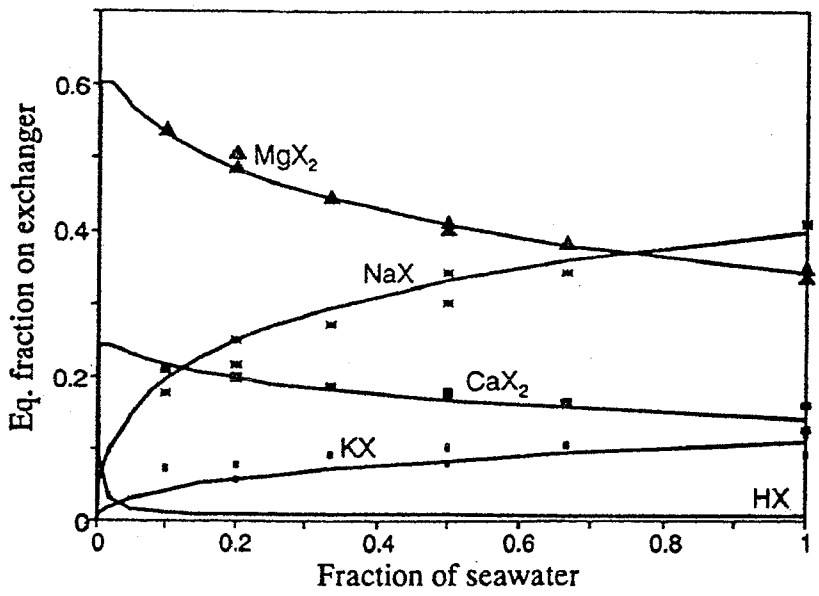

Figure 3.1: Equivalent fractions of exchangeable cations in mixtures of seawater and distilled water. Measured fractions (symbols) are from Van der Molen (1958) and modeled lines are from Appelo (1994a). The selectivity coefficient used for modelling the observed Na^+ was made variable by decreasing it with half a log unit going from the freshwater to the seawater in order to better fit the observed Na^+ in the seawater. Reprinted from Appelo (1994a).

potassium (K^+) and ammonium (NH_4^+). This lead to multicomponent exchange reactions where several ions compete for the exchange sites at the same time.

The composition of a cation exchanger in equilibrium with different mixtures of sea- and fresh water have been measured for two soils by Van der Molen (1958), and modeled by Appelo (1994a) using the Gaines-Thomas convention as shown in Figure 3.1. This shows that it is possible to model the exchanger composition for solutions varying from seawater to freshwater using the Gaines-Thomas convention. Figure 3.1 also shows the non-linear effects on the cation exchanger composition as the water composition changes from seawater to freshwater. As the seawater fraction increases, the affinity for divalent ions decrease as is especially clear for Mg^{2+} where the equivalent fraction (β_{Mg}) decreases even though the solute concentration of Mg^{2+} increases with increasing seawater fraction.

In order to better fit the observed Na^+ (in Fig. 3.1) in the seawater, the selectivity coefficient used for modelling of the observed Na^+ was made variable by decreasing it with half a log unit going from the freshwater to the seawater. The difficulties of fitting Na^+ in Fig. 3.1 illustrate the problems related to finding a consistent thermodynamic theory/model for the calculation of multicomponent ion exchange reactions in natural systems. This probably stems from the fact that the cation exchange complex in a natural sediment is a composite of different minerals and organic compounds each with varying specific affinities for different cations and varying exchanger properties with changes in salinity, pH, etc. In most natural aquifer sediments clay minerals and organic compounds largely dominate the cation exchanger. In Appelo and Postma (1993) the CEC is related to the clay and organic matter content by the empirical relationship:

$$CEC(meq/100g) = 0.7 \cdot (\%clay) + 3.5 \cdot (\%C) \qquad (3.5)$$

During refreshening (freshwater displacing seawater) of an aquifer, ion exchange may lead to a separation of the cations Ca^{2+}, Mg^{2+}, K^+ and Na^+ also termed chromatographic separation. This separation is a consequence of the cations having a varying affinity to the cation exchanger with the affinity decreasing from $Ca^{2+} > Mg^{2+} > K^+ > Na^+$. During refreshening the cation separation is particularly clear for two reasons, 1) the exchange fronts are sharpening fronts (i.e. a cation with high affinity displacing a cation with lower affinity) and 2) the low ionic strength of the displacing

solution separates the exchange fronts from the salinity front (the decrease in Cl^-). The sharpening fronts tend to counteract the spreading, otherwise caused by dispersion and diffusion (Appelo, 1996).

The non-linear nature of equation (3.2) reveals an interesting feature of heterovalent exchange reactions. A change in the salinity in a solution/exchanger system will due to the quadratic relationship in equation (3.2) lead to a change in the molar ratio of monovalent and divalent cations. A dilution, such as freshwater displacing seawater, will increase the solute concentration of monovalent cations and decrease the solute concentrations of multivalent cations.

In cases when the pool of exchangeable cation equivalents is considerably larger than the aqueous pool of cations, a change in salinity will cause a shift in the aqueous ratio of divalent over monovalent cations after the salinity front has passed. This is because the ratio of the same ions on the exchanger will be largely maintained during the salinity shift and therefore dictates a change in the aqueous concentration of the cations. Therefore a 10-fold change in the solute concentration of a monovalent cation (Na^+) will give a 100-fold change in concentration of a divalent cation (Ca^{2+}) (Appelo, 1996). Thus divalent cations (Ca^{2+}) are favoured more strongly by the exchanger when the salinity decreases and will exchange with monovalent cations on the exchanger (Na^+). The salinity effect has clearly been documented in aquifers associated with salt- or freshwater pulses either injected or natural (Valocchi et al (1981a), Ceazan et al., 1989, Bjerg et al., 1993, and Hansen and Postma, 1995).

The effect of salinity changes can clearly be seen when freshwater displaces seawater, because of the low total cation equivalents of the displacing solution compared to the total pool on the exchange complex (Valocchi et al., 1981a,b, and Bjerg et al., 1993). This is especially clear in the injection experiment described by Valocchi et al. (1981a,b) where the concentrations of Ca^{2+} and Mg^{2+} after the salinity front drops well below their freshwater levels. The phenomenon of refreshening have been studied in great detail and documented as a naturally occurring process in many aquifers (Chapelle and Knobel, 1983, Appelo and Willemsen, 1987, Beekman, 1991, Stuyfzand, 1993, Melo et al., 1999). And also from injection experiments where freshwater is injected into a brackish or saline aquifer (Valocchi et al., 1981a and Valocchi et al., 1981b).

The exchange processes when water with higher salinity displaces fresh groundwater have been studied extensively in laboratory column experiments (Beekman, 1991, Cerník et al., 1994, Gomis-Yagües et al., 1997) and also in field injection experiments (Dance and Reardon 1983, Ceazan et al., 1989, Bjerg et al., 1993, Van Breukelen et al, 1998). So the ion exchange processes that can be expected during a seawater intrusion experiment are quite well understood and documented. In spite of many rapports of salinisation of freshwater aquifers the chromatographic cation patterns related to ion exchange processes during seawater intrusion are rarely studied in detail in the field (Appelo and Postma, 1993). This is partly because the passage of the exchange fronts during seawater intrusion is much faster than the passage of the exchange fronts during refreshening. The reason being the difference between the total solute cation loads in the displacing solutions compared to the exchanger. The transition from an exchanger complex with a freshwater composition to a seawater composition will be relatively fast for a small or moderate CEC of 0.5 to 2-3 meq/100g typical for sandy sediments (Dance and Reardon, 1983, Beekman, 1991, this study). This could well explain why detailed documentation of cation exchange processes seldom has been obtained in the field for seawater intrusion events in aquifers.

3.2 Redox-processes

Redox-processes have been studied extensively in marine environments and have also been documented quite well in fresh groundwater aquifers. Less often redox-processes have been studied in the transition zone between seawater and freshwater (Edmunds and Walton, 1983, Magaritz and Luzier, 1985, Smart et al., 1988, Beekman, 1991, Stoessell et al., 1993, Stuyfzand, 1993).

Organic matter degradation is often the driving force for redox-processes in aquifers. The organic matter in an aquifer can be divided into two pools: 1) The sedimentary pool where the organic matter is deposited with the sediment and 2) a dissolved pool being leached down into the aquifer from the soil. The sedimentary pool is commonly by far the largest, but often have a low reactivity especially in old sediments (Jakobsen and Postma, 1994). In marine sediments the organic matter is largely consisting of plant remains such as seaweed and plankton with the addition of animal remains (Appelo and Postma 2001, in prep).

Microbiological mediated degradation of organic matter can broadly be described as a three-step process where at first fermenting bacteria, by hydrolysis, breaks down complex organic compounds such a polysaccharides to sugars and amino acids (Lovley and Chapelle, 1995). Other groups of fermenting bacteria further breaks down the organic matter to small organic molecules as acetate, formate and H_2, which finally are oxidized by the terminal electron accepting processes (TEAP's) to CO_2 and CH_4. However, microorganisms utilizing oxygen and nitrate are able to directly oxidize the complex organic compounds in one step (Lovley and Chapelle, 1995, Appelo and Postma, 2001 in prep.).

Redox conditions in sedimentary systems have been shown to occur as a spatial sequence of TEAPs, in a groundwater system, typically along a flow path (Champ et al., 1979 and Lovley and Chapelle, 1995). The sequence is beginning with the reduction of oxygen followed by nitrate, manganese-oxides (MnO_2), Fe(III)-oxides and –hydroxides, sulfate and finally methanogenesis. Along a flow path the TEAPs are from a thermodynamic sense generally proceeding from high energy yielding processes and towards processes of low energy yield. The sequence of redox reactions has previously been explained as competitive exclusion amongst groups of microorganisms using different TEAPs, but competing for the same limited substrate (Chapelle and Lovley, 1992). However, in recent years many of these TEAPs have been shown to be able to occur simultaneously, in a variety of environments, such as the reduction of sulfate and Fe(III) as pointed out by Postma and Jacobsen (1996). This was attributed to the large variation in the Fe(III)-oxide reactivity. But also sulfate reduction and methanogenesis have been shown to occur simultaneously (Parkes et al., 1990, Jakobsen and Postma, 1999). Postma and Jakobsen (1996) explain these concurrent redox-processes by a partial equilibrium model where the organic matter reactivity (or the initial step in the organic matter degradation: the fermentation) is the overall rate-controlling step. The TEAP's are therefore occurring close to equilibrium. This is in conflict with the competitive exclusion model based on the thermodynamic argument. The implication of the partial equilibrium model is that the rate of organic matter degradation is independent of the TEAP. This model is probably most applicable in aquifer systems where the reactivity of the organic matter and the organic matter content is low. Jakobsen and Postma (1994) determined organic matter degradation rates by radiotracer methods and found rates in the order of 0.1 - 9 mM-C/yr for Holocene and Pleistocene aquifers. For a much older Cretaceous aquifers Chapelle and McMahon (1991) obtained rates four orders of magnitude lower ($1.4 - 30 \cdot 10^{-5}$ mM-C/yr).

In the following focus will be devoted to sulfate reduction and methane formation in aquifers, processes being relevant to the field site. Sulfate concentrations are generally low in freshwater environments, but comparatively high in seawater. Sulfate reduction by microbial organic matter oxidation can be written as:

$$2CH_2O + SO_4^{2-} \rightarrow H_2S + 2HCO_3^- \qquad (3.6)$$

Organic matter is represented here as zero valent C simplified as the carbohydrate CH_2O, carbohydrates being the dominating substrates for organic matter oxidation in sediments (Conrad, 1999). The produced H_2S my react with Fe(III)-oxides present in the sediment to form Fe-monosulfides and eventually pyrite (Appelo and Postma, 1993).

The rate of sulfate reduction was found to be independent of the sulfate concentration down to a concentration of 1 mM (Berner, 1981) indicating that the amount and reactivity of organic matter is controlling the rate. At lower concentrations the rate becomes first order with respect to the sulfate concentration (Boudreau and Westrich, 1984).

Methanogenesis has been shown to occur microbiologically along two pathways (Appelo and Postma, 1993). As a reduction of CO_2:

$$CO_2 + 4H_2 \rightarrow 2H_2O + CH_4 \qquad (3.7)$$

And fermentation of acetate:

$$CH_3COOH \rightarrow CH_4 + CO_2 \qquad (3.8)$$

Acetate fermentation is according to Whiticar (1999) dominating in freshwater environments. Whereas in marine environments CO_2 reduction is the dominating pathway, mainly because the preceding sulfate reduction has depleted acetate as the organic substrates (Whiticar, 1999). However, Hansen et al., (2001) found the CO_2 reduction pathway to be by far the dominating in a

freshwater aquifer. So in reality things are not that simple. In this project only the bulk pathway for methane formation will be considered:

$$2CH_2O \rightarrow CH_4 + CO_2 \qquad (3.9)$$

Sulfate has in a number of studies been shown to be able to oxidize methane as observed in marine sediments (Barnes and Goldberg, 1976, Martens and Berner, 1977, Reeburgh, 1980 and Iversen and Jørgensen, 1985, Hoehler et al., 1994). This has also been shown for freshwater environments (e.g. Whiticar, 1999). Re-oxidation of methane by sulfate may be written as:

$$CH_4 + SO_4^{2-} \rightarrow HS^- + HCO_3^- + H_2O \qquad (3.10)$$

However, Hoehler et al. (1994) have shown for marine sediments that the mechanism is more complex. Methanogene bacteria are by a reversal of (3.7) able to oxidise methane. But they seem to require the presence of sulfate reducing bacteria which are responsible for maintaining a low H_2 concentration, a prerequisite for making the reversal of (3.7) energetically favourable for the methanogene bacteria (Hoehler et al., 1994).

During a seawater intrusion event the high sulfate content of seawater makes it likely that sulfate reduction becomes the dominating TEAP. Depletion of sulfate is a common observation in seawater intrusion studies (Nadler et al., 1980, Hahn, 1991, Stuyfzand, 1993, Barker et al., 1998 and Logan et al., 1999).

a) Piezometers and transect wells

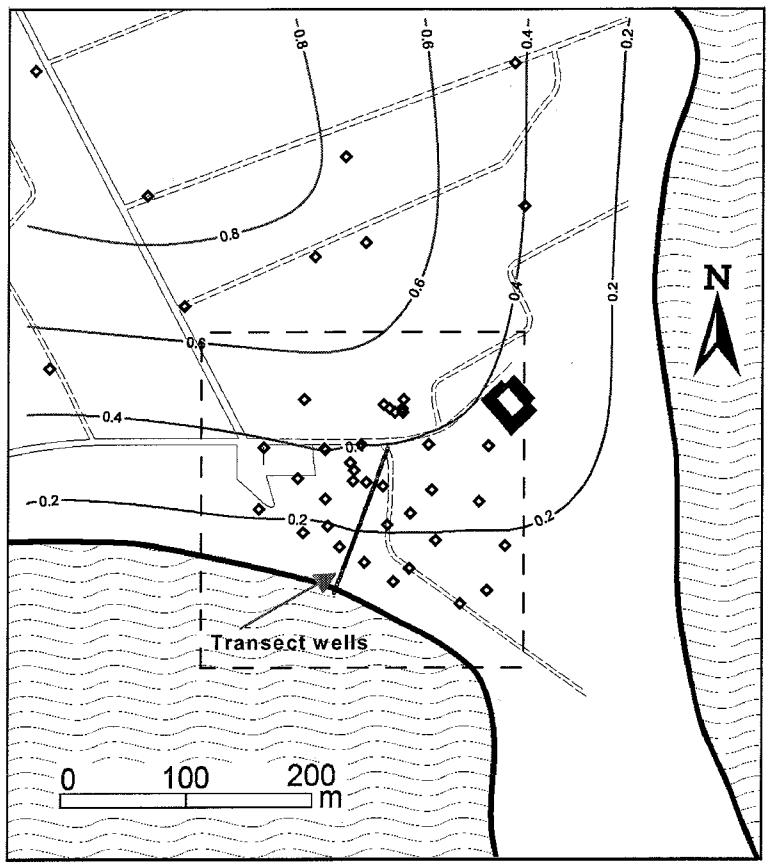

b) Pumping wells, El-logs, water chemistry profiles
& sediment lithology profiles

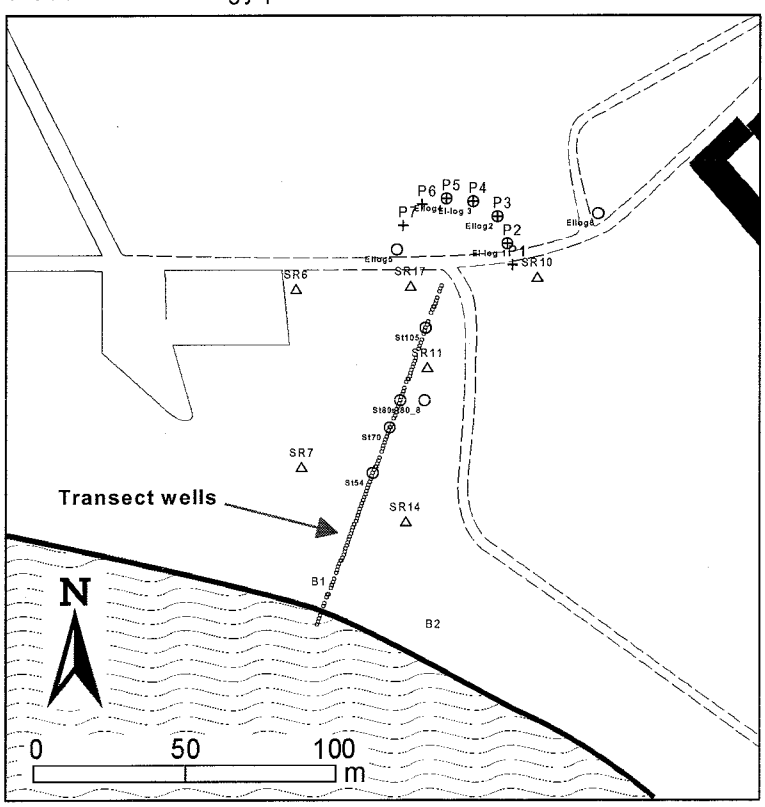

Figure 4.1: Positions of a) Piezometers (◊) and transect line of 106 wells (o) b) Positions of pumping wells P1 to P7 (+), El-logs (O), water chemistry profiles (△) & sediment lithology profiles (B1 & B2). (Fig. 4.1b is the broken line frame inserted in a).

4. METHODOLOGY

4.1 Field work

4.1.1 Installation of wells and piezometers

Piezometers

Piezometers were installed at several stages. The first set of piezometers was installed by hand auger to a depth of 0.5 to 1 m below the groundwater surface. These piezometers are constructed of 16 mm PVC piping fitted at the bottom with 0.3 mm nylon mesh. About 20 of this type of piezometers were installed in the area. A second set of about 20 piezometers was installed later to get a better coverage of the area. They were placed a few meters below the water table in order to avoid drying up as a result of the drawdown created by the intrusion experiment. These piezometers were similar to the monitoring wells of the transect (described below). The positions of the piezometers are shown in Figure 4.1a.

Transect of monitoring wells

Based on head measurements in the first 20 piezometers a transect line was defined, perpendicular to the coastline and roughly parallel to the direction of the natural groundwater flow (see Fig. 4.1a). Along this line 106 monitoring wells were installed over a distance of 120 meters. The monitoring wells are named St followed by a suffix number indicating the distance to the coast. The wells were screened at different elevations between –1 and –9 meters creating a sampling grid (Figure 4.2). This system of single level wells was chosen over multilevel nested monitoring wells because more evenly distributed information is obtained from a given number of sampling ports. Furthermore single level wells eliminate the risk of flow between sampling ports in a multilevel well (Fetter, 1993).

Each monitoring well ends in a 12 cm screen designed for both hydraulic testing and for sampling of groundwater (Figure 4.3). The monitoring wells were constructed entirely of polyethylene (PE). The casing consists of 25 mm OD black PE pipe suitable for water supply. Filter tips were constructed of 25 mm (OD) white PE pipe with four rows of drilled holes and a spiral groove for easing the access of groundwater into the well. On the outside the filter tips were clad with a 50μm PE mesh. The top of the filter is equipped with a sharp edge that fits a Teflon ball, which serves as a

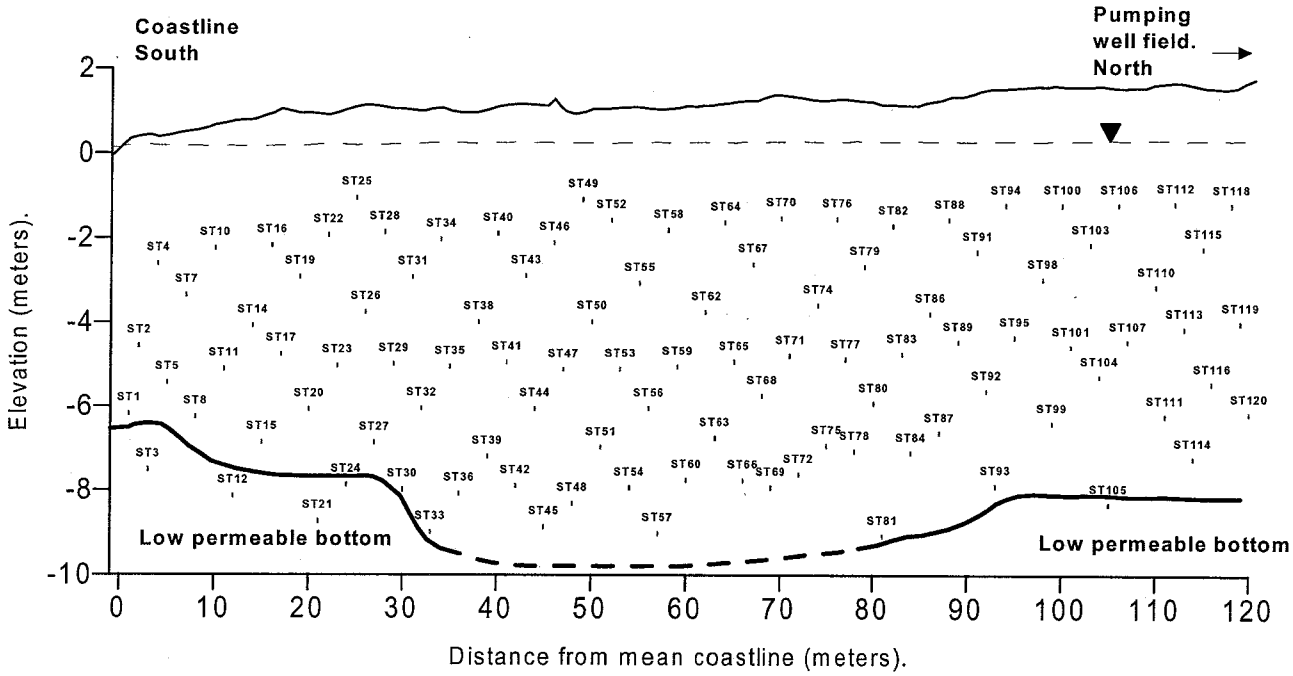

Figure 4.2: Vertical cross-section showing filter screen positions in the transect of monitoring wells.

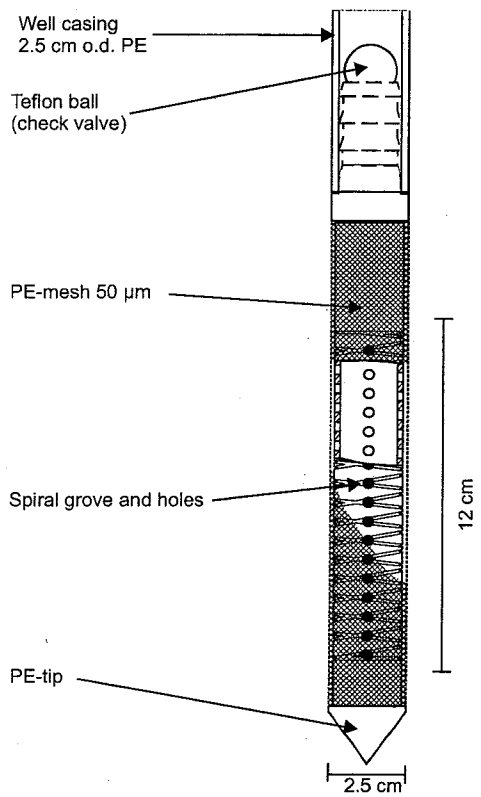

Figure 4.3: Filter-tip for groundwater sampling and hydraulic testing for monitoring wells. All parts are in PE (Poly Ethylene).

check valve during groundwater sampling. Between sampling the Teflon ball is removed from the well.

The monitoring wells were installed using 54 mm (OD) treaded steel pipes driven into the ground by a Geoprobe 54 DT model drilling rig. The bottom 1.3 m pipe was stainless steel and fitted with a PE tip, which was knocked out at the desired installation depth. The monitoring well casing was quickly lowered into the steel pipes, and then the steel pipes were retracted with the Geoprobe. At the ground surface the well was completed with a vented protective cap. Stainless steel and PE was chosen to minimize effects on redox processes (Bjerg et al., 1997)

Pumping wells

A pumping well field was established at the landward end of the monitoring transect (Fig. 4.1b), for the forced seawater intrusion experiment. The seven pumping wells are situated on a half circle symmetrically around the extension of the monitoring transect. The half circle is centred 10 meters inland from Monitoring well no. St120 and has a radius of 20 meters. There is approx. 10 meters between neighbouring borings on the circle periphery. 8-inch diameter boreholes were drilled with a hollow stem auger rig to a depth of 9 – 10 metres. The wells were cased with 110 mm polyethylene (PE) pipes and screened from 3 m.b.s. to the bottom with slotted PE casing covered on the outside with a double PE sock with a mesh size of 0.3 mm.

Drive point wells – water sampling

Seven reconnaissance water chemistry profiles were conducted within the field area. The groundwater samples were obtained by driving 1 inch steel pipes fitted with a 6 cm long filter tip into the ground with a Cobra MK 1 pneumatic hammer. The filter tip is constructed of stainless steel and clad with a 50 µm stainless steel screen. Intervals between samples varied from 0.25 to 1 m. Locations of the water chemistry profiles are shown in Figure 4.1b.

4.1.2 Sediment sampling

To map local geology

Sediment samples for lithological descriptions and grain size analysis were taken by a bottom-loading-bailer technique. A 100 mm ID PVC casing was worked in to the ground as sediment was

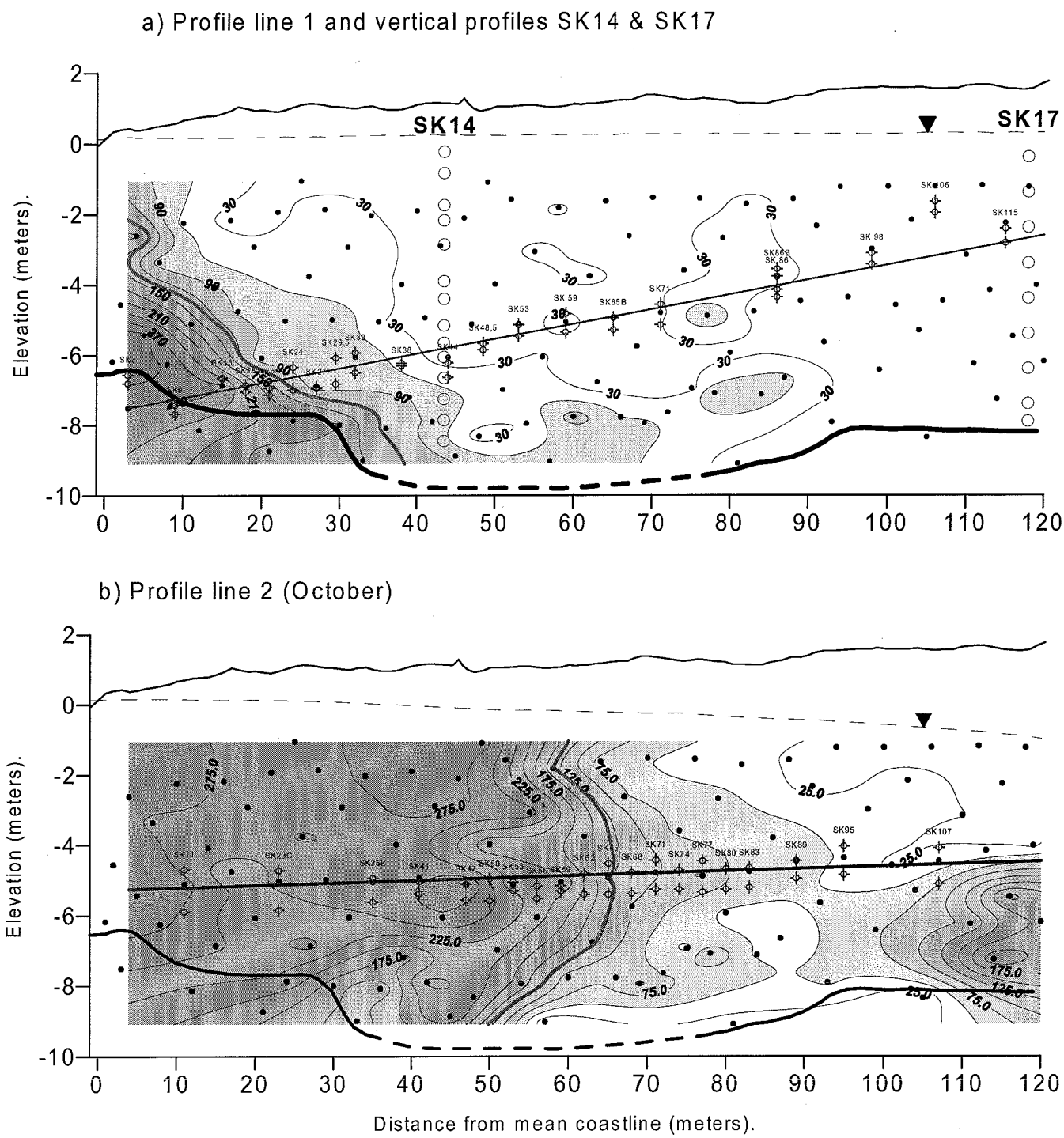

Figure 4.4: Sediment cores collected in or near the transect: a) Profiles SK14 and SK17 obtained during the steady state situation August-September 1999 and profile line 1: Cores taken prior to the forced seawater intrusion, but after the inundation March-April 2000 and b) profile line 2: Cores sampled during the seawater intrusion September-October 2000. The two (¤) marks for each boring in the profiles 1 and 2 indicate maximum and minimum sample position depths given by the depth positioning uncertainty. Chloride concentrations (in mM) are contoured as background.

removed from the interior of the casing by the pumping motion of a bottom-loading-bailer (Eijkelkamp). At regular intervals the bailer was brought to the surface and emptied for sediment. A disadvantage of this technique is that the sediment tends to get mixed and becomes somewhat sorted by the lapping motion of the bailer within the liner. These borings could rarely be taken deeper than 6 m. The locations of two of these borings (B1 & B2) are shown in Figure 4.1b.

Sediment coring

Relatively intact sediment cores were taken in or near the transect for various chemical analysis. The coring was undertaken by two different methods in three campaigns:

1) In the pristine steady state situation August-September 1999
2) After the storm induced seawater inundation in March-April 2000, but prior to the intrusion experiment
3) During the seawater intrusion September-October 2000

During the first campaign the cores were taken as vertical depth profiles at two locations SK14 16.5 m east of St38 in the transect and SK17 10 m vest of St120 at same positions as water chemistry profiles SR14 and SR17 in Fig. 4.1b. The length of the depth profiles was 8 m (SK14) and 7.5 m (SK17). These cores were taken with a piston-corer in 50 mm stainless steel pipes, in lengths of up to 4 m. The piston corer was driven into the ground by a pneumatic hammer (Cobra MK 1). After the cores were pulled to the surface they were immediately sectioned into lengths of 1 meter, sealed and kept below 8 °C. Sub samples were taken for laboratory analysis for every half-meter in SK14 and every meter in SK17 (see Figure 4.4a).

In each of the two last campaigns 20 single cores of up to about 1 m in length were taken in positions parallel to and less than 1 meter from the transect, resulting in 2 sub-horizontal profile lines as shown in Figure 4.4a and 4.4b. For these two last campaigns a different coring technique was employed: A Geoprobe 54 DT Model were used to drive and retract the coring device in to the ground. Again a piston coring system was used, this time with 1.2 m long 43 mm ID PVC liners.

Often the PVC liners were only partly filled when retracted to the surface. Generally a position was re-cored if a liner was less than half filled with sediment. In a few cases this was not possible

because of difficulties in obtaining enough sample. Several explanations can be given for the partially filled PVC liners. The sediment may slide out of the liner as it is retracted to the surface. Alternatively the sediment entry in to the core line may be obstructed by stones or by friction in the sediment and the coring system. Most often the exact cause could not be determined. Because of this, some uncertainty is associated with the depth of the cores. For a core liner only half full (60 cm of sediment) the error on the depth could be as high as 60 cm. At times the coring device had to be driven more than 1.2 m to obtain a sufficiently large sediment sample. For a few cores the maximum error was therefore as much as 1 m. In coarse-grained core samples some of the pore water was lost due to drainage.

4.1.3 Positioning of wells

Positioning of installed wells and sediment coring locations were done with a Trimble Pathfinder Pro XRS DGPS (Differential Global Positioning System). Measuring time at each position varied from 10 to 30 minutes depending on satellite coverage. The precision in the plane is better than 1 m. Levels of well heads were obtained by using traditional levelling equipment.

4.1.4 Geophysical logs and surveys

El-logs

Continuous electrical conductivity logs (El-logs) were drilled with a 54 DT Geoprobe employing a hydraulic hammer for driving down the SC400 log-tool. The log tool is mounted just behind the drive point and consist of a Wenner array of four electrodes with a spacing of a = 25.4 mm. Measurements were conducted every 1.5 centimetres. The location of the El-logs is shown in Figure 4.1b.

The primary purpose of these El-logs was to determine the depth to the bottom of the aquifer. At the field site the aquitard generally has a higher electrical conductivity than the aquifer. The depth to the bottom aquitard can also be identified by other methods: 1) Levels in water sampling profiles that yield no water 2) A slugtest showing low permeability and 3) Visual identification of low permeable layers in sediment cores. However, these methods are not as precise as the El-log. The two first methods are based on discrete point measurements typically separated 0.5 to 1 m vertically

resulting in considerable uncertainty. These methods are thus more qualitative indicators of the presence of the aquitard. The sediment coring methodology also has considerable uncertainty in depth positioning (see section 4.1.2). The El-log method is the most reliable in accurately locating the aquifer/aquitard interface, except close to the coast where it becomes more problematic, due to high electrical conductivity of the pore water.

Natural gamma logs

Natural gamma logs were obtained, using a Nucletronics equipment with a 15 mm o.d. gamma scintillation detector, in two deep monitoring wells St21 (-8.7 m) and St81 (-9 m). The purpose was to detect variation in clay content of the aquifer or bottom aquitard.

GPR survey

GPR (Ground Penetrating Radar) surveys were conducted on the surface with the purpose of detecting subsurface structures in the aquifer. An antenna with a transmitting frequency of 300 MHz was used. The penetration depth of the system was up to 6 m in the part of the aquifer containing fresh groundwater. The penetration depth was reduced to less than 2 m, where the aquifer contained salt- or brackish water. This is caused by attenuation of the signal due to the high electrical conductivity of the pore water.

4.1.5 EC measurements

Electrical conductivity (EC) measurements of groundwater samples were used to measure the saltwater content and to monitor the progress of the seawater intrusion during the experiment, because of the ease of acquiring data in the field. Groundwater samples for EC measurements were obtained using a sampling tube with a tip that fits tightly into the top of the screens in the monitoring wells. In this way the total water volume in the well need not to be flushed before the measurement. The groundwater samples were pumped from the filter tip, using a peristaltic pump (Ismatec ISM058-0213), through a flow cell with an EC probe (WTW Tetracon 96) connected to a conductivity meter (WTW LF-196). EC-readings (corrected to a reference temperature of 25 °C) were taken after a few minutes when the EC-value had stabilised.

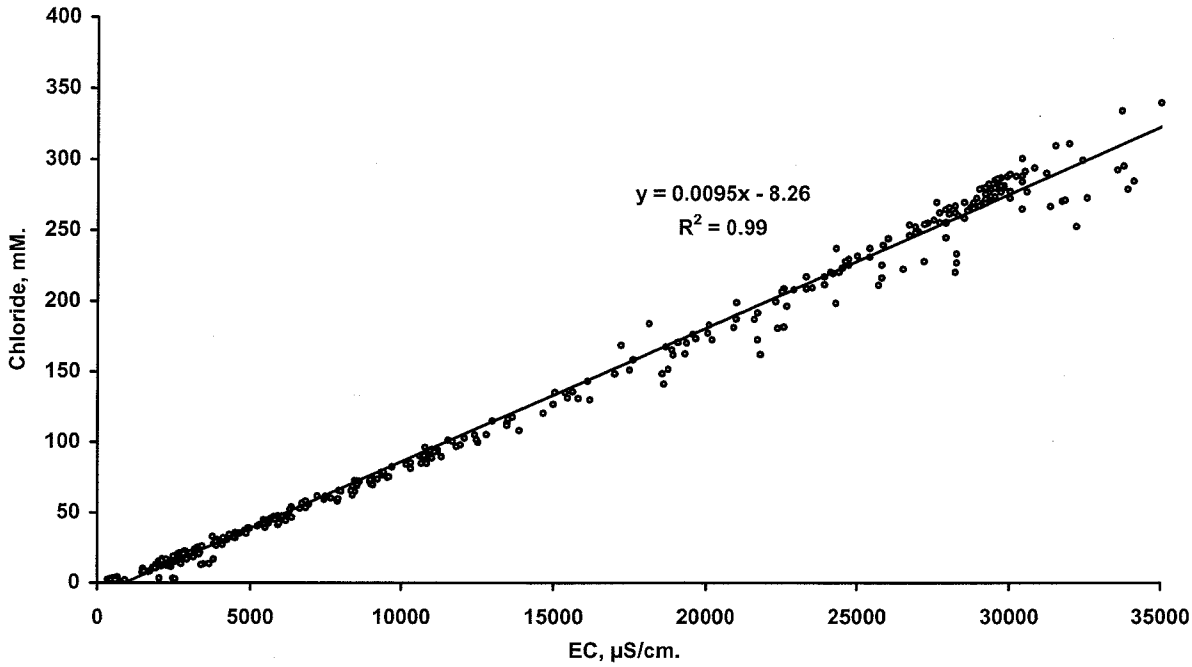

Figure 4.5: Electrical conductivity (EC) in µS/cm vs. chloride concentration in mM. The plot includes all groundwater samples from the four groundwater sampling campaigns of August 1999, March 2000, October 2000 and January 2001, using all sampling points in the transect.

In Figure 4.5 the EC is plotted vs. the chloride concentration, which behaves conservatively and is thus a measure of the seawater component. A good correlation between EC and the chloride concentration is obtained. For low EC and chloride concentrations the correlation deviates because the dominant ions, Ca^{2+} and HCO_3^-, in freshwater significantly influence the conductivity. However, for the purpose of getting the general saltwater distribution the EC is sufficiently accurate.

Continuous EC measurements

Continuous measurements of groundwater EC were performed in selected borings. Laboratory 2 pole conductivity cells (Radiometer CDC 745-9) were modified for in-situ groundwater installation. The dimensions of the Radiometer cells allowed installation directly within the filters of the transect wells, in the flowing groundwater. The cells were fitted with 10 m cables and connections were made waterproof. Aquatronic microloggers (versions 3.0-4 and 3.0-7) were used for collecting data. The electrical configuration of the EC-cell/data-logger system necessitated the incorporation of a 100-ohm resistor on the cable in order to extend the measuring range of the system, to encompass the electrical conductivities of the field site. Each EC-cell/data-logger system was calibrated in the laboratory using a standard series of KCl-solutions enabling the conversion of the logged signal to true EC.

4.1.6 Temperature determinations

The groundwater temperature at the filter level in the monitoring wells was measured shortly after groundwater sampling when the wells were filed with fresh groundwater. A temperature probe Ebro TFN-1093 with 10 m cable was lowered directly into the well filter and allowed to stabilise for a few minutes. The sensitivity of the probe is $\pm$ 0.2 °C.

4.1.7 Hydraulic head measurements

Measurements of hydraulic head was performed regularly using a manual dip-meter in the piezometers and in the transect wells. Pressure transducers (Druck) connected to data-loggers (Tinytalk II, Gemini Data) were installed in selected monitoring wells for collecting time series of the hydraulic head.

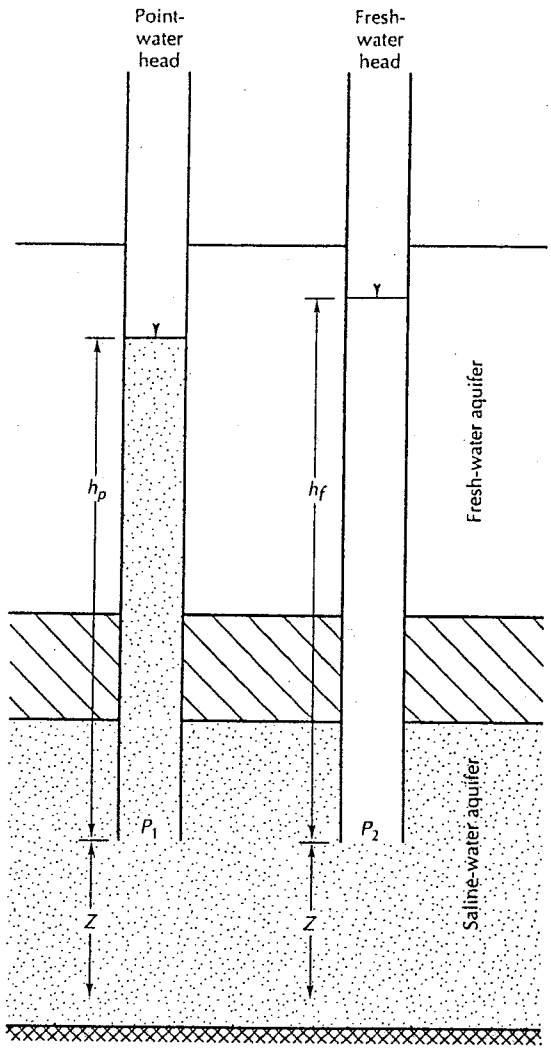

Figure 4.6: Point-water head (h_p) and freshwater head (h_f) above a datum (z) in an aquifer of varying density. a) Not corrected b) corrected (from Fetter, 1994).

Correcting hydraulic head measurements

In an area of varying salinities, and thus varying densities, the measured water level from a partially screened well must be density corrected, to enable a correct interpretation of the hydraulic head distribution (Kohout, 1964 and Fetter, 1994). The density correction is necessary in deeper wells where the density effect becomes larger than the measuring uncertainty. The correction is accomplished by converting the observed point-water pressure head h_p, which is the distance from the measured water level in a well to the filter, to a freshwater pressure head h_f (Lusczynski, 1961):

$$h_f = h_p \cdot (\rho_s / \rho_f) \tag{4.2}$$

where ρ_s is the saltwater density in the given well and ρ_f is the freshwater density (see Figure 4.6). The freshwater pressure head (h_f) is added to the elevation (z) of the filter for each well to obtain the freshwater head.

The water density was derived from the electrical conductivity (EC) according to the relation (Stuyfzand, 1989):

$$TDS = 0.69778 \cdot 10^{-6} \cdot EC_{20} \tag{4.2}$$

and

$$\rho = \left(1 + 0.805 \cdot TDS - 6.5 \cdot 10^{-6} \cdot (T - 4 + 221.4 \cdot TDS)^2\right) 1000 \tag{4.3}$$

where EC_{20} is EC at the references temperature of 20 °C (in µS/cm), TDS is total dissolved solids in (kg/kg solution), T is temperature in Celsius and ρ is the density (kg/m^3). First the EC has to be corrected from the measurement reference temperature of 25 °C (in this study) to 20 °C. By applying the Arps (1953) equation (as given in Worthington et al, (1990)) the EC can be temperature corrected assuming that mainly Na^+ and Cl^- control the EC:

$$EC_{T1} = EC_{T2} \cdot \frac{(T_1 + 21.4)}{(T_2 + 21.4)} \tag{4.4}$$

For the deepest monitoring wells in the saline part of the aquifer the density correction changes the groundwater heads with up to 11 cm.

4.1.8 Calculating pore water conductivity from el-log bulk conductivities

Continuous vertical profiles of pore water conductivities σ_w (µS/cm) were calculated from the bulk electrical conductivities σ_b (µS/cm) obtained by El-logs. The conversion was achieved by applying Archie's relation (Archie, 1942) as given in Telford et al. (1990) for fully water saturated sand:

$$\sigma_w = a \cdot \phi^{-m} \cdot \sigma_b \qquad (4.5)$$

Where ϕ is porosity and a and m are constants depended on the tortuosity of the pore space, degree of cementation, etc. For fluvial deposited sands (Danish Forest and Nature Agency, 1987) gives the relation:

$$\sigma_w = 1.26 \cdot (0.35)^{-1.2} \cdot \sigma_b \qquad (4.6)$$

For Skansehage a porosity of 0.35 with a standard deviation of $\pm$ 0.025 is used (for porosity determination see section 4.2.2) giving:

$$\sigma_w = 4.44 \cdot \sigma_b$$

Where the factor of 4.44 varies from 4.09 to 4.85 with the standard deviation on the porosity. The logs were also corrected for temperature (from 10 to 25 °C) with the Arps equation (4.4) (see section 4.1.7) to enable comparison with direct groundwater EC measurements from the transect.

4.1.9 Hydraulic tests

Estimates of the hydraulic conductivity were obtained by performing slugtests in all the monitoring wells in the transect and by a pumping test in the pumping well field.

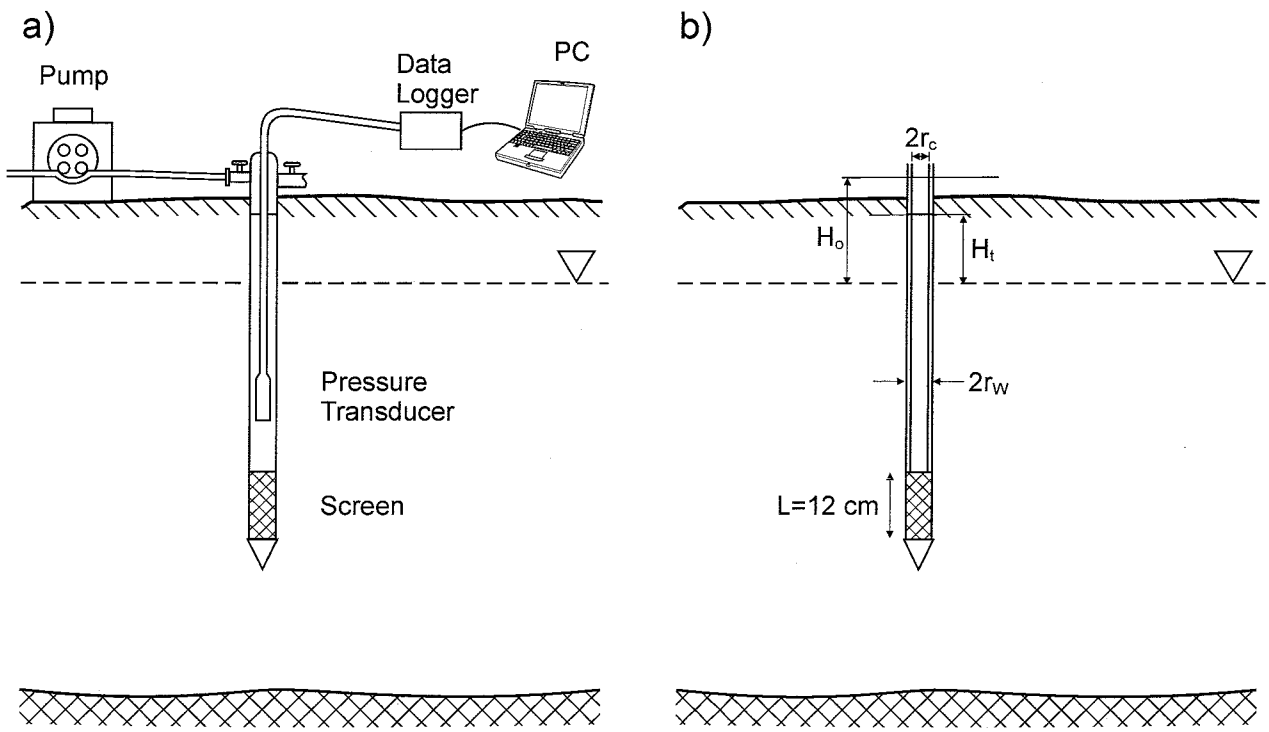

Figure 4.7: Slugtest system a) Schematics of vacuum method b) Geometry of the system

Slugtests

A slugtest method using vacuum (Hinsby et al., 1991) was employed as sketched in Figure 4.7a. Prior to the slugtest the wells were pumped for 10-15 minutes or until the pumped water was clean. The difference between the initial head and the head created by the vacuum was typically in the order 1 to 1½ meters. The vacuum was maintained for 5 minutes and then released instantaneously. The recovery of the water level was monitored with a small generic pressure transducer set for logging every second (with a Tinytalk II data-logger). For wells screened in low permeable layers with a hydraulic conductivity (K) less than $1 \cdot 10^{-6}$ m/s the vacuum method was not used. Instead a volume of water was pumped out, lowering the water level in the well by 1 to 2 meters and the recovery of the water level was monitored manually with a dip meter.

The slugtest data of heads versus time was analysed by the Hvorslev method (Hvorslev, 1951). Figure 4.7b shows the geometry of the Hvorslev method. If the relative head difference $(Ht-H_0)/H_0$ is plotted vs. time in a semi logarithmic plot a straight line with the slope λ should be obtained. The hydraulic conductivity (K) can then be derived from (Hvorslev, 1951):

$$K = \frac{\ln(L/\ r_w) \cdot r_c^2}{2 \cdot L} \cdot \lambda. \qquad (4.7)$$

Where: K is hydraulic conductivity (m/s)

L is screen length (m)

r_c is inner radius of casing (m) (corrected for the presence of the pressure transducer)

r_w is outer well screen radius (m)

λ is the slope (s^{-1}) in a semi logarithmic plot of the relative head difference $(Ht-H_0)/H_0$ vs. time (s).

For equation (4.7) to be valid L/r_c must be larger than 8. The well screens in the transect were designed so that $L/r_c = 12$.

Pumping test

A pumping test was conducted in one of the pumping wells (well 5) in the pumping well field to the north of the monitoring transect (Fig. 4.8). The well was pumped with an initial rate of 9 m^3/h for

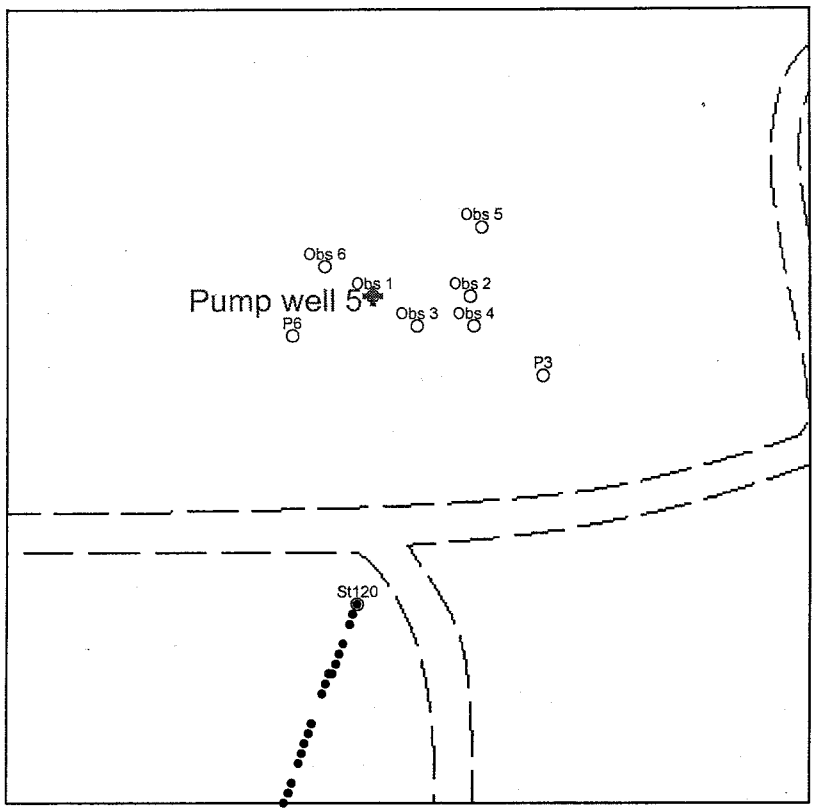

Figure 4.8: Pumptest geometry: Postion of pumping well 5 (+), observation wells (O) and transect wells (o).

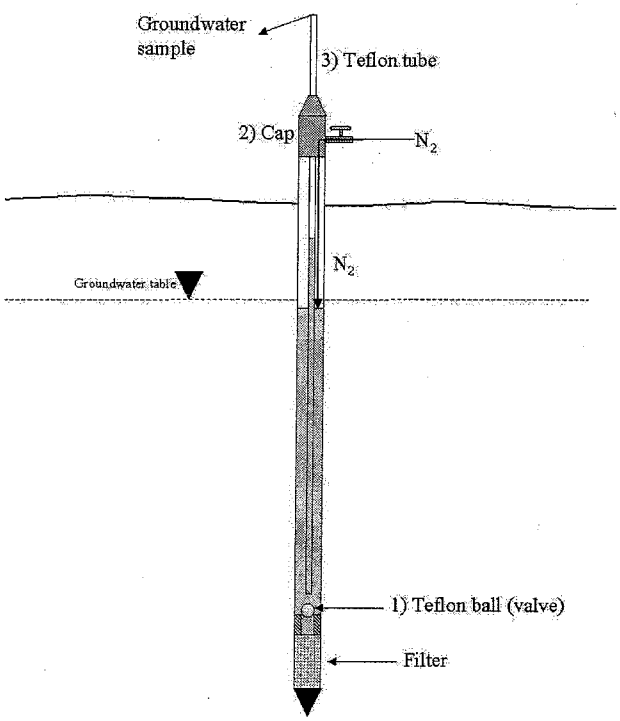

Figure 4.9: Groundwater sampling by gas-lift.

24 hours. The water table drawdown was monitored in 9 observation wells. The drawdown and recovery curves were analysed with the Jacobs and the Theis methods modified for the unconfined condition (Kruseman and de Ridder 1983).

4.1.10 Instrumentation of the pumping well field

Each pumping well was fitted with a SQE-7 Grundfos submersible pump placed 2 meters above the bottom of the boring. A Grundfos CU-300 control unit for each pump was hooked up to a gateway G-100 serving as a data logger and communication unit. The G-100 was connected to a modem enabling remote monitoring of pump performance and interactive operation of pump settings such as speed etc. The G-100 could also be directly connected to a computer for direct manipulation at the field site. Each pump had a mechanical flow meter fitted on the discharge pipe. Digital pulse sensors on the flow meters recorded the cumulative discharge, which was stored in the gateway G-100. The pumped groundwater was discharged into the fjord to the east of the field site. Figure 4.1b show the placement of the pumping wells.

4.1.11 Groundwater sampling procedure

Groundwater was sampled from the monitoring wells with a gas-displacement technique using nitrogen gas (Figure 4.9). In short this method consist of: 1) a Teflon ball which serves as a check valve on top of the filter 2) a cap with a valve for pressurising the boring and 3) a Teflon tube (6 mm I.D.) for leading the water sample to the surface. When the boring is pressurised with $N_2(g)$ at the top, the Teflon ball will prevent water within the boring to flow out into the formation. Instead the water will be forced up through the Teflon tube. Once the over pressure is released, fresh groundwater from the formation will enter the boring through the filter and past the Teflon ball. The Teflon ball can be removed after sampling, enabling hydraulic testing and other investigations in the monitoring wells. Between ½ and 1½ bar of N_2-pressure was used for sampling depending of the depth of the well.

The gas-lift technique has several advantages as opposed to sampling with a suction pump: 1) The well volume will be completely emptied each time the well is pressurised and water representing the chemistry in the formation can quickly be obtained. 2) The water sample will not be stripped for

volatile gases such as CO_2, H_2S, CH_4, etc. to the same extent as when suction is used. 3) Nitrogen is an inert gas and will not react with redox-sensitive components in the water.

Although Nitrogen gas is inert, gasses dissolved in the water will have a tendency to be stripped from the solution and into the N_2 gas phase. This stripping has a measurable impact on the chemistry of the water in close contact with N_2. This will happen at two places in the boring: At the gas/water interface in the Teflon tube and at the gas/water interface in the boring itself. Therefore, the first and the last portion of water being sampled in one well volume will be affected by gas stripping. For this reason the first and the last couple of hundred ml of water from each sampled well volume was discarded.

The discharge Teflon tube from the well was connected to an inline flow cell equipped with probes for O_2, pH and EC. The monitoring wells were purged at least three times or until the water was not turbid and until reasonably constant readings of electrical conductivity and pH were obtained.

4.1.12 Field analysis and storing of groundwater samples

The electrical conductivity (EC) was measured with a WTW Tetracon 96 EC probe connected to a conductivity meter (WTW LF-196). pH was measured with a WTW SenTix 41 electrode connected to a WTW 196 pH-meter. Dissolved O_2 was measured with a WTW EO 196-1,5 electrode connected to a WTW OXI 196 Oximeter. All three parameters were measured directly on unfiltered groundwater in the in-line flow cell.

Samples for methane (CH_4) were taken directly from the discharge Teflon tube. A syringe needle was attached to the tube and the sample injected through a butyl rubber stopper into a weighed and pre-evacuated 10 ml Venoject glass VT-100. About 2 - 5 ml sample was injected leaving a headspace of 8 - 5 ml for collecting the methane. The vial was frozen upside down immediately after sampling thereby trapping the gas phase. Samples for all succeeding parameters were collected in 60 ml syringes and filtered through 0.2 µm Sartorius Minisart cellulose acetate (CA) filters. Sub samples for major cations and anions were all taken from the same 60 ml syringe.

Ferrous iron (Fe^{2+}) was measured in the field by the spectrophotometric Ferrozine method (Stookey, 1970). A Dr Lange spectrophotometer LPG-125 was used. 2.0 ml sample was directly filtered in to a cuvette containing 0.1 ml of Ferrozine. Alkalinity was determined by the Gran-titration method (Stumm and Morgan, 1981). 10 or 20 ml of sample was titrated with a 0.1 M HCl solution to a pH of about 4.5 where upon acid was added in 0.05 ml steps for a minimum of 8 steps and the pH recorded for each step. 50 ml samples for the cations: Na^+, Ca^{2+}, Mg^{2+} and K^+ were preserved with a 2 % 7 M HNO_3 solution and refrigerated until analysis in the lab. Samples for the cation NH_4^+ and the anions Cl^-, SO_4^{2-}, and PO_4^{3-} were collected in 20 ml PE-vials and frozen immediately after sampling. Sulfide was filtered directly into a 5 ml vial containing 2 ml 4 % Zn-acetate solution and refrigerated. The amount of sample, about two grams, was determined in the field by weight (with 3 decimals). The Zn-acetate solution retains the volatile sulfide by precipitating it as insoluble ZnS_2. Samples for dissolved organic carbon (DOC) were collected as both filtered and unfiltered sub samples in 20 ml glass vials and the pH was adjusted to about 2 with 2M HCl and refrigerated. 5 ml of sample was collected for formate and acetate, filtered into PE vials and frozen immediately after.

4.2 Laboratory work

4.2.1 Water analysis

The cations (Ca^{2+}, Mg^{2+}, Mn^{2+} and total Fe) were analysed by Atomic Absorption Spectrophotometry (AAS) using a GBC 932AA. Na^+ and K^+ were determined by emission on the same equipment. NH_4^+ was determined by Flow Injection Analysis (FIA) on a Tecator FIAstar 5010 analyser. Sulfate and chloride, were determined on an Ion Chromatograph (IC) using a Jasco HPLC 800 series system fitted with a Vydac 302IC column. Formate and acetate were also determined with IC but with a Dionex Ion Pac ICE-AS1 column using an ion-exclusion and suppressor technique. Sulfide was measured spectrophotometrically on a Dr Lange LPG-125 by the Methylene blue method (Cline, 1967). Phosphate was also measured spectrophotometrically on a Dr Lange LPG-125 by the Ammonium molybdate method (EN 1189, 1996). Methane was determined on a SRI 8610A gas chromatograph (GC). DOC was analysed on a Shimatzu 5000 TOC analyser.

For most groundwater samples the total error of analysis (Electro Neutrality) was generally in the order of 2 to 3% and less than 5% except for a few samples.

PHREEQC speciation

The code PHREEQC (Parkhurst and Appelo, 1999) was used to calculate the speciation for the water samples, especially the speciation of the carbonate system. The program takes into account the alkalinity contributions from dissolved sulfide and phosphate species in deriving the dissolved total inorganic carbon (TIC). For a few water samples HS^- make up 5% of the total alkalinity. The alkalinity contribution from deprotonated organic acid groups (contained in the DOC) are not included, but they probably only amount to 1-2% even for the samples with DOC levels up to 22 mM. Also saturation indexes for different relevant minerals such as calcite, gypsum, etc. were calculated with PHREEQC.

4.2.2 Sediment analysis

Grain size analysis

Grain size analyses were obtained by sieving of about 100 g of dried sediment sample. Sieve sizes were 0.063, 0.09, 0.125, 0.180, 0.250, 0.355, 0.500, 1.000, 2.000, 2.830 and 4.000 mm.

Water content

The water content of sediment samples was determined as the weight loss of a 10 g sub sample dried at 105 °C for 24 hours.

Porosity determination

The porosity (ε) was determined on all the core sub-sections taken for CEC analysis. The wet sediment mass (M_{wet}) was obtained by weighing the core liner with sediment and subtracting the weight of the empty core liner afterwards. The volumes (V_{tot}) of the respective core liner sections were estimated both by measuring average dimensions of the not perfectly cylindrical sections and by weighing sections filled with distilled water. Comparable results were obtained with the two methods. The dry sediment mass (M_{dry}) was obtained by using the volumetric water content (W_w): $M_{dry} = M_{wet} \cdot (1-W_w)$. The solid density ($\rho_s$) of the sediment was assumed equal to that of quartz ($\rho_{qaurtz} = 2.65$ g/cm^3). An estimate of the porosity can be found: $\varepsilon = 1-((M_{dry}/\rho_s)/V_{tot})$. Also the bulk density (ρ_b) can then be calculated: $\rho_b = M_{dry}/V_{tot}$. The assumption of $\rho_s = \rho_{quartz}$ is not valid for the

samples containing peat, which has a lower solid density. For the peat samples a realistic porosity estimate can be made by: $\varepsilon = (M_{wet} \cdot W_w)/V_{tot}$ because only minimal drainage occurred for the core sections containing peat. A potential error with these porosity estimates is that the porosity could have changed when the sediment entered the liner during the coring being either compacted or packed more loosely than in situ.

CEC and exchangeable cations

The content of the exchangeable cations Ca^{2+}, Mg^{2+}, Na^{+}, K^{+} and ammonium on the sediment was determined by ion displacement using separately a 1 M NaCl solution and a 1M NH_4Cl solution (Van der Molen 1958, and Appelo, 1996). The CEC (cation exchange capacity) was calculated as the sum of these exchangeable cations. Exchangeable cation concentrations were determined on the core sections from profile 1 and 2 in Figure 4.4a&b.

The cores were sectioned into 10 cm pieces and mixed thoroughly. From the mixed sample two 10 g sub-samples of sediment were taken for the determination of the water content. A sub sample of about 20 g was used for the determination of adsorbed cations and CEC. The remaining sediment was centrifuged at 3000 rpm for 30 min in order to extract the pore water for the determination of cations in solution.

Sub samples for CEC were divided in two 10 g portions, one for treatment with a 1 M NaCl solution the other with a 1M NH_4Cl solution. Prior to this treatment the samples were percolated with ethanol (as suggested by Appelo, 1996) in a Buchner like funnel over a 0.45μm (Whatman) polypropylene filter. The purpose of this ethanol percolation is to displace the pore water from the sediment. This is necessary because the contribution of cations from the pore water in sediment samples with saline or brackish pore water can be more than ten times greater than the exchangeable fraction. 10 ml of 96% ethanol was carefully poured on the sediment sample and drawn through the sediment by suction. The ethanol remaining in the sediment was removed by overnight evaporation. The sediments were transferred to small 35 ml Polycarbonate centrifuge tubes. About 30 ml of a 1 M NaCl solution was applied to one set of sub-samples and 1 M NH_4Cl solution was added to the other set. The centrifuge tubes were shaken end over end (using a Gerhardt RA20) for 20 min and subsequently centrifuged at 3000 rpm for 30 min in order to settle

the fines. After this the supernatant was removed with a syringe and filtered through a 0.2μm Satorius Minisart (CA) filter.

From the NaCl supernatant about 15 ml was used for the analysis of Ca^{2+}, Mg^{2+}, and K^+ and preserved with 1 % 7M HNO_3. A 5 ml sub sample was used for analysis of NH_4^+ and conserved by freezing. The NH_4Cl supernatant was used for determination of Na^+ and also preserved with 1 % 7M HNO_3. The cations Ca^{2+} and Mg^{2+} were analysed by Atomic Absorption Spectrophotometry (AAS) using a GBC 932AA. Na^+ and K^+ were determined by Emission. Standards for Ca^{2+}, Mg^{2+} and K^+ were prepared with the 1 M NaCl solution. NH_4^+ was determined by Flow Injection Analysis (FIA) also using 1 M NaCl solution for preparing the standards. For Na^+ the 1 M NH_4Cl solution was used for preparing the standards. A sub sample of 6 ml was taken from both supernatants for immediate alkalinity analysis by Gran titration (Stumm & Morgan, 1981).

A second extraction, with a new addition of NaCl- or NH_4Cl- solution, was performed as described above. The overall contact time between sediment and the exchange solutions was about 1 hour in each extraction. Initial experiments with a third extraction revealed that a third extraction would contribute with less than 2 % to the total amount of exchangeable cations.

The exchangeable cation concentrations are converted from meq/100g to equivalent fractions (β_I) as (Appelo & Postma, 1993):

$$\beta_I = \frac{meq_{I-Xz}}{\sum_{I,J...} meq_{I-Xz}} \qquad (4.8)$$

where I,J,... are exchangeable cations, $meq_{I\text{-}Xi}$ is normally given in meq/100g dry sediment and $\Sigma meq_{I\text{-}Xi}$ is essentially equal to the CEC, ignoring minor amounts of Fe^{2+}, Mn^{2+}, etc.

Alkalinity determination

Sub samples of the CEC supernatants (NaCl and NH_4Cl) was analysed by the Gran titration method. The primary purpose of the titration is to correct the exchangeable Ca2+ for any Ca^{2+} derived from calcite dissolution during the ion exchange procedure, according to:

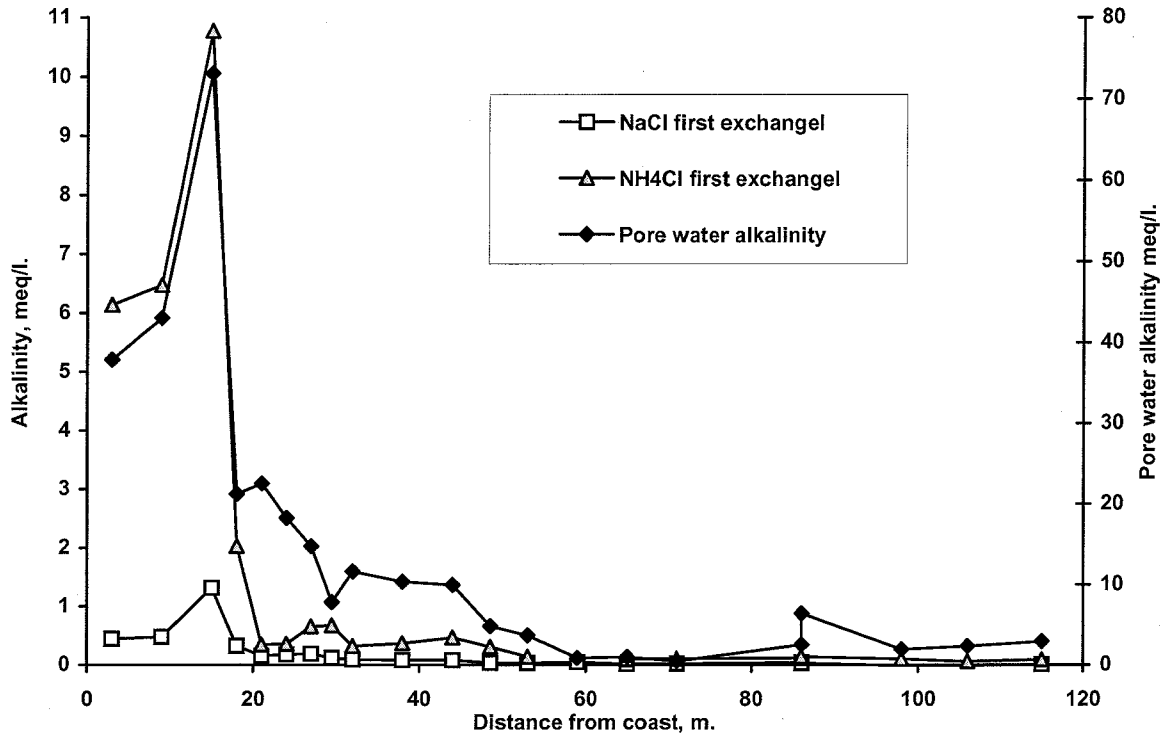

Figure 4.10: Alkalinity (meq/l) for pore water, NaCl- and NH_4Cl-supernatants for the sediment samples of profile 1 (March 2000).

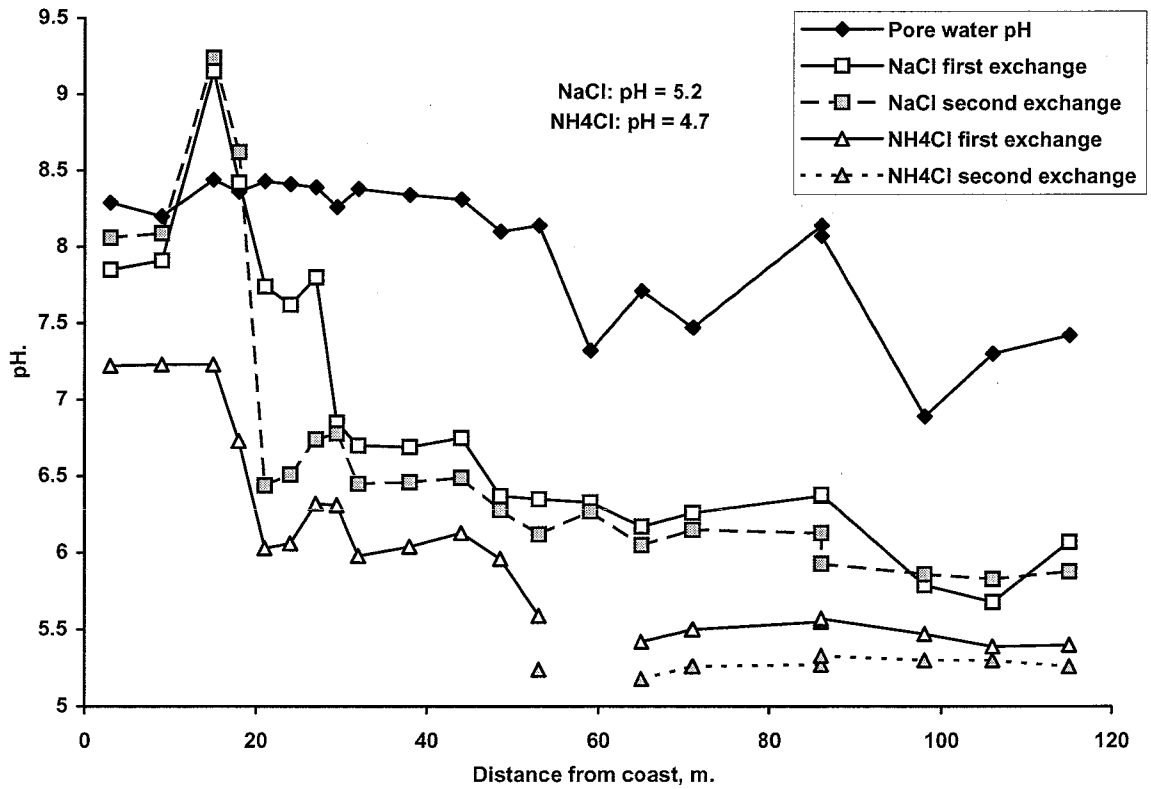

Figure 4.11: pH for pore water, NaCl- and NH_4Cl-supernatants for the sediment profile 1 (March 2000).

$$H_2CO_3 + CaCO_3 \leftrightarrow Ca^{2+} + 2HCO_3^- \quad (4.9)$$

Two moles of bicarbonate are thus produced for each mole of calcite dissolved. The alkalinity measurement data also provides a relative measure of the readily dissolvable calcite contained in the sediment sample.

In Figure 4.10 the alkalinity from the pore water and the NaCl- and NH_4Cl-supernatants are shown for the sediment profile of March 2000. Because of the resemblance of the supernatant alkalinities with the pore water alkalinities, the alkalinity in the supernatants could at first appear to be a diluted residual from the pore water, indicating that the pore water has not been properly displaced by ethanol. This is however, not the case, since the alkalinity contributions from the NH_4Cl supernatants are systematically higher compared to the NaCl supernatants. The observed alkalinities are therefore not simply diluted pore water alkalinity, but must come from calcite dissolution. The differences in supernatant alkalinities are presumably a result of faster calcite dissolution kinetics in the NH_4Cl-solution, having a lower initial pH of 4.7 than the initial NaCl-solution (pH = 5.2) (Fig. 4.11). The lower pH in the pure NH_4Cl-solution is caused by dissociation of the NH_4^+ ion. Also, once in contact with the sediment the NH_4^+ ion is able to deprotonate more H^+ from the sediment than Na^+ leading to a larger subsequent calcite dissolution (Appelo, 1996).

If calcite dissolution is partly caused by deprotonation of H^+ from the sediment, the actual amount of dissolved calcite may be larger than the estimate given by equation (4.9) above, because then the stoichiometry between $CaCO_3$ and HCO_3^- is one to one according to:

$$H^+ + CaCO_3 \leftrightarrow Ca^{2+} + HCO_3^- \quad (4.10)$$

The ion exchange procedure was by no means designed to dissolve calcite and considering the contact time of about 1 hour in each exchange sequence it is unlikely that all calcite did dissolve. However, the alkalinity decreased considerably from first to second extraction indicating that the bulk of readily dissolvable calcite was dissolved in the first extraction. The calculated estimate of readily dissolvable calcite is based on the alkalinity from the NH_4Cl supernatants.

Determination of sedimentary organic carbon and carbonate

Sub samples of the centrifuged sediment (containing less than 2% pore water) were dried at 50 °C for 2 to 3 days. Subsequently the dried sediment was crushed and homogenised in an Agate mortar. A sub sample of 0.5 g was treated 4 times with 3 ml of sulphurous (H_2SO_3) acid (5-6% SO_2) and subsequently evaporated in order to remove all sedimentary carbonate leaving only organic carbon in the sample. These sub samples were dried at 90 °C for 12 hours. The total carbon content of sulphurous acid treated samples and untreated sub samples were determined on a LECO furnace with an IR 225 detector. The content of sedimentary carbonate was calculated as the carbon loss between untreated sub-samples and sub-samples treated with sulphurous acid.

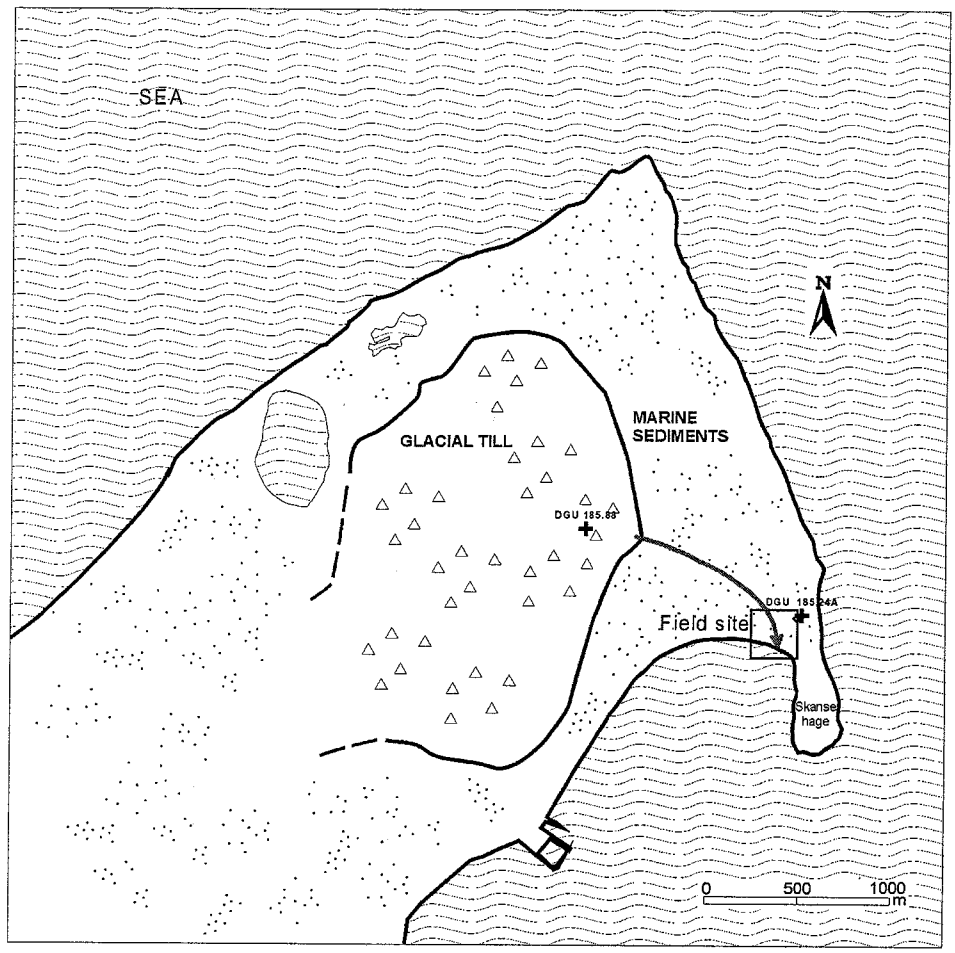

Figure 5.1: The Rørvig peninsula. The frame shows the position of the Skansehage field site. The arrow indicates the main groundwater flow direction from the moraine till towards the field area. +: Indicate positions of water supply wells.

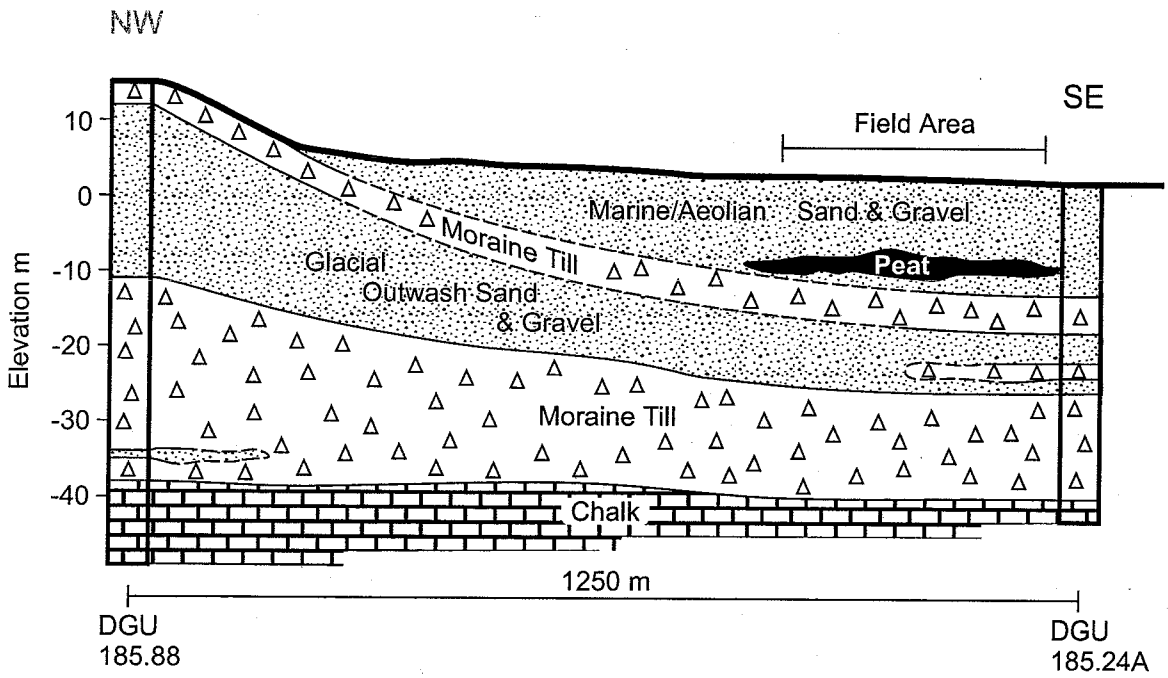

Figure 5.2: Geological cross section between water supply wells DGU 185.88 and 185.24A located on Figure 5.1.

5. GEOLOGY AND HYDROGEOLOGY

This chapter describes the geology and hydrogeology of the field site and provides the background for the following description of the groundwater geochemistry.

5.1 Geology of Skansehage

The Skansehage field site, indicated by the frame in Figure 5.1, is situated in an area of marine sand and gravel beach deposits of Holocene age (or sub recent). Lithological information concerning the area was obtained from two water supply wells (DGU 185.88 and 185.24A) indicated on Figure 5.1. In Figure 5.2 a geological cross section is constructed from these two borings. At –40 m Cretaceous chalk forms the basis for a sequence of glacial deposited sediments. This chalk formation is the main water supply aquifer in the area. The bottom unit of the glacial sequence is a moraine till deposit, up to 30 m thick. On top of the till a 10 to 20 m thick glacial (Weichselian age) outwash deposit of sand and gravel is found. Capping this sand and gravel aquifer is a till deposit a few meters thick. The continuity of the top till is not known with certainty and it may be absent in parts of the area. Above the till, up to an elevation of 5-6 m, postglacial marine deposited sediments are found. At water supply well DGU 185.24A these sediments are found down to an elevation of –11 m. The upper level of the postglacial marine sediments at 5-6 m marks the maximum sea level of the Littorina sea in the Skansehage area (Mertz, 1924). Since the largest extension of the Littorina sea, isostasy has uplifted the area and exposed the marine sediments. Thus the marine sediments are young deposits, probably of Holocene age (not older than 8000 years BC). In part of the area also eolian sand was deposited. Within the lower part of the marine sequence a layer of marine peat, a few meters thick, has been encountered. The extent of the peat will be addressed later (in section 5.12). At the field site (indicated in Figure 5.2) the upper 10-13 m of the sediment sequence consist of these young Holocene deposits. The field investigations and experiment of this project are all carried out within this sequence of marine beach and eolian deposits.

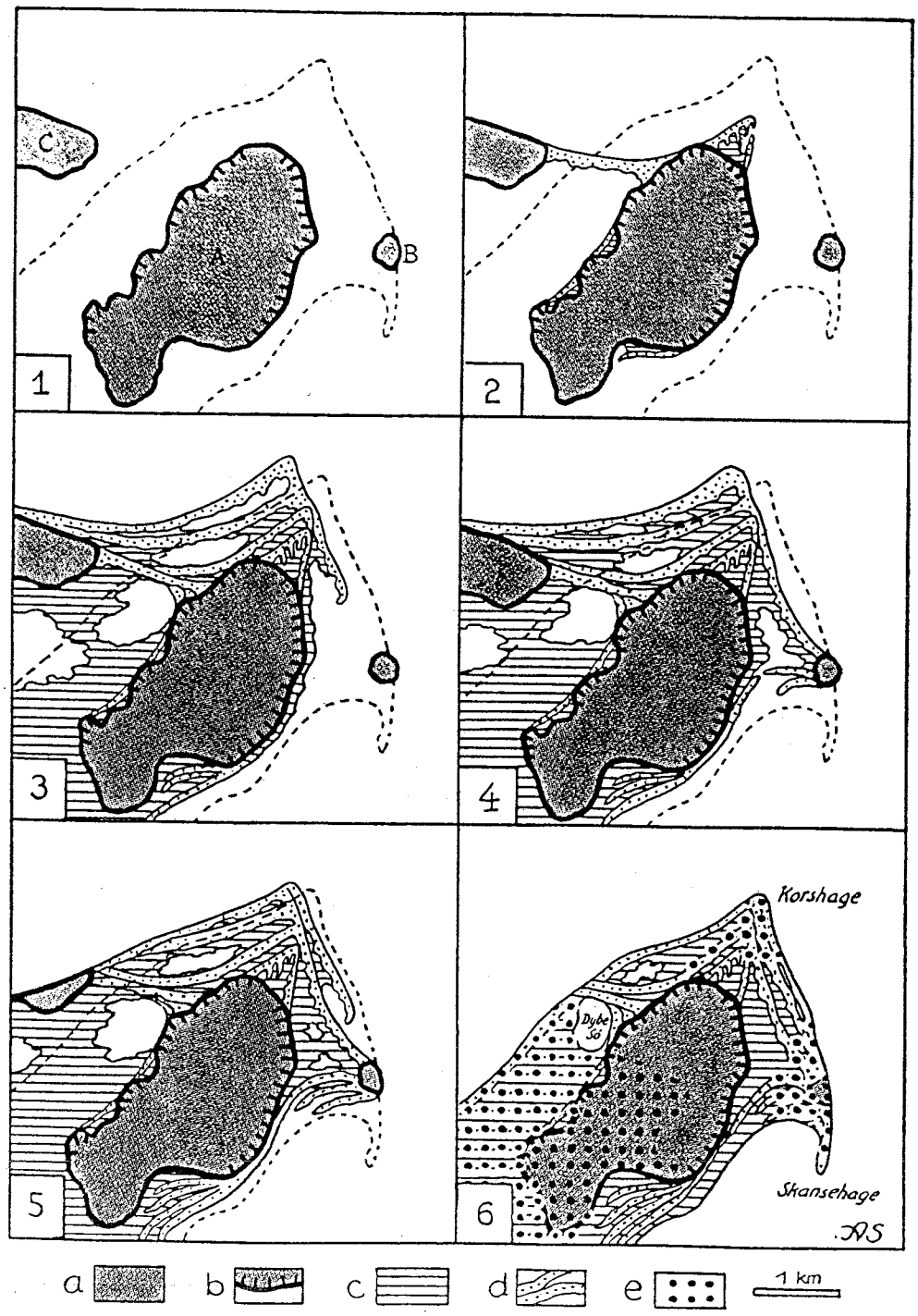

Figure 5.3: Hypothetical sketch of the postglacial development of the Rørvig peninsula and Skansehage a) Moraine till b) Coastal cliff c) Protected foreland deposit d) Beach ridge e) Eolian sand (from Schou, 1945).

Figure 5.3 shows a sketch of the postglacial development of the Rørvig peninsula (Schou, 1945). The glaciers of the Weichlian ice age left till deposits as islands (Fig. 5.3.1). Beach ridges developed perpendicular to the dominating wind and wave direction (Fig. 5.3.2) and behind these, protected forelands started forming (Fig. 5.3.3). Of particular interest for the field site is the small till island B to the east in Figure 5.3 (1). Westwards from this island beach ridges have been formed across the field site in an east-west direction (Fig. 5.3.4 and 5). The sediments in these gravel beach ridges are very coarse (stones of cobble size have been observed). At a later time a spit formed southwards from the small till island B (Fig. 5.3.6). The bay south of the field site became more sheltered and finer sand and gravel was deposited south of the beach ridges. Deposits of fine-grained eolian sand also covered part of the area (Fig. 5.3.6). Formation of peat deposits has occurred in lakes and bogs within the low lying sheltered areas of the protected foreland (Fig. 5.3.3-6). The marine peat layer sketched in the bottom of the marine sequence in Figure 5.2 represents buried mats of dead seaweed (*Fucus vesiculosus*) and eelgrass (*Zostera marina*) deposited on the bottom of the fjord. Remains of these marine plants have been identified in the peat. At present a thick layer of dead seaweed and eelgrass is also found on the bottom of the fjord south of the field site.

Two wells were drilled with a bottom-loading bailer at about 10 meters from the coast for characterizing the sediments. Their positions are shown in Figure 4.1b (and as insert in Fig. 5.4b). Boring B1 (Fig. 5.4a) is next to the transect of monitoring wells, and boring B2 (Fig. 5.4b), 30 m to the east. Generally the sediment consists of medium to coarse-grained sand (d_{50} = 0.5 mm). Boring B1 contains a gravely layer at an elevation of –5.5 to –6 m possibly reflecting the more unsheltered beach situation in (4) and (5) of Figure 5.3. This layer is not encountered in B2. Comparison of the two grain size distributions B1 and B2 show considerable lateral variation, with B1 being more coarse.

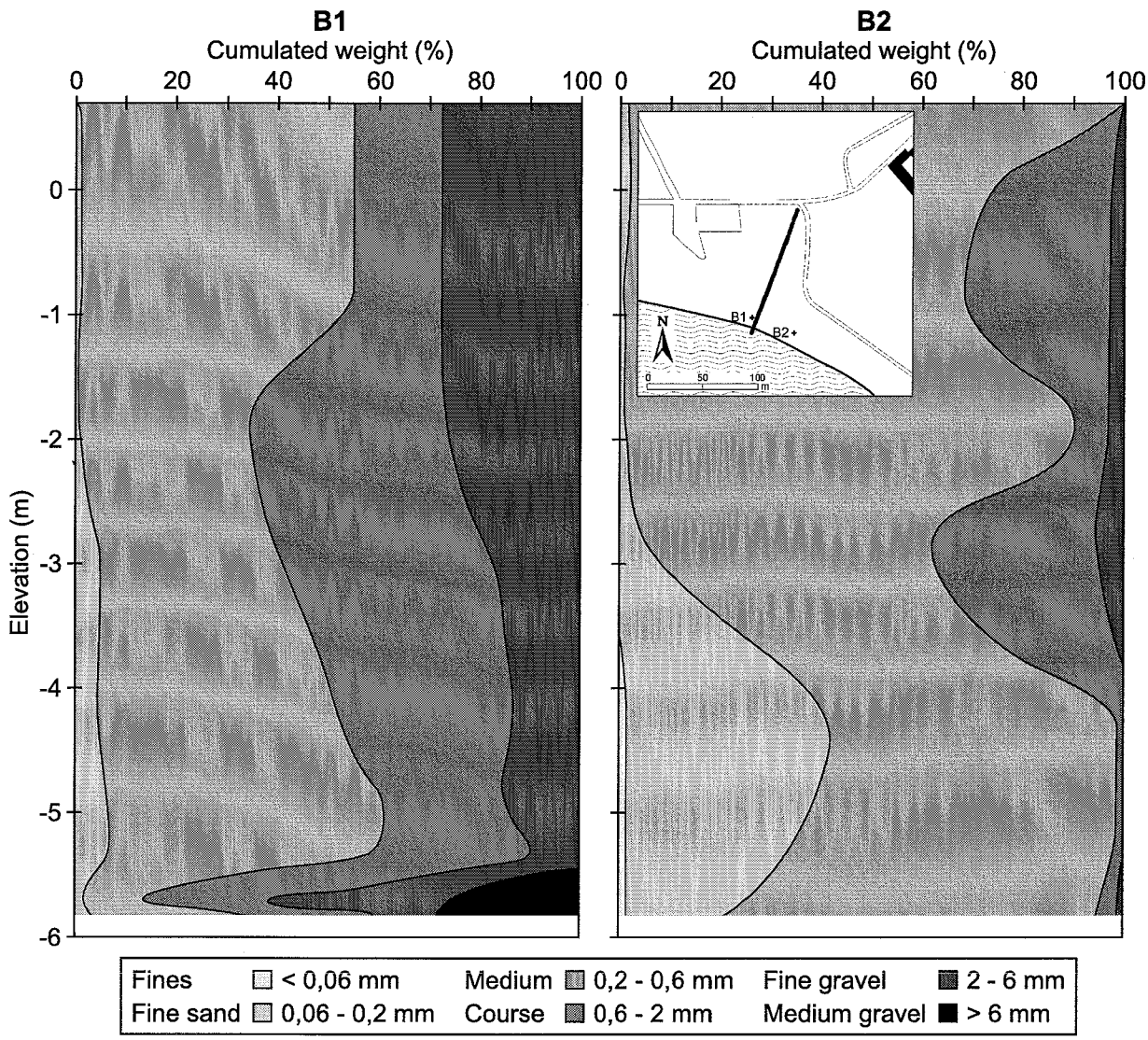

Figure 5.4: Grain size distribution (cumulated weights in %) for two borings. a) B1 is located 10 m from the coast at the monitoring transect and b) B2 is located 10 m from the coast, about 30 m east of B1 (see insert).

GPR Profiles (Ground Penetrating Radar) were made in a north-south direction over the field site. Interpretation of the GPR profile shows reflections gently dipping 2-3 degrees towards the south (Fig. 5.5). The structures are a result of grain size and porosity variations and indicate the position of former beach-forsets (Andreasen, 1999, unpublished data). These beach-forsets could also be present closer to the coastline, but here the GPR-reflections are attenuated by the high electrical conductivity of the pore water near the coast.

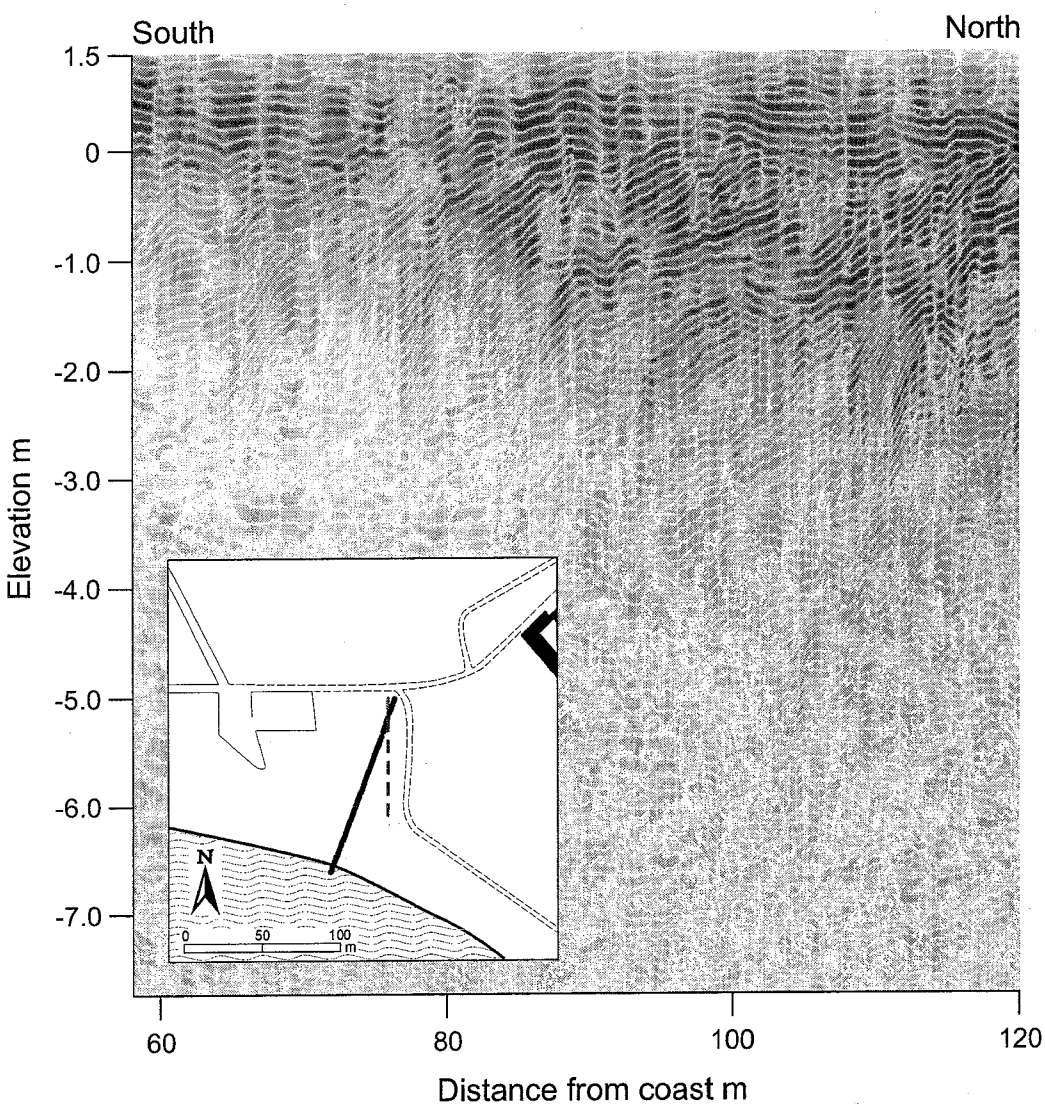

Figure 5.5: Ground Penetrating Radar profile (GPR) conducted in a north-south direction (given by the dotted line) roughly parallel to the monitoring transect (Andreasen, 1999, unpublished data).

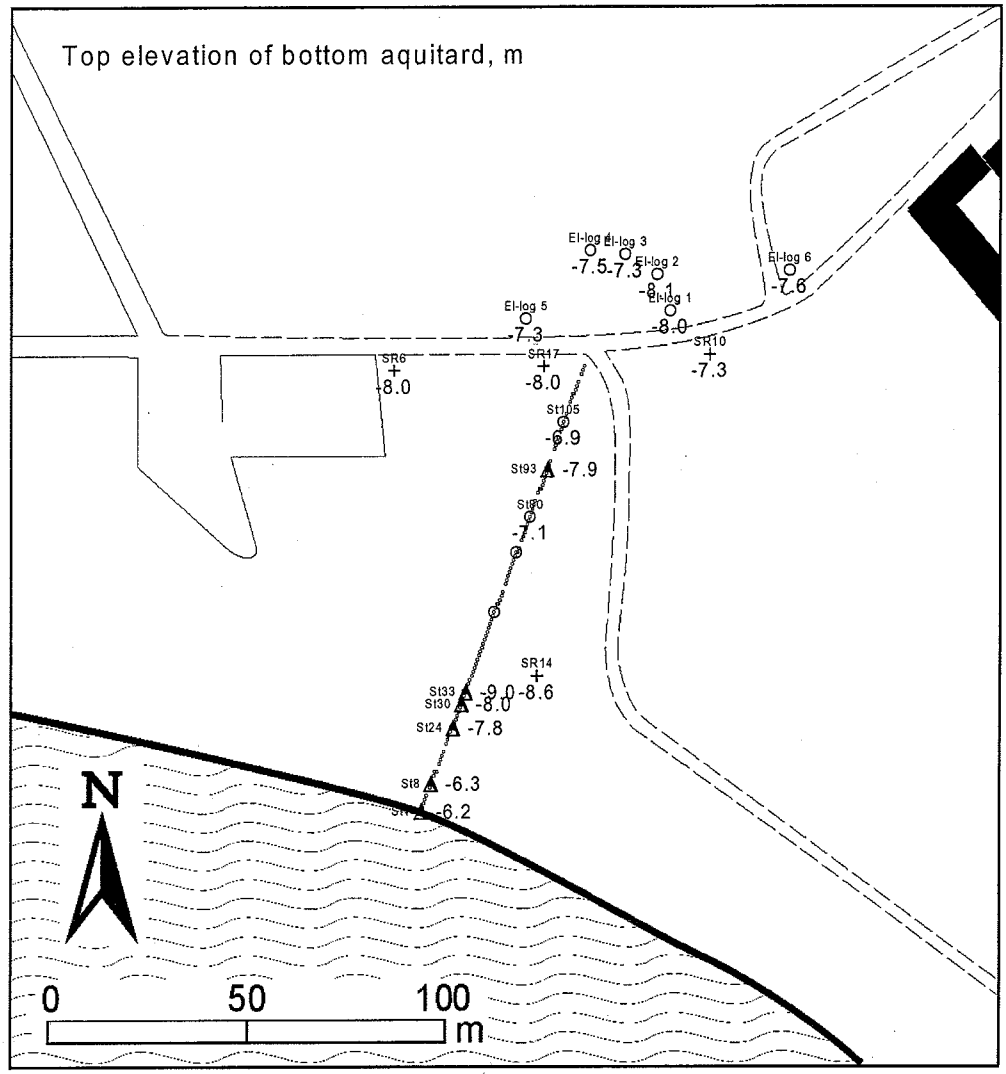

Figure 5.6: Top elevation of bottom aquitard, m. Estimated from: El-logs (O), impermeable zones in water chemistry profiles (+), Slugtests K < 10-5 m/s (△). Transect wells are shown as (o) .

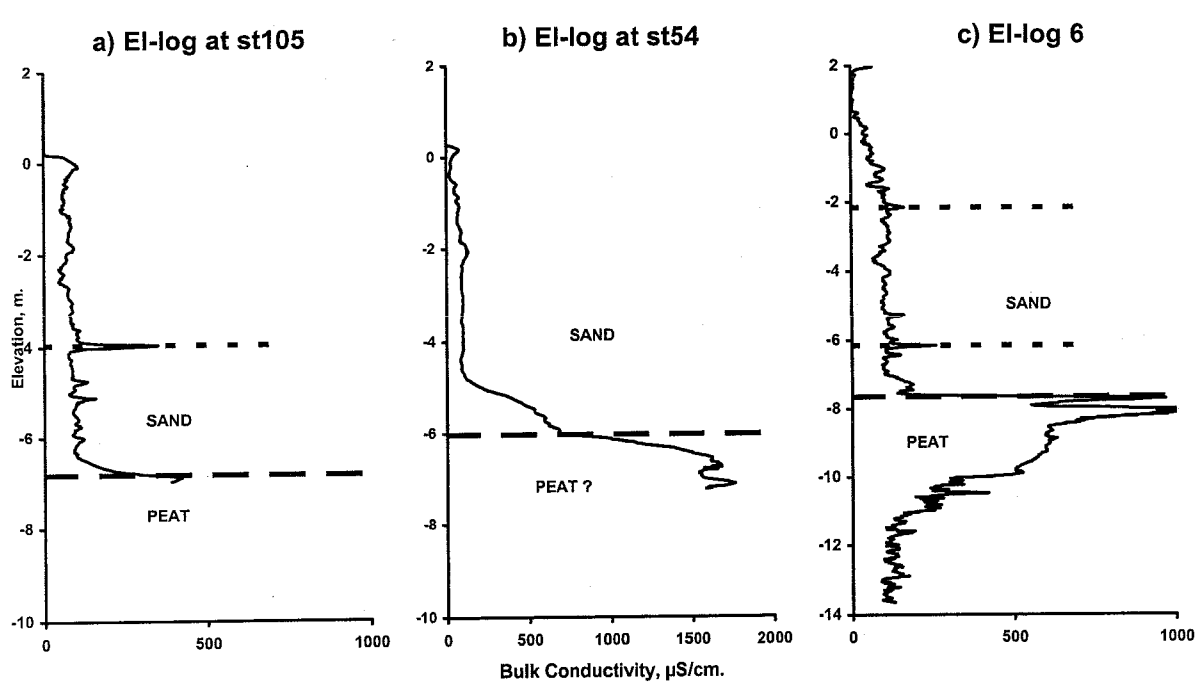

Figure 5.7: El-logs at a) St105, b) St54 in the transect and c) El-log 6. Thick dashed horizontal line is the top of the bottom aquitard at roughly 500 µS/cm. Small dashed lines represents minor peat layers.

5.1.1. Distribution of aquitards and the bottom of the aquifer

The marine peat layer is several meters thick, and underlies the marine sand and gravel deposits in most of the field site, and acts as the bottom of the upper unconfined aquifer. During early field reconnaissance, borings were drilled for sampling groundwater. In these borings low-permeable zones that did not yield water easily were detected at about –7 to –9 m. A number of continuous electrical borehole logs (El-logs) were conducted at the field site to detect aquitards and delineating the bottom of the aquifer. The location of the el-logs and some of the reconnaissance borings can be seen in Figure 5.6. Figure 5.7 (St105a, St54b and el-log 6) shows three representative el-logs. The bulk conductivity for the saturated aquifer containing fresh water is around 100-200 μS/cm corresponding roughly to a pore water conductivity of 500-1000 μS/cm (see section 4.1.8). The abrupt increase in bulk conductivity to more than 400 μS/cm at –7 to –8 m (Fig. 5.7a&c) is interpreted as a change in lithology from sand to peat and represents the bottom of the aquifer. If the increase in bulk conductivity was caused by as increase of salinity of the pore water within a homogeneous sediment layer, then dispersion would lead to a more gradual transition as seen in the el-log at St54 (Fig. 5.7b) in the interval –5 to –4 m. For most el-logs the position of the aquifer bottom was estimated to be at a bulk conductivity of 500 μS/cm where the increase in conductivity is particularly steep. Hydraulic tests (slugtests see section 4.1.9) confirmed that the zone below this depth has low permeability, and in subsequent sediment core samples the layer was identified as being marine peat. In the el-log in Fig. 5.7c the bottom aquitard was penetrated to estimate it's thickness, which was found to be more than 2 meters.

In some of the el-logs high conductivity peaks of 10 to 30 cm in thickness, can be identified. Some of these peaks even seem to correlate from borehole to borehole. Particularly three layers show up in several logs at elevations of –1.5 to –2.0 m, –4.0 m and at –6.0 to -6.5 m (Fig. 5.7a and c). The layer at –4 m was later identified as a thin peat layer in a core sample.

The bottom aquitard was encountered in most el-logs and water sampling borings and the surface seems to be quite flat at an elevation of –7 to –8 m (Fig. 5.6). The depth estimates from the el-logs next to St54 and St70 are omitted from Figure 5.6, because the high pore water conductivity in these logs make identification of the peat layer difficult. Therefore the estimates of depths to the

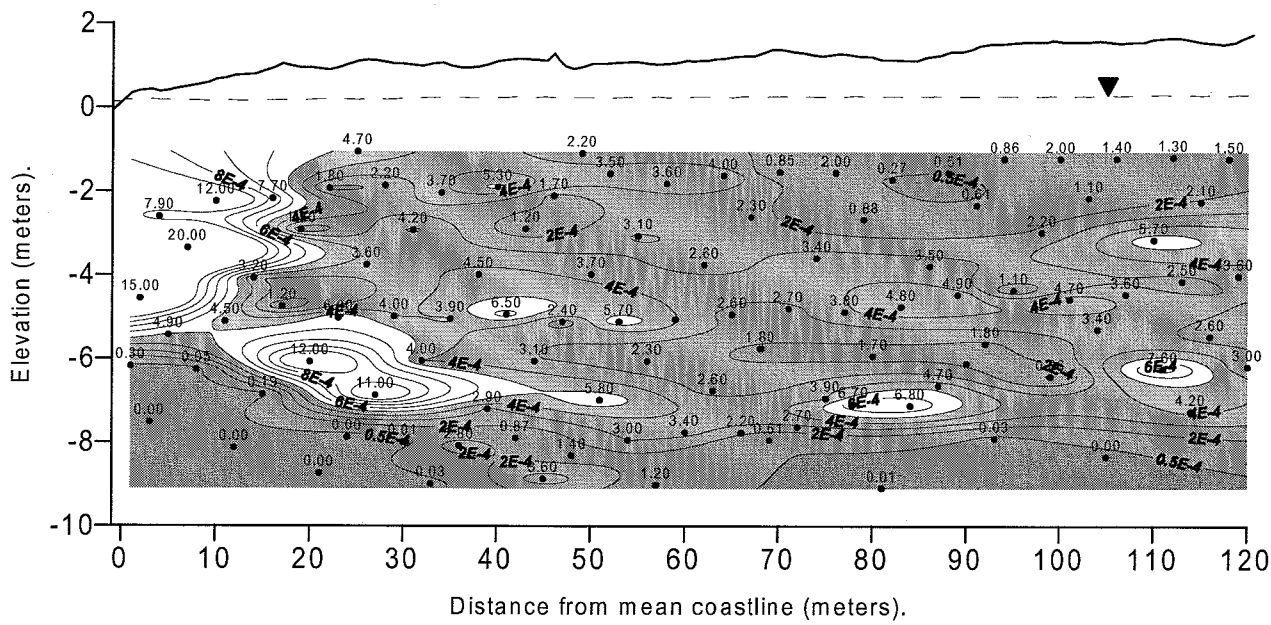

Figure 5.8: The hydraulic conductivity distribution in 10-4 m/s as determined by slugtests in the monitoring wells.

bottom aquitard are most reliable away from the high pore water conductivity near the coast (Fig. 5.7b st54).

Natural gamma logs conducted in the two deep monitoring wells St21 (-8.7 m) and St81 (-9 m) revealed little variation in the clay content of the aquifer or bottom aquitard. The natural gamma count was constant down through the aquifer and into the bottom peat layer. The well St21 penetrates about 1 m into the bottom aquitard. This supports the finding that peat is the primary constituent in the bottom aquitard.

5.2 Hydrogeology

5.2.1 Hydraulic conductivity

Slugtest results

The hydraulic conductivity distribution along the monitoring transect is shown in Figure 5.8. In the upper sandy part of the aquifer the hydraulic conductivity ranges from $0.3 \cdot 10^{-4}$ to $20 \cdot 10^{-4}$ m/s, with an average of $2.0 \cdot 10^{-4}$ m/s. Some of the deeper wells are screened in the low permeable peat layer with hydraulic conductivities between $1.0 \cdot 10^{-5}$ and $3.6 \cdot 10^{-9}$ m/s. A horizontal stratification with alternating high and low hydraulic conductivities can be inferred from the data. At the top of the aquifer (at an elevation of –1 to –3.5 meter, 20 to 120 m from the coast), a zone of slightly lower hydraulic conductivities of 0.3 to $2.0 \cdot 10^{-4}$ m/s is found. Below this zone a higher hydraulic conductivity layer (2.0-$5.0 \cdot 10^{-4}$ m/s) of about 1-2 m in thickness is seen. This layer is followed by a thinner (<1 m) layer of lower hydraulic conductivity (<$2.0 \cdot 10^{-4}$ m/s) at 45 to 120 meters from the coast. Beneath this layer there is a 1 to 2 m thick high hydraulic conductivity layer (2.0-$12.0 \cdot 10^{-4}$ m/s). Finally the hydraulic conductivity gradually decreases from an elevation of –6 to –7 m. The gradual decrease indicates a gradual fining of the sediment (and/or maybe an increase in the frequency of thin peat layers). Near the coast (from 0 to 10 meter) at an elevation from –2 to –5 meters a zone with very high hydraulic conductivity (10-$20 \cdot 10^{-4}$ m/s) is situated. Also two borings at 20 and 27 m from the coast and at an elevation of about –6 to –7 m have a high hydraulic conductivity of about $10 \cdot 10^{-4}$ m/s. These two borings could be connected to the high conductivity zone at the coast. The hydraulic properties may also vary perpendicular to the plane of the transect.

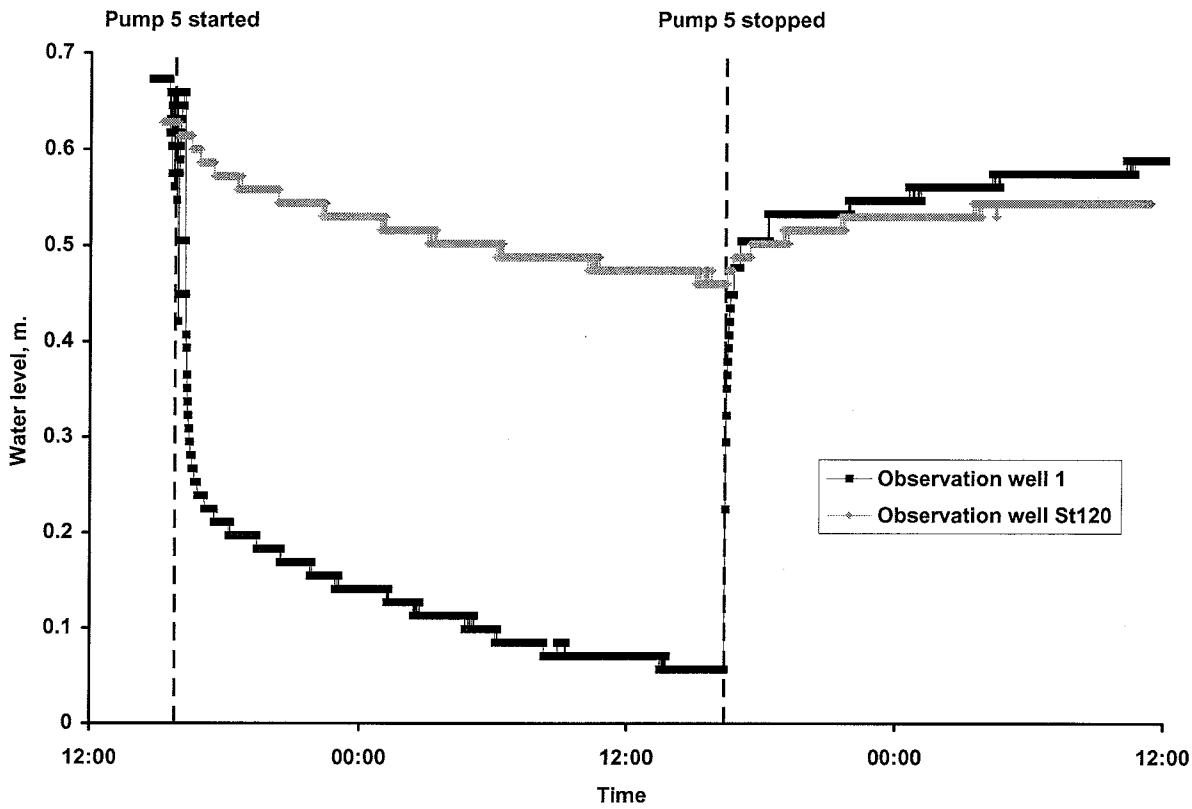

Figure 5.9: The drawdowns and the recovery of the water table in a) observation well 1, 2 m from pumping well 5 and b) transect well St120, 29 m from pumping well 5.

The presence of variations perpendicular to the transect are hinted by the geological variations observed between the borings B1 and B2 (Fig. 5.4).

Pumping test results

The results of the pumping test (see section 4.1.9) in the well field to the north of the transect are summarised in Table 5.1. Drawdown and recovery in the nearest and farthest of these wells (Obs1 and St120) is shown in Fig, 5.9a,b located respectively 2 and 29 m from the pumping well. The analysis of the pumping data yielded hydraulic conductivity's in the order of $5 \cdot 10^{-4}$ m/s which is only slightly higher than found by the slugtests in the monitoring wells of the transect. The reasonably uniform values for a given method in Table 5.1 indicate that the aquifer is quite homogeneous within the pumping test area. The hydraulic conductivity estimated from the recovery data ($8 \cdot 10^{-4}$ m/s) was twice as high as estimated from the drawdown data. The explanation for this discrepancy is not known, but heavy rain during the pumping test could maybe affect the recovery of the drawdown cone and give a higher conductivity estimate.

Table 5.1: Hydraulic conductivity (10^{-4} m/s) determined from the pumping test using the Jacob's and the Theis methods for an unconfined aquifer. Observation well numbers refer to Fig. 4.8.

Well	Jacobs method pumping 10^{-4} m/s	Jacobs method recovery 10^{-4} m/s	Theis method pumping 10^{-4} m/s	Theis method recovery 10^{-4} m/s
Observation 1	3.6	8.2	3.1	6.7
Observation 2	4.8	9.5	2.8	8.2
Observation 3	5.0	10	4.1	8.2
Observation 4	4.1	3.5	4.1	8.2
Observation 5	-	7.7	-	7.5
Observation 6	4.5	9.5	6.2	8.2
Pumping well 3	7.6	10	5.9	9.5
Pumping well 6	5.3	10	4.2	9.4
Average	5.0	8.6	4.3	8.2

5.2.2 Porosity

The mean porosity of the sandy sediments (33 samples) was found to be 0.35 with a standard deviation of 0.025. No trends in porosity could be discerned within the two sampling campaigns or between them. Therefore a uniform porosity of 0.35 for the sandy part of the transect will be used henceforward. A higher mean porosity of 0.55 was found for the peat samples of (3 samples).

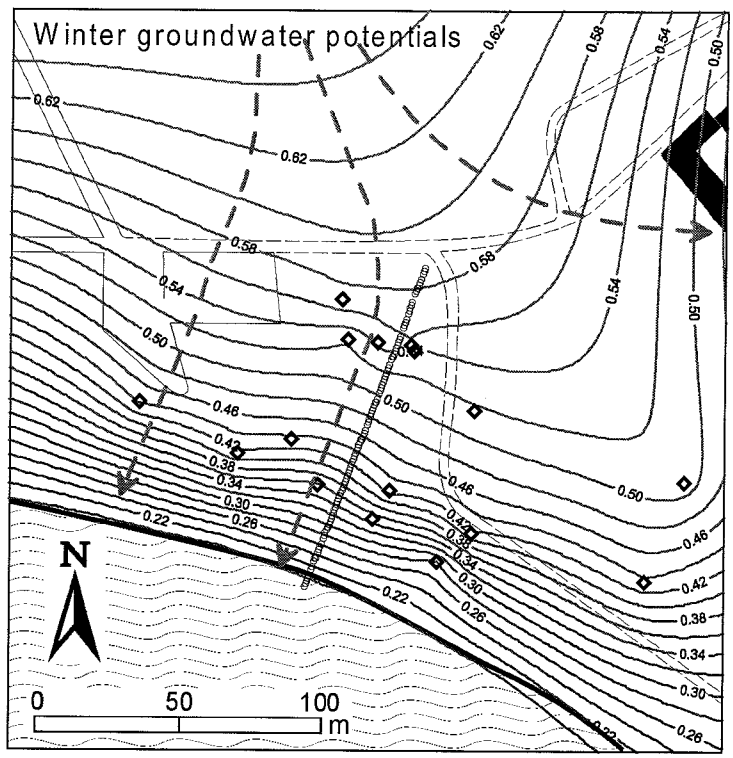

Figure 5.10: Lines of equal hydraulic head contoured from heads measured February 2000. Equidistance of contour lines is 0.02m. Head observations in piezometers (◊); Transect wells (o); Arrows indicate direction of groundwater flow; Current sea level 0.20 m.

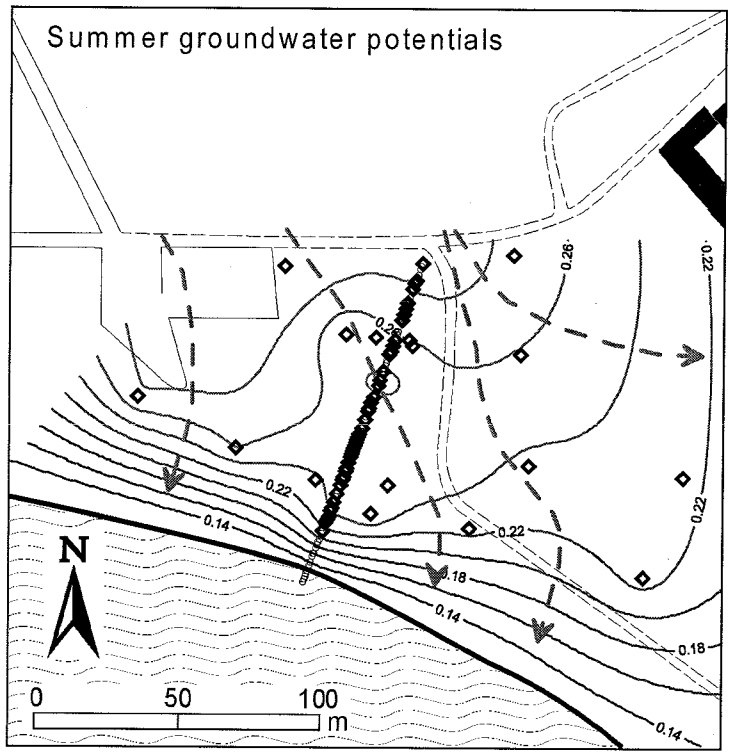

Figure 5.11: Lines of equal hydraulic head contoured from heads measured June 1999. Equidistance of contour lines is 0.02m. Head observations in piezometers (◊); Transect wells (o); Arrows indicate direction of groundwater flow; Current sea level 0.115 m.

Somewhat higher standard deviations for the peat samples of 0.185 partly reflect a varying peat content.

5.2.3 Groundwater flow

The mean annual infiltration for the area is about 100 - 200 mm/year (Hansen, 1980). The position of the regional groundwater divide is not known exactly, but presumably runs along the centre of the Rørvig peninsula and the general groundwater flow direction south of the divide is south east (see Fig. 5.1). Towards the tip of the peninsula the groundwater must diverge and some of the flow must be toward the east.

The groundwater potentiometric surface was determined several times prior to the intrusion experiment. In Figure 5.10 the lines of equal hydraulic head are shown for a winter situation (February). The lines are generally parallel to the coastline inferring groundwater flow perpendicular to the coast (Figure 5.10) in general and more specifically along the monitoring transect. In the summer situation (June) the lines are not as parallel to the coast and the groundwater flow is more towards the east, crossing the transect (Fig. 5.11). The hydraulic head gradient is generally higher in winter than in summer most likely due to the seasonal variations in recharge. The average summer head gradient is 0.55‰ whereas the winter (Fig. 5.10) head gradient is 2.75‰. In both seasons the head gradient is found to be steeper from 0 to 40 m from the coast (summer = 5.5‰ and winter =5.2‰), The gradient becomes steeper because the part of the aquifer available for freshwater flow is reduced by to the presence of the saltwater wedge. The reduced thickness of the aquifer towards the coast will also have an influence (Fig. 5.8). The head gradient near the coast is variable and often levelled out or reversed due to fluctuations in the sea level (see section 5.2.5).

Flow velocities

Using the hydraulic head gradients determined above, pore water flow velocities can be calculated assuming Darcian flow:

$$v_p = \frac{K}{\varepsilon} \cdot \frac{dh}{dx} \qquad (5.1)$$

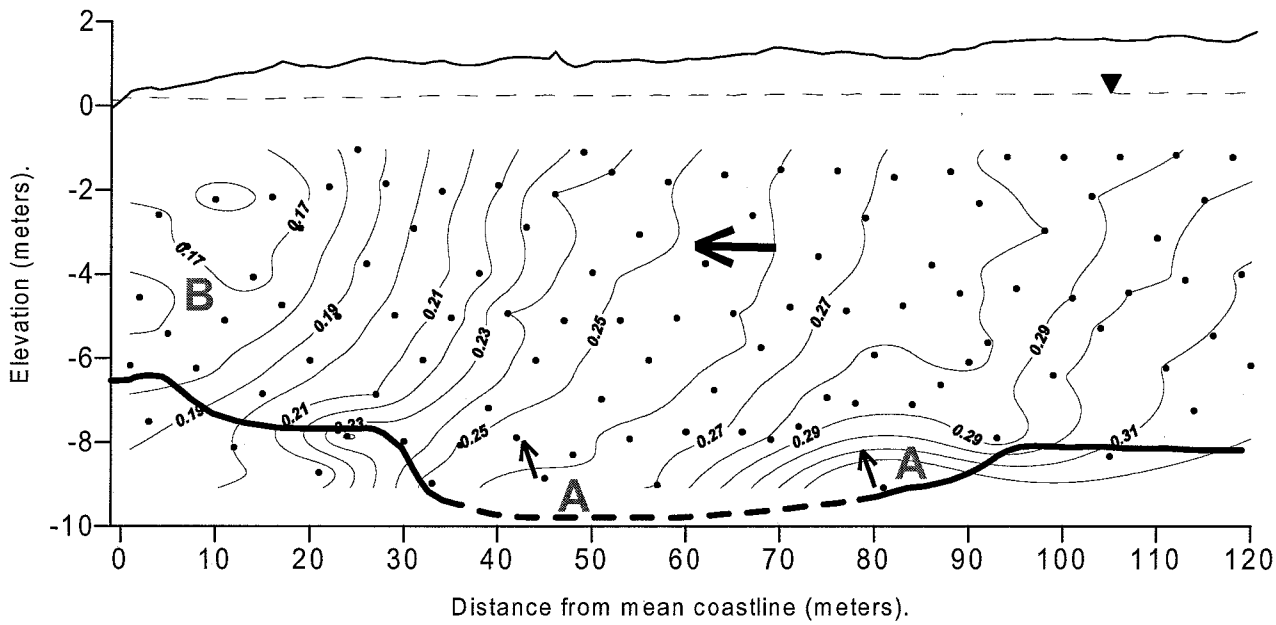

Figure 5.12: Contoured values of density corrected hydraulic freshwater heads in the monitoring transect (July 1999). Contour intervals are 1 cm. At A near the bottom of the aquifer upward gradients are observed. Head pattern at B indicate possible influence of sea level fluctuations.

Where v_p is pore water velocity (m/s), K is hydraulic conductivity (m/s), ε is the porosity and dh/dx is the head gradient (m/m). For the sandy part of the aquifer at Skansehage the average K is $2 \cdot 10^{-4}$ m/s and the porosity is 0.35. Combined with the average hydraulic head gradients calculated above the average pore water velocities are:

Summer: 0.027 m/d (10 m/y)
Winter: 0.14 m/d (50 m/y)
Near the coast (0 to 40 m from the coast), a maximum velocity of: 0.64 m/d (234 m/y)

The pore water velocity near the coast was calculated using a use a higher K of $5 \cdot 10^{-4}$ m/s corresponding to a mean of the first 40 m of the transect (Fig. 5.8).

5.2.4 Ground water flow along the monitoring transect

Figure 5.12 shows hydraulic freshwater heads measured in July 1999. In general the lines of equal freshwater head indicate an upward flow component in the whole of the transect. The most obvious explanation is that the freshwater discharging to the sea has to flow over the saltwater wedge and the threshold created by the elevated bottom of the aquifer at the coastline (Fig. 5.8). Elevated hydraulic heads within the saline water body near the coast (at B Fig. 5.12) may also indicate a slight upward movement of the saline water. Potential upward leakage through the bottom aquitard is indicated by the higher fresh water heads observed near/in the bottom of the aquifer (at A in Fig. 5.12). An upward leakage could explain the almost horizontal contours of equal freshwater head further inland from the saltwater wedge. Finally vertical anisotropy of the aquifer created by the near horizontal layering/variations of the hydraulic conductivity can cause the observed sloping of the lines of equal freshwater head (Fetter, 1994). If anisotropy is significant then the assumption of flow perpendicular to the lines of equal freshwater head is not valid. Near the coast (at B Fig. 5.12) the freshwater head contours do not show a clear flow direction. This is probably because of the influence of sea-level fluctuations at the time of measuring.

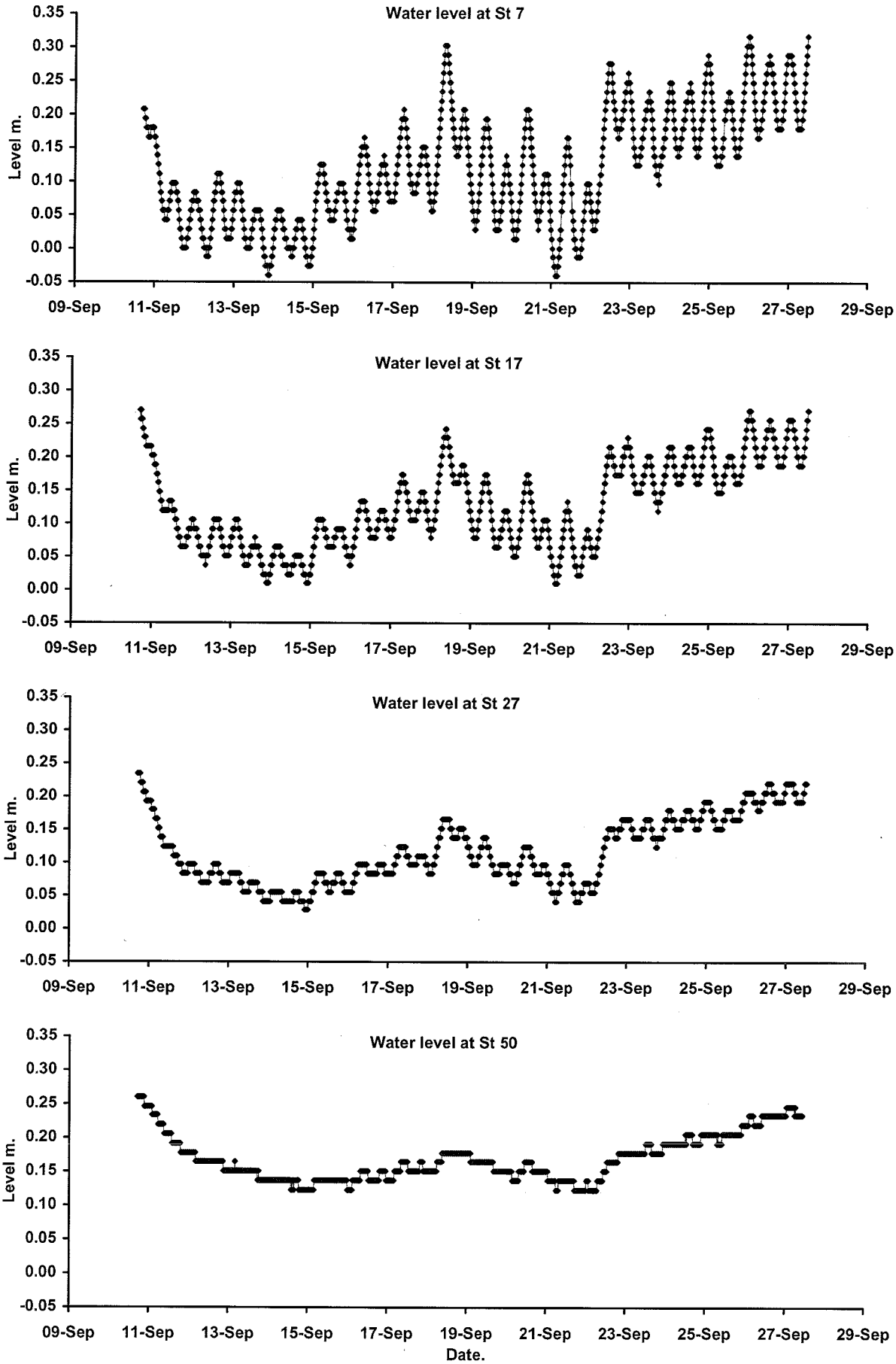

Figure 5.13: Water levels in wells 7, 17, 27, and 50 meters from the coast. Recorded with pressure transducers at 20 min intervals, between 10/9 and 27/9 1999.

5.2.5 Water level fluctuations

Water level fluctuations in the aquifer were recorded using pressure transducers measuring at 20 min intervals. Figure 5.13 shows water level records from 17 days in September 1999. In the monitoring wells closest to the coast (e.g. St7) there are both short semi-diurnal tidal fluctuations and larger scale fluctuations due to wind-induced surges. Further inland at well St50 (50 m) the short tidal fluctuations have dampened and only the large-scale trends in the water level are observed. At well St7 the tidal fluctuations have maximum amplitude of 30 cm with an average of about 10-15 cm. 10 meters further inland at well St17 the fluctuations are dampened to about 5 cm on average. The longer lasting fluctuations probably have a larger effect than the semi-diurnal tidal fluctuations on the movement of the sea-/freshwater interface.

5.3 Position of the sea-/freshwater interface

The position of the undisturbed sea-/freshwater interface in the aquifer can be inferred from Cl^- or EC measurements in the transect. Figure 5.14a&b shows two contoured plots of the EC from summer (August, 1999) and winter (March, 2000), respectively. In the summer situation (Fig. 5.14a) the EC varies in the transect from 500 µS/cm for freshwater at the shallowest and most landward part of the aquifer to a maximum of 33500 µS/cm deep in the aquifer near the coast. These electrical conductivities correspond to salinities of 0.3‰ and 21‰ respectively. For comparison the average EC of the seawater was 30000 µS/cm (salinity = 17‰) in a period of 1½ year prior to the EC transect measurements in August 1999. The position of the sea-/freshwater interface is in the following delineated by the 15000 µS/cm contour representing 50% seawater. The saltwater body is wedge shaped and the 50% seawater contour of the summer situation (Fig. 5.14a) is located at an elevation of –4 meters at the mean coastline and dips landwards to intersect the bottom of the aquifer at an elevation of –9 to –10 meters about 40 meters from the coast.

During winter (Fig. 5.14b) the sea/-freshwater interface is steeper. At the coastline the interface is encountered at the shallow elevation of –2 m. This is due to the higher mean EC of the fjord during winter and to the more frequent occurrence of a high sea level. Deeper in the aquifer (at –6 to –7 m) the interface is only slightly displaced towards the coast, perhaps because of a higher freshwater head in the aquifer during winter. Further landward in the aquifer, at 60 and 80 m from the coast,

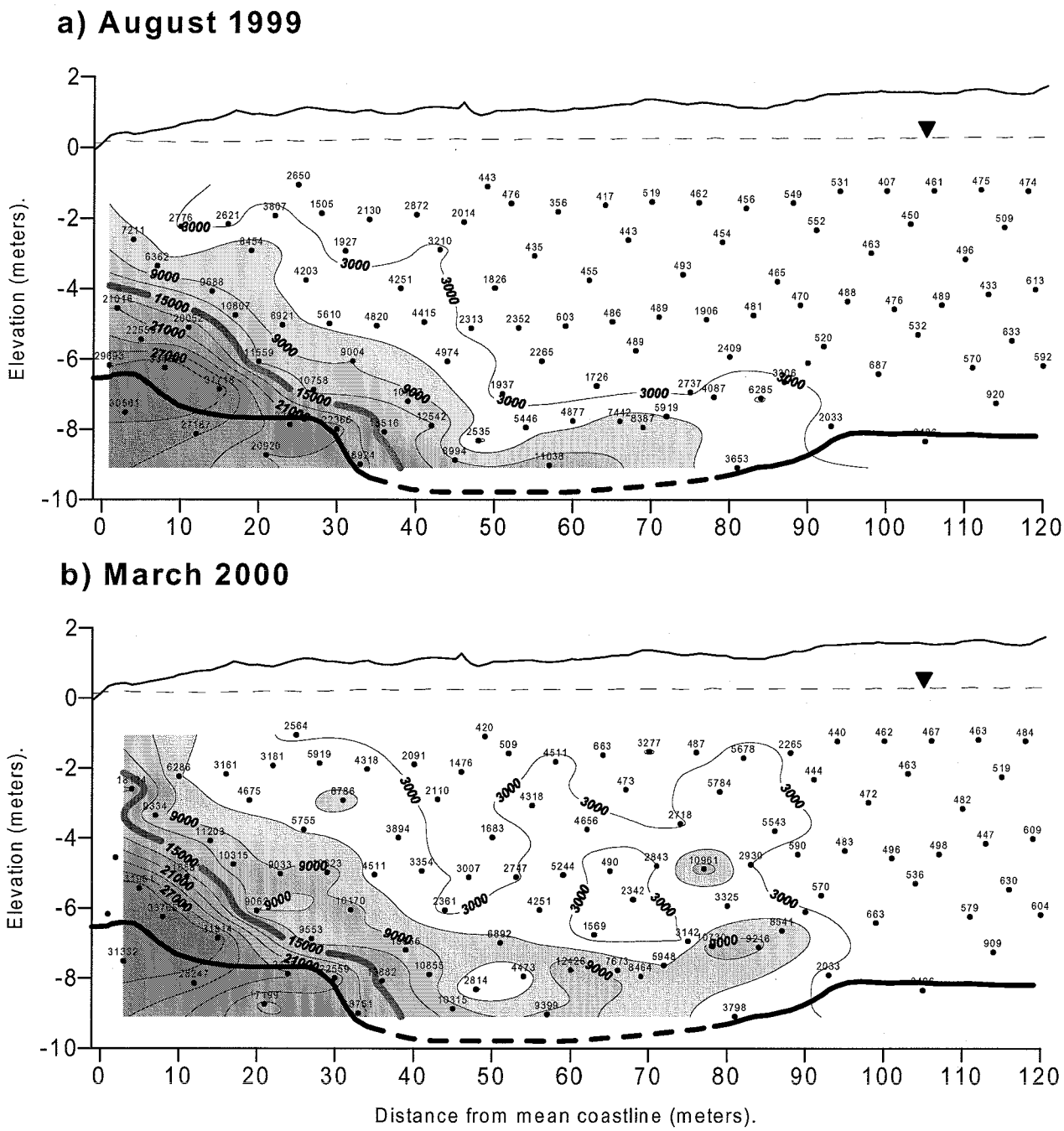

Figure 5.14: Contoured electrical conductivity (EC) in µS/cm measured in the monitoring transect in a) August 1999 and b) March 2000. The thick grey line represents 50% seawater i.e. the fresh-/seawater interface. The lower thick black line is the approximate position of the aquifer bottom.

the freshwater has an enhanced EC caused by a seawater inundation event (see section 5.5). Overall the differences in the position of the sea/-freshwater interface during summer and winter are small.

The position of the sea-/freshwater interface can be calculated using several analytical solutions. Most analytical solutions assume the interface between sea- and freshwater to be a sharp. The simple Ghyben-Herzberg relation relies only on observed hydraulic heads and the density of sea- and freshwater:

$$z = \frac{\rho_f}{\rho_s - \rho_f} \cdot h_f \qquad (5.2)$$

Where z is the depth to the interface in meters, h_f is the hydraulic head in meters, and ρ_s and ρ_f are densities of sea- and freshwater in kg/m^3. A serious limitation of the Ghyben-Herzberg relation is that it does not allow for discharge of freshwater at the shore face. Another limiting factor is the proximity of the field site to the sea, because sea level induced fluctuations of the water table cause an erroneous variation in the estimated depth to the interface. The Glover solution (Glover, 1964) allows a freshwater discharge to the sea (an outflow face), but requires more knowledge of the sites hydrogeological parameters. In Cheng & Ouazar, (1999) the Glover solution gives the vertical distance (z) to the sea-/freshwater interface as:

$$z = \sqrt{\frac{2qx}{\Delta s K} + \frac{q^2}{\Delta s^2 K^2}}, \qquad \text{Where:} \qquad \Delta s = \frac{\rho_s - \rho_f}{\rho_f} \qquad (5.3)$$

x is distance from the coastline in meters, K is the hydraulic conductivity in m/s. At Skansehage the densities of sea- and freshwater are 1014 and 1000 kg/m^3 respectively. The average hydraulic conductivity in the upper permeable part of the aquifer is about $2 \cdot 10^{-4}$ m/s. q is the freshwater outflow per meter coastline in m^3/m·s. q can be estimated from the product of net infiltration w (m/s) and the distance to the water divide L (m), provided that all the water is discharged through the aquifer in question. L is set equal to the distance to the moraine hill (see Figure 5.1 and 5.2 geology) with L = 875 m, assuming that only the water infiltrated in the marine sediments is discharged through the upper aquifer. Thus recharge by surface run off from the moraine till is assumed to be zero. And recharge through the till is considered to discharge to the sea through

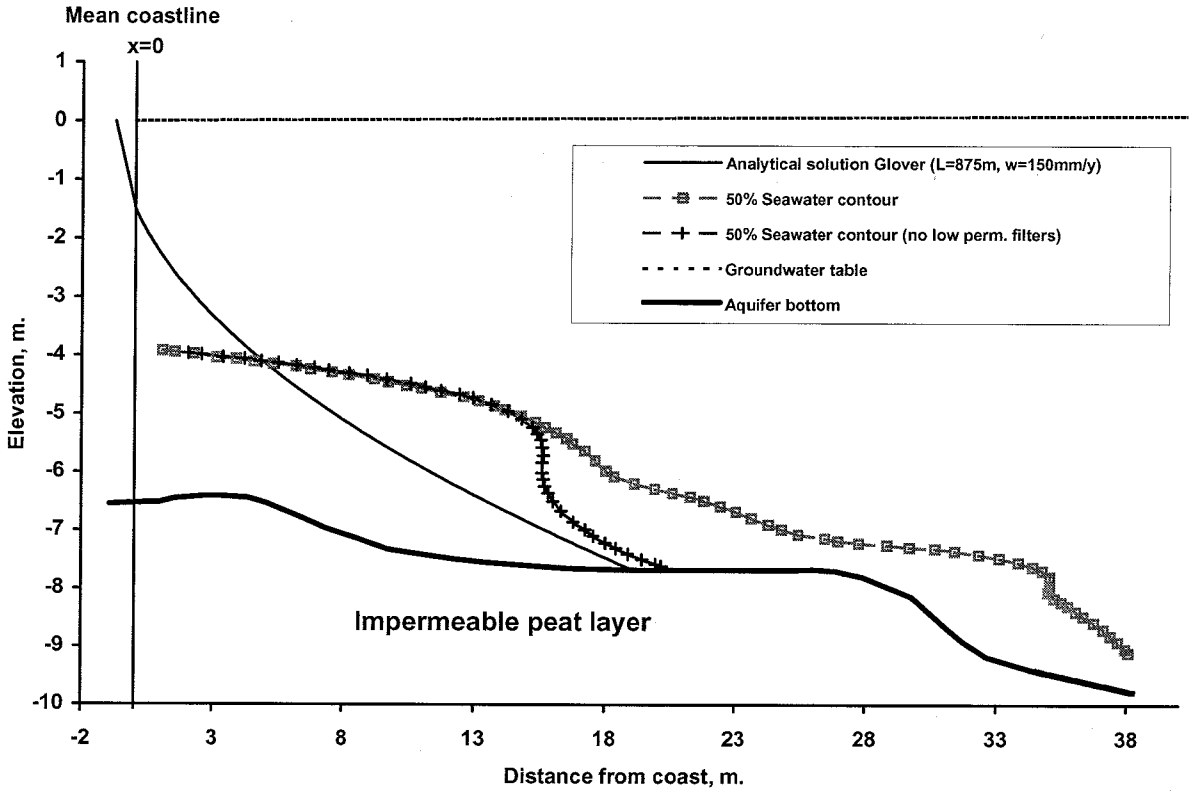

Figure 5.15: Observed sea-/freshwater interface calculated as the 50% seawater EC contour for the transect with and without the filters in the low permeability peat layer and the positions of a sharp interface calculated by the Glover solution with: ρ_s = 1014 kg/m³, ρ_f = 1000 kg/m³, $K = 2 \cdot 10^{-4}$ m/s, L = 875 m and w = 150 mm/y.

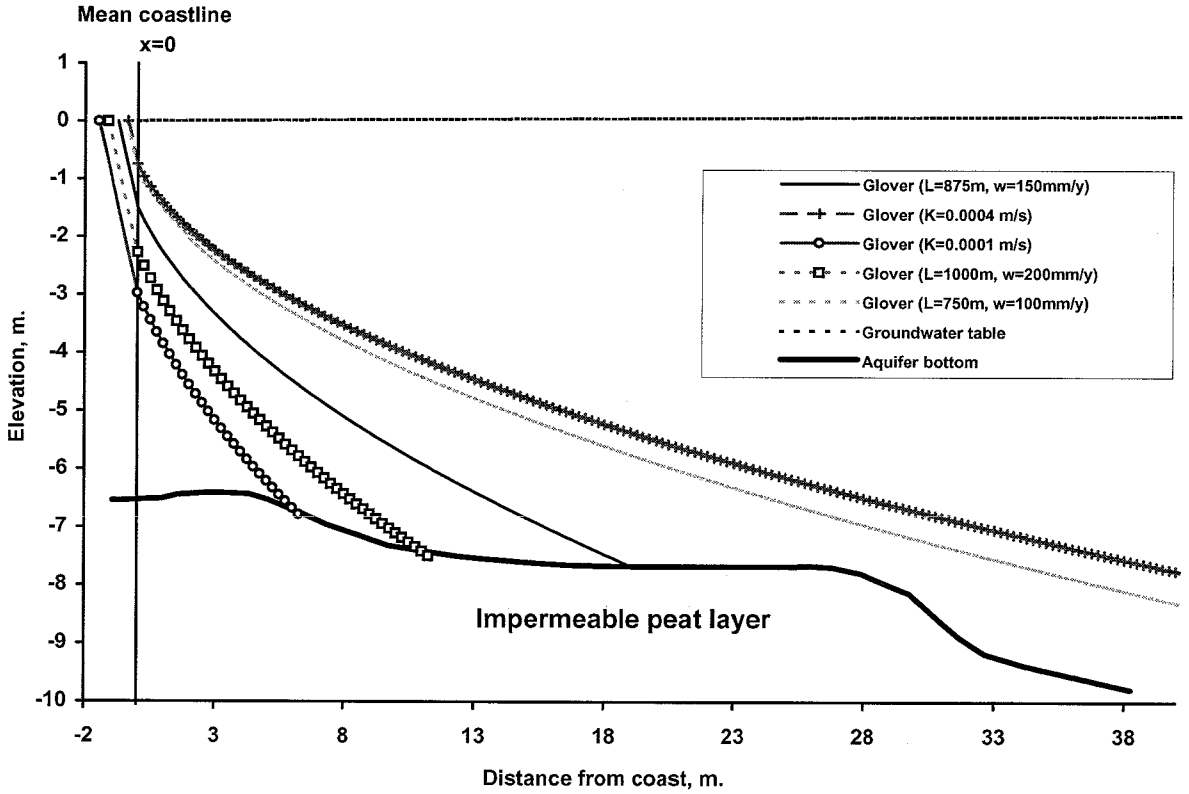

Figure 5.16: Sensitivity analysis of the sharp interface position with varying hydraulic conductivity K ($1 \cdot 10^{-4}$ to $4 \cdot 10^{-4}$ m/s) and fresh water outflow q (750m·100mm/y to 1000m·200mm/y) calculated by the Glover solution (equation 5.3).

deeper aquifers. The mean annual infiltration w is estimated to be about 150 mm/year, well within the range of mean annual infiltration for the area given by Hansen (1980) of 100 - 200 mm/year. The estimated freshwater discharge is then $q = 4.2 \cdot 10^{-6}$ m^2/s.

An independent estimate of the freshwater outflow q can be calculated using Darcy's law:

$$q = K \cdot D \cdot \frac{dh}{dx} \qquad (5.4)$$

Where D is the thickness of the outflow zone. The total freshwater flux is probably most correctly calculated right at the coastline, but it is difficult to measure a reliable average hydraulic gradient (dh/dx) near the coast due to rapid sea level fluctuations. Instead the calculation is performed at 50 m from the coast were the influence of sea level changes is sufficiently dampened (see Fig. 5.13). At 50 m the aquifer thickness D is about 9 m. The summer hydraulic gradient of 0.55‰ and the average hydraulic conductivity (K) of $2 \cdot 10^{-4}$ m/s are used. This gives a summer flux q of $1.0 \cdot 10^{-6}$ m^2/s. For winter the flux q is $5.0 \cdot 10^{-6}$ m^2/s using the winter gradient of 2.75‰. These values are bracketing the average estimate of q from $w \cdot L$ ($= 4.2 \cdot 10^{-6}$ m^2/s). Although the summer flux is a bit low, the parameters used in the Glover solution are substantiated.

In Figure 5.15 the observed 50% seawater contour (from summer 1999) is compared with the Glover interface position calculated using the average hydrogeological parameters. The observed position of the interface coincide reasonably well with the sharp interface calculated using Glovers solution. However, the observed interface is flatter, lying below the Glover interface near the coast and above it away from the coast. An explanation to this could be anisotropy in the aquifer caused by horizontal layering. According to Stuyfzand (1993) such anisotropy will result in a shallower sea-/freshwater interface inland while the beach portion of the interface will be deeper and further seaward, resulting in a flatter interface. Wicks and Herman (1995) showed by numerical modelling that placing a single high conductive layer in an otherwise homogeneous aquifer could have a substantial effect on the location and shape of the sea-/freshwater interface. They obtained the largest effect by placing the high conductive layer in the upper part of the aquifer where it would serve as a conduit for the freshwater and forced the interface further seaward, but then this also caused a considerable landward displacement of the interface below the high conductive layer. That

anisotropy may play a role in the Skansehage aquifer is hinted by the horizontal layering of the hydraulic conductivity (Fig. 5.8) and by the contours of equal hydraulic head dipping towards the coast (Fig. 5.12).

A sensitivity analysis of the various parameters in the Glover equation (5.3) was carried out (Fig. 5.16). The hydraulic conductivity K was varied from $1 \cdot 10^{-4}$ to $4 \cdot 10^{-4}$ m/s and the fresh water outflow q was varied as the product of $w \cdot L$, from a minimum of 750m·100mm/y to a maximum of 1000m·200mm/y. All the curves underestimate the depth to the interface at the coast. Using a high K and a low q yield better agreements with the observed interface in the landward part of the aquifer, although the values used are at the limits of the average hydrogeological observations. An alternative explanation for the observed discrepancy in the landward part of the transect is that not all the infiltration from the groundwater divide recharges the upper aquifer, but also deeper aquifers. This has not been investigated further, but freshwater is present at larger depth. Also the proximity of the coastline to the east could lead to a lower freshwater outflow, because divergence in the groundwater flow is to be expected towards the intersection of the southern and eastern coastlines (see Fig. 5.1, 5.10 and 5.11).

It could be argued that the high salinity in the low permeable peat is caused by stagnant seawater in the peat from the time of deposition. The observed interface could thus be a result of these relic conditions. A 50% seawater contour was drawn omitting the EC-values from all the low permeable filters (see Fig. 5.15). This new 50% contour is consistent with the 50% seawater contour based on all the filters between the coast and 16 m inland. Therefore the interface in this portion of the aquifer must be recent. Inland beyond 16 m, where no filter in the permeable sandy part of the aquifer attains an EC higher than 15000 µS/cm the two 50% seawater contours deviate, with the contour omitting the low permeable filters only reaching 20 m inland. There is a better agreement between this modified 50% seawater contour and the Glover sharp interface. Therefore the contour line based on all filters could possibly be affected by stagnant seawater in the peat further inland. Finally the geometry of the aquifer bottom may also influence the interface position. If seawater gets past the threshold at 28 m it may flow down along the landward dipping aquifer bottom and get trapped at 30 to 40 m because of its higher density.

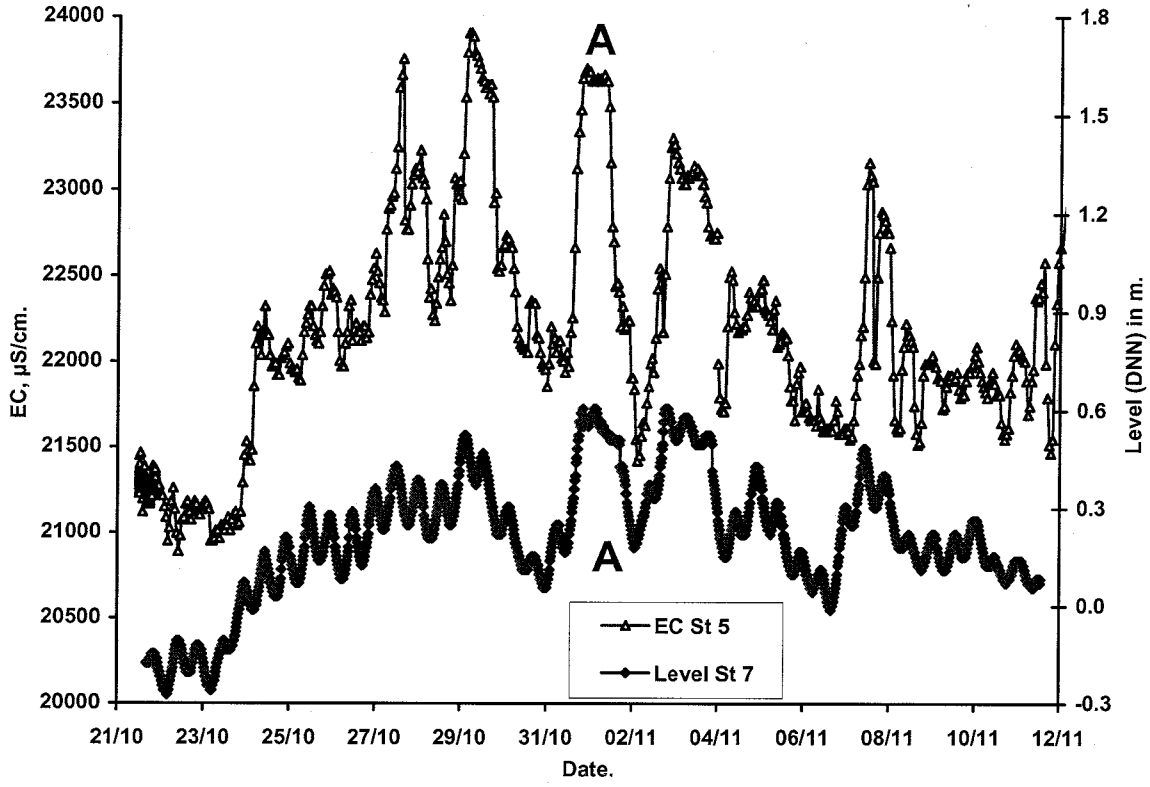

Figure. 5.17: EC- and head-fluctuations during a 22-day period in two monitoring wells 5 m (EC) and 7 m (head) from the coast.

5.4 Dispersion of the sea-/freshwater interface

The interface between sea- and freshwater is not a sharp boundary, but a dispersed mixing zone. In Figure 5.14a the zone between 3000 µS/cm and 27000 µS/cm corresponds roughly to seawater fractions from 0.1 to 0.9. Therefore the part of the aquifer affected by more than 10% seawater, extends from the upper part of the beach, 20 m from the coast, all the way to 90 m from the coast at an elevation of –8 m. The thickness of this mixing zone increases away from the coastline. If the thickness of the mixing zone is taken as the distance between 90% and 10% seawater then 10 meters from the coast the thickness is 3.4 m (Fig. 5.14a). The 90% seawater contour only penetrates inland to 17m, so further inland the thickness is roughly estimated as 2 times the distance between 10% and 50% seawater, assuming symmetry around the 50% line. This results in a calculated mixing zone thickness increasing to more than 10 m at 38 meters from the coast.

There are several physical processes, which may contribute to increasing the mixing zone thickness. Among these are: 1) Sea-level variations 2) Seasonal variations in recharge and thus fresh water outflow 3) Upwards leakage through the bottom aquitard 4) Heterogeneities in the aquifer 5) Flow of seawater induced in the seawater wedge by loss of salts across the fresh-/seawater interface. And finally 6) Mixing caused by density plumes of inundating seawater (this will be treated separately). In the following effects of these processes will be discussed.

Movement of the interface due to tidal sea level fluctuations was assessed by continuous measurements of EC in selected monitoring wells. Figure. 5.17 shows how the EC, in a monitoring well (St5) 5 m from the coast, fluctuates simultaneous with changes in head in a nearby well (St7). Around the 31st of October, at A in Figure. 5.17, a change in head of 0.44 m corresponds to a change in EC of 1764 µS/cm. This head change is large compared to the normally small tidal fluctuations in the fjord. The vertical EC gradient at monitoring well St5 is estimated from the contoured EC-plot (august 1999 Fig. 5.14a) and is 5614 µS/cm per meter. A change in EC of 1764 µS/cm is then equivalent to a displacement of the interface of 30 cm. The same calculations were conducted for wells 11 and 23 meters from the coast yielding displacements of 15 cm and 8.6 cm respectively. Oscillations in the interface position as a result of tidal fluctuations decrease rapidly away from the coast. Therefore tidal effects are not likely to be responsible for the increased thickness of the mixing zone with distance from the coast.

Still, repetitive tidal fluctuations may induce mixing. Numerical simulations of a shallow unconfined aquifer by Ataie-Ashtiani et al. (1999) (using a modified SUTRA code (Voss, 1984)) showed that tidal activity both forces the seawater further inland and increases the thickness of the mixing zone as compared to a situation without tidal activity. For tidal amplitudes comparable to those at Skansehage Ataie-Ashtiani et al. (1999) found that the change in position of the 50% seawater contour is insignificant, but it does cause a larger mixing zone. The modelled effects on the mixing zone are most pronounced near the beach.

Because the effects of tidal- and other sea-level fluctuations decrease inland (see Figure 5.13) this effect is not likely to lead to significant dispersion inland. Instead seasonal variations in the groundwater outflow, which act on a larger time scale, allowing time for movement of the interface, is a more likely candidate. However, for the particular summer and winter situations shown in Figure 5.14a&b differences in the interface positions are small. To assess the maximum effect of seasonal variations on the interface position, the outflow flux q is estimated on the basis of the head gradients obtained from the groundwater potential maps for winter (Fig. 5.10) and summer (Fig. 5.11). In the summer situation a low gradient of 0.55‰ is obtained if the steep gradient in the coastal part (0-40m) is neglected. For the winter situation a gradient of 2.75‰ is obtained (again neglecting the part from 0 to 40m). Combining Darcy's law (5.1) and a water balance equation (5.5) for the aquifer, an average seasonal recharge w^* can be calculated which then can be used in the Glover solution (5.3) to calculate a new interface equilibrium. The water balance equation is given by:

$$v = \frac{w \cdot L}{D \cdot \varepsilon} \tag{5.5}$$

Where v is pore water velocity (m/s), w is recharge (m/s), L is length of the aquifer (m), D is thickness of the aquifer (m) and ε is the porosity. Combined with Darcy's law:

$$w^* = D \cdot \frac{K \cdot dh}{L \cdot dx} \tag{5.6}$$

Where K is the hydraulic conductivity (m/s) and dh/dx is the head gradient. This approach is only an approximation because transient changes in head gradients and a delayed effect of change in

infiltration are neglected. The summer recharge obtained is: $w^* = 36$ mm/y and for winter: $w^* = 178$ mm/y. The change in the interface position is largest at the toe, where the interface intersects with the aquifer bottom. For the winter recharge the toe only moves about four meters seaward whereas the summer recharge moves the interface a considerable distance inland reaching 80 m from the coast at an elevation of –8 m. However, there is the question of time required for the interface to reach the new equilibrium. Numerical modelling using HST3D (Kipp, 1987) of a homogeneous aquifer with varying recharge indicates that the time required for equilibrium to be attained is much longer than the period of the seasonal changes (Christensen, unpublished data). Model simulations with and without seasonal recharge variations show little difference in mixing zone appearance. The slow response in the movement of the interface is also supported by observations during the intrusion experiment (Fig. 7.5 in section 7.3) where the interface moved only slowly landward at a rate of 10 m/month under the influence of a landward hydraulic gradient of 6‰ (Fig. 7.2 section 7.1), which is much larger than it is to be expected in a natural situation. Still long-term changes in the freshwater flux can have a significant effect, not only on interface position, but also on the mixing zone thickness. Ataie-Ashtiani et al. (1999) demonstrated by numerical simulations that a five fold decrease in freshwater flux (or hydraulic gradient) not only forces the sea water further landward but also creates a thicker mixing zone. The mixing zone length at the base of the aquifer (from 10% to 90% seawater) increased with a factor of 2.75.

In a zone from roughly 30 - 80 m from the coast, there are indications for upward leakage of water from the aquifer underneath (Fig. 5.12). This water has a different salinity and mixing with the overlying water may create a larger apparent mixing zone.

The low topography at the field site makes the area prone to inundations at extremely high sea levels, induced by storms. The inundation leads to formation of seawater ponds in depressions and subsequently due to its higher density the seawater percolates down through the aquifer. The increased mixing zone thickness could be a result of such events. Especially the higher EC at elevations of –7 m to –9 m at 50 to 85 meters from the coast could be seawater from a previous inundation slowly being leached from layers of low permeability. The flow and chemistry of an actual inundation event will be treated in section 5.5 and in section 6.3.

Also a heterogeneous permeability distribution will increase the apparent dispersion, both because of a heterogeneous flow pattern and because of diffusion out of low permeable zones (Cooper, 1964).

Finally convection of seawater within the saltwater wedge could also contribute to increased mixing. The convection was hypothesized by Cooper (1964) and is believed to be driven by a loss of seawater from the saltwater wedge due to dispersive mixing of the seawater into the discharging freshwater across the interface. The loss of seawater leads to a reduction of the density in the wedge causing a renewed density driven inflow of seawater. It is also a commonly seen phenomenon in numerical modelling of flow associated with a sea-/freshwater interface (Reilly and Goodman, 1985, Bear et al., 1999, Christensen et al., 2001). In the field, this convective flow was shown to take place in an aquifer in Florida by Kohout (1964) and it could also be taking place in the Skansehage aquifer. Numerical simulation of the field site by Christensen (unpublished data) indicate that the landward flow in the wedge reaches 10 to 20 m into the transect before curving up and back towards the sea, but transverse dispersion included in the model caused effects 10 to 20 meters further landward. However, several of the effects described above may overprint the effect of this rather slow but perpetual convective flow. Therefore direct physical field evidence for the convective flow is difficult to obtain.

The decrease in mixing zone thickness towards the coast is not what intuitively is expected, since mixing near the coast should be higher due to sea level fluctuations, tidal action, wave setup and subsequent percolation of seawater through the beach deposits. The explanation for this apparent discrepancy is probably the reduction in the cross sectional area available to fresh water outflow near the coast. This reduction is caused by the presence of the saltwater wedge and the shallow position of the peat layer at the coast. The fresh water is forced up over the saltwater wedge, compressing the flow lines and reducing the mixing zone thickness. If the thickness of the mixing zone is proportional to the decrease in area, ignoring all other processes, then the following calculation can be made: The part of the aquifer with flow directed towards the coast at 35 meter is about 9 m and the mixing zone thickness is 8 m (2 · thickness from 10% to 50%). At 10 meter from the coast the outflow thickness is about 4 m. Based on the ratio between the outflow thickness at 10 and 35 m, a calculated mixing zone thickness of 3.6 m (=8m·4m/9m) should be expected at 10 m from the coast. This is very close to the observed thickness of 3.4 m.

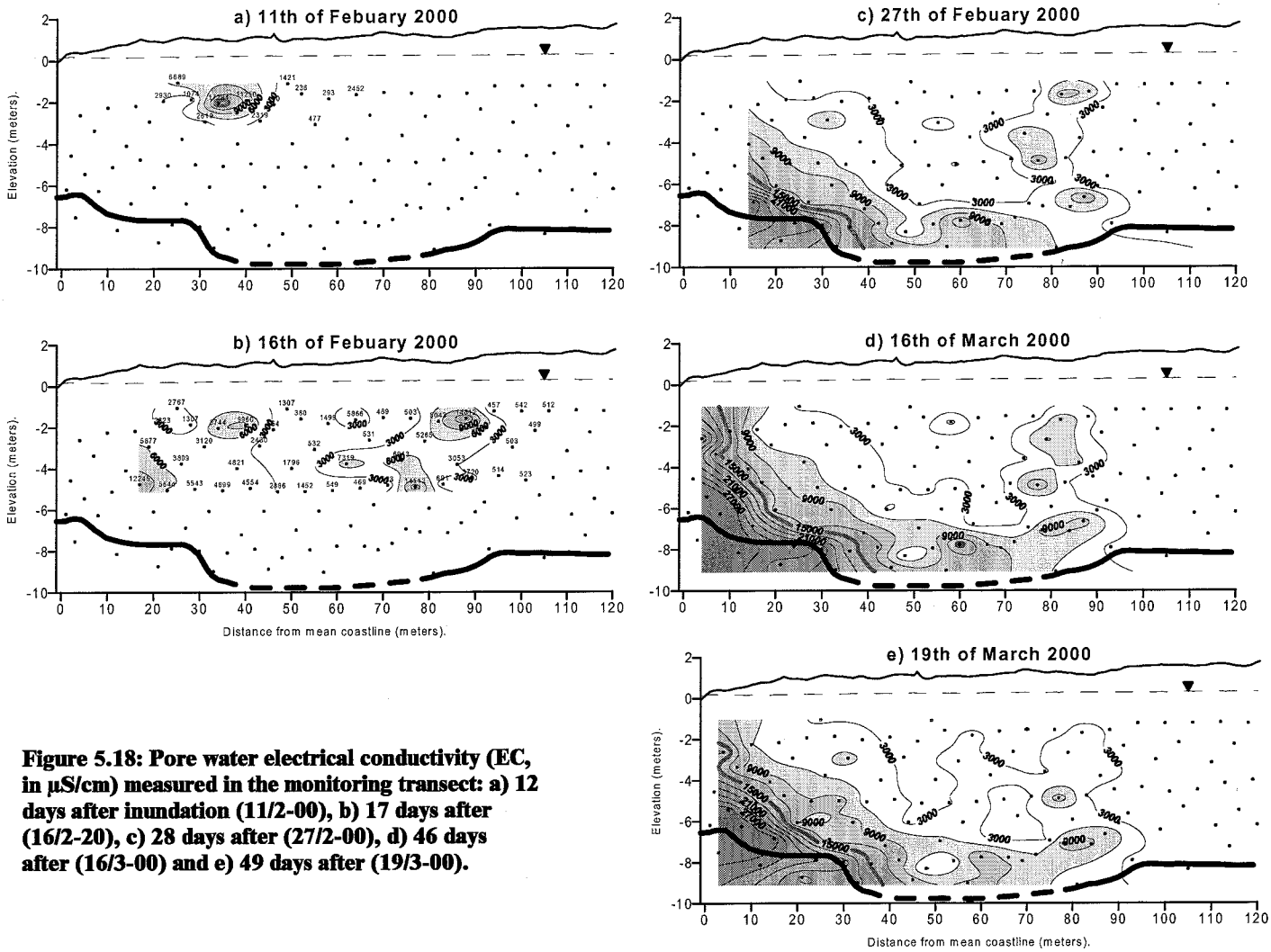

Figure 5.18: Pore water electrical conductivity (EC, in µS/cm) measured in the monitoring transect: a) 12 days after inundation (11/2-00), b) 17 days after (16/2-20), c) 28 days after (27/2-00), d) 46 days after (16/3-00) and e) 49 days after (19/3-00).

In summary the effects on the mixing zone by tidal action and smaller wind induced frequently occurring irregular sea-level fluctuations are small and restricted to the zone near the coast (< 20 – 40 m). But due to their frequent occurrence the effect may accumulate and lead to some dispersion over time. Also the effects of convective circulation seem to be restricted to the zone near the coast (< 40 m). Seasonal variations in the recharge will in comparison have a greater effect further from the coast, but the slow response in the interface movement probably only gives rise to a few meters of landward transport in the wedge before being pushed seaward by the following high winter recharge. The most significant of the mixing processes is presumably the inundation events caused by storms, which the field site is vulnerable to because of the low topography. A particular inundation event will be discussed in more detail in the following section.

5.5 Winter storm induced inundation

During the winter of 2000 a northwesterly to northerly storm caused part of the low-lying field area to be inundated with seawater. The inundation occurred on the 29 and 30 of January. A maximum sea level of 1.4 m above DNN (mean Danish sea-level) was recorded nearby at Hornbæk in the Sea of Kattegat. In the transect a sea level rise of 1.4 m intersects the terrain at the monitoring well St90, 90 m from the coast.

The inundation caused ponding of seawater in local topographical depressions. Here the seawater infiltrated through the unsaturated zone and continued as plumes migrating down through the aquifer driven by their higher density. The data indicate that this occurred at mainly three places along the transect; at 35, 65 and 85 meters from the mean coastline, as is shown by the pore water EC measurements from the transect at 12, 17, 28, 46 and 49 days after the inundation event (see Figure 5.18a,b,c,d&e).

The early stage of the seawater plume migration down through the aquifer, in the transect, was only partially sampled (Fig. 5.18a and5.18b). A saltwater body with an EC of up to 17300 µS/cm at 3 m below the water table, 35 m from the coast was recorded only 12 days after the inundation event. This corresponds to somewhat more than 50 % seawater. Five days later saltwater bodies are found at least 5 m below the water table. As the saltwater, moves downward in the transect and disperses the EC peaks decrease. At later times the maximum measured pore water EC-values in the transect

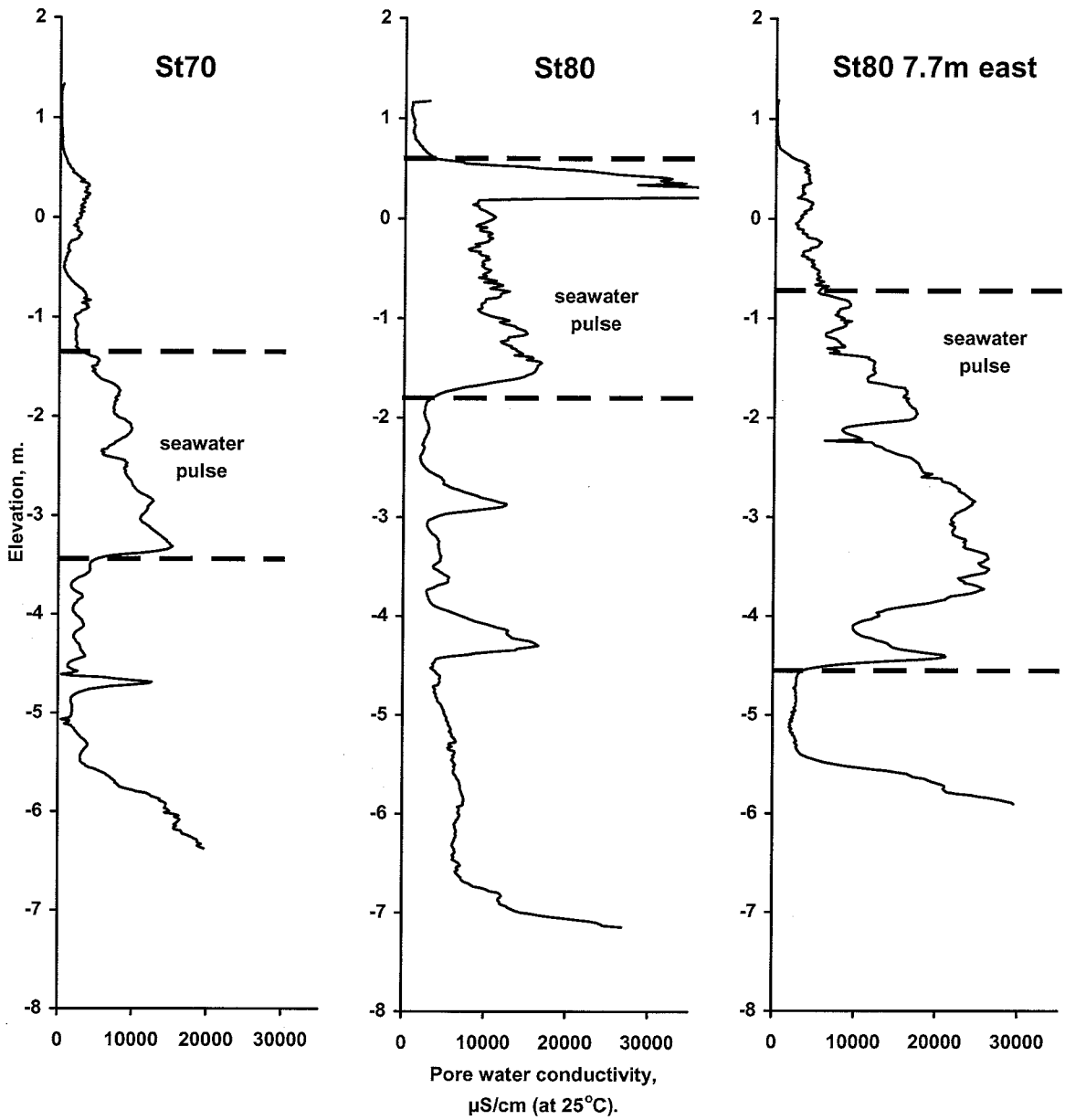

Figure 5.19: Pore water electrical conductivities (in µS/cm) calculated from bulk electrical conductivities. From El-logs driven with a Geoprobe, 32 days (2nd of March 2000) after the inundation next to borings a) St70, b) St80 and c) St80_7.7E (7.7 m east of St80).

are between 10000 and 14800 μS/cm. The pattern of downward migration is quite complex. This can be exemplified by the plume at about 60 meters (Fig. 5.18), which was not detected in the shallower monitoring wells. The plume is either very narrow bypassing the shallower wells or the plume is infiltrating sideward of the transect and spreading at depth to reach the transect from the side. The complexity is also indicated by the pore water EC-development over time and depth of a single plume at 85 m from the coast (Fig. 5.18b,c,d&e). Fig. 5.18c show how the plume at 85 m path is not straight vertical, and seem to have several high EC peaks. Downward migration of the individual EC-peaks in this plume cannot completely be followed over time and some parts of the aquifer in the path of the plume do not seem to be affected at all. Possible explanations are a combination of: 1) The flow path varies in three dimensions and is not resolved by the two dimensional monitoring transect and 2) small scale variations in the hydraulic conductivity distribution not resolved by the slugtests (Figure 5.8) in the monitoring wells.

A better depth resolution of the vertical extension of the seawater plumes is obtained from El-logs. Three El-logs were performed 32 days after the inundation event next to the wells at St70, St80 and 7.7 m east of St80 (St80_7.7E). Figure 5.19 show the pore water conductivity σ_w of the El-logs recalculated from the bulk electrical conductivity σ_b. This pore water conductivity σ_w is equivalent to the pore water EC as long changes in geology and porosity are small. The electrical conductivity logs of Figure 5.19 exhibits σ_w variations almost on a centimetre depth scale. They also reveal that the seawater plumes apparently split into a slower main plume of a few meters in thickness and into fast fingers reaching deeper levels in the aquifer as illustrated by the peaks at –3 and –4.5 m in the El-log at St80 (Fig. 5.19b). An alternative explanation for the deeper peaks is that they are caused by earlier inundation events. The main plumes generally show a steep EC increase at the front and a gradual EC decrease in the tail due to mixing.

Comparison of El-logs performed next to monitoring well St70 before and after the inundation illustrate that the deeper high σ_w peaks must be caused by the inundating seawater (Fig. 5.20). Before the inundation (Fig. 5.20a) the conductivity log is smooth with no peaks through most of the aquifer and only increasing towards the bottom where the peat layer is found. The peak at –4.5 m in the El-log after the inundation event (Fig. 5.20b) must therefore be related to the percolating seawater. But the presence of these deeper seawater peaks must be due to complex geological variations. The homogeneous electrical conductivity of the El-log at ST70 prior to the inundation

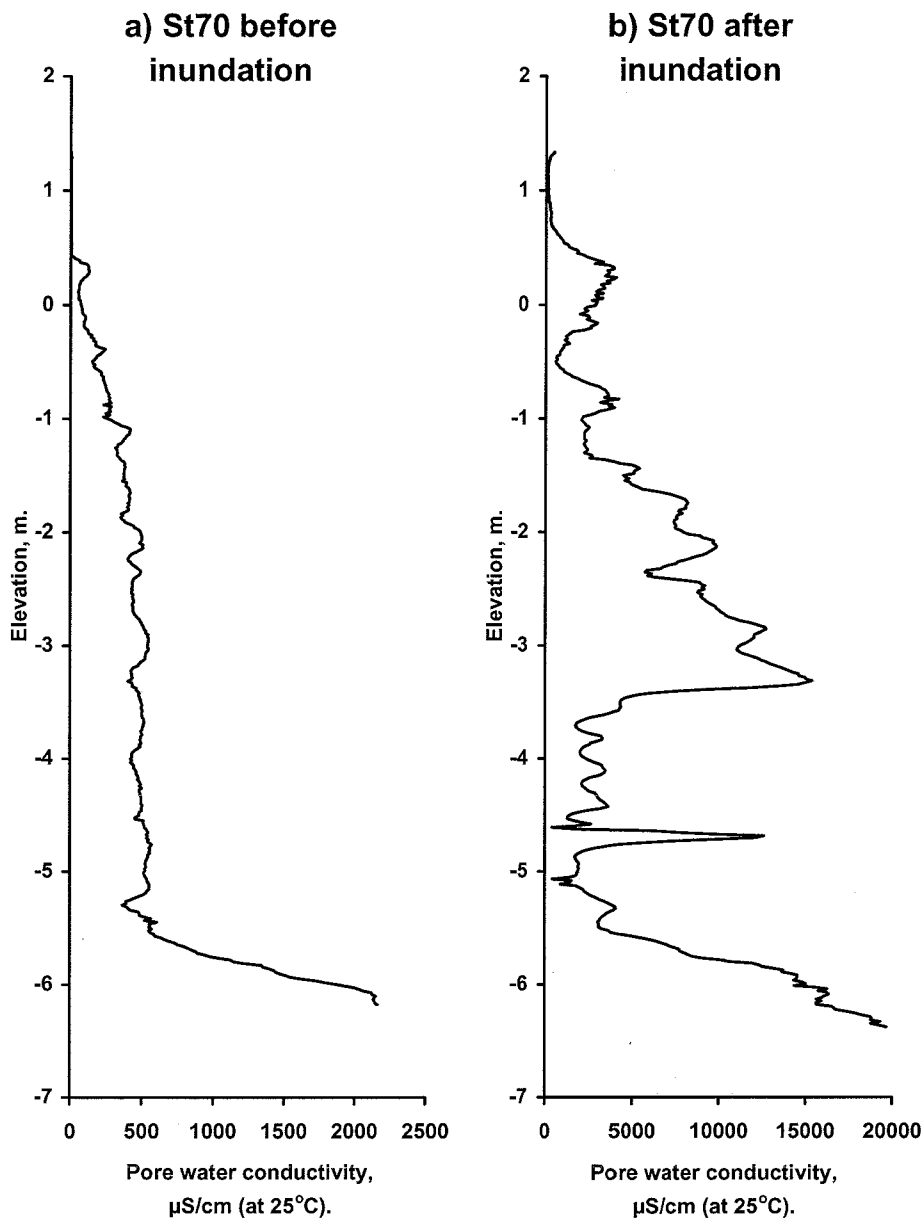

Figure 5.20: Comparison of pore water electrical conductivities, (ρ_w in µS/cm) from continuous El-logs driven with a Geoprobe next to boring St70 a) before inundation the 12/7-1999 and b) 2/3-2000, 32 days after the inundation. Note difference in the electrical conductivity scale.

wrongly indicates a relatively uniform geology and/or pore water conductivity probably due to a uniform porosity. But, after the inundation the El-logs clearly reveal a high degree of variation in permeability affecting vertical (and probably also horizontal) flow of percolating seawater. These permeability variations can evidently not be fully recognized from sediment descriptions and grain size curves, because of disturbance or mixing of layers during coring and sampling.

The El-logs reveal large variations in both the percolation depth of the seawater plumes and in the size of σ_w within a small horizontal distance (less than 10 m) as illustrated by the El-logs after the inundation (Fig. 5.19). In the log at St80 a zone of high pore water conductivity up to 16700 µS/cm is encountered at an elevation from +0.6 m to –1.8 m. Whereas in the log at St70 the high pore water conductivity zone (up to 15300 µS/cm) is found deeper at –1.4 m to –3.5 m. At St80_7.7E the high pore water conductivity zone is found even deeper and over a larger depth interval of –0.6 to –4.5 and the maximum pore water conductivity is as high as 26300 µS/cm. Generally the maximum σ_w are higher in the logs than the pore water EC's measured in the transect. This again is probably a result of the higher resolution of the El-logs, whereas the EC measurements on pumped groundwater samples lead to averaging of a larger aquifer volume.

In the log at St80 (Fig. 5.19b) a zone of extremely high pore water σ_w of more than 35000 µS/cm is found at an elevation of 0.6 to 0 m. This zone, located on the border of the saturated/unsaturated zone, is probably a low permeable peat layer retaining some relatively undiluted seawater. The occurrence of such a layer could explain the slower migration of the plume at St80 compared to the plumes at St70 and St80_7.7E. The very high conductivity of the layer could well be overestimated if it is in fact a peat layer, because the porosity used in the conversion from bulk conductivity σ_b to pore water conductivity σ_w would then be too low.

The variations in the elevation of the high pore water conductivity zones between the different El-logs are probably a function of both permeability variations and variations in salt concentration/load of the different plumes. Variations in the salt concentration due to the mixing with the fresh water will affect the plume density, which in turn affects the flow velocity of the density flow. The vertical flow velocity in the initial phase of the plume migration is difficult to estimate due to the lack of measurements in the initial stage, but may well exceed 0.30 m/d (= 120 m/y). The most reliable estimate of the average flow velocity is probably obtained from the El-logs measured 32

days after the inundation event Figure 5.19. The main plumes in Figure 5.19 represents average velocities from the soil surface to the front of the plume in the range from 0.09 m/d (St80) to 0.16 m/d (St80_7.7E). Higher velocities, 0.17 - 0.19 m/d are obtained for the deeper maximum in σ_w. These velocity estimates assume a straight vertical flow path. The actual flow path could well be longer and the actual flow velocity therefore higher.

A theoretical expression for the vertical advective plume migration velocity (v) in the saturated zone is given by Post et al., (2001):

$$v = \frac{\Delta\rho \cdot g \cdot k_i}{4 \cdot \mu \cdot \varepsilon} \tag{5.7}$$

Where $\Delta\rho$ is the density contrast between the freshwater and the plume water (kg/m^3), g is the gravitational acceleration (m/s^2), μ is the fluid viscosity (kg/m·s), ε is the porosity and k_i is the intrinsic permeability (m^2). k_i is related to the hydraulic conductivity (K) by:

$$K = k_i \cdot \frac{\rho \cdot g}{\mu} \tag{5.8}$$

By combining the equations (5.7) and (5.8), and assuming that the hydraulic conductivity was determined in freshwater (which holds true for the wells in the landward and upper part of the transect) and assuming that the viscosity is constant, the velocity can be expressed as:

$$v = \frac{\Delta\rho \cdot K}{\rho_f \cdot 4 \cdot \varepsilon} \tag{5.9}$$

Here ρ_f is the density of freshwater. The density of freshwater and saltwater are calculated from the EC by equations (4.2) and (4.3) (Stuyfzand, 1989). In Table 5.2 the vertical plume migration depths are estimated for the three El-logs in Fig. 5.19 after 32 days (and also after 50 days). A constant migration velocity (x = v·t) is assumed implying a constant density contrast and a constant plume EC. An average hydraulic conductivity of $2 \cdot 10^{-4}$ m/s was used and the percolation through the unsaturated zone, which is probably in the order of a few days, is neglected. Good agreement of the

theoretical estimate and the observed depth position of the plume fronts after 32 days in figure 5.19 are obtained. For St80 a lower hydraulic conductivity is probably more correct as indicated by the hydraulic conductivity distribution in Figure 5.8 and also by the high electrical conductivity peak in the El-log at 0.5 m, which might hint the presence of a low permeability layer. If the K-value is halved for this plume to $1 \cdot 10^{-4}$ m/s then also the migration depth is halved to –1.7 m giving a better agreement.

Table 5.2: Theoretical vertical plume migration velocities and migration depths calculated according to equation (5.9) using a hydraulic conductivity of $2 \cdot 10^{-4}$ m/s, a freshwater density of 1000.04 kg/m^3 (calculated from a freshwater EC of 500 µS/cm) and a porosity of 0.35.

El-log	EC µS/cm	Density kg/m^3	Velocity M/d	Days after inundation	Migration depth m	Observed position of plume front after 32 d
St70	15300	1008.14	0.10	32	-3.2	-3.5
				50	-5.0	-
St80	16700	1008.90	0.11	32	-3.5	-1.8
				50	-5.5	-
St80 7.7m east	26300	1014.11	0.17	32	-5.6	-4.5
				50	-8.7	-

The initial mixing proportions of seawater and freshwater is difficult to asses. The initial seawater fraction in the plumes was probably somewhat higher than 50% as indicated by the maximum pore water EC of 17300 µS/cm recorded 12 days after the inundation occurred (Fig.5.18a). Also the El-logs at St70 and St80, 32 days after the inundation, with maximum pore water EC's of 15300 and 16700 µS/cm respectively, support that the initial seawater fraction was somewhat more than 50%. However, for the El-log 7.7 m east of St80 the percentage of seawater after 32 days is as high as 88% indicating less initial mixing for this plume.

As a plume migrates down, it mixes with the surrounding groundwater and leaves a diluted tail in its path. This is illustrated by the decreasing EC values measured in the transect. After about 50 days (Fig.5.18e) the maximum measured pore water EC in the transect is reduced to about 10000 µS/cm (corresponding to 1/3 seawater). If El-logs were performed at this time local zones of higher EC would probably be encountered. In both the El-logs and the pore water EC measurements at late

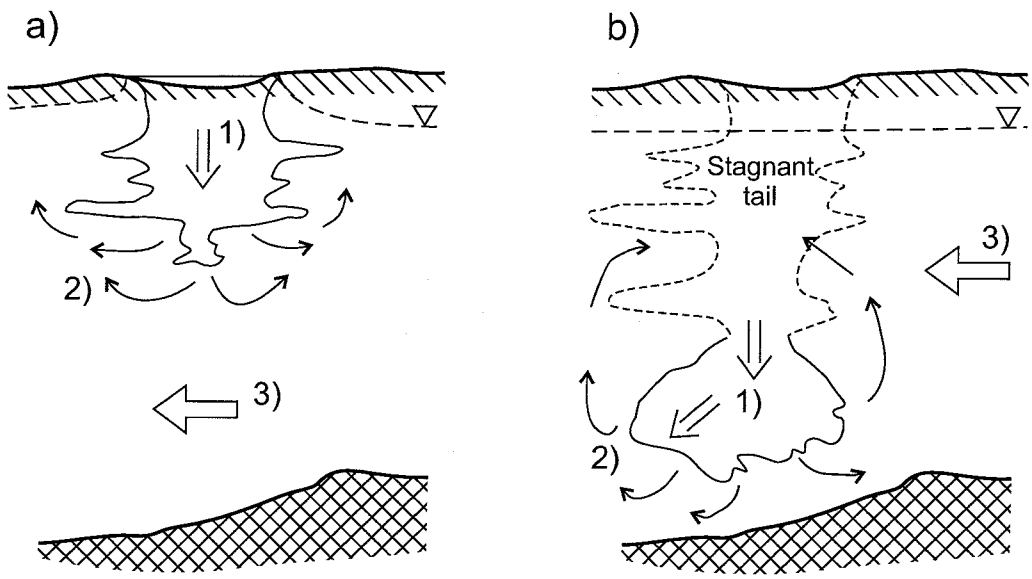

Figure 5.21: Schematics of the physical processes during density driven seawater plume migration in a heterogeneous aquifer. a) During seawater inundation, b) Some time after inundation with development of stagnant tail.

times the formation of tails with elevated EC-values of about 3000 to 5000 µS/cm can be observed. During the inundation and the downward migration of the density driven plumes considerable mixing of the seawater with fresh water thus seem to have taken place. The loss of density due to mixing must slow down the migration velocity. Density loss in the tails due to mixing with freshwater flowing back into the path of the plume will halt this part of the plume all-together and a slow seaward transport will start to dominate. With a winter ground water velocity of 50 m/y a seaward transportation of about 7 m should have occurred between the 31st of January and the 19th of March. This will increase the mixing, smoothen out and decrease the EC-values.

Figure 5.21 summarises the mechanism of the percolating seawater. The plume of denser seawater displaces the freshwater and when encountering layers of lower permeability spread out in the high permeability layer leading to the high electrical conductivity peaks (Fig. 5.19). As the plume spreads out it encounters vertical high permeability conduits where the downward migration can resume. As the plume passes, freshwater flows back into the path of the plume and mix with the tail of the plume. The tail water is eventually driven towards the sea by the groundwater flow.

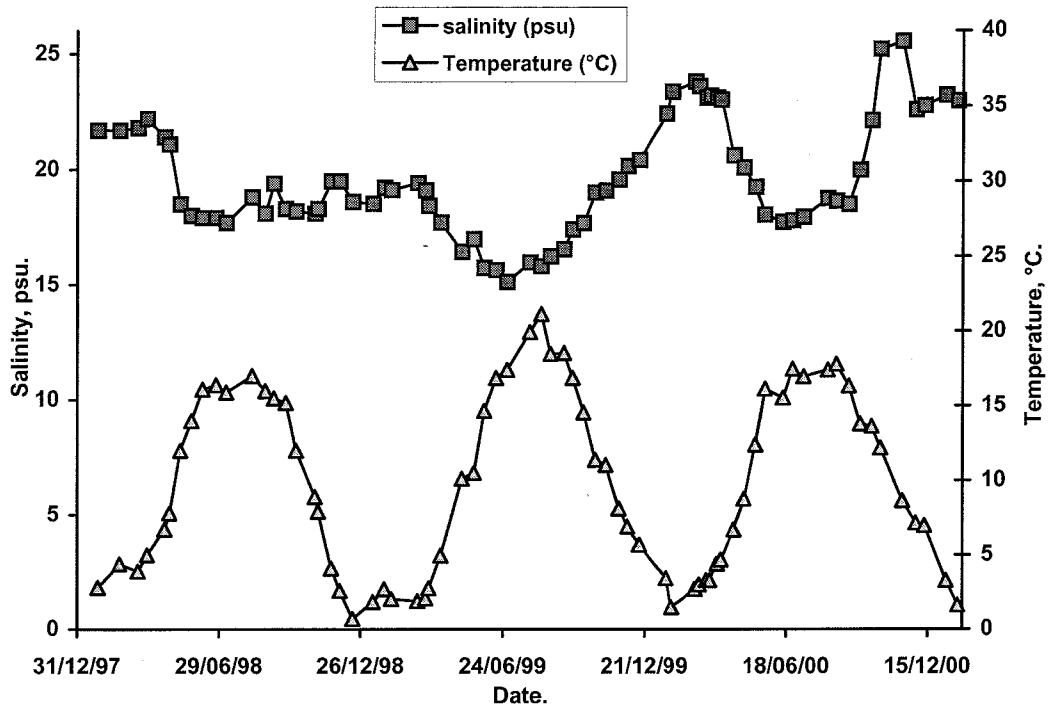

Figure 6.1: Salinity and temperature measured in the central part of Isefjord from 26/1-1998 to 23/1-2001 at a depth of 7 m (data from the County of Western Zealand).

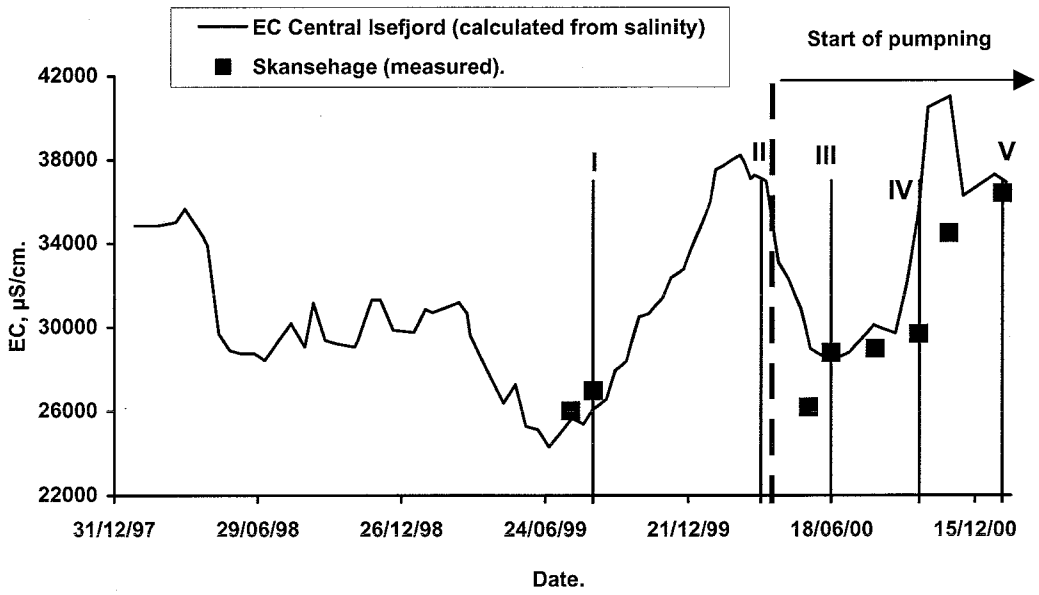

Figure 6.2: EC (µS/cm) measured in the immediate vicinity of the field location Skansehage compared with EC calculated on the basis of the salinity time series from the central part of the Isefjord. EC = (Salinity/0.69778·10^{-3})·1.12 (Stuyfzand 1989; Arps 1953). Roman numbers refer to times where water samples were collected in the transect of monitoring wells (see also Table 6.1).

6. CHEMISTRY: NATURAL SITUATION

Before presenting the results of the groundwater chemistry, the varying salinity and the chemical composition of the Isefjord seawater will be introduced, as it is an important boundary condition for the aquifer.

6.1. Isefjord seawater chemistry

Isefjord is a brackish fjord with seasonally varying salinity. Figure 6.1 shows the variation of salinity and temperature over a 3-year period in the central part of Isefjord (data from the County of Western Zealand). Salinity varies between 15 and 25 ‰ (equal to ~1/2-3/4 of the salinity of ocean seawater), with a mean value of 19.6 ‰. The winter peak is caused by autumn and winter storms forcing saltier seawater from Kattegat into the fjord. In the quieter summer periods stream- and groundwater discharge decreases the salinity in the fjord. There is an inverse correlation between salinity and temperature, which varies from 20 °C (summer) to near 0 °C (winter). In Fig. 6.2 the salinity of Fig. 6.1 is converted to electrical conductivity (EC) and compared to EC values measured in the fjord near the field site. The agreement is good and therefore the EC time series from the central part of Isefjord is used as the boundary condition for EC. The fluctuation in salinity in the fjord has implications for the interpretation of the seawater intrusion data and for understanding the shape of the sea-/freshwater boundary near the coast.

The chemical composition of the fjord water changes with the EC as seen in Table 6.1. However, for the major ions (Na^+, Cl^-, Mg^{2+}, Ca^{2+}, K^+ and SO_4^{2-}) the ratio of the ion over chloride is near constant and close to the ratio in ocean water (from Appelo and Postma, 1993). For these ions the contribution from the fresh stream- and groundwater to the fjord is negligible. The Alkalinity/Cl^--ratio is higher for the fjord water than for ocean water and the ratio increases with decreasing Cl^--concentration indicating that the contribution of alkalinity from the fresh stream- and groundwater to the fjord is significant.

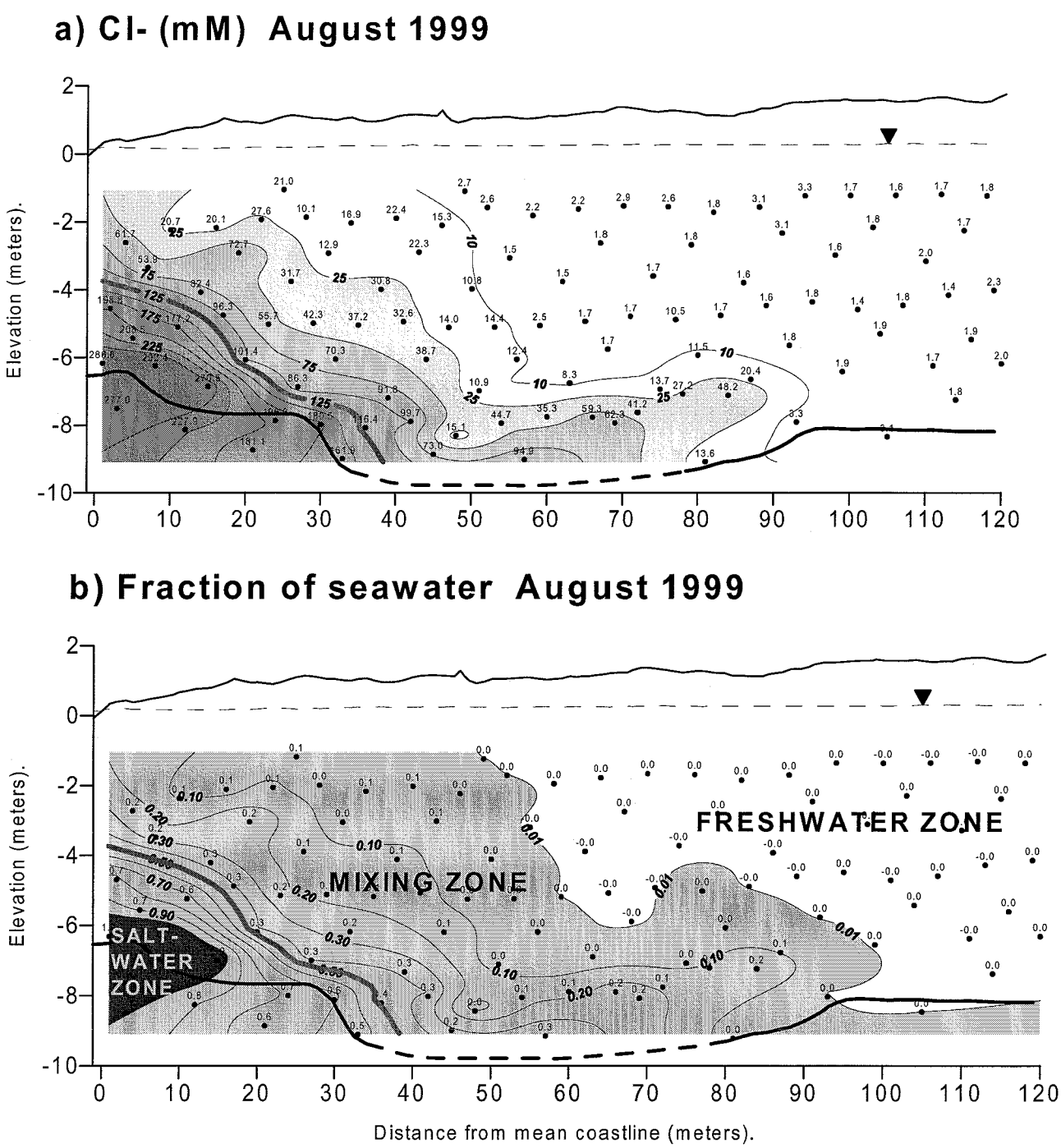

Figure 6.3: a) Chloride concentrations (mM) in the transect b) Fraction of seawater in the transect calculated on the basis of chloride.

Table 6.1: Chemical composition of the seawater from Isefjord

Boring	Date of sampling	EC µS/cm	pH	Alkalinity meq/l	NH_4^+ mM	Ca^{2+} mM	Mg^{2+} mM	K^+ mM	Na^+ mM	Cl^- MM	SO_4^{2-} mM
R1-R5	30-06-98	27635	8.24	3.35	0.028	5.4	24.3	5.0	248.8	256.1	12.9
Sr14	20-11-98	35300	8.14	2.45	0.021	9.5	28.8	7.5	273.2	339.2	16.5
Sr15	25-02-99	33800		2.41	0.003	5.6	29.4	5.6	281.9	323.0	5.1
Trace I	23-08-99	27000	8.07	2.03	0.008	6.2	24.9	4.6	220.3	248.8	13.1
Trace II	19-03-00	35729				7.4	32.5	6.4	298.3	333.0	18.0
Trace III	17-06-00	28800	8.02	1.92	0.003					277.6	14.1
Trace IIII	05-10-00	29700	8.18	1.93	0.001	5.2	26.7	5.6	235.1	269.6	15.0
Trace V	18-01-01	36400	8.09	2.07	0.006	7.5	31.1	6.2	280.6	358.8	18.2
Mean values		31796	8.123	2.31	0.010	6.7	28.2	5.8	262.6	300.7	14.1
Appelo & Postma, 1993		60257	8.2	2.4	0.021	10.7	55.1	10.6	485	566	29.3

6.2 Groundwater chemistry: The natural situation

6.2.1 Chloride

The chloride concentration in the transect, of August 1999, is shown in Fig. 6.3a. As Cl^- is the dominating anion in seawater the distribution resembles the EC data of Fig. 5.13a, clearly showing the dense seawater wedge underlying the lighter freshwater.

6.2.2 Fraction of seawater

Chloride is a key parameter towards understanding the non-reactive advective transport and mixing in the transect. The fraction of seawater (f_{sea}) contained in a water sample can be calculated from the chloride concentrations as (Appelo and Postma, 1993):

$$f_{sea} = \frac{m_{Cl-,sample} - m_{Cl-,fresh}}{m_{Cl-,sea} - m_{Cl-,fresh}} \qquad (6.1)$$

The fraction of seawater is however, influenced by the fluctuating salinity in the fjord (Fig. 6.2). The calculated seawater fraction can therefore vary up to 10 – 20% depending on the choice of a seawater end-member. If the chloride concentrations shown in Fig. 6.3a are converted to fractions

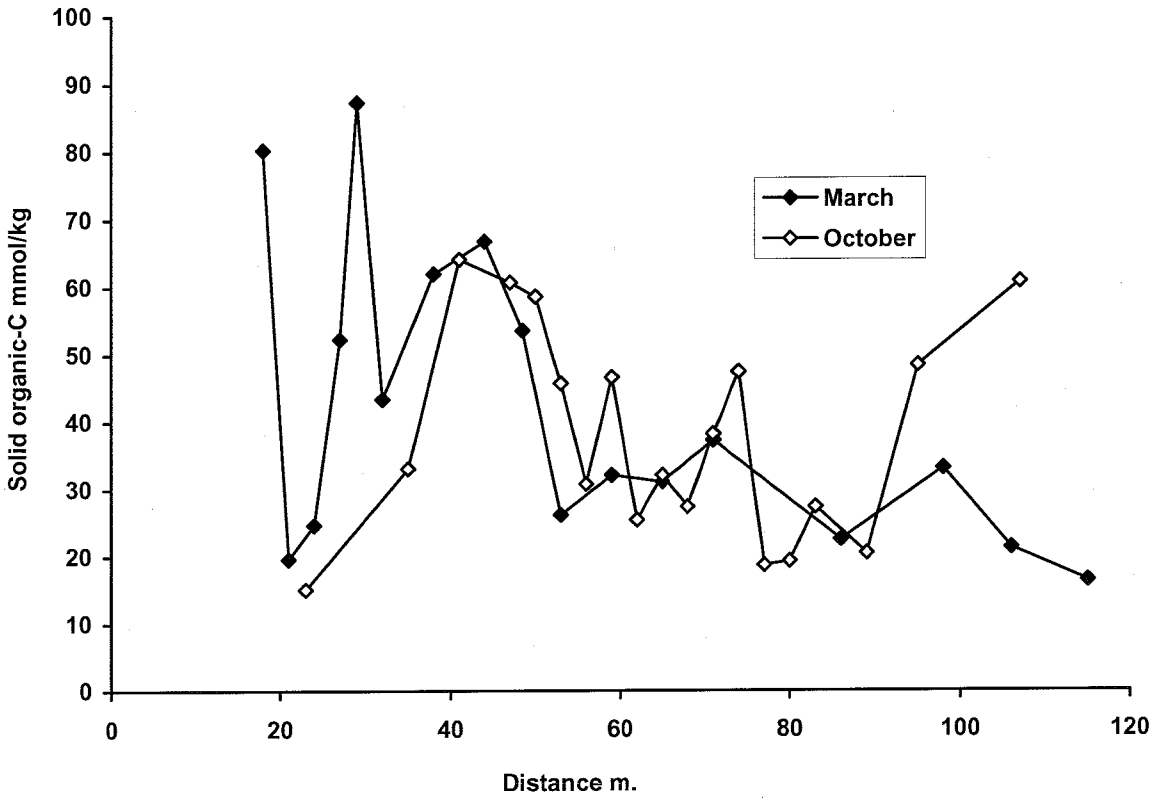

Figure 6.4: Organic carbon content in mmolC/kg for sand samples.

of seawater, three zones stand out clearly (Fig. 6.3b). These three zones have distinctly different chemical characteristics and the zones will be treated independently in the following. The seawater fraction was calculated using a seawater Cl^- concentration of 300 mM, a mean of the period from 31/12-1997 to 23/07-1999 prior to the sampling of the transect in August.

Using the seawater fraction, the expected concentrations ($m_{i,mix}$) of other dissolved species can be predicted as a result of non reactive mixing:

$$m_{i,mix} = f_{sea} \cdot m_{i,sea} + (1 - f_{sea}) \cdot m_{i,fresh} \qquad (6.2)$$

Where $m_{i,sea}$ and $m_{i,fresh}$ are the measured sea- and freshwater concentrations of the species *i* in mmol/l. The first part of the equation is thus the seawater contribution and the second part is the freshwater contribution. If the mix-concentration of a species is subtracted from the measured concentration a measure of the enrichment or depletion of the species *i* is obtained (Δm_i):

$$\Delta m_i = m_{i,sample} - m_{i,mix} \qquad (6.3)$$

A positive Δm_i indicates the groundwater to be enriched for species *i* and a negative Δm_i indicates depletion. By evaluating Δm_i, geochemical reactions such as ion exchange can more easily be delineated. The value of Δm_i is not affected by the choice of seawater end-member as long as the ion/Cl^- ratio is constant for varying salinity, as indicated in Table 6.1. However, the choice of freshwater end-member can considerably affect the value of Δm_i, especially for freshwater samples with a composition close to that of the chosen freshwater end-member. Deviation in Δm_i of more than 5% was observed by using different freshwater samples as end-members. But the effect is small for the more saline samples.

This mixing approach is not applicable for species showing non-linear behaviour upon mixing such as H^+, CO_2, HCO_3^- nor for saturation states of minerals such as calcite etc. Mixing, involving species showing non-linear behaviour, will be treated in section 7.3.

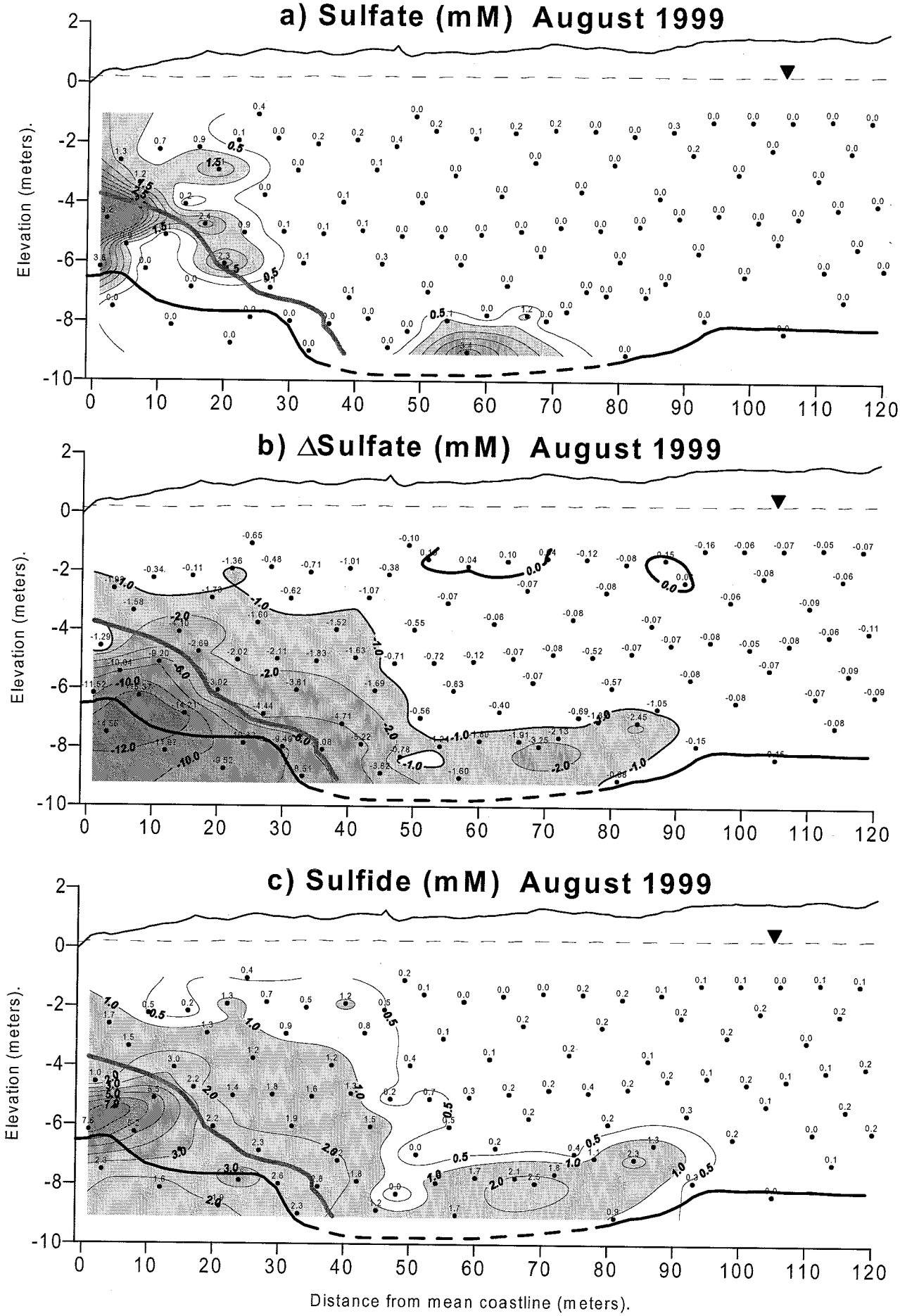

Figure 6.5: Sulfate concentration in the transect in mM a) measured concentrations b) Δmsulfate in mM and c) sulfide concentrations in mM.

6.2.3 Redox-conditions

Generally the aquifer is anoxic. The concentration of dissolved ferrous iron is very low in the range 0.2-1.6 μM in the saltwater part of the aquifer and 0.5-12.5 μM in the freshwater part. Likewise the concentration of dissolved manganese is very low (< 3 μM).

Organic matter content

The sedimentary (solid) organic carbon content of the sandy core samples is shown in Figure 6.4. In the sandy part of the aquifer the organic carbon content varies between 15 and 90 mmolC/kg. In samples from the peat layers the content was much higher ranging between 200 and $4.8 \cdot 10^3$ mmol C/kg.

Sulfate

The sulfate concentration is high (14 mM) in Isefjord seawater and low in the fresh groundwater (<0.02 mM). Therefore if sulfate behaved as a conservative parameter its distribution should resemble that of chloride. In the 25 m of the transect closest to the coastline and at an elevation of –4 to –5 m sulfate is only present in a concentration of about 2 mM, with a maximum of 9.2 mM near the coastline (Fig. 6.5a). At about 60 m from the coast and at an elevation of –8 to –9 m, sulfate is also found in a concentration of up to 3.4 mM. This sulfate is possibly transported upward from the underlying aquifer. Fig. 6.5b show the depletion of sulfate ($\Delta m_{sulfate}$) compared to the contribution of seawater sulfate. The general picture is that sulfate is strongly depleted and $\Delta m_{sulfate}$ is negative throughout the transect with values up to –14 mM (Fig. 6.5b). At the same time the concentration of sulfide (up to 7.8 mM) is high in a zone roughly coinciding with the zone of high sulfate depletion (Fig. 6.5c), the suggested process is therefore reduction by organic matter:

$$2CH_2O + SO_4^{2-} \rightarrow H_2S + 2HCO_3^- \qquad (6.4)$$

Organic matter is represented here as zero valent C simplified as the carbohydrate CH_2O.

Even though the concentration of sulfide is very high, it remains less than the amount of sulfate missing. In the mixing zone only about 30% to 80% of the dissolved sulfide expected from the sulfate depletion is found. The reason could be that some of the sulfide has been precipitated in the

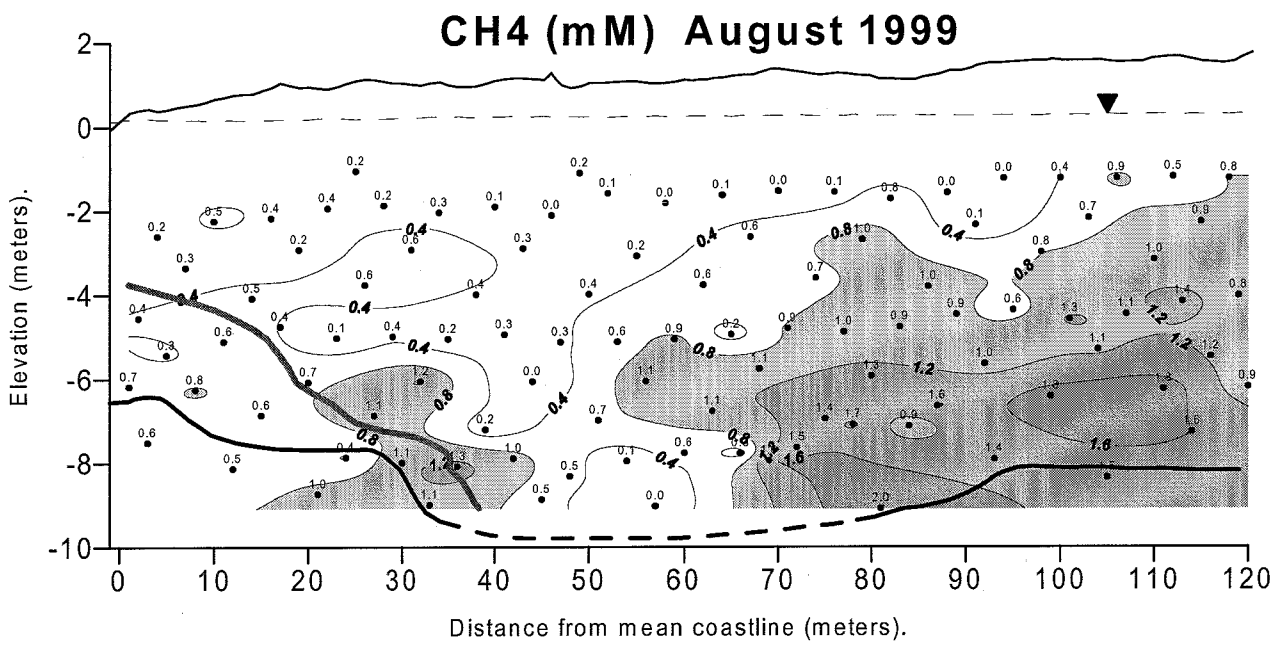

Figure 6.6: Methane concentrations (mM) in the transect.

sediment as pyrite and/or iron-mono-sulfides. This is supported by the very low Fe^{2+} concentrations. In the saltwater part of the peat layer less than 30 % of the expected dissolved sulfide is found almost certainly indicating some precipitation as iron-sulfides. Another explanation could be loss of the volatile hydrogen sulfide by degassing.

Methane

Methane is found in most of the transect in concentrations between 0.5 and 2 mM highest in the fresh part of the aquifer from 60 m landward (Fig. 6.6). The concentration is generally increasing over depth. In the more salty part of the transect methane is also found, in concentrations of 0.5 to 1.3 mM, but is low or even absent where sulfate is present. This is seen near the coast down to –4 m depth and at about –8 m to –9 m depth 60 meters from the coast, where sulfate containing water seems to be leaking up through the bottom of the aquifer. Methanogenesis is therefore the dominating redox-process in the aquifer except where sulfate is present. The overall or bulk pathway for methane formation can be written as a fermentation of organic matter:

$$2CH_2O \rightarrow CH_4 + CO_2 \qquad (6.5)$$

6.2.4 DOC, ammonium and phosphate

In reality organic matter in the aquifer has a more complex composition than shown in the equations (6.4) and (6.5). If the organic matter has a composition as in marine algae then a better representation of the organic matter stoichiometry is the Redfield ratio (Redfield et al., 1963):

$$(CH_2O)_{106}(NH_3)_{16}(H_3PO_4) \qquad (6.6)$$

Other compositions have been observed for sedimentary organic matter depending on its origin. Generally the C/N and C/P ratios are lower for organic matter of terrestrial origin (Stuyfzand, 1993). In any case, ammonium and phosphate are products of organic matter decomposition. Figure 6.7a shows the ammonium concentrations to range from 0 to 0.3 mM, above an elevation of –4 m. Below this depth the ammonium concentration increases towards the bottom to 2 mM. The highest concentrations of up to 3.5 mM are found above the bottom peat layer in the saltwater near the coast

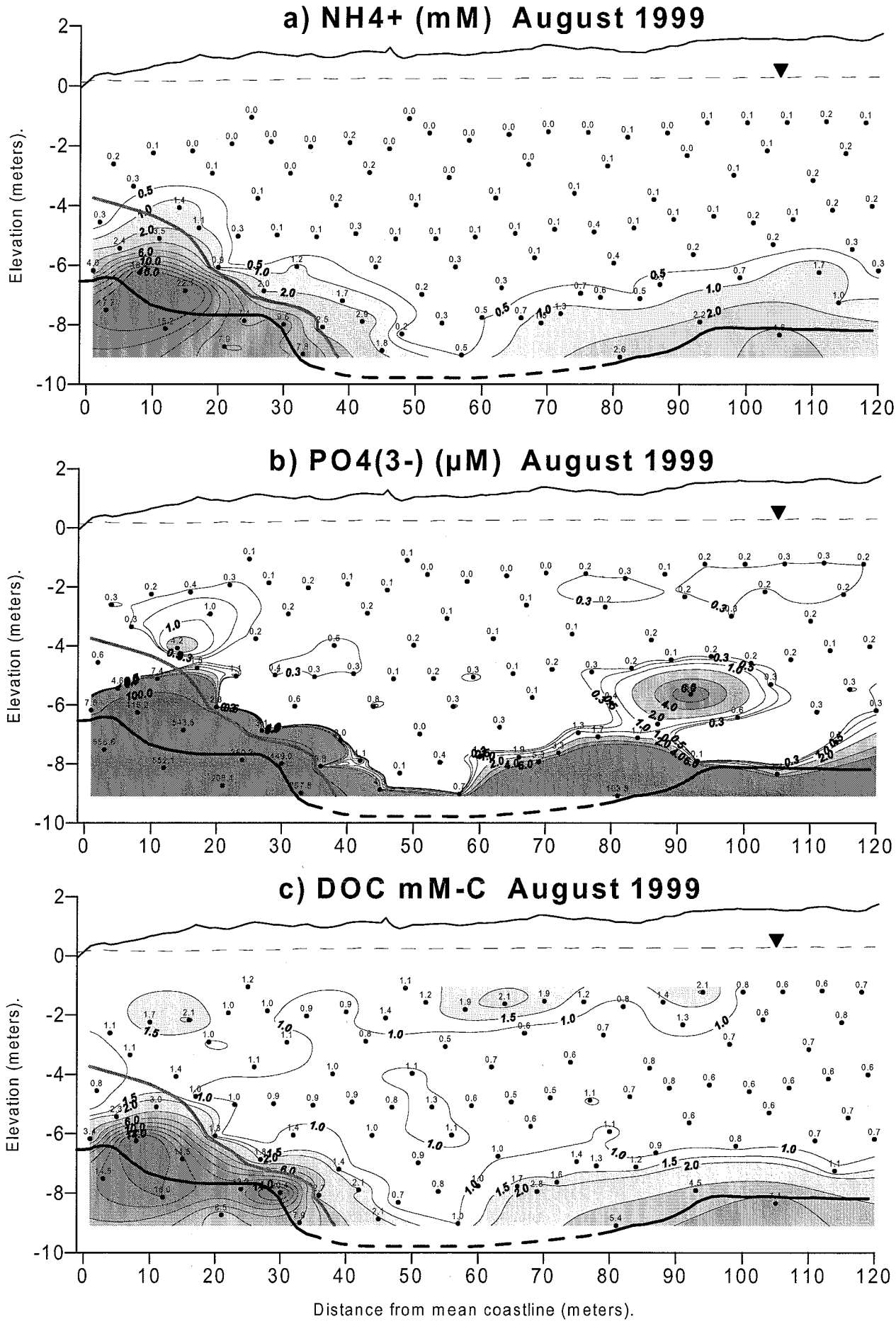

Figure 6.7: a) Ammonium concentrations (mM), b) Phosphate concentrations (µM) and c) DOC (mM-C) in the transect.

from 0 - 45 m. The phosphate concentration (Fig. 6.7b) is low in the aquifer, generally below 10 μM.

The DOC level (Dissolved Organic Carbon) in the fresher part of the aquifer is relatively low and varies from 0.5 to 1 mM (Fig. 6.7c). This zone of low DOC concentration extends from 30 m from the coast and landward and is confined to a depth interval from –2 m and down to –6 m. Above this zone towards the top of the aquifer an elevated DOC-level concentration is observed with concentrations from 1 to 2.1 mM indicating leaching of DOC from the root zone. Below the beach (from 0 to 15 m) where there is no root zone the DOC must originate from decaying seaweed. In the vicinity of the bottom peat the DOC concentration is higher, ranging between 1 and 3 mM (Fig. 6.7c). The Role of DOC is ambiguous, but DOC levels do seem to build up where organic matter decomposition occurs similar to what is seen by Jakobsen and Postma, (1999). This is further corroborated by the fact that DOC correlates quite well with the ammonium concentration.

Both the low concentration levels of ammonium, phosphate and DOC indicate a lower rate of organic matter degradation in the freshwater and the low salinity part of the mixing zone. The concentration of these products of organic matter degradation is higher in the saltwater part of the mixing zone and near the bottom peat layer close to the coast. Evidence of very extensive organic matter oxidation is found in the bottom peat close to the coast (0 to 33m). A high concentration of ammonium, phosphate and dissolved organic matter (DOC) are associated with this zone. In the peat, ammonium concentrations range from 7 to 22 mM (Fig. 6.7a). Phosphate is found in concentrations up to 560 μM in the peat, which is about 50 times higher than in the aquifer above (Fig. 6.7b). DOC in the peat ranges from 6.5 to 22 mM-C (Fig. 6.7c). Also alkalinity as high as 90 meq/l is measured in this zone (see Fig. 6.8b). However ammonium released by organic matter degradation will exchange with cations on the exchanger and phosphate may sorb to mineral phases or precipitate. Thus aqueous concentration levels of ammonium and phoshate are only a qualitative indicator of the ongoing organic matter mineralisation.

6.2.5 pH and alkalinity

The pH varies between 6.3 and 7.6 with the lowest values in the freshwater furthest away from the coast and near the water table (Fig. 6.8a). In the surface seawater pH is around 8.1-8.2 (table 6.1).

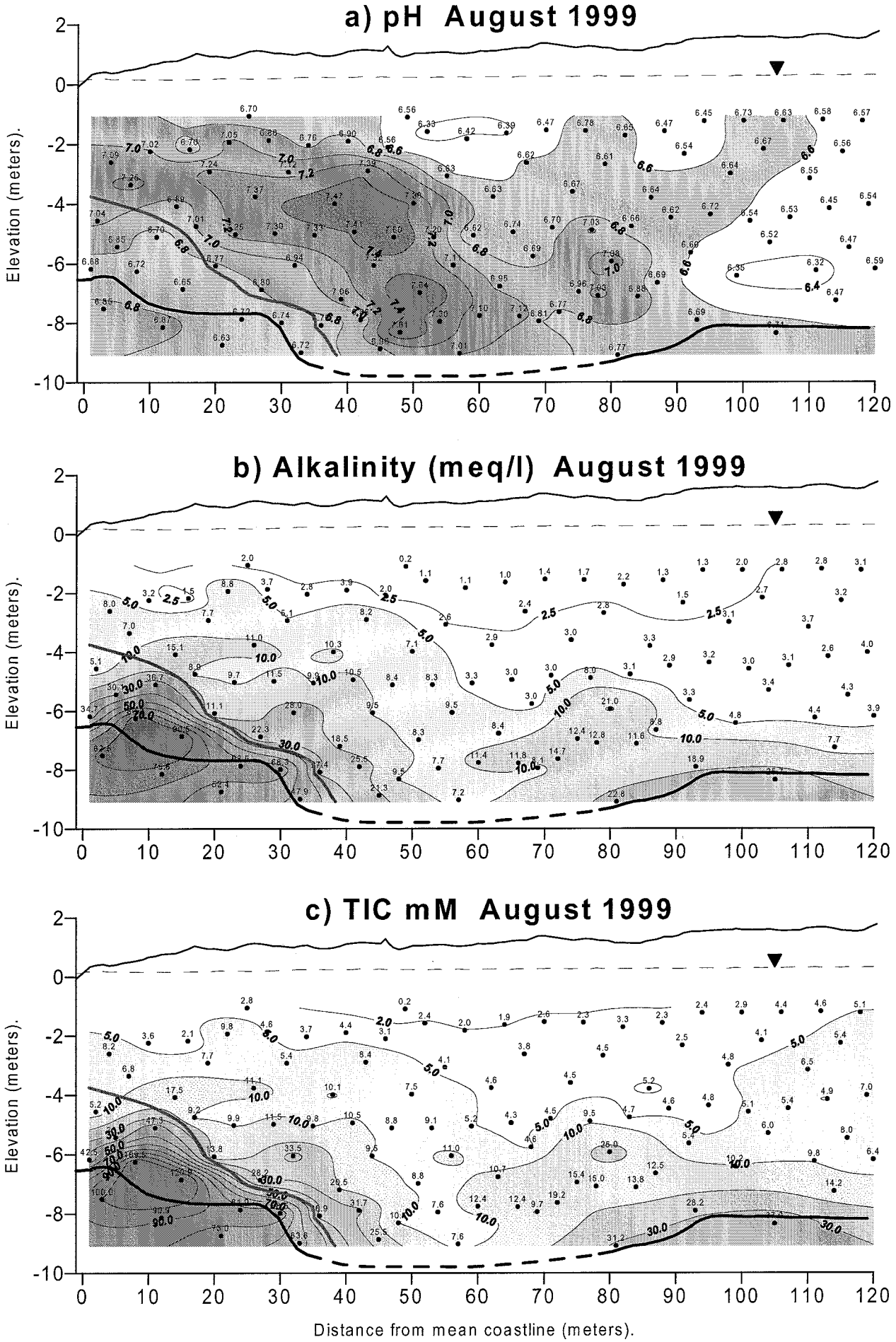

Figure 6.8: Measured a) pH, b) alkalinity (meq/l) and c) calculated dissolved TIC (Total inorganic Carbon) (mM) in the transect.

Relatively low values of 6.6 to 6.9 are associated with the salty part of the mixing zone (below –5 m) and the peat layer near the coast. A zone of higher pH values from 7 to 7.6 is located in a band going from the coast at –2 to –4 m's elevation running horizontally to around 40 to 50 m from the coast, where the zone bends down towards the bottom at –9 m. The zone coincides with the less salty part of the mixing zone ($f_{sea} < 0.5$). The processes involved in forming this zone will be addressed in section 7.4.

In the fresh part of the aquifer the alkalinity ranges from 1 meq/l in the upper part of the aquifer increasing to about 5 meq/l near the bottom (Fig. 6.8b). In the mixing zone, the alkalinity varies from about 3 to 36 meq/l, highest in the saltwater part of the mixing zone and towards the bottom of the aquifer (at –4 to –9 m depth from 0 to 40 m from the coast). In the surface seawater the alkalinity ranges between 2 and 3 meq/l (Table 6.1).

The zone of high alkalinity in the saltwater (up to 36meq/l) roughly corresponds to the zone of high sulfate depletion (Fig. 6.5b). Sulfate reduction reaction (6.4) is probably the main process responsible for the high alkalinity and explains most of the alkalinity increase.
In Figure 6.8c the dissolved total inorganic carbon (TIC) is calculated using PHREEQC on the basis of pH and the alkalinity. In the freshwater with low pH values around 6.5 the TIC is twice as high as the alkalinity. Also in the high alkalinity zone near the coast associated with the peat layer and the saltwater part of the mixing zone where the pH is around 6.7 the TIC is 20 to 30% higher than the alkalinity. In these zones of lower pH a substantial part of the TIC is therefore present as dissolved CO_2. As mentioned earlier, alkalinities are extremely high in the peat layer near the coast (50-90 meq/l), leading to TIC levels of up to 120 mM, again supporting extensive mineralisation of organic matter. This level of inorganic carbon is far to high too be explained by sulfate reduction alone and in addition a combination of methane formation and calcite dissolution will have to be included in order to explain this water chemistry (see section 7.2).

6.2.6 Dissolved gasses

The preceding sections reveal that degradation of organic matter leads to the production of different dissolved gasses primarily CH_4, CO_2, and H_2S as indicated by equations (6.4) and (6.5). If the production of dissolved gasses is substantial the bubble formation point in the groundwater system

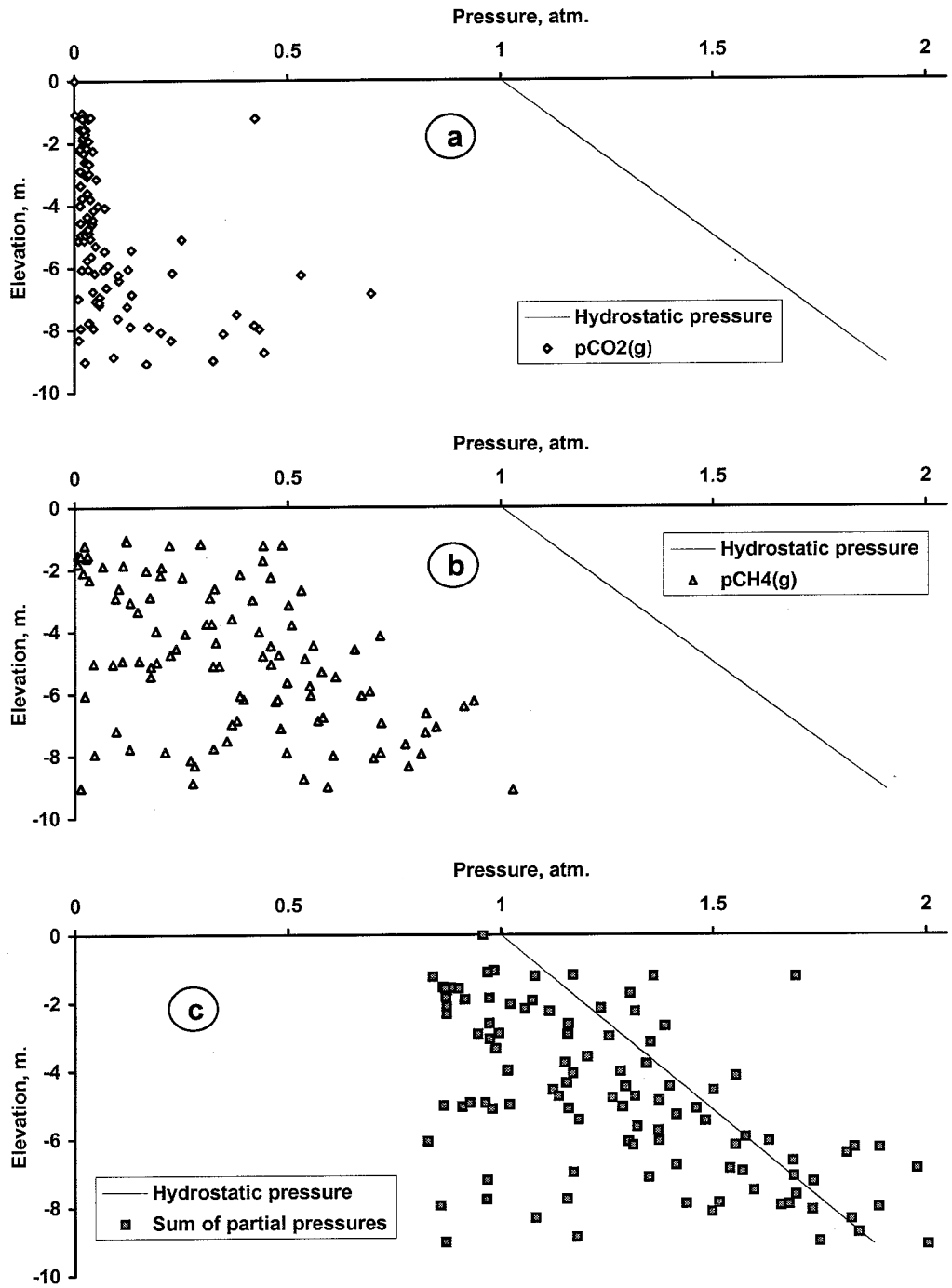

Figure 6.9: Calculated partial pressures (atm.) for the water compositions of August 1999 (using PHREEQC). a) CO_2, b) CH_4 and c) Sum of the partial pressures (CH_4 + CO_2 + N_2 + H_2S). Dissolved N_2 was not measured, but assumed to be in equilibrium with atmospheric N_2. The solid line indicates the hydrostatic pressure ($P = B + 9.87 \cdot 10^{-6} \cdot \rho \cdot g \cdot h$).

could be exceeded and a gas phase may start to form. This has been shown to take place in marine sediments (Martens and Berner, 1977 and Martens and Klump, 1980) and in aquifers. The formation of a gas phase will take place if the sum of partial pressures for dissolved gasses exceeds the pore water pressure. Using PHREEQC the partial pressures for (CH_4, CO_2, H_2S and N_2) were calculated for the August 1999 water samples in the transect. Dissolved N_2 was not measured, but assumed to be in equilibrium with the atmospheric N_2 (during infiltration). The pore water pressure is assumed equal to the hydrostatic pressure and effects on the pressure from the aquifer sediment matrix and flow of groundwater are assumed to be minor. So the hydrostatic pressure P (in atm) at a filter point is given as: $P = B + 9.87 \cdot 10^{-6} \cdot \rho \cdot g \cdot h$ where B is the barometric pressure (~ 1 atm), ρ is the density (kg/m^3), g is the gravitational acceleration (~ 9.82 m/s^2), h is the height of the water column (m). Figure 6.9a,b show the calculated partial pressures of CO_2 and CH_4 and Figure 6.9c shows the sum of the partial pressures (essentially: $CH_4 + CO_2 + N_2$). The contribution from H_2S is insignificant. Apart from the inert N_2 the largest contribution to the total pressure is CH_4 due to its low solubility. The hydrostatic pressure curve seems to, with a few exceptions, coincide with the upper limit for the sum of partial pressures observed in the transect. It is therefore probable that bubbles are forming or have been developing in the aquifer at some stage, especially for water compositions with high methane concentrations (and partly also high CO_2-partial pressures). This indicates that gas formation and migration may be a significant process in the aquifer as a consequence of organic matter degradation primarily by methanogenesis. The process also places an upper constraint on the concentration of dissolved gaseous reaction products.

6.2.7 Major cations

At first inspection, the major cations (Na^+, Mg^{2+}, Ca^{2+} and K^+) follow the distribution of chloride with high concentrations in the saltwater part of the aquifer, decreasing through the mixing zone to the freshwater zone (Fig. 6.10a) to d)). Typical concentrations for the four cations in the three zones are tabulated in Table 6.2. However, calcium (Fig. 6.10c) deviates somewhat from this general trend by displaying a more or less triangular shaped zone of low concentrations (0.2-1mM) extending from about 10 to 100 meters from the coast and from the surface down to –6 m at the deepest point. Further inland and deeper in the aquifer freshwater calcium concentrations are higher from 1 to 1.3 mM.

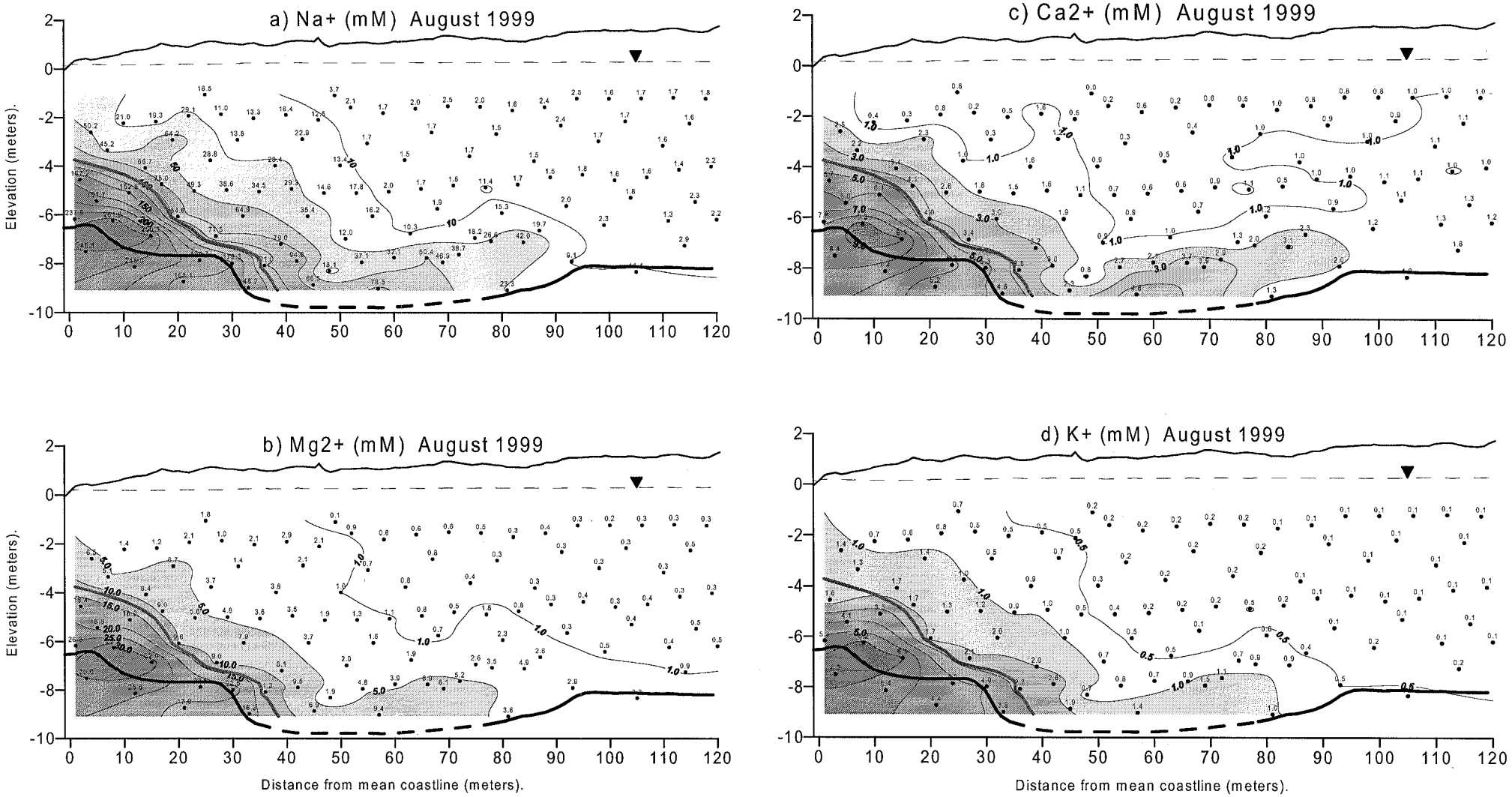

Figure 6.10: Concentrations in mM of a) Sodium b) Magnesium c) Calcium and d) Potassium. Measured in the transect August 1999.

Table 6.2: Typical concentrations for the four major cations Na^+, Mg^{2+}, Ca^{2+} and K^+ in the fresh aquifer water, the salty aquifer water and the mixing zone.

Water type	Na^+ (mM)	Mg^{2+} (mM)	Ca^{2+} (mM)	K^+ (mM)
Freshwater	1.5-2.5	0.2-0.5	0.2-1.3	0.1-0.3
Saltwater	215-262	26-33	7.4-9.3	5-6
Mixing zone	10-180	1-20	1.5-6	0.5-4

More detailed information on the processes affecting the distribution of cations in the transect can be extracted by calculating enrichment or depletion compared to the concentration predicted by conservative mixing of freshwater and seawater i.e. the Δm_i-concentration (Fig. 6.11). The Δm_i-values were calculated using the average surface seawater in Table 6.1 as the seawater end member and an average of four freshwater samples from an elevation of about –4 m (St101, St107, St113 and St119) as the freshwater end member.

In the upper 2 to 4 m of the aquifer Δm_{Ca} (Fig. 6.11c) is negative (–0.2 to –1.0 mM). In the central part of the transect (at 40 to 50 m from the coast) the zone of Ca^{2+} depletion extends all the way to the bottom of the aquifer. Below this zone Δm_{Ca} is positive, indicating enrichment of Ca^{2+} with Δm_{Ca}-values generally ranging from 0 to +2 mM. Towards the coast, Ca^{2+} enrichment is observed in a zone encompassing the saltwater part of the mixing zone and the bottom peat layer. In the lower part of the mixing zone the Δm_{Ca} ranges here between +1 and +2 mM. The highest Ca^{2+} enrichment is found within the peat layer where Δm_{Ca}-values reach 3 mM.

For Δm_{Mg} (Fig. 6.11b) the picture is somewhat more complex than for Δm_{Ca}. In the upper freshwater part of the aquifer the Mg^{2+} concentrations are generally low (see Fig. 6.10b) and the Δm_{Mg}-values are close to zero. Further down the Δm_{Mg} increases. At around 80 m and towards the coast the Δm_{Mg}-values are increasing to around 0.5 mM indicating enrichment of Mg^{2+}. This zone of Mg^{2+} enrichment, extending the full depth of the aquifer, continues until about 50 m from the coast. Here a narrow, vertical 10 m broad discontinuous zone of slight Mg^{2+} depletion appears with Δm_{Mg}-values down to –0.5 mM. Further towards the coast in the saltwater part of the mixing zone (from 5 to 40 m and below an elevation of –4 m) Mg^{2+} enrichment shows up again with Δm_{Mg}-values up to 1.3 mM. The enrichment of Mg^{2+} is highest in the peat layer near the coast (2 - 6.6

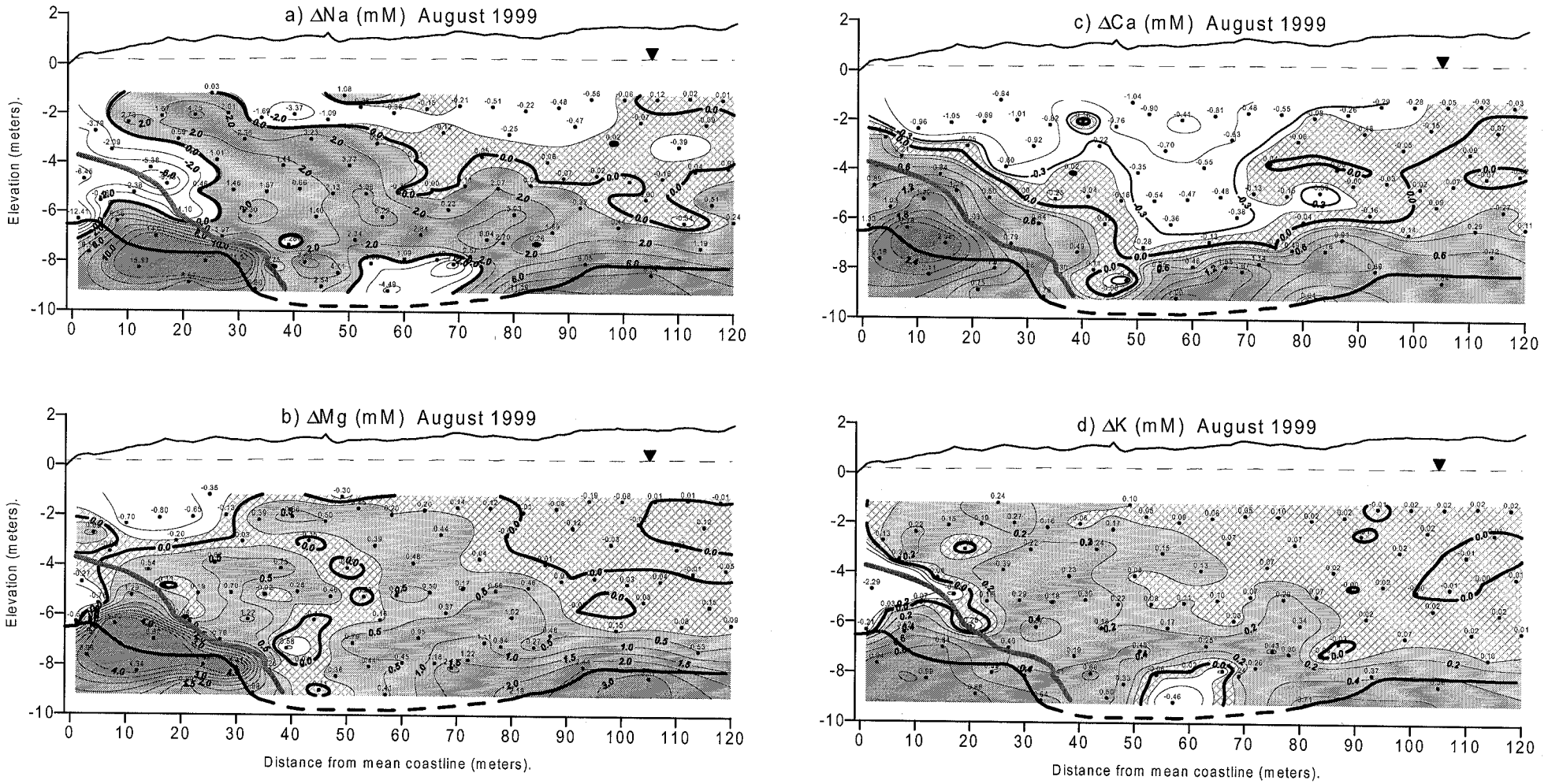

Figure 6.11: Δmi-concentrations in mM of a) Sodium b) Magnesium c) Calcium and d) Potassium in the transect. Crosshatched areas represents a Δmi of + 0.2 mM i.e. essentially little or no depletion or enrichment (for ΔmK the area is +0.1 mM).

mM). Mg^{2+} depletion with Δm_{Mg}-values as low as –0.8 mM is found near the coast reaching 0 to 5 m inland, from an elevation of –4 m down to –6 m and also in a shallow zone (above –3 m) extending 30 m landward.

The depletion/enrichment for Na^+ (Fig. 6.11a) broadly follows the patterns described above for Mg^{2+}, with some differences. A slight Na^+ depletion with Δm_{Na} = -0.5 mM is generally observed in the shallow part of the freshwater zone 60 to 110 m from the coast and down to –4 to –5 m. Below this zone, there is Na^+ enrichment, with Δm_{Na}-values ranging between 2 and 6 mM. This zone of Na enrichment extends towards the coast and the top of the aquifer, which is reached at 10 to 30 m from the coast. The Na^+ enriched zone is found closer to the coast than the Mg^{2+} enriched zone. In the deepest parts of the transect, associated with the bottom peat layer, a high enrichment of Na^+ is seen, as was the case for Mg^{2+}. The Na^+ enrichment in the peat layer is between 6 and 23 mM, highest near the coast. Na^+ depletion, with Δm_{Na}-values as low as –12 mM, is observed in a zone from the coast and 20 m into the aquifer at a depth interval from –2.5 to –6 m. Depletion is also found for a few deep samples (–7 to –9 m) in an isolated zone 50 to 70 m from the coast. This zone of depletion seems to emanate from the bottom aquitard.

For K^+ the aquifer is generally slightly enriched (Fig. 6.11d), with a pattern of enrichment/depletion resembling that of Na^+. The most distinct feature being a zone of relatively high K^+ enrichment (Δm_K = 0.5 mM) located in a diagonal band running from an elevation of –9 m 70 to 80 m from the coast to the top of the aquifer 10 to 40 m from the coast. Again, a high enrichment (Δm_K-values up to 1 mM) is found in the bottom peat layer. As for Na^+, a zone of K^+ depletion is observed from the coast and 20 m into the aquifer in a depth interval of –4 to –6 m narrowing into the aquifer. The deep isolated zone of depletion 50 to 70 m from the coast seen for Na^+ is also found for K^+.

Four general features can be extracted from the Δm_i-plots.1) In the central part of the transect there are adjacent diagonal bands of enrichment for the seawater derived cations Na^+, Mg^{2+} and K^+ coinciding with a zone of Ca^{2+} depletion. 2) From the coast and about 20 m inland there is a zone of depletion with seawater derived cations Na^+, Mg^{2+} and K^+ and enrichment of Ca^{2+}. 3) There is a small zone at the bottom of the aquifer between 50 an 70 m from the coast with depletion of Na^+ and K^+ and enrichment for Ca^{2+}. 4) A high enrichment of all four cations is found in the bottom peat layer. These patterns of depletion and enrichment for the major cations indicate the occurrence of

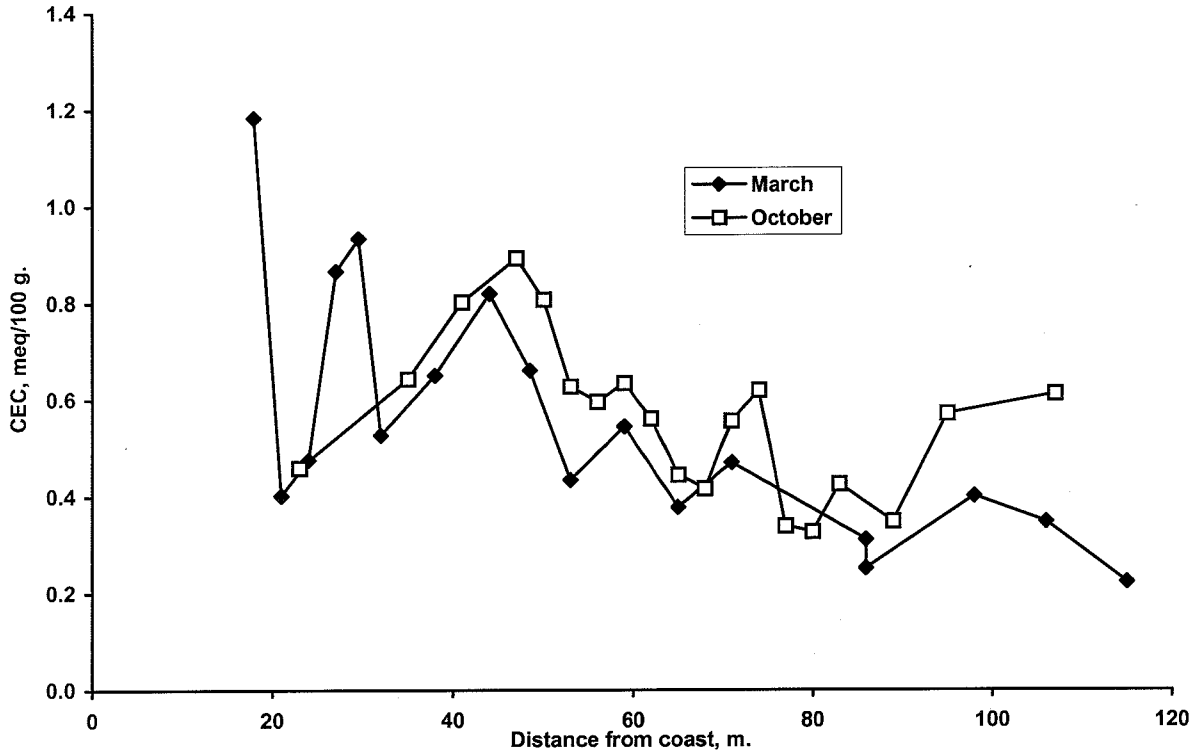

Figure 6.12: CEC (meq/100g sed.) from cores in profile 1 and 2 (Fig. 4.4a,b) as a function of distance from the coast.

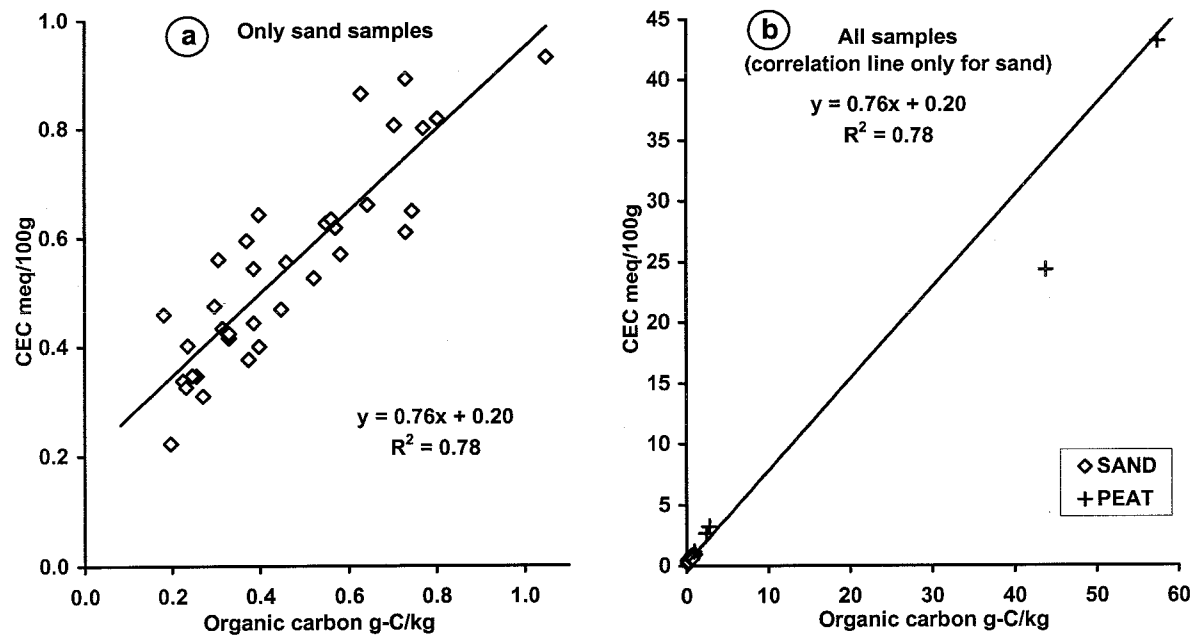

Figure 6.13: CEC (meq/100g sed.) vs. organic carbon content (g-C/kg) a) for sand samples and b) for all samples. The trend line is calculated for the sand samples alone.

cation exchange processes in the aquifer. In the central part of the transect where Ca^{2+} is depleted and enrichment of both Mg^{2+}, Na^{+} and K^{+} is observed the exchange processes could be as follows:

$$Ca^{2+} + Mg - X_2 \leftrightarrow Mg^{2+} + Ca - X_2 \qquad (6.7)$$

$$\tfrac{1}{2} Ca^{2+} + Na - X \leftrightarrow Na^{+} + \tfrac{1}{2} Ca - X_2 \qquad (6.8)$$

Where (6.8) conforms to the Gaines-Thomas convention (Gaines and Thomas, 1953). The partial separation into a Mg^{2+} enriched zone and a Na^{+} enriched zone may indicate that Ca^{2+} displaces Mg^{2+}, which in turn displaces Na^{+} (and K^{+}). In the zone near the coast with depletion of the seawater derived cations and enrichment of Ca^{2+} the exchange processes seem reversed with Mg^{2+}, Na^{+} and K^{+} displacing Ca^{2+} from the exchanger. The simultaneous enrichment of all four cations in the peat layer will be addressed in section 7.2.

6.2.8 CEC (Cation Exchange Capacity)

The sandy aquifer shows a CEC fluctuating between 0.3 and 1 meq/100g with an average value of about 0.5 meq/ 100g, as seen in Figure 6.12. The three samples (not shown) near the coast in the profile from March (Fig. 4.4a) and the first sample (not shown) in the profile from October (Fig. 4.4b) contain peat and have a high CEC ranging from 2.5 to as high as 43 meq/100g.

There is a good correlation between CEC and the content of organic carbon in the sand samples as seen in Figure 6.13a. The correlation indicates that the content of organic matter in the Skansehage aquifer is the primary cation exchanger. Furthermore the linear extension of the correlation between CEC and organic carbon content in the sand samples extends rather close to where the peat samples plot (Fig. 6.13b). There is some scatter indicating that not all the organic matter (such as large plant debris) necessarily contributes significantly to the CEC. The correlation of 7.6 meq/g-C (Fig. 6.13a) is twice as high as the value of 3 meq/g-C (at pH 7) given by Scheffer and Schachtschabel, (1970), as cited in Appelo and Postma (1993). A correlation between the size of the CEC and pH, as expected for an organic exchanger, was not found. This is probably due to the small pH variations observed. Scheffer and Schachtschabel, (1970) gives the following relation: CEC (meq/100g-C) = 51·pH –59. According to this the maximum pH variations of the transect should only give a

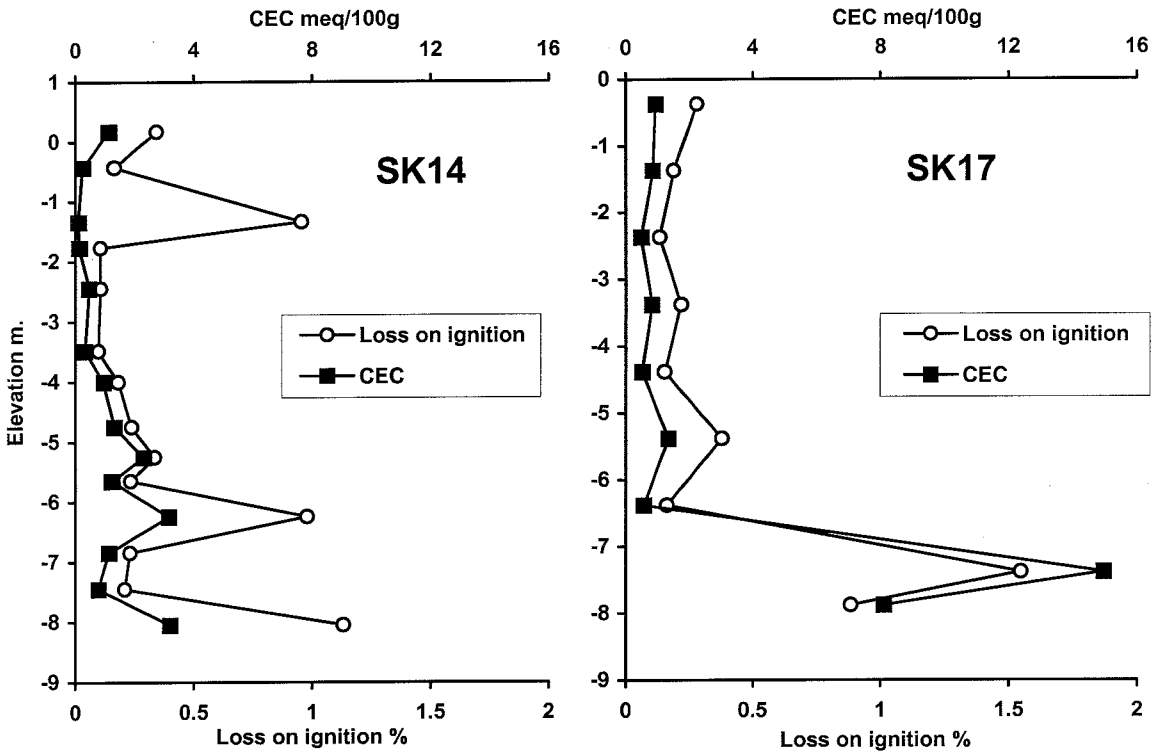

Figure 6.14: CEC (in meq/100g sed.) and loss on ignition (%) for the two vertical core profiles: SK14 and SK17. Positions of borings can be seen in Fig. 4.1b and Fig. 4.4a.

maximum CEC variation of less than 0.66 meq/g-C (= 0.03 meq/100g sed. for the field site given an organic matter content of 0.046 g-C/ 100g sed.).

The CEC in the samples taken in March and October (Fig. 6.12) are internally consistent although not exactly the same depths were sampled. Over depth the CEC tends to increase as seen in the two vertical sediment cores SK14 and SK17 (Fig. 6.14). The CEC in the two profiles are seen to correlate with the loss on ignition (Fig. 6.14), which in turn has been found to correlate with the organic carbon content (not shown). It is therefore very probable that the content of organic matter increases with depth and thus it is likely that the CEC is also increasing with depth (at least at SK14).

6.2.9 Exchangeable cations

The amounts of exchangeable cations (Ca^{2+}, Mg^{2+}, Na^{+}, K^{+} and NH_4^{+}) were measured on the sediment core samples taken in March 2000 and October 2000 (profile 1 and 2 Fig. 4.4) representing a variation in water composition from freshwater to seawater, covering the salinity range measured in the transect. Holding these data against the measured aqueous concentrations selectivity coefficients for the different cations may be calculated or alternatively the data may be used to validate the coefficients used in the PHREEQC database. The time of sampling is of minor importance in this context.

Figure 6.15a show, as symbols, the equivalent fractions for Ca^{2+}, Mg^{2+}, Na^{+}, K^{+} and NH_4^{+} determined on core sections from profile 1 sampled in March (Fig. 4.4a). The three samples closest to the coast are from the bottom peat layer with high CEC values. Calcium dominate the exchanger in the freshwater farthest from the coast with β_{Ca} around 0.66, decreasing towards the coast where $\beta_{Ca} = 0.15$. The opposite trend is observed for sodium with $\beta_{Na} = 0.4$ near the coast, decreasing to 0.1 farthest from the coast. β_{Mg} also decreases away from the coast from 0.4 to 0.12 inland. However, β_{Mg} remains high (0.3) up to 70 m from the coast. β_K is near constant around 0.1 in most of the transect except in the peat samples where it is as low as 0.025. Ammonium is near constant and generally below 0.05. Between 50 and 90 m from the coast the picture is slightly disturbed due to the effect of the density plumes (see Section 6.3).

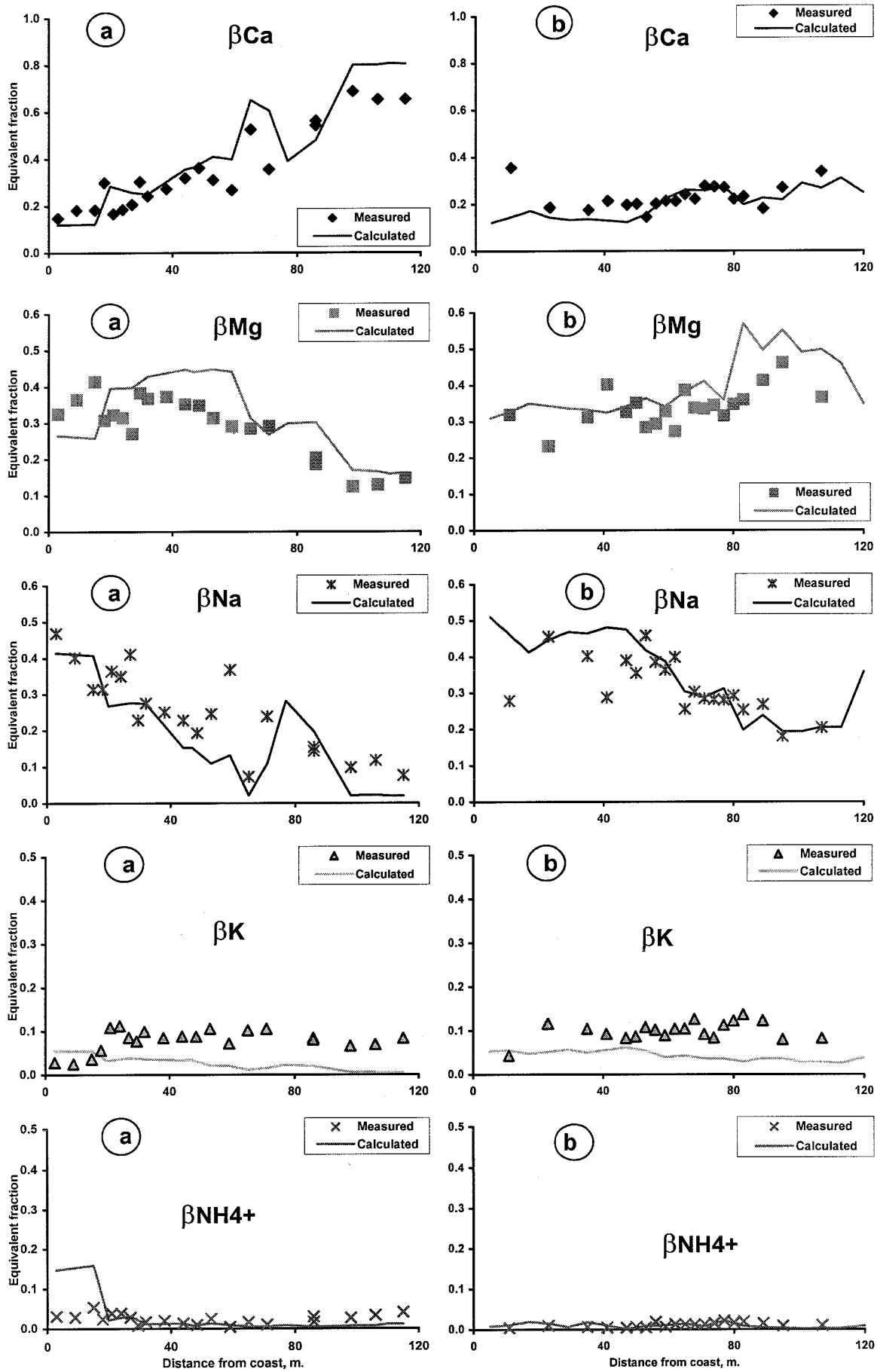

Figure 6.15: Equivalent fractions of Ca^{2+}, Mg^{2+}, Na^{+}, K^{+} and NH_4^{+} on the exchanger measured on core samples (symbols) and calculated using PHREEQC from the groundwater composition in a nearby filter (solid lines). a) March 2000 (profile 1 Fig. 4.4a), b) October 2000 (profile 2 Fig. 4.4b).

The equivalent fractions calculated with PHREEQC to be in equilibrium with the aqueous concentrations are shown as solid lines in Figure 6.15a. They are based on the water compositions from March 2000 and the standard selectivity coefficients in the PHREEQC database. The location of the core samples used for analysing the exchanger may differ from the water sampling filters, used for calculation of the exchanger composition, vertically by up to 1 m and there is up to 3 weeks difference in time between the coring and the water sampling. Both the spatial and the temporal shift may cause variability and the difference is particularly important because the density plumes resulting from the inundation were still migrating down during the coring (see section 6.3). Still there is a good agreement between the measured composition of the exchange complex and the composition calculated from the water chemistry. In the freshwater end the selectivity coefficients for Ca^{2+} and Na^{+} tends to overestimate β_{Ca} and underestimate β_{Na} while towards the coast in the seawater influenced end the selectivity coefficients underestimate the β_{Na} and overestimates the β_{Mg}. In the three peat samples near the coast the β_{Mg} is underestimated. For potassium the agreement is quite poor with the observed β_K on the sediment more than twice the predicted β_K. An exception is again the peat samples near the coast where the disagreement is reversed with a higher predicted than measured β_K. Also the observed β_{NH4} on the sediment is generally a bit higher than the predicted. Again a disagreement is observed for ammonium in the peat layer with 3 times higher predicted β_{NH4} than what is in fact observed. The reason for the observed discrepancies for β_{NH4} and β_K is presently not known.

The equivalent fractions for Ca^{2+}, Mg^{2+}, Na^{+}, K^{+} and NH_4^{+} determined on core sections from October 2000 are shown in Figure 6.15b as symbols. The sample closest to the coast is from the bottom peat layer with a CEC value of 2.7 meq/100g. Variations in the equivalent fractions along the transect are not as prominent as in the March data before the beginning of the intrusion experiment (Fig 6.15a). This is because of the higher seawater content in the transect in October, with Na^{+} and Mg^{2+} being the dominating cations. β_{Ca} is only increasing slightly from 0.2 near the coast to 0.3 farthest from the coast. Like wise for β_{Mg}, which increases from 0.3 to 0.45 and possibly peaking around 90-100 m from the coast. β_{Na} decreases away from the coast from 0.45 to 0.2. The equivalent fractions of potassium are fairly constant around 0.1 in most of the transect except for the peat sample where the β_K becomes lower than 0.05. β_{NH4} is fairly constant and very low, generally below 0.02.

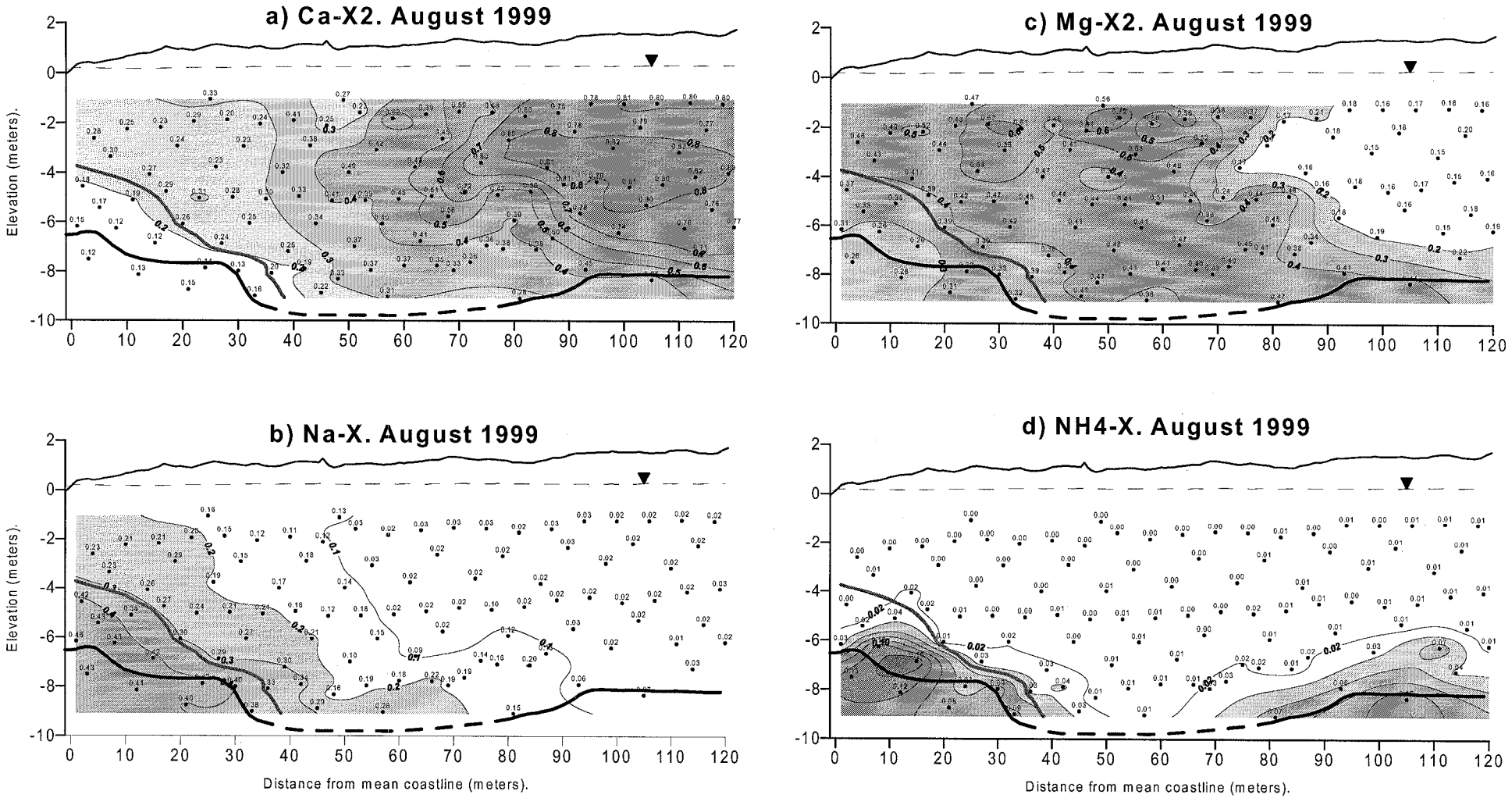

Figure 6.16: Equivalent fractions of a) Ca2+ b) Mg2+ c) Na+ and d) NH4+ on the exchanger August 1999 calculated from the groundwater composition using PHREEQC and the standard selectivity's in the PHREEQC database.

Again equivalent fractions calculated with PHREEQC from aqueous concentrations (sampled October 2000) are shown as solid lines in Fig. 6.15b. The agreement between equivalent fractions calculated with PHREEQC and the measured fractions on the sediment are quite good. There is some scatter in the observed β_{Na} from the coast to 50 m. As for the March 2000 data the observed β_{Mg} is a little bit lower than predicted by PHREEQC. For β_K the agreement is quite poor with the observed β_K of 0.1 on the sediment being twice as high as the predicted β_K of 0.05, but this has little effect on the other β_i's. The peat sample near the coast stands out with a higher observed β_{Ca} than predicted, and a lower observed β_{Na} and β_K.

Generally for both March and October, however, the deviations between the observed and the measured exchanger composition are small and therefore the standard PHREEQC database selectivity coefficients are found suitable for modelling of the Skansehage field data. However, a higher selectivity for K^+ by introducing a lower selectivity coefficient ($K_{Na/K}$) could profitably have been chosen for K^+. But as K^+ is a minor component in terms of ion exchange it was chosen not to use data to fit a better value.

6.2.10 Calculated cation composition of the cation exchanger in the transect August 1999

Based on the above validation of the selectivity coefficients in the standard PHREEQC database it seems reasonable to use PHREEQC to calculate the cation composition of the exchange complex from the aqueous concentrations of August 1999 for all sampling points in the transect. The water chemistry data from August 1999 leads to the following distribution on the exchanger (Fig. 6.16). Ca^{2+} occupies 70 to 80% of the exchanger sites in the fresh part of the aquifer, from 70 to 120 m to a depth of –7 m (Fig. 6.16c). Towards the coast the Ca^{2+} equivalent fraction decreases to 0.12 in the saltwater zone. The opposite trend is observed for Na^+ with the highest equivalent fractions of 0.46 in the saltwater zone and near the bottom (Fig. 6.16a). In the fresh water zone the Na^+ fraction is as low as 0.02. Mg^{2+} is dominating in a zone in between the Na^+ and Ca^{2+} zones with average fractions of 0.45 –0.50 (Fig. 6.16b). The highest fraction of Mg^{2+}, up to 0.7, is calculated for the fresher and shallower parts of the mixing zone. The pattern of potassium distribution on the exchanger roughly follows that of sodium, though the highest fractions are less than 0.06 (data not shown). In the sandy part of the transect the ammonium equivalent fraction is very low, but quite considerable

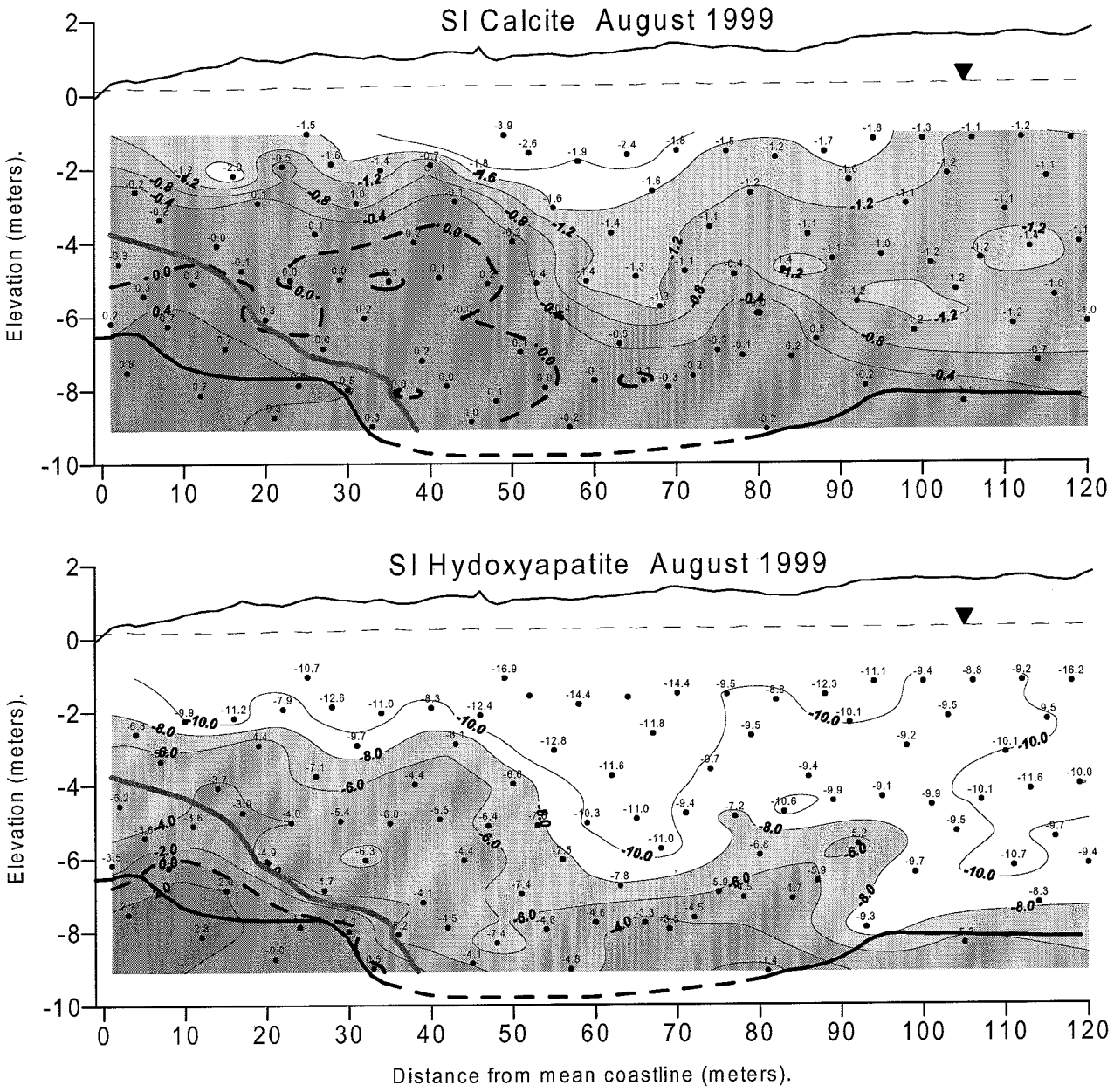

Figure 6.17: Saturation state (SI) calculated using PHREEQC for a) calcite and b) hydroxyapatite.

equivalent fractions of ammonium, up to 0.15, are calculated for the low permeable peat layers and to a lesser extent near these layers (0.04) (Fig. 6.16d).

In summary the relative distribution of cations on the exchanger support the ongoing ion exchange processes proposed in section 6.2.7, especially in the central part of the transect where the high equivalent fraction of Mg^{2+} must be undergoing displacement by Ca^{2+} as the Ca-HCO_3 water flows towards the coast.

6.2.11 Saturation states for solid phases

Using PHREEQC the saturation index (SI = log(IAP/K)), where IAP is the ion activity product) was calculated for a number of minerals. For calcite ($CaCO_3$) (Fig. 6.17a) the saturation index increases with depth and towards the mixing zone. In the freshwater, 100 m and landwards from the coast, the subsaturation is relatively constant around –1.2 from –1 m and all the way down to an elevation of –6/-7 m. Between this zone and the mixing zone (50 to 100 m) and reaching down to –6 m there is a zone where the SI is particularly low (<-1.2 with a minimum of –3.9). This same area was recognised in the distribution of Ca^{2+}, Δm_{Ca} and the alkalinity (Figures 6.10c, 6.11c and 6.8b). Apparently little or no calcite is available for dissolution in this particular area. A mechanism that may explain the depletion of calcite will be given later (section 7.4). Saturation is attained in the lower part of the mixing zone from an elevation of –4 to –9 m 30 to 50 m from the coast. A slight supersaturation of SI = 0.25 is observed in the lower salty part of the mixing zone (–5 to –6 m), near the coast (0 to 15 m). A supersaturation of up to SI = 0.8 was calculated for samples from within the peat layer near the coast.

The SI for aragonite gives the same picture as calcite, with SI-values 0.16 lower than for calcite corresponding to the difference in the K-values. The SI for dolomite mimics that of calcite, but with a higher maximum supersaturation. The field of supersaturation for dolomite is slightly larger than that for calcite. The aquifer is generally subsaturated for hydroxyapatite ($Ca_5(PO_4)_3(OH)$) (Fig. 6.17b), but all samples within the peat layer near the coast are supersaturated (up to 2.8), due to the enhanced phosphate concentration (Fig. 6.7b).

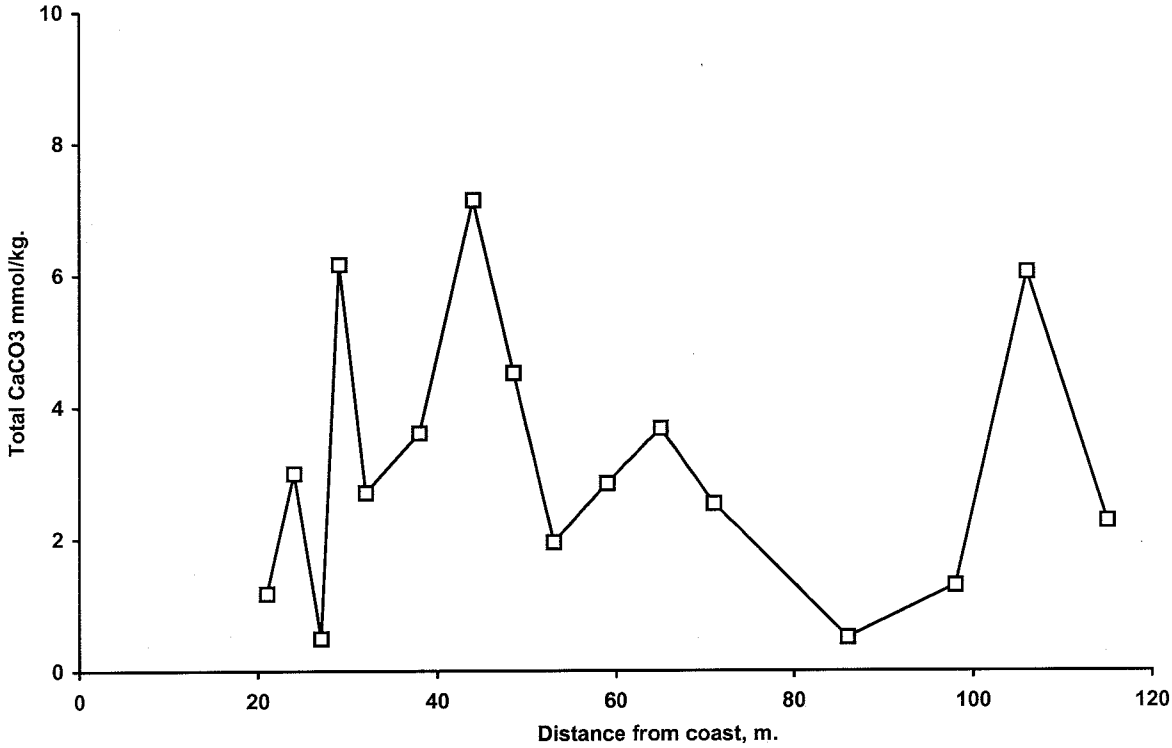

Figure 6.18: Sedimentary inorganic carbon content in mmol IC/kg for sand samples. Samples are from the profile line 1 Figure 4.4.

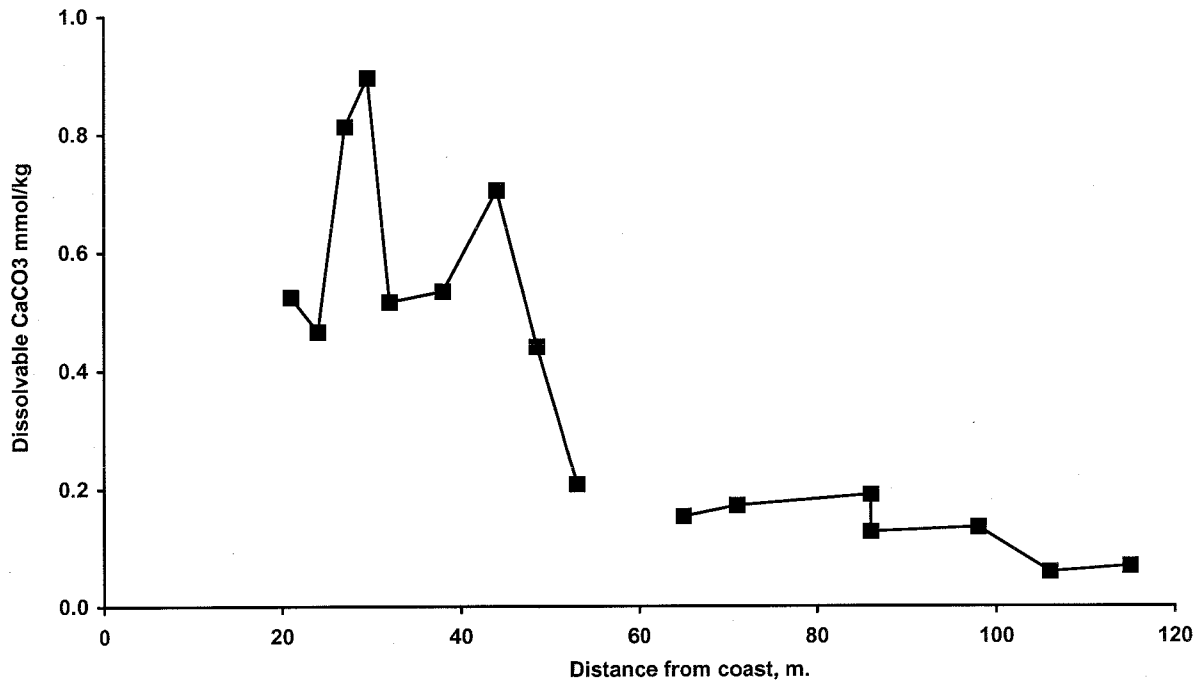

Figure 6.19: Amount of inorganic carbon dissolved (mmol IC/kg) by treated with a 1 M NH_4Cl-solution (sand samples only). Samples are from the March sediment profile (profile 1, Fig. 4.4a).

Generally the transect was found to be subsaturated for the minerals gypsum ($CaSO_4 \cdot 2H_2O$), siderite ($FeCO_3$), rhodochrosite ($MnCO_3$) and vivianite ($Fe_3(PO_4)_2$). Supersaturation was found for pyrite (FeS_2) in the whole of the transect. Amorphous FeS is generally subsaturated except for a few patches in the most landward part of the transect. For mackinawite (FeS), supersaturation was observed from 50 to 60 m from the coast and landward. For pyrite, FeS, etc. the saturation index was calculated using the aqueous redox-couple sulfate/sulfide to define the redox-potential.

6.2.12 Calcite dissolution/precipitation

Sedimentary carbonate

The total sedimentary inorganic carbon (SIC) content determined by the indirect method (section 4.2.2) on 20 core samples in the March profile (profile 1, Fig. 4.4) is shown in Figure 6.18. The content varies between 0.5 and 7 mmol IC/kg for the sandy sediments with an average of 3 mmol IC/kg. In the peat layers (values not shown) the carbonate content is high, 12 - 280 mmol IC/kg, and here shell fragments have been identified as well. A sand sample from the current shoreline yielded 125 mmol IC/kg, which is between 20 and 250 times more than in the sandy aquifer samples. Figure 6.18 shows that a small amount of solid carbonate is still present in the transect, at least along the sampling line in Figure 4.4. However, the low calcite saturation index (Fig. 6.17) of the uppermost part (2 m) of the transect suggest that this part is virtually free of calcite.

In the procedure for the determination of CEC some carbonate is dissolved during the NH_4Cl-treatment (section 4.2.2). This readily dissolvable carbonate has a concentration of 0.6 mmol IC/kg near the coast, decreasing inland to less than 0.1 mmol IC/kg (Fig. 6.19). Comparison with Fig. 6.18 shows that the total sedimentary inorganic carbon content is an order of magnitude higher than the content of readily dissolvable inorganic carbon. The peat samples (3 first samples) near the coast clearly contain a high amount of readily dissolvable inorganic carbon, since between 2.5 and 26 mmol IC/kg were found (values not shown). In a zone from 20 to 50 m from the coast an intermediate amount of 0.4 to 0.9 mmol IC/kg were present (Fig. 6.19). This zone coincides with the part of the mixing zone with saturation to slight supersaturation for calcite as seen in Figure 6.17. Further landwards about 0.06 mmol IC/kg was found, confirming that very little readily dissolvable inorganic carbon is present in this zone.

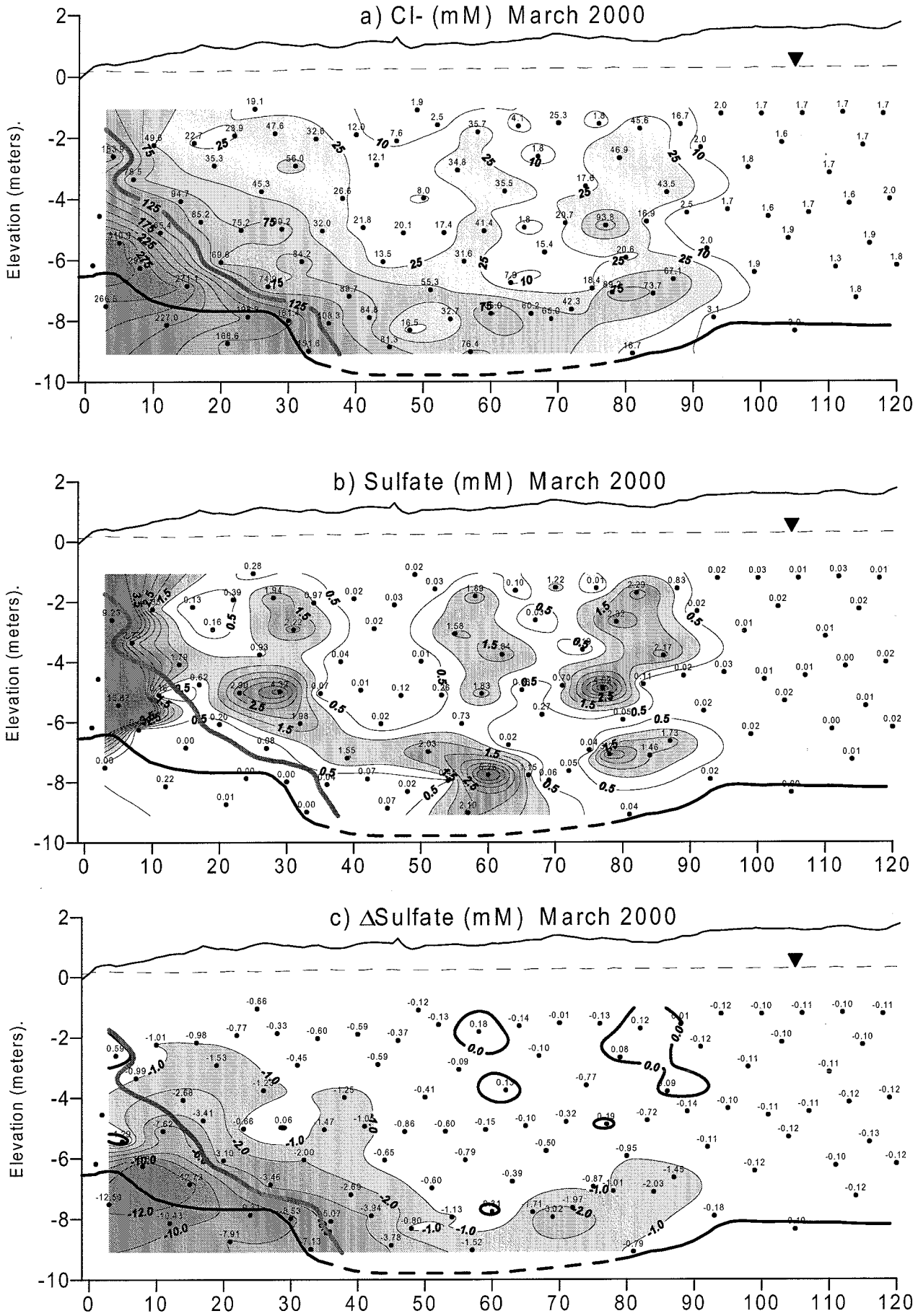

Figure 6.20: a) Chloride concentrations in the transect in mM b) Sulfate concentrations in mM. c) Δmsulfate in mM. Measured in the transect 49 days after the inundation event.

Dissolution or precipitation of calcite, in contact with carbonic acid, can be written as:

$$H_2O + CO_2 + CaCO_3 \leftrightarrow Ca^{2+} + 2HCO_3^- \quad (6.9)$$

A rough calculation shows that calcite dissolution could explain the concentration of Ca^{2+} (Fig. 6.10c) and ~2/3 of the alkalinity (Fig. 6.8b) in the fresh part of the aquifer upstream from St80. In the remaining part of the transect the actual dissolution or precipitation of calcite is more difficult to assess and appears to be intimately linked to redox-processes and ion exchange reactions.

6.3 Groundwater chemistry: The seawater inundation event

As described in section 5.3 the field site was inundated by seawater during a storm. Water samples collected in the transect in March 2000 about 50 days after the inundation event shows three seawater plumes migrating down into the aquifer. In the chloride data Fig. 6.20a, they appear as irregular vertical plumes 10 to 20 meters wide with elevated chloride concentrations up to about 100 mM corresponding to a content of about 1/3 seawater. The plumes stretch from an elevation above –1 m down to about –8 m. In the upper segment (–1 to –4 m) chloride concentrations have dropped to about 30- 50 mM. The plume located 30 m from the coast has merged with the sea-/freshwater interface and is therefore partly obscured by this. Because of the short time since the inundation and because of the relatively slow rate of sulfate reduction, sulfate can qualitatively be used to trace new surface seawater in zones with a high chloride content prior to the inundation. The sulfate distribution (Fig. 6.20b) correlates nicely with the chloride distribution and the seawater plume at 30 m from the coast does show more clearly by looking at the sulfate. Sulfate concentrations in the plumes are around 2 mM with a maximum of 4.6 mM. By comparing the sulfate distribution of Fig. 6.20b to the sulfate distribution prior to the inundation (Fig. 6.5a) it becomes clear how the plume waters from the plumes at 30 and 60 m have spread out at depth through permeable layers. This is not obvious by just comparing the Cl^- content before and after the inundation, because increasing Cl^- concentrations not necessarily imply that freshly percolated seawater has reached these areas. An example of this can be seen at 80 m from the coast at an elevation of –6 to –8 m where sulfate concentrations are about 2 mM.

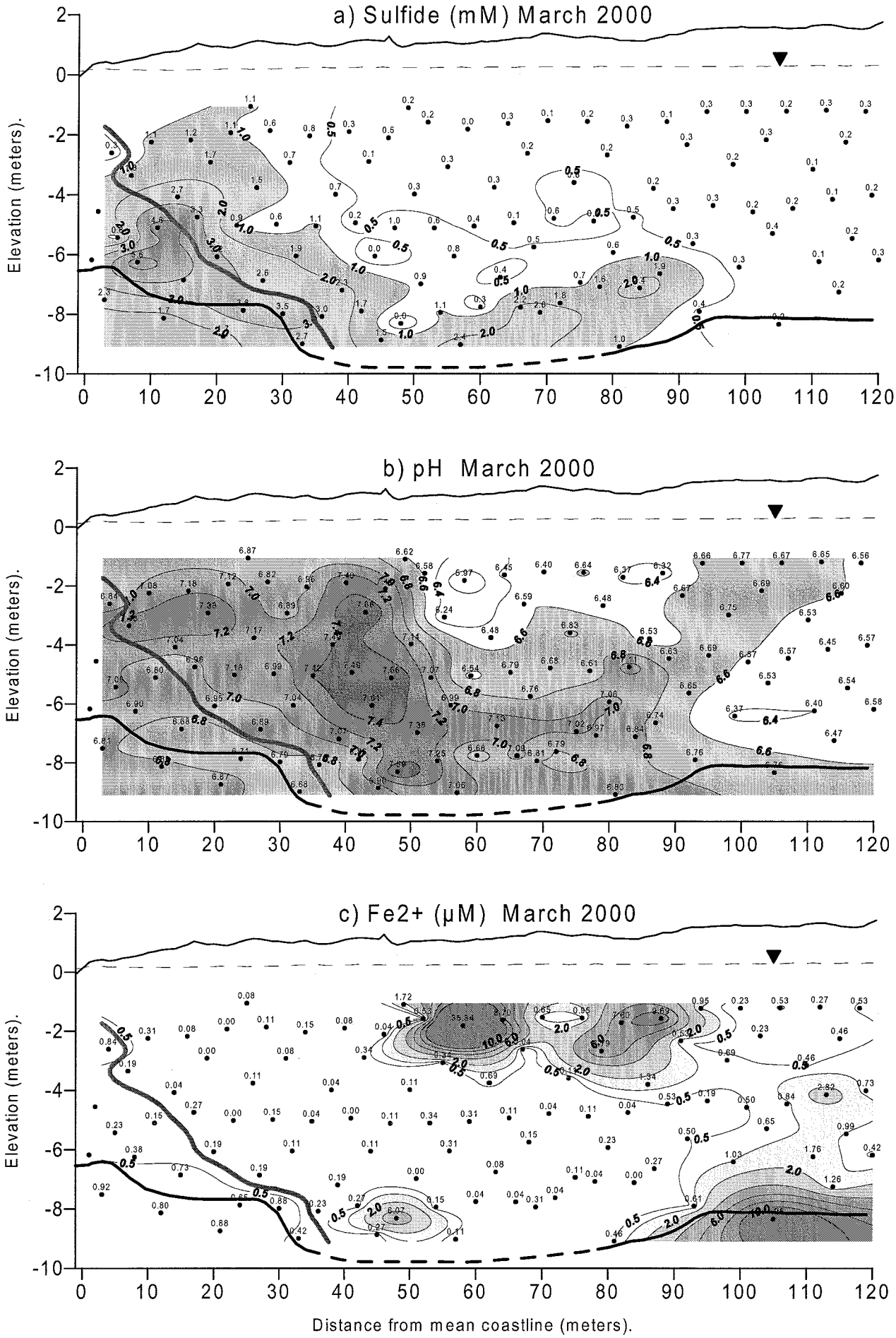

Figure 6.21: a) Sulfide concentrations in mM b) pH c) Fe2+ in µM. Measured in the transect 49 days after the inundation event.

In the following only the parameters that have changed considerably compared to the August data will be presented.

6.3.1 Redox-conditions

The seawater plumes have introduced a fresh load of electron acceptors into the aquifer, most noticeable sulfate, as seen in Figure 6.20b.

No oxygen was measured in the aquifer at the time of sampling. But the inundation seawater must have contained some oxygen when entering the aquifer. The oxygen introduced must therefore have been consumed in the aquifer. The nitrate concentration of the seawater at the time of inundation was insignificant, less than 3.5 µM (data from the County of Western Zealand). Oxygen was probably partly removed by partial re-oxidation of pyrite (or iron mono-sulfides) in the upper parts of the plumes. Partial oxidation of pyrite proceeds according to:

$$FeS_2 + 7/2\,O_2 + H_2O \rightarrow Fe^{2+} + 2SO_4^{2-} + 2H^+ \qquad (6.10)$$

According to this equation (6.10) there should be an increase in concentrations of Fe^{2+} and sulfate and a decrease in pH, as seen in the plots of $\Delta m_{sulfate}$ (Fig. 6.20c), pH (Fig. 6.21b), and Fe^{2+} (Fig. 6.21c) from March. Positive, but small, $\Delta m_{sulfate}$ values of +0.1 to +0.2 mM indicating enrichment of sulfate can be seen near the surface (–1 to –3 m) for the plumes located at 60 and 80 m from the coast. $\Delta m_{sulfate}$ is negative (> -0.1 mM) in the remaining freshwater area. A low pH of 6 to 6.3 is found near the surface in the same zones (Fig 6.21b). Also the Fe^{2+} concentration has increased in these zones from close to zero to a maximum of 35 µM (Fig. 6.21c)

Sulfate reduction

$\Delta m_{sulfate}$ in the lower parts of the plumes are negative, probably reflecting the mixing of plume water with the surrounding sulfate depleted aquifer water (Fig. 6.20c). Overall $\Delta m_{sulfate}$ has not changed significantly compared to the August data, indicating that only small amounts of the freshly introduced sulfate have had time to be reduced. Given a rate of sulfate reduction of 1 mM SO_4^{2-}/y as determined by radiotracer methods (Nyvang, unpublished data), only about 0.13 mM SO_4^{2-} should have been reduced during the 49 days since the inundation. This is supported by the

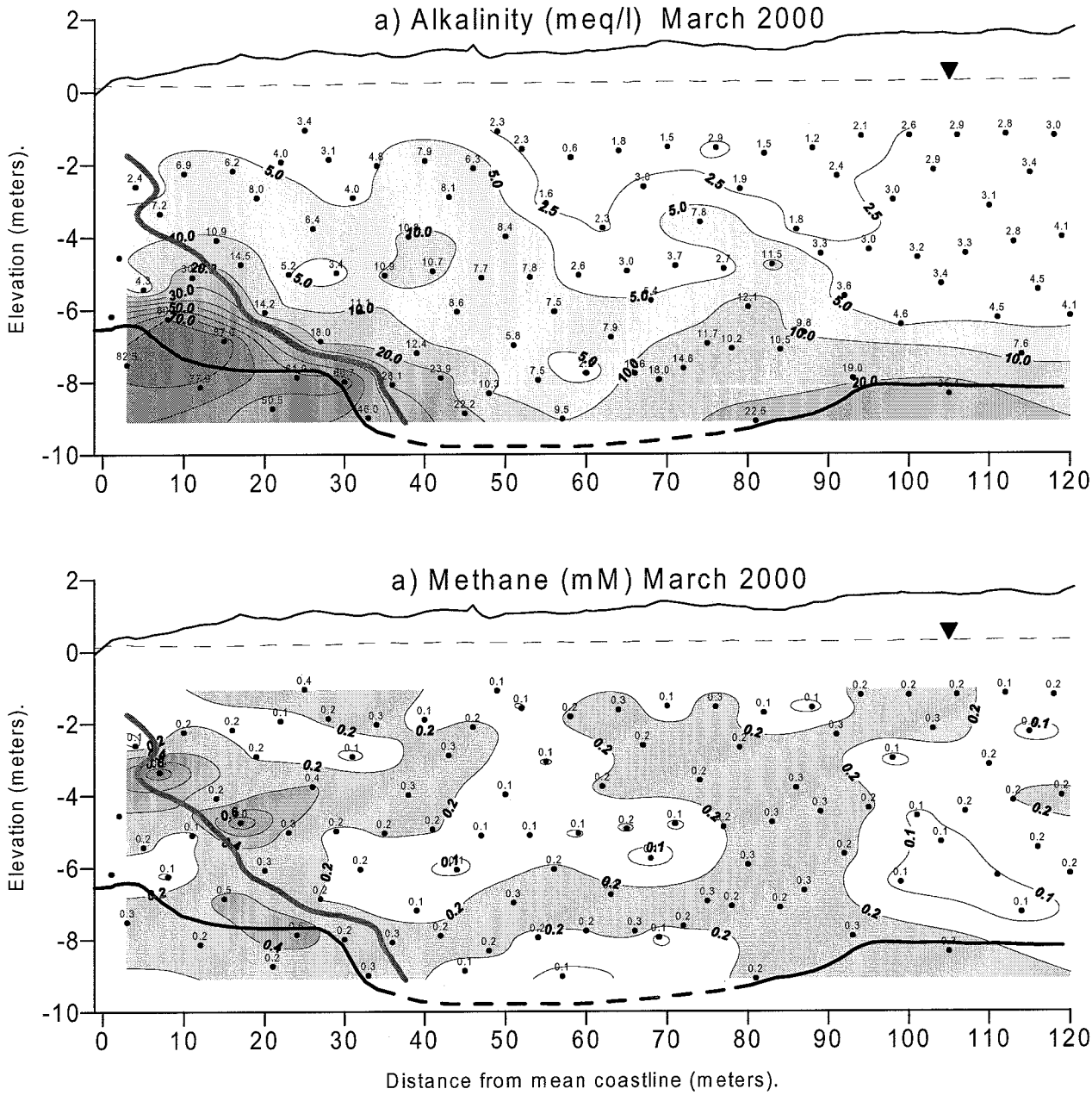

Figure 6.22: a) Alkalinity in meq/l b) Methane concentrations in mM. Measured in the transect 49 days after the inundation event.

hardly visible increase in sulfide concentrations in the plumes (Fig. 6.21a) compared to the August data (Fig. 6.5c), and little change in the alkalinity can be detected (Fig. 6.22a).

Methane
The methane concentration (Fig. 6.22b) has generally decreased in the entire aquifer compared to August (Fig. 6.6). This was to e expected in the parts of the aquifer where sulfate has been introduced by the inundation, because the presence of sulfate can lead to re-oxidation of methane (Barnes and Goldberg 1976, Reeburgh 1980, Iversen and Jørgensen 1985; Hoehler 1994). However the expected increase in sulfide due to the reduction of sulfate is not observed. It is also intriguing that the methane concentration landwards of 90 m has decreased dramatically, as there is no other data indicating that this zone has been affected by seawater.

6.3.2 Distribution of major cations

Most noticeable are the effects of cation exchange on the cation distribution. High concentrations of the three cations Na^+, Mg^{2+} and Ca^{2+} are associated with the plumes. Na^+ concentrations range from 20 – 80 mM, highest at the lower parts (–7 to –8 m) of the plumes at 60 and 80 m (Fig. 6.23a). The concentration of Mg^{2+} ranges from 3 –10 mM and is highest in the plume closest to the coast (30 m) and in the lower part (–4 to –8 m) of the plume at 80 m (Fig 6.23b). Also an enhanced concentration of Ca^{2+} of 2 to 6 mM is seen, highest in the plume furthest from the coast at about –5 m and –7 m (Fig 6.23c).

The plot of Δm_{Ca} (Fig. 6.24c) shows enrichment of Ca^{2+}, especially for the plumes at 80 m and 60 m. Two zones of Ca^{2+} depletion are found in the upper part of the aquifer. One zone extends from the coast inland to 70 meter, generally with an elevation above –3 m, but dropping to –6 m between 40 and 50 meters from the coast. Another small zone of depletion is seen inland from 80 m above –3 m. The enrichment of Ca^{2+} associated with the plumes, is related to the depletion of Na^+ (Fig. 6.24a), Mg^{2+} (Fig. 6.24b) and K^+ (not shown). The zone of Na^+ depletion exhibits a complex pattern, but basically contains two main zones. One zone dips towards the coast from the surface at 60 to 80 m reaching the bottom of the aquifer at 50 to 60 m from the coast. The other zone of depletion starts at the coast at –2 to –4 m running landward down along the saltwater wedge merging with the former zone at –6 m about 50 m from the coast. The geometry of this pattern of Na^+ depletion is very closely resembled by the sulfate distribution (Fig. 6.20b). A shallow zone

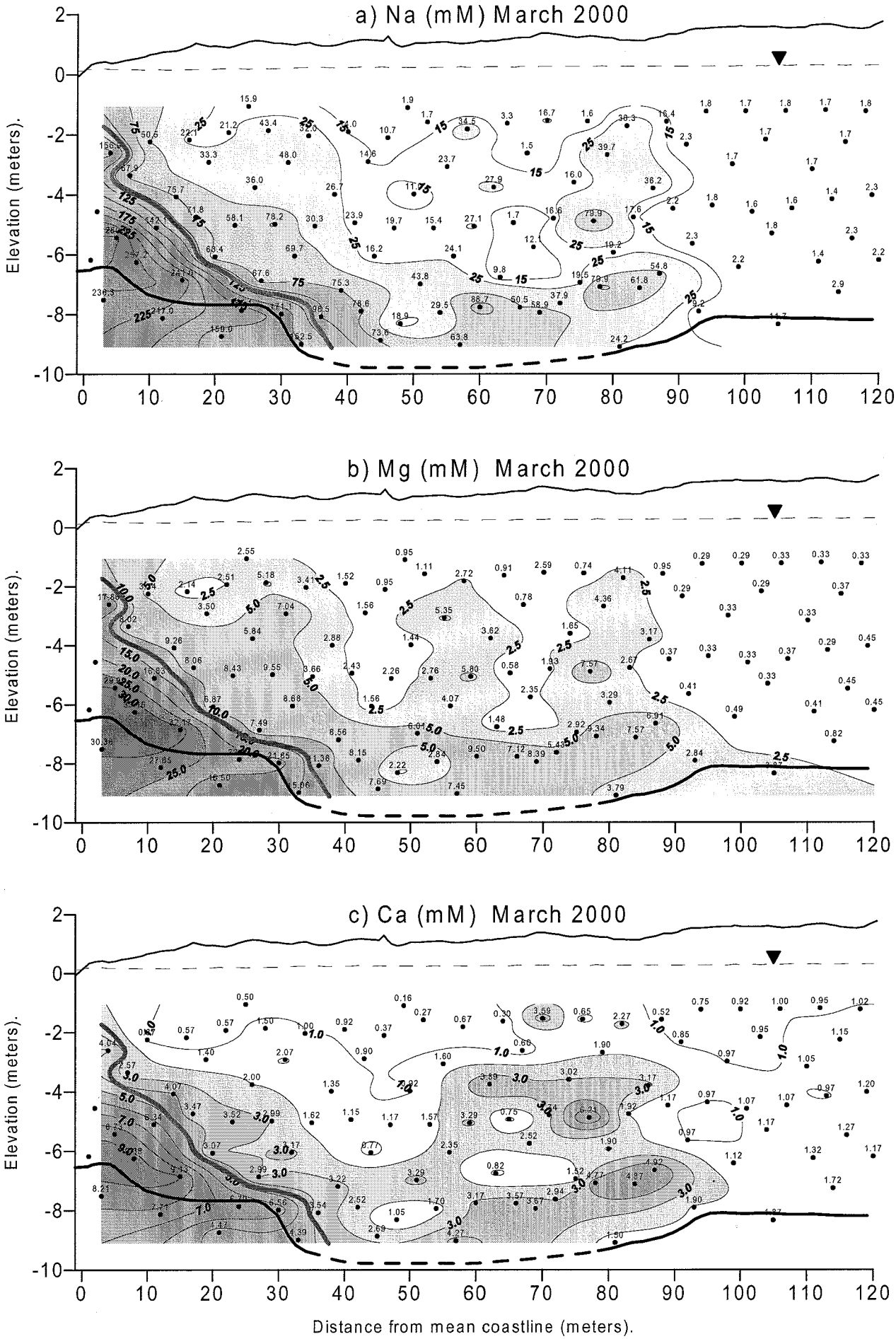

Figure 6.23: a) Sodium concentrations in the transect in mM b) Magnesium concentrations in mM. c) Calcium in mM. Measured in the transect 49 days after the inundation event.

enriched in Na^+ is found 30 - 50 m from the coast, at –1 to –6 m. The depletion of Mg^{2+} is not quite as extensive and mainly observed for the most landward plume at 80 m and only reaches an elevation of –4 m (70 to 80 meters from the coast). In the two plumes closer to the coast (at 30 and 60 m) an enrichment of Mg^{2+} is observed.

The zone 40 to 50 meters from the coast (from –1 to –6 m) with depletion of Ca^{2+} (Fig. 6.24c) and enrichment of Na^+ (Fig. 6.24a) coincide with a zone of low salinity and must be freshwater entrapped between the saltwater plumes. The observed depletion of Ca^{2+} and enrichment of Na^+ in this fresh zone could partly be a result of the existing depletion/enrichment prior to the inundation. But part of the explanation could be upward displacement of freshwater compensating for the downward migrating seawater plumes (Fig. 5.21). Thus freshwater relatively rich in Ca^{2+} is being forced up into an area with an exchanger dominated by Na^+. A decrease in salinity in this zone can be observed from August to March where the Cl^- concentration decrease from 20-30 to 10-20 mM, further enhancing the exchange of Ca^{2+} for Na^+.

6.3.3 Calculated cation composition on the cation exchanger

Again the relative exchanger cation composition can be calculated for every sampling point in the transect as was done for the August data in Figure 6.16(a to d). Figure 6.25(a to d) shows the cation composition on the exchange complex calculated from the aqueous concentrations. The over all picture is similar to August (Fig. 6.16). The main deviation is the decrease in β_{Ca} in the most landward of the plumes at 80 m from a β_{Ca} of 0.6 – 0.8 down to a minimum β_{Ca} of 0.3 (Fig. 6.25a). This decrease is counterbalanced by an increase in β_{Na} and partly in β_{Mg}. β_{Na} increases in the upper part of the plume at 80 m from 0.02 to a maximum of 0.2 (Fig. 6.25b). The changes in β_{Mg} are more ambiguous. In the uppermost part (–1 to –3 m) of the plume at 80 m the β_{Mg} increases from 0.2 to about 0.4 (Fig. 6.25c). Deeper in the plume (–3 to –6 m) and slightly more towards the coast (at around 70 m) β_{Mg} rather decreases from 0.45 to 0.3. Here counterbalanced by increases in β_{Na} and β_{Ca}.

Overall the enrichment and depletion of cations suggests ion exchange with seawater Na^+ displacing Ca^{2+} from the exchanger into the solution. The Ca^{2+} release is most pronounced furthest from the coast where observed Δm_{Ca} is highest and also the fraction of the exchanger occupied by Ca^{2+} prior to the inundation is highest (Fig. 6.16c). Closer to the coast, Mg^{2+} was dominating the

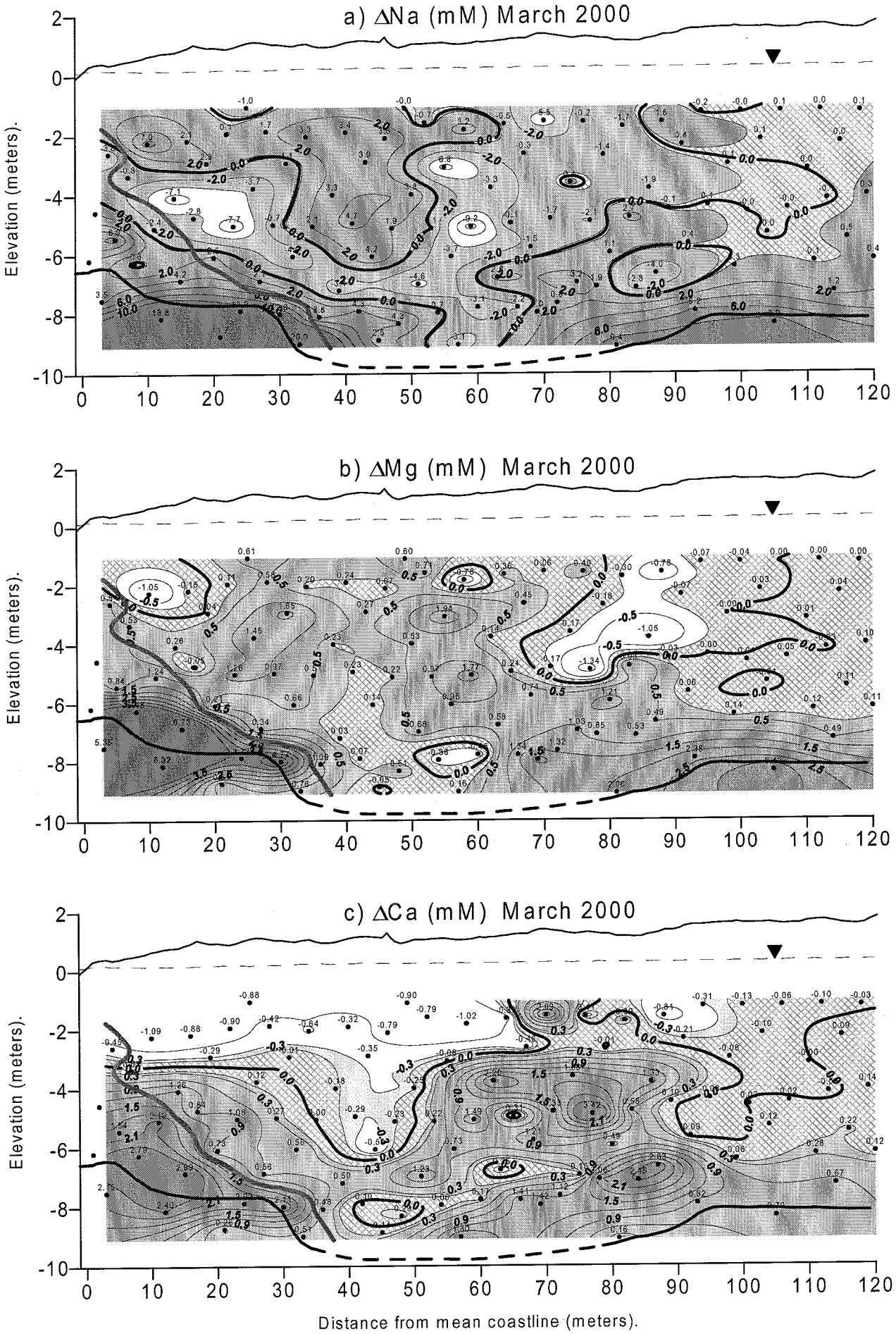

Figure 6.24: Δmi-concentrations in mM of a) Sodium b) Magnesium and c) Calcium in the transect. Crosshatched areas represents a Δmi of + 0.2 mM i.e. essentially little or no depletion or enrichment. Measured in the transect 49 days after the inundation event.

exchanger prior to the inundation (Fig. 6.16b). Here Na^+ is displacing Mg^{2+} on the exchanger, giving excess of Mg^{2+} in the two plumes closest to the coast (Fig. 6.24b). There is a close correlation between the location of the two plumes (at 30 and 60 m) and the zones with maximum depletion for Na^+ and maximum enrichment of Mg^{2+}. The release of Mg^{2+} and the depletion of Na^+ is probably caused by the increase in salinity creating a relatively higher affinity for monovalent than divalent cations on the exchanger.

6.3.4 Saturation states for solid phases

The area with saturation for calcite (Fig. 6.26) in the mixing zone has been somewhat reduced after the inundation compared to August (Fig. 6.17), especially in the zone invaded by the seawater plume 30 m from the coast. Further inland the calcite saturation state is still negative and has only increased slightly despite the release of Ca^{2+} from the exchanger. The decrease in the calcite saturation state is probably due to the low alkalinity of the surface seawater and because mixing, to be discussed in section 7.3, lowers the saturation index and thus counteracts the effects of increased calcium concentrations.

6.3.5 Calcite dissolution/ precipitation

The increased Ca^{2+} concentrations in the seawater plumes are probably not due to calcite dissolution since the alkalinity (Fig. 6.22a) does not increase as compared to the August data (Fig. 6.8b). Actually the alkalinity in the affected part of the aquifer has decreased somewhat due to the low alkalinity of the seawater. However, the slight reduction in the area of calcite saturation (at 25 - 45 m) observed between the August data (Fig. 6.17) and the March data (Fig. 6.26) could possibly lead to some additional dissolution of calcite.

Conclusion on inundation

The overall effect of the seawater inundation comprises a shift in the redox conditions from methanogenic conditions towards more oxidised conditions. In the initial stage of the percolation of the density plumes the introduction of oxygen re-oxidises reduced species (such as pyrite) in the upper part of the aquifer. Subsequently sulfate reduction becomes the over all dominating redox-process. The contribution of Na^+, Mg^{2+} and K^+ in the inundated seawater displace Ca^{2+} from the

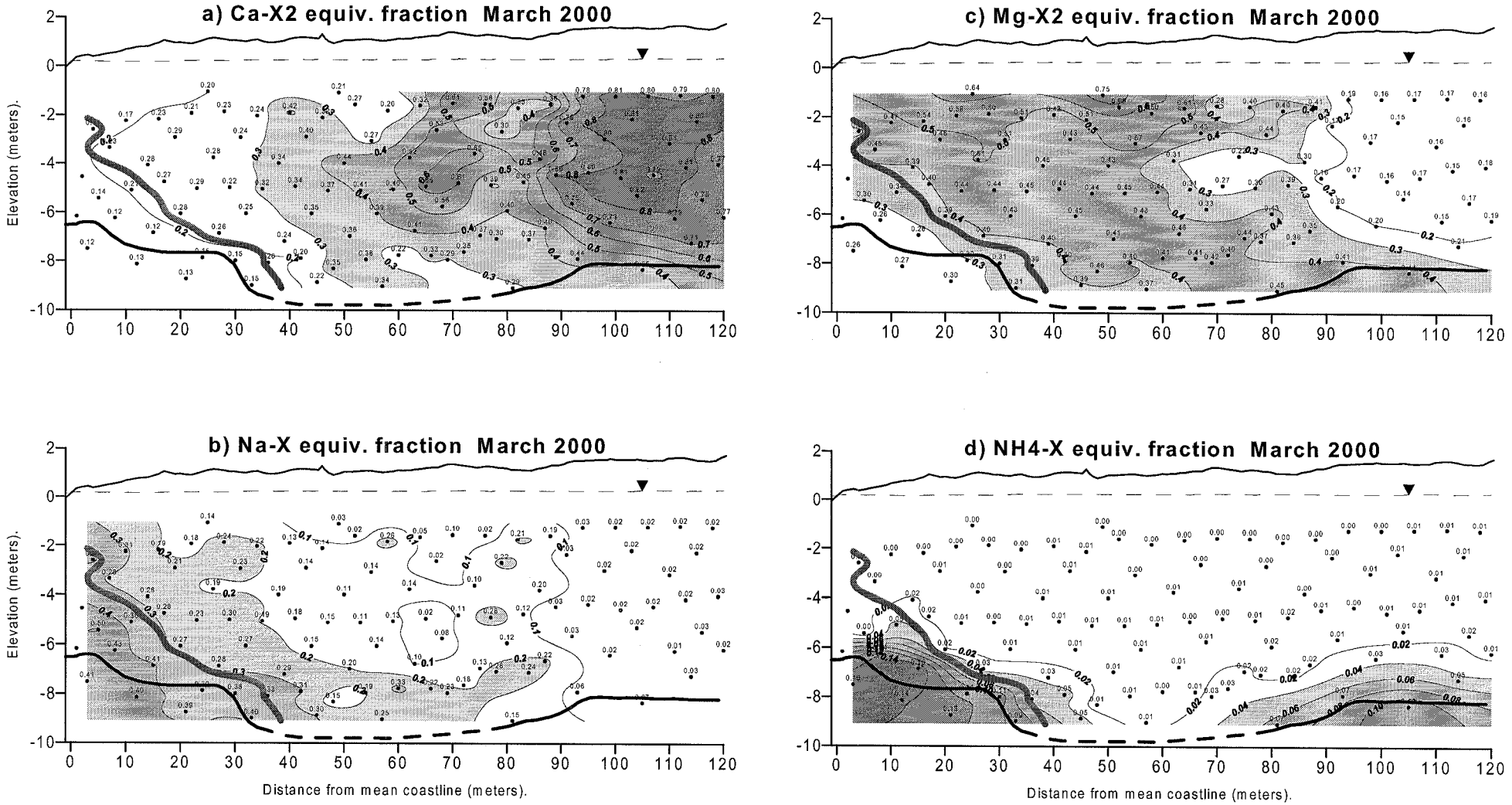

Figure 6.25: Equivalent fractions of a) Ca2+ b) Mg2+ c) Na+ and d) NH4+ on the exchanger calculated from the groundwater composition using PHREEQC and the standard selectivity's in the PHREEQC database. Measured in the transect 49 days after the inundation event.

exchanger. In zones where Mg^{2+} was previously dominating the exchanger Na^{+} is also displacing Mg^{2+}.

The inundation event also explains the observed distribution of the cation composition on the exchanger prior to the inundation. The high fraction of Mg^{2+} on the exchanger in the fresh part of the aquifer prior to the inundation (August data Fig. 6.16) is most likely stemming from a previous inundation. The mixing of high salinity plume water and freshwater seem to cause a slight decrease in the calcite saturation and possibly lead to some additional dissolution of calcite.

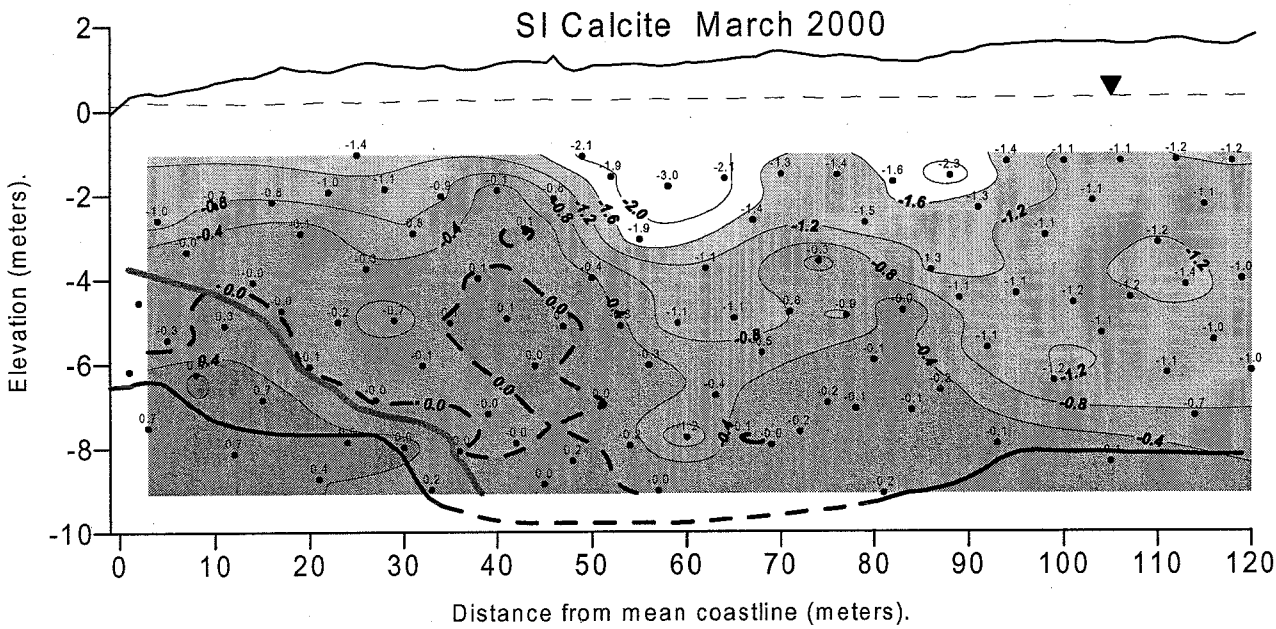

Figure 6.26: Saturation state (SI) for calcite calculated using PHREEQC. Measured in the transect 49 days after the inundation event.

7. DISCUSSION I: CHEMISTRY OF THE NATURAL SITUATION

In the following, the chemical evolution of the freshwater and saline water in the aquifer will be discussed. Then the effects of the mixing of fresh- and seawater on carbonate equilibrium will be evaluated first without including redox-reactions or ion exchange processes. A series of 1-D reactive transport models constructed in PHREEQC will be presented to understand the relative effects of ion exchange, redox-reactions and calcite equilibrium, as seawater is being displaced by freshwater. These processes will be summed up in a model combining the processes of ion exchange, redox-reactions and calcite equilibrium and compared to the field data. Finally, chemical aspects of the migration of the density plumes will be modelled and discussed

7.1 Chemical evolution of the freshwater

Understanding the chemical processes controlling the composition of the freshwater is a natural starting point before embarking on the complex processes occurring in the mixing zone. The fresh water landwards from St80 and above an elevation of –6 m has a uniform chemical composition with only slightly increasing concentrations of some species with depth (see Figs. 6.3 to 6.10). The average composition of this freshwater is given in column 1 in Table 7.1.

In Table 7.1 the sea salt contribution of the different cations is calculated using chloride as a conservative tracer and the relative composition in seawater. The most pronounced difference between the observed composition and calculated sea salt contribution is the excess calcium and alkalinity in the groundwater. A likely explanation is calcite dissolution. However, there is less Ca^{2+} than expected from the stoichiometry of 2 moles HCO_3^- for every mole of Ca^{2+}. The Ca^{2+} released by calcite dissolution could displace Mg^{2+}, Na^+ and K^+ from the exchanger. The measured composition on the exchanger in the fresh water zone is $Ca\text{-}X_2$ = 66%, $Mg\text{-}X_2$ = 13%, Na-X = 10%, K-X = 7% and NH_4-X = 3%, the mean of 3 core samples, see Fig. 6.15a. Since 30% of the exchanger is covered by marine cations, recent inundation events must have occurred. Displacement of some of the Mg^{2+} and Na^+ from the exchanger by Ca^{2+} is accordingly a likely process. For calcite

an average subsaturation of SI = –1.1 is observed in the zone. The subsaturation for calcite is either due to slow reaction kinetics of the calcite in the aquifer, perhaps consisting of relatively few dispersed shell fragments, and/or because of a gradual production of the CO_2 driving the calcite dissolution.

The redox chemistry of the freshwater is dominated by methane with an average concentration of about 1 mM showing highly reducing conditions. Only traces of sulfate can be seen in the most shallow of the borings. Also sulfide is present at a concentration of about 0.14 mM. Part of the observed inorganic carbon (TIC ~ 6 mM) must therefore also come from organic matter degradation by redox-processes. The redox-parameters are quite constant, although there is a slight increase in methane with depth.

Table 7.1: 1) Observed average concentrations from the fresh water zone (landwards from St80 and above –6 m); 2) Calculated sea salt contribution using the observed chloride concentration as tracer and the composition of diluted seawater; 3) Infiltration water equilibrated with calcite (SI = -2.5) and a CO_2 partial pressure of 0.01 atm; 4) Results from a batch model in PHREEQC with: CEC=0.5meq/100g, $SI_{calcite}$=-1.1 and 5 mmol CH_2O.

	1) Observed average concentrations	2) Calculated sea salt contribution	3) Infiltration composition with P_{CO2} = 0.01 atm. and $SI_{calcite}$ = -2.5	4) PHREEQC batch model results
Cl^- mM	1.78	1.78	1.78	1.78
Ca^{2+} mM	1.07	0.04	0.32	1.05
Mg^{2+} mM	0.40	0.17	0.17	0.47
Na^+ mM	1.80	1.56	1.56	1.82
K^+ mM	0.10	0.034	0.034	0.05
Alkalinity meq/l	3.44	0.014	0.57	3.10
TIC mM	5.99	0.03	1.10	4.87
Log(P_{CO2})	-1.35	-3.5	-2.0	-1.48
PH	6.57	6.36	6.46	6.66
SI calcite	-1.1	-	-2.5	-1.1
SO_4^{2-} mM	0.005	0.083	0.083	0
S^{2-} mM	0.14	0	0	0.083
CH_4 mM	1.00	0	0	2.42

It seems that the freshwater composition can be explained by a combination of organic matter degradation, ion exchange processes and calcite dissolution. In order to verify and quantify the proposed processes a PHREEQC model was set up. The lack of information on geology, hydrogeology and water chemistry upstreams from the monitoring transect makes it most appropriate to use a batch model.

In the PHREEQC model, seawater and distilled water are mixed to fit the observed chloride concentration in the fresh water. This mixed water is equilibrated with CO_2 at a partial pressure of 0.01 atm ($Log(P_{CO2}) = -2.0$) and calcite to a saturation of SI = -2.5. The resulting water composition is shown in column 3 in Table 7.1. The CO_2 partial pressure of 0.01 atm is a reasonable value reflecting respiration in the root zone. The calcite saturation of –2.5 is slightly lower than the observed value and chosen in order to obtain realistic values for the calcium concentration in the infiltration water and the initial exchanger composition. The water is equilibrated with an exchanger with a CEC of 0.5 meq/100g, which is the average for the sandy part of the aquifer (Fig. 6.12). The CEC was recalculated to $2.46 \cdot 10^{-2}$ mol/l pore water by the following expression:

$$CEC_{mol/l} = CEC_{meq/100g} \cdot f \cdot \frac{(\rho_s \cdot (1-\varepsilon))}{\varepsilon} \qquad (7.1)$$

Where f is a conversion factor of 10^{-2}, ρ_s is the solid density of quartz (=2.65 g/cm^3) and ε is the average porosity of 0.35.

After equilibration the exchanger composition is then: Ca-X_2 = 72%, Mg-X_2 = 24%, Na-X = 3.2% and K-X = 0.4% (Table 7.2). Subsequently the water and exchanger system are allowed to equilibrate with calcite to the observed saturation of SI = -1.1 and organic matter (CH_2O) is added in increments of 0.2 mmol. The organic matter is added until a reasonable fit with the observed water chemistry is obtained. First organic matter reduces the minor amount of sulfate present and then proceeds to produce methane and CO_2. The CO_2 lowers the pH and drives the additional dissolution of calcite. In turn the released calcium will partially exchange with the marine cations mainly Na^+ on the exchanger. The concentrations of all cations in solution therefore increase as the organic matter is oxidized.

Table 7.2: Exchanger composition in equivalent fractions 1) measured in core samples (average of three samples) 2) calculated from water compositions using PHREEQC and standard selectivity coefficients of the PHREEQC database 3) Initial exchanger composition in equilibrium with infiltration freshwater with calcite (SI = -2.5) and a CO_2 partial pressure of 0.01 atm 4) Final exchanger composition resulting from a batch model in PHREEQC with: CEC=0.5meq/100g, $SI_{calcite}$=-1.1 and 5 mmol CH_2O.

	1) Measured in core samples	2) Calculated from water compositions	3) Infiltration composition with P_{CO2} = 0.01 atm. and $SI_{calcite}$ = -2.5	4) PHREEQC batch model results
Ca-X_2	0.66	0.77	0.72	0.76
Mg-X_2	0.13	0.19	0.24	0.22
Na-X	0.10	0.03	0.03	0.02
K-X	0.07	0.007	0.004	0.003
NH_4-X	0.03	0.007	- (not included)	- (not included)

As seen in Table 7.1 a reasonable match was obtained with the field data for most parameters after an addition of about 5 mmol/l of CH_2O. The calculated cation distribution agrees well with the observed cation distribution. Accordingly there is also a good agreement between the cation exchanger composition of the model and calculated from the observed water composition (Table 7.2). However, the modeled cation exchanger composition does not fit the measured composition too well. The measured cation exchanger composition seems to contain a smaller fraction of divalent cations (Ca^{2+} and Mg^{2+}) and a higher fraction of the monovalent cations (Na^+ and K^+). The exact reason for this is unknown, but a probable explanation is that in reality advective transport could have some effects on the exchanger composition in the form of chromatographic separation of the cations.

The largest discrepancies in the water chemistry are seen for alkalinity, TIC and methane. The model predicts an alkalinity and TIC that are too low and a methane concentration that is too high. The reason for this could be effects of other redox-processes producing inorganic carbon, which is not accounted for in the model (such as NO_3^-- or $Fe(OH)_3$-reduction). Also the sulfate concentrations in the infiltrating water might in reality be higher judging from the measured average sulfide concentrations of 0.14 mM compared to the 0.083 mM in the model (derived from seawater). It is not unlikely that there is an additional atmospheric contribution of sulfate from air pollution. This extra sulfate together with some nitrate will increase the alkalinity and TIC in the

model and decrease the CH_4. And alternative explanation is bubble formation caused by the high methane concentrations as illustrated in Figure 6.9. Part of this methane could evade to the atmosphere and part of it could be re-oxidized higher in the aquifer and thus contribute to the TIC.

In summary the fresh water composition can be explained by a combination of calcite dissolution, ion exchange, methane formation and to a lesser extent sulfate reduction.

7.2 Evolution of water chemistry in the peat layer

In the other end of the spectrum is the pore water of the peat layer near the coast, exemplified by a water sample from St15 in Table 7.3. Most noticeable for this water composition is a Cl^- concentration comparable to the fjord seawater, a very high alkalinity, high concentration of ammonium and a simultaneous surplus of all major cations as compared to seawater using Cl^- as a conservative tracer.

This pore water composition seems to be largely the result of degradation of organic matter by a sequence of redox-processes of which the two most important seem to be sulfate reduction and methane formation, producing CH_4, H_2S and inorganic carbon (CO_2). The redox-processes, especially methanogenesis, may also lead to dissolution of carbonate minerals especially of calcite present as shell fragments in the peat (up to 57 g IC/kg ~ 1385 mmol IC/l pore water). The calcite dissolution is however constrained by the calcite solubility constant and an alkalinity of up to 90 meq/l will never be reached by simple calcite dissolution, unless there is some sink for calcium. A large cation exchanger, initially in equilibrium with seawater and therefore dominated by Na^+ and Mg^{2+} could serve as the sink for the calcium released by dissolution. The exchange of calcium for sodium, magnesium and potassium will then increase the solution concentrations of these cations. Also ammonium derived from the organic matter degradation will adhere to the exchange complex and displace the seawater-derived cations. A similar water composition was observed in Holland in brackish waters associated with organic rich layers (Stuyfzand, 1993).

Modelling was done for sampling site St15 (Table 7.3) in the peat layer. The low hydraulic conductivity indicates the absence of advective transport, and justifies the use of a batch PHREEQC model. The modelling is somewhat more difficult than for modelling of the freshwater case,

because the high concentration of ammonium of 22 mM in the pore water indicating that the organic matter being oxidised cannot be simply represented by CH_2O. In lack of actual measurements of the organic matter composition the Redfield composition for marine plankton (Redfield et al., 1963) of $(CH_2O)_{106}(NH_3)_{16}H_3PO_4$ is employed in the model. Also the lack of consistency between the measured exchangeable fraction of ammonium in the peat and the fraction predicted by using PHREEQC as seen in Fig. 6.15a pose a problem for using the standard database in modelling the observed water chemistry. This modelling exercise should therefore be viewed as a more qualitative insight into the coupling of the processes.

As a starting point seawater (89%) (the mean in Table 6.1) and freshwater (11%) were mixed in proportions giving a chloride concentration of 270 mM, equal to the observed concentration. The mixed water was equilibrated with an exchanger containing a CEC of 250 mmol/l ~ 5 meq/100g. This value is however subject to considerable uncertainty in as much as the measured CEC in the peat range from 2 to 43 meq/100g. Also uncertainty regarding the porosity and bulk density gives additional uncertainty in the conversion from meq/100g to mmol/l pore water. Equilibrium with calcite (SI = 0) is also included in the model.

Table 7.3 show the results of the model compared with the measured water composition. In the model an alkalinity of 83 meq/l is reached by oxidizing 3.4 mmol Redfield organic matter (~360 mmol-C), added by an irreversible reaction. This high alkalinity, comparable with the measured, could be reached with the proposed coupling of processes and at the same time the cation composition is modelled reasonably well with deviations of 5% or less. The modelled pH (6.05) is half a unit lower than the observed pH (6.65). NH_4^+ is an exception with a deviation of more than 10%, with less aqueous ammonium than observed. But the total amount of ammonium in the model is larger than what is measured in the field as can be seen from a mass balance for ammonium:

$$m_{tot} = CEC \cdot \beta_{NH_4^+} + C_{NH_4^+} \qquad (7.2)$$

For the model this gives:

$$m_{tot,model} = 250 mmol/l \cdot 0.14 + 19.6 mmol/l = 54.6 mmol/l$$

And in the field, assuming an exchanger of the same size:

$$m_{tot,field} = 250 mmol/l \cdot 0.05 + 22 mmol/l = 34.5 mmol/l$$

This indicates that either the organic matter in reality contains less ammonium or that less organic matter is oxidised. Also substantial deviations are observed for methane, sulfide and phosphate with very high concentrations in the model. The low measured dissolved sulfide concentration could be caused by precipitation with ferrous iron as iron-mono-sulfides or pyrite. It is likely that the sediment still contain some Fe(III)-oxides with which the sulfide can react (Jakobsen, 1995). Accommodating for a Fe(III)-oxide mineral phase in the model (as e.g. equilibrium with goethite $Fe(OH)_3$) and allowing precipitation of FeS will reduce the amount of dissolved sulfide. Including goethite in the model will have little effect on the other parameters of the model, except for a little decrease in the amount of methane produced, because the goethite will also serves as an electron acceptor and contributes to the organic matter degradation and the production of inorganic carbon as illustrated by the oxidation of CH_2O:

$$4Fe(OH)_3 + CH_2O + 4H_2S \rightarrow 4FeS + CO_2 + 11H_2O \qquad (7.3)$$

The low concentration of dissolved sulfide is thus explained, but the large deviation for methane still remains to be explained. Unless there is some large source of alkalinity not accounted for, the only remaining explanation is degassing of the methane produced (and other gasses) and subsequent upward gas migration in the aquifer. The formation of a gas phase seem likely when recalling that the hydrostatic pressure line in Fig. 6.9 seem to represent an upper limit for the summed partial pressure of dissolved gasses (especially methane). Degassing is also expected to yield a higher pH due to the degassing of CO_2. A degassing of CO_2 could perhaps also explain the observed calcite supersaturation of SI = 0.7, because the calcite is predominantly dissolved during the early stages of methane formation. As the gas phase starts to form CO_2 will be lost, creating supersaturation for calcite, but re-precipitation could be prevented by the inhibitory effects of the high concentration of Mg^{2+} (Berner, 1975), phosphate (Walter and Hanor, 1979), and DOC (dissolved organic carbon) (Berner et al., 1978). An alternative explanation for the apparent supersaturation is that the pore water might be in equilibrium with a more soluble Mg^{2+}-rich calcite formed on the surfaces of the carbonate shell fragments.

The modelled concentration of phosphate is much higher than the measured indicating that either the organic matter contains less phosphorus or that sorption or some mineral phase such as hydroxyapatite ($Ca_5(PO_4)_3(OH)$) is controlling the aqueous concentration of phosphate. The

PHREEQC speciation for the August data did show a supersaturation (of SI = 2) for hydroxyapatite in the peat layer and precipitation of this phase could well explain the low phosphate concentration.

Table 7.3: Comparison of the measured (Aug 1999) and the water compositions modelled with PHREEQC for observation well St15: Exchanger = 250 mmol/l; Moles of Redfield organic matter = 3.4 mmol (= 360 mmol-C); equilibrated with calcite SI = 0. * The observed sulfide concentration was not measured but estimated from the contours in Fig. 6.5c.

	pH	Alkalinity meq/l	Ca^{2+} mM	Mg^{2+} mM	K^+ MM	Na^+ MM	NH_4^+ MM	Phosphate mM	Sulfide mM	CH_4 mM
Observed chemistry St15	6.65	90.54	9.11	32.01	6.06	250.29	22.06	0.54	3.00*	0.64
Model: CEC 250 meq/l; Redfield 3.4 mmol; SI calcite 0.0										
Sea-fresh water mix	7.26	2.40	6.13	25.40	5.22	236.30	0.04	0.00	0.00	0.00
Final model	6.05	83.02	9.21	33.90	5.94	251.74	19.61	3.40	12.69	167.68
Deviation %	8.98	8.31	-1.04	-5.90	1.91	-0.58	11.12	-526	-323	-26182

Table 7.4: Observed and modelled exchanger composition for the model of Table 7.3 and amount of calcite dissolved as predicted by the PHREEQC model.

	$Ca\text{-}X_2$ eq frac.	$Mg\text{-}X_2$ eq frac.	Na-X eq frac.	K-X eq frac.	$NH_4\text{-}X$ eq frac.	Calcite dissolved mM
Observed chemistry St15	0.18	0.41	0.31	0.04	0.05	
Model: CEC 250 meq/l; Redfield 3.4 mmol; SI calcite 0.0						
Sea-fresh water mix	0.128	0.332	0.481	0.058	0.000	
Final model	0.120	0.265	0.421	0.056	0.140	2.10
Deviation %	34	36	-34	-56	-160	

2.1 mmoles of calcite is dissolved in the model (Table 7.4), which is in between 0.15% and 3.5% of the maximum and minimum amount of sedimentary carbonate measured in the peat. From the oxidation of Redfield organic matter, 35 mmol NH_4^+ is going on to the exchanger (Table 7.4) thus, in the model, being far more important than Ca^{2+} in displacing the seawater derived cations Mg^{2+}, Na^+ and K^+ from the exchanger and into the solution. In fact about 0.95 mmoles of Ca^{2+} is displaced from the exchanger in the model. However, the measured fraction of Ca^{2+} on the exchanger is 0.18 whereas the final Ca^{2+} fraction in the model is 0.12. For ammonium the discrepancy is larger with a measured fraction of NH_4^+ of 0.05 and a modelled NH_4^+ fraction of 0.14. This indicates that in reality the amount of calcite dissolution and transfer of Ca^{2+} on to the exchanger may be much

larger than indicated by the model. A mass balance for Ca^{2+} between the observed chemistry and the sea-/freshwater mix composition (rows 1 and 2 in tables 7.3 and 7.4) indicate a dissolution of calcite in the order of 9-10 mmoles and 6-7 mmoles of Ca^{2+} transferred to the exchanger.

In the case of a gas phase forming the subsequent upward migration of gas through the aquifer above will probably have an effect on the water composition in the aquifer. When the migrating gas phase is mixed with the aquifer groundwater with lower partial pressures the gases will to some extent re-dissolve and a portion of it discharge into the fjord, with the groundwater flow. Part of the methane could potentially be re-oxidised by sulfate as observed for marine sediments (Iversen and Jørgensen, 1985, Hoehler, 1994) or other electron acceptors higher in the aquifer. Re-oxidation of methane by sulfate leads to an increased alkalinity according to:

$$CH_4 + SO_4^{2-} \rightarrow HS^- + HCO_3^- + H_2O \qquad (7.4)$$

The re-dissolution of the CO_2 gas could also lead to increased alkalinity by dissolution of carbonate minerals. The extent of these effects will of course depend on the rate of organic matter degradation, the extent and rate of gas migration and the groundwater flow above the peat layer. Given an average oxidation rate of 2 mM Org-C/yr the water composition would have taken 180 years to develop! And furthermore the rate would probably decrease with time (Stuyfzand, 1993). Because of this the effects are probably small compared to the groundwater convection in the saline wedge, which by numerical modelling was estimated to be between 3 - 12 m/yr, increasing away from the bottom (Christensen, unpublished results).

In conclusion: The high alkalinity of 90 meq/l in the peat layer can be explained by a combination of redox-reactions, calcite dissolution and cation exchange reactions. In the model of Tables 7.3 and 7.4 sulfate reduction contributes with about 25 meq/l, calcite dissolution with about 4.2 meq/l and the remaining 50 meq/l is due to methanogenesis and the subsequent buffering of the produced CO_2. In reality calcite dissolution could probably contribute to the alkalinity with up to 20 meq/l. The ammonium released by the organic matter degradation and the Ca^{2+} released from calcite dissolution displaces the cations Na^+, Mg^{2+} and K^+ from the exchanger and creates a solution enriched in all cations compared to a conservative mixture of seawater and freshwater. The substantial degradation of organic matter may cause a gas phase to form consisting mainly of CH_4

and CO_2, explaining the moderate observed aqueous concentrations of CH_4 and H_2S, and the slightly elevated pH. Also the reduction of goethite and the precipitation of FeS or pyrite could constrain the concentration of dissolved sulfide. The most important processes of this system are probably the methanogenesis with the subsequent buffering of the produced CO_2 by calcite dissolution and the possible formation of a gas phase.

7.3 Mixing

In the mixing zone the chemical patterns become more complicated and transport processes cannot be ignored. But before we turn to aspects of reactive transport, we will first look into some aspects of pure mixing of sea- and freshwater to see how much of the observed chemistry can be explained by simple mixing.

Several authors have shown that mixing of sea- and freshwater can lead to subsaturation in the mixed water for minerals such as calcite, even though both water types were saturated or supersaturated prior to mixing (Plummer, 1975, Wigley and Plummer 1976, Bögli, 1978 and Sanford and Konikow, 1989). Plummer (1975) showed, for a system closed with respect to CO_2, that the development of subsaturation for calcite in mixtures is a function of the P_{CO2}, the degree of calcite saturation, the ionic strength, formation of complexes, the temperature and the pH of end member solutions prior to mixing. The degree of subsaturation will increase with increasing ΔP_{CO2} between the end member solutions and is mainly caused by the redistribution of all inorganic carbon species during mixing. In this redistribution CO_3^{2-} is consumed thereby increasing the amount of calcite subsaturation in the mixed solution. Also increasing difference of ionic strength between the end member solutions will give increased subsaturation in the mixed solution due the non-linear dependence of activity coefficients on ionic strength (Wigley and Plummer, 1976). Redistribution of or formation of complexes during mixing can lead to either increased or decreased saturation depending on the presence of complex forming cations and the distribution of inorganic carbon species. Increased calcite supersaturation of end members will tend to reduce the degree of subsaturation of the mixed solution. A lower pH of end member solutions will increase the subsaturation. Decreasing the temperature will increase the range of mixtures being subsaturated (Plummer, 1975).

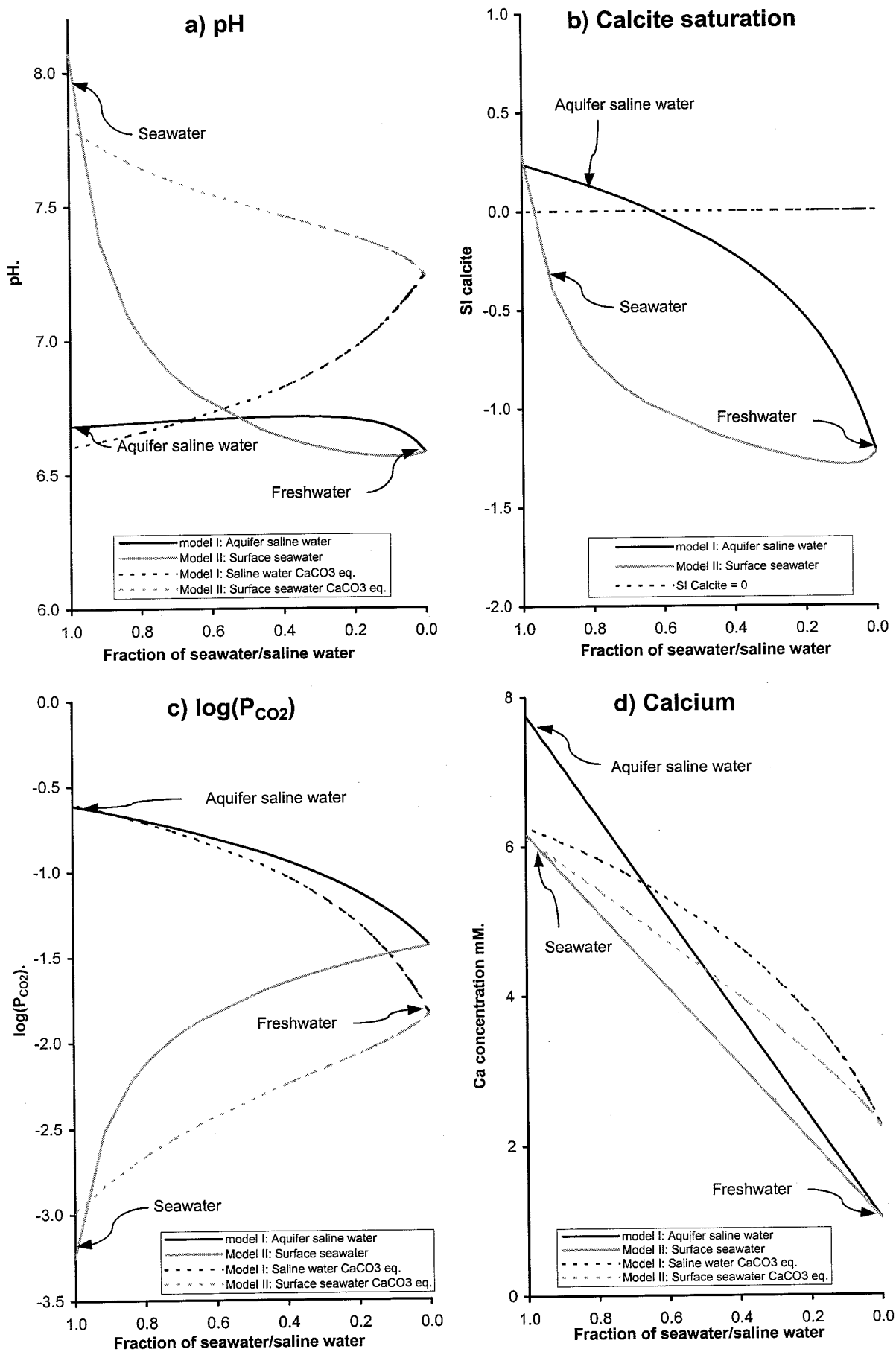

Figure 7.1: Mixing curves of seawater and freshwater calculated with PHREEQC for: a) pH, b) Calcite saturation index, c) log(P_{CO2}) and d) Calcium concentration (mM). Black lines are for mixtures of the aquifer saline end-member (St1, Aug. 1999) and freshwater (St112, Aug. 1999) and grey lines are for mixtures of surface seawater (23/8-1999 Table 6.1) and freshwater (St112). Broken black and grey lines are for the mixtures equilibrated with calcite (SI = 0).

7.3.1 Simple batch-mixing

Table 7.5: End-member compositions used for mix calculations: Surface seawater, Aquifer saltwater (St1), freshwater (St112).

Sample	EC	pH	Alkalinity	Cl	Na	Ca	Mg	K	Sulfate	Sulfide	NH4+	CH4
	µS/cm		Meq/l	mM	mM	mM	mM	mM	mM	mM	mM	mM
Mean surface seawater	31796	8.12	2.31	300.7	262.6	6.7	28.2	5.8	14.1	0	0.01	0
Aquifer saltwater (St1)	30800	6.68	34.67	286.6	237.9	7.8	26.3	5.3	3.6	7.56	4.01	0.68
Aquifer freshwater (St112)	494	6.58	2.84	1.7	1.7	1.02	0.33	0.10	0.02	0.08	0.16	0.54

Mixing curves, for a closed system with respect to CO_2, were calculated with PHREEQC by using seawater and freshwater as end members. One freshwater end member and two saline end members were used (Table 7.5). The saline end members used, were a surface seawater sample from the Isefjord (23/8-1999, Table 6.1) and a saline aquifer sample from –6 m depth at the coast (well St1, august 1999). The reason why both a surface seawater and a saline aquifer end-member are used is that saline water can enter the fresher parts of the aquifer in two ways, either though the seafloor or through the unsaturated zone as density plumes from inundating surface seawater. The primary differences between the two saline end-members are a high pH of 8.1 in the surface seawater as opposed to 6.68 in the saline aquifer end-member, a high alkalinity of 35 meq/l in the saline aquifer end-member as opposed to 2.03 meq/l in the surface seawater. Both saline end-members are supersaturated for calcite with SI = 0.4 for the surface seawater and SI = 0.2 for the aquifer saline end-member. A shallow aquifer sample collected at 112 m from the coast (St112, August 1999) was chosen as the freshwater end member having a pH of 6.58, an alkalinity of 2.84 meq/l and a SI for calcite of –1.2. The saline end-members were each mixed with the freshwater end-member in a series of different sea- and freshwater proportions. For the mixed waters the pH, the saturation state for calcite, the CO_2 partial pressure and the calcium concentration were calculated. The mixed solutions were subsequently equilibrated with calcite. In Figure 7.1a) to d) the mixing curves for the two types of saline end-member mixed with the freshwater are shown. The grey lines in the Figure are mixing curves for surface seawater and freshwater, the dashed lines with calcite equilibrium

imposed. Black lines are for the mix-calculations of saline aquifer end-member and freshwater, again the dashed lines with imposed calcite equilibrium.

The pH of the mixture of surface seawater and freshwater (Fig. 7.1a, grey line) decreases rapidly for even very small amounts of freshwater mixed into surface seawater. At 90% seawater pH has decreased from 8.1 to 7.5 and at 75% to about 7. A pH minimum of 6.56 is seen at 8.4% seawater. The calcite saturation index (Fig. 7.1b) shows the same dramatic decrease for small fractions of freshwater mixed into the surface seawater and the mixture shifts from supersaturation to subsaturation at a freshwater fraction of less than 5%. The calcite saturation index has a minimum SI = -1.3 around a seawater fraction of 8.4% and this is lower than that in the pure freshwater. The $\log(P_{CO2})$ (Fig. 7.1c) is rapidly increasing from that of the surface seawater by in-mixing of a small fraction of freshwater. The reason for the rapid decrease in the calcite saturation is basically that in the surface seawater with a pH around 8 the carbonate system is displaced towards the HCO_3^-/CO_3^{2-} end whereas in the freshwater the carbonate system is displaced towards the H_2CO_3 end. Upon mixing the carbonate species are redistributed towards the HCO_3^- (Plummer, 1975 and Appelo & Postma, 1993). The decrease in pH seems to be caused by the net formation of Metal-HCO_3 - complexes. Because H_2CO_3 of the freshwater is much more abundant than CO_3^{2-} in the seawater, the HCO_3^- in the complexes will partly come from the dissociation of H_2CO_3 and lead to a release of H^+.

The mixing curves for the aquifer saline end-member and the freshwater are fundamentally different (black lines in Figure 7.1). The change in pH as a function of mixing is small with a small pH maximum of 6.7 at a fraction of 20% saline water. The mixing curve for the calcite saturation index (Fig. 7.1b) is convex and all mixtures have a higher saturation index than the freshwater end member. The shift from supersaturation to subsaturation is taking place at a saline water fraction of 65%. The reason for this shape of the curve is probably a combination of the equal pH values of the end member solutions and the much higher P_{CO2} in the aquifer saline end-member compared to the freshwater. Because of the similar pH in the two end member solutions the relative distribution of inorganic carbon species must also be close to identical in the two solutions. Therefore, the buffering of CO_3^{2-} by H_2CO_3 as mentioned above is not an important effect in the mixing of the saline aquifer end-member and the freshwater. The convex shape of the saturation index curve is

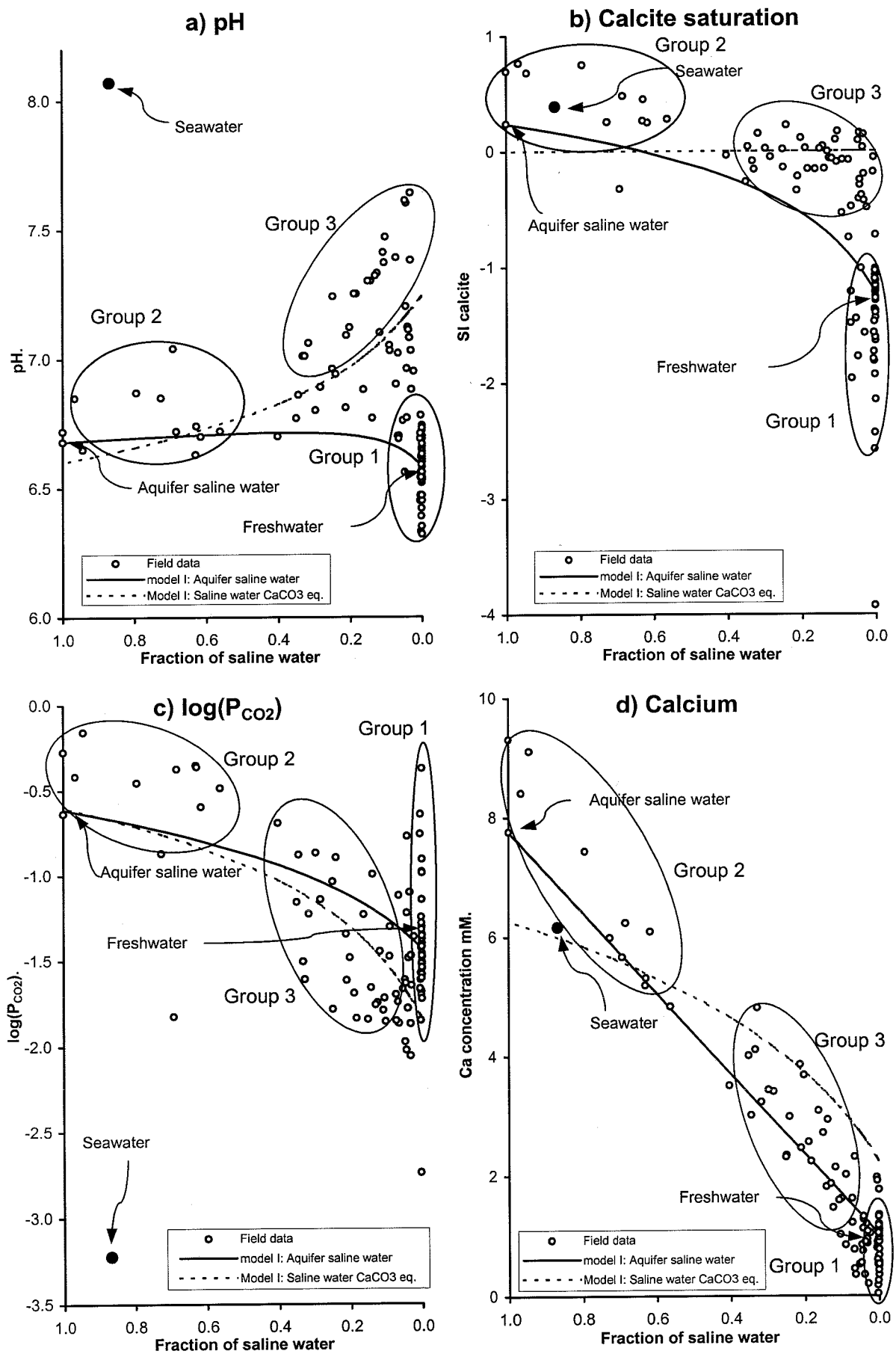

Figure 7.2: Mixing curves as a function of seawater fraction for: a) pH, b) Calcite saturation index, c) log(P_{CO2}) and d) Calcium concentration (mM). Symbols are field data Aug. 1999. Solid lines are for mixtures of the aquifer saline end-member (St1, Aug. 1999) and freshwater (St112, Aug. 1999. Broken lines are for the mixtures equilibrated with calcite (SI = 0).

probably caused by redistribution of metal complexes increasing the activity of the free Ca^{2+} ion in the mixed solution.

When these mixed water compositions are equilibrated with calcite to an SI of zero the effects (shown as broken lines in Fig. 7.1) are most pronounced for the mixing-curves of surface seawater and freshwater, because of the larger field of subsaturation for this mixing curve (grey line Fig. 7.1b) compared to the mixing curve of aquifer saline water and freshwater (black line Fig. 7.1b). For subsaturated waters calcite dissolves according to:

$$CaCO_3 + CO_2 + H_2O \leftrightarrow Ca^{2+} + 2HCO_3^- \qquad (7.5)$$

For the equilibrated surface seawater the pH of the mixing-curve increases to more than 7.3, the $\log(P_{CO2})$ decreases by more than half a log unit and the calcium (Fig. 7.1d) increases due to dissolution from 0 mM at 100% seawater to a little more than 1 mM at 100% freshwater. For the mixtures with the aquifer saline end-member, equilibration with calcite gives more moderate changes, except towards 100 % freshwater. For fractions of seawater larger than 65%, calcite is precipitated, decreasing the pH, increasing the $\log(P_{CO2})$ (barely visible) and decreasing the calcium concentration by almost 2 mM.

In Figure 7.2a-d) the mixing curves of the aquifer saline end-member and freshwater are plotted together with the field data of August 1999, because these mixing curves generally show a better agreement with the field data. The better fit implies that the water compositions in the transect is more likely a result of mixing aquifer saline water and fresh groundwater rather than mixing surface seawater and fresh groundwater.

The field data roughly fall into three groups most clearly seen from the pH and the calcite saturation index (Fig. 7.2 a and b). A group of pure freshwater samples (group 1) has a low pH of about 6.5 (Fig. 7.2a). A second group (group 2) with a chloride content corresponding to 50% to 100% seawater, has a pH near or slightly above the line for the mix pH. The third group has a low to intermediate seawater fraction (3% to 40%) and plots around the pH mixing line with calcite equilibrium. The observed calcite saturation index (Fig. 7.2b) shows the group 3 samples to be near equilibrium with calcite. This observed equilibrium for calcite seawater fractions from 3% to 40%

is most probably obtained by calcite dissolution, given by the agreement between the field data and the mixing curves for equilibrium with calcite. It is confirmed by the increase in pH (Fig. 7.2a), the decrease in P_{CO2} (Fig. 7.2c) and the increase in Ca^{2+} (Fig. 7.2d) when calcite equilibrium is imposed. Spatially the range of seawater fractions from 3% to 40% corresponds to the fresher part of the mixing zone in Figure 6.3b.

For some samples in group 3 the pH is higher than expected from the mixing curve with calcite equilibrium, this could indicate that other processes are involved. Ion exchange processes may be involved where calcium released from calcite dissolution goes on the exchanger allowing additional calcite dissolution with an accompanying additional pH increase. This is further supported by the field Ca^{2+}-values of group 3 generally being below the mixing curve for equilibrium with calcite (Fig 7.2d). Alternatively, the mixing of freshwater and surface seawater (Fig. 7.1a) with calcite equilibrium imposed better fits these higher pH values pointing towards mixing of surface seawater and freshwater. This could be a previous inundation event with surface seawater.

For the samples of group 2 with high fractions of seawater (> 50%) other processes also seem to be involved indicated by the high P_{CO2} of the field data (Fig. 7.2c). Here the principal explanation for the deviation in P_{CO2} is the production of inorganic carbon by organic matter degradation by sulfate reduction and methanogenesis as described in section 7.2. Going from the aquifer saline mixing curve towards equilibrium with calcite would in this salinity range imply the precipitation of calcite. However the field data does not suggest this to take place as indicated by the supersaturation of 0.2 to 0.7 for calcite (Fig. 7.2b). Presumably this supersaturation is due to inhibition of crystal growth by Mg^{2+}, phosphate, or DOC (dissolved organic carbon) (Berner, 1975, Walter and Hanor, 1979, Berner et al., 1978) or a combination of these.

Some of the freshwater samples in group 3 have a high P_{CO2} (Fig. 7.2c) probably originating from processes in the root zone. This CO_2 has not yet been consumed by calcite dissolution in the upper calcite depleted part of the aquifer

In summary, the variations of pH, SI calcite, CO_2 and Ca^{2+} in the transect can to a large degree be explained by mixing between freshwater and a saline aquifer water composition with a moderate pH and a high content of dissolved inorganic carbon (exemplified by St1). A substantial part of the

reactions (such as organic matter degradation) can therefore in principle be taking place in the seafloor or in the offshore part of the aquifer.

The theory of mixing induced calcite dissolution has been used to explain cave formation and increased porosity in the mixing zone of coastal carbonate aquifers (Back et al., 1979, Back et al., 1986, Smart et al., 1988, Sanford and Konikow, 1989, Jankowski and Jacobson, 1991). Sanford and Konikow (1989) modeled a sea-freshwater mixing zone in a carbonate aquifer and calculated the porosity changes due to mixing dissolution of calcite. They found that the change in porosity was largest at the top and bottom of the fresher part of their mixing zone and for a seawater fraction of less than 0.5. From the analysis above dissolution of calcite at Skansehage also seem to be occurring in the fresher part of the aquifer. An increased porosity in the Skansehage aquifer due to mixing dissolution has not been documented. The dissolution of sedimentary carbonate could possible affect the permeability. Such an effect has not been documented either, and the effect is probably limited due to the unconsolidated and un-cemented nature of the aquifer sediment.

Finally possible effects of ion exchange and redox-processes occurring within the transect should by no means be rejected on the basis of the analysis carried out above.

7.4 Chemical processes during displacement of freshwater-seawater interfaces

In conjunction the physical and the chemical data indicate that transport of salty water or seawater may takes place in the aquifer by three different processes: 1) Irregular reoccurring inundation events with surface seawater, which subsequently migrate down in the aquifer and mix with the freshwater, 2) Seaward flushing of the brackish water resulting from the inundations and 3) Slow intrusion or cycling of seawater within the saline wedge and the mixing zone. In this section the main emphasis is placed on the chemical aspects related to the seaward flushing of the brackish water.

7.4.1 Flushing of brackish water

In section 6.3 it was shown that the particular recorded inundation event had a sufficient seawater volume to percolate by density driven flow all the way through to the bottom of the aquifer leaving

a tail of diluted seawater or brackish water affecting the full depth of the aquifer. This brackish water must subsequently be flushed from the aquifer by the discharging freshwater.

The seaward flushing of the brackish water is believed to give rise to a cation distribution pattern resembling that of refreshening with a chromatographic separation of the cations. The cation with the lowest affinity to the exchanger will be displaced first. Refeshening patterns have been observed on all scales from lab-scale to aquifers10 to 100 km in length (Chapelle and Knobel, 1983; Edmunds and Walton 1983, Beekman, 1991, Stuyfzand, 1993, Melo et al., 1999). A particularly fine example of ion exchange processes during freshwater displacing seawater is the Aquia aquifer in Maryland, USA (Chapelle and Knobel, 1983, Appelo, 1994a). In the Aquia aquifer a distinct separation of the cations Ca^{2+}, Mg^{2+}, K^{+} and Na^{+} is observed. The cation separation, during seawater being displaced by freshwater, becomes particularly clear for two reasons, 1) the exchange fronts are sharpening fronts (i.e. a cation with high affinity displacing a cation with lower affinity) and 2) the low ionic strength of the displacing solution (i.e. low total amount of cation equivalents) separate the exchange fronts from the salinity front (the decrease in Cl^{-}) (Appelo, 1996).

The effect of salinity changes, where the exchanger with a seawater composition dictates the water composition after a decrease in salinity (see section 3.1) can clearly be seen when freshwater displaces seawater. Because of the low total cation equivalents of the displacing solution compared with the often much higher total pool on the exchange complex, the effect will show up as an extended plateau with low concentrations of the divalent cations (Appelo, 1996). This has been observed in the field in injection experiments (Valocchi et al., 1981a,b, and Bjerg et al., 1993). It is especially clear in the injection experiment described by Valocchi et al. (1981a,b) where the concentrations of Ca^{2+} and Mg^{2+} after the decrease in salinity drops well below their freshwater levels.

In the freshwater zone and the fresher part of the mixing zone (20 m to 80 m from the coast) the Δm_i-plots for the seawater-derived cations Mg^{2+}, Na^{+} and K^{+} show a small but general enrichment (Fig. 6.11). These cations show a chromatographic sequence with zones partly separated from each other. Calcium is dominating in the freshwater (further inland than 80 m), further towards the coast follows magnesium and finally sodium and potassium. In the same zone from 40 to 80 m negative values for Δm_{Ca} are found. Lowest values of Δm_{Ca} correspond to the zone with elevated Δm_{Mg}. The

order of the sequence is somewhat similar to that observed during a refreshening of an aquifer. The sequence observed is normally Ca^{2+}, Mg^{2+}, K^{+}, Na^{+} following their affinity to the exchanger, as it has been observed in e.g. the Aquia aquifer (Chapelle and Knobel, 1983 and Appelo, 1994a). In the Skansehage aquifer the refreshening like pattern could be explained by the flushing of brackish water containing seawater derived cations brought in to the aquifer by a former seawater inundation event (see section 6.3). The calcium of the freshwater is thus displacing magnesium, which in turn displaces sodium (and potassium) further down stream towards the coast. The exchange reactions of Ca^{2+} for Mg^{2+} and Mg^{2+} for Na^{+} can be written as:

$$Ca^{2+} + Mg - X_2 \leftrightarrow Mg^{2+} + Ca - X_2 \qquad (7.6)$$

$$\tfrac{1}{2} Mg^{2+} + Na - X \leftrightarrow Na^{+} + \tfrac{1}{2} Mg - X_2 \qquad (7.7)$$

Where (7.6) and (7.7) conforms to the Gaines-Thomas convention (Gaines and Thomas, 1953).

However, in the data from the transect the position of the peak in K^{+} does not fit the sequence described above. Here K^{+} is found simultaneous with, or even a little in front of, the peak in Na^{+}. According to the normal sequence it should be found in between Na^{+} and Mg^{2+}. This may suggest a somewhat lower affinity of K^{+} toward the cation exchanger. The fact that organic matter dominates the cation exchanger may support this, because an organic exchanger may not have the same high specific affinity for K^{+} as some clay minerals e.g. illite (Appelo, 1996). An explanation for the seemingly abnormal behaviour of K^{+} could be that the peaks in Na^{+} and K^{+} are mainly caused by the decrease in salinity favouring divalent over monovalent cations on the exchanger.

The new input of seawater into the aquifer will also affect the redox-conditions by introducing oxic surface seawater, which due to the fast density percolation will penetrate deeper into the aquifer than oxygen is able to by normal infiltration. The primary effect is, however, the introduction of large amounts of sulfate, for a period of time shifting the redox-conditions from methanogenic to sulfate reducing during the flushing.

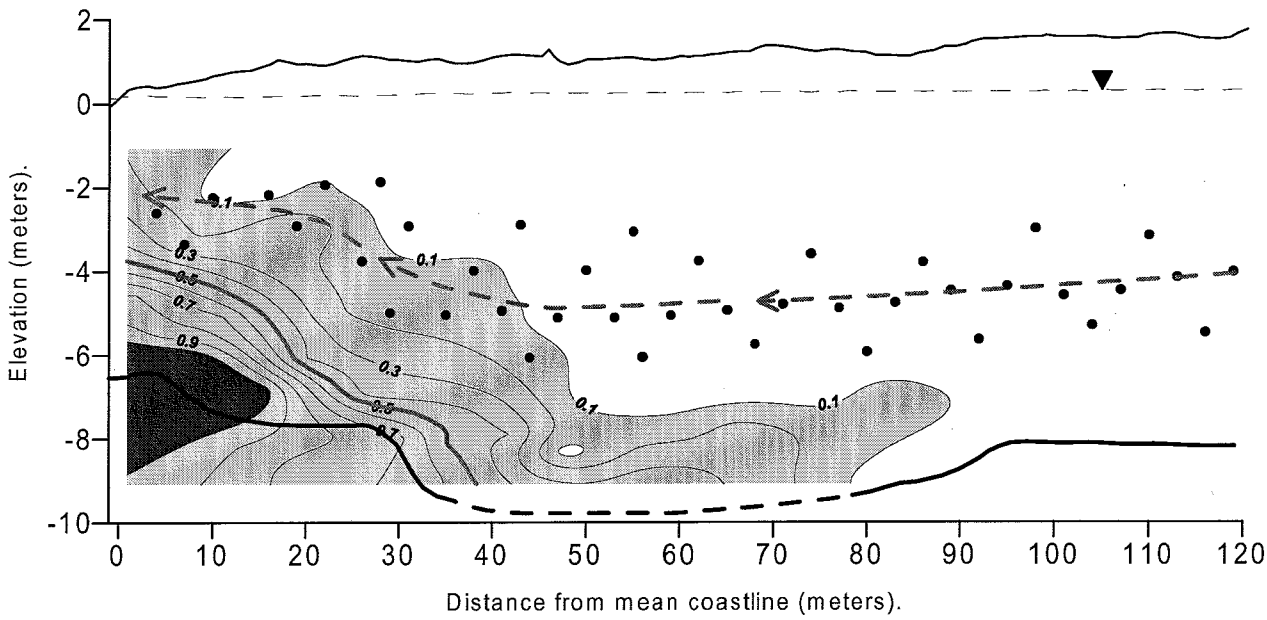

Figure 7.3: Approximate flow path for the modelling of freshwater flushing percolated inundation seawater. Dots are sampling points for observed water compositions (Aug, 1999) for comparison. In the background, seawater fractions of August 1999 are contoured.

7.4.2 Modelling seaward flushing of saltwater

The flushing of brackish water by freshwater has been modelled conceptually with PHREEQC where a column containing seawater is flushed with freshwater. Model transport simulations with either redox-processes, or ion exchange reactions were carried out to see the isolated effects of these two types of chemical processes. In subsequent model simulations calcite equilibrium was superimposed on these model simulations. Then a model comprising the combined effects of redox-processes and ion exchange was set up, and finally this was extended by imposing calcite equilibrium, combining all three processes. By this approach the relative importance of the different processes can be determined and the coupling of the processes unravelled. The models conducted are summarised in Table 7.6.

Table 7.6: Overview of processes modelled with PHREEQC for simulating brackish-/seawater being displaced by freshwater.

	Processes modelled	Calcite equilibrium
Model I a	Ion exchange	-
Model I b	Ion exchange	+
Model II a	Redox-reactions	-
Model II b	Redox-reactions	+
Model III a	Ion exchange & redox-reactions	-
Model III b	Ion exchange & redox-reactions	+

A column of 120 m, divided into 30 cells of 4 meter in length, was used. The model results are to be compared with a flow path beginning at 120 m from the coast, in the elevation interval from –3 to –6 m, running towards the coast and curving slightly upwards at 40 m, as depicted in Figure 7.3, to discharge at the coast at an elevation of about –2 m. The water compositions employed were: Surface seawater with an average composition as given in Table 6.1 and a freshwater which is an average of 4 freshwater samples from the elevation interval of –3 to –6 m (August 1999, St101, St107, St113 and St119). Surface seawater is used because of the assumed inundation origin. In these simulations a dispersivity of 0.4 m was employed, which is in the range of dispersivities

determined from EC-breakthrough curves from the intrusion data (Christensen, unpublished data). A groundwater flow velocity of 50 m/yr was used and a total modelling time of 2 years displaces the conservative chloride front to until 20 m from the coast.
A constant CEC of 0.5 meq/l (Fig. 6.12) was used in the model, since no major trends in CEC could be disclosed. The CEC was recalculated to $2.46 \cdot 10^{-2}$ mol/l pore water using an average porosity of 0.35.

The reactivity of organic matter in the sediment is assumed to control the rate of organic matter oxidation/degradation, in agreement with the partial equilibrium model (Postma and Jakobsen, 1996) and is given by one single rate expression incorporated in the PHREEQC input. Only sulfate reduction and methanogenesis are considered and mineralization of organic carbon by both processes will occur at the same rate. In the model the processes do not occur concurrently, but according to the redox-conditions (in this case sulfate availability). The rate expression used is given as:

$$m_{\Delta t} = k \cdot m_0 \cdot \left(m / m_0 \right)^{2/3} \qquad (7.8)$$

Where k is the rate constant in mol/s. $m_{\Delta t}$ is the amount of organic matter in mol reacting/released to the solution with in a time step of Δt in seconds. m_0 is the initial mass of organic matter in moles at the start of the simulation and m is the mass remaining at the current time step. The expression $(m/m_0)^{2/3}$ reflects that the reactivity of organic matter should decrease with time as it is used up. Boudreau and Ruddick (1991) show that the reactivity of organic matter in sediment can be described using a gamma distribution function. Postma (1993) shows that this is equal to a power function of the form in equation (7.8). The exponent of 2/3 reflects that the organic matter, lacking a better description, is assumed a spherical shape. The initial mass of organic matter (m_0) is set to 0.2 moles/l in the models, the average of the sand samples in Fig. 6.4. Modeling times are relatively short, so only a small fraction of the original organic matter is used during the simulations and the rate is practically constant over time ($(m/m_0)^{2/3} \approx 1$).

At Skansehage the rates of sulfate reduction and of methanogenesis were determined by in-situ incubation techniques utilising radiotracer methods (Nyvang, unpublished results). The rates of the

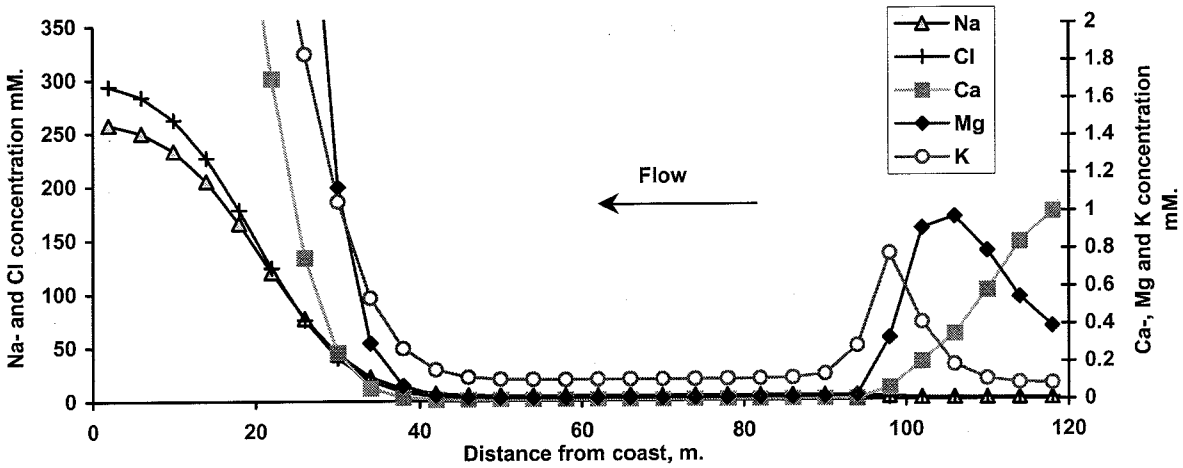

Figure 7.4: Distribution of Na^+, Cl^-, Ca^{2+}, Mg^{2+}, and K^+ (mM). Modelled PHREEQC results of ion exchange reactions with a CEC of 24.6 meq/l pore water, in a column, initially containing seawater, flushed with freshwater from 120 m to 20 m from the coast (model Ia Table 7.6).

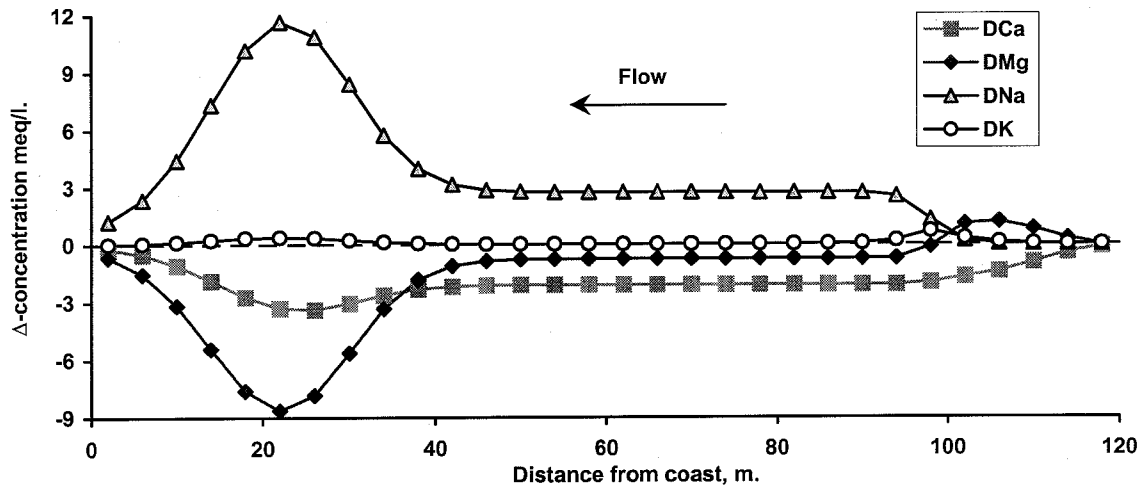

Figure 7.5: Concentrations changes relative to conservative mixing of seawater and freshwater (Δm_i-values) for Na^+, Ca^{2+}, Mg^{2+}, and K^+ (meq/l). Modelled PHREEQC results of ion exchange reactions (CEC = 24.6 meq/l pore water) in a column, initially containing seawater, flushed with freshwater from 120 m to 20 m from the coast (model Ia Table 7.6).

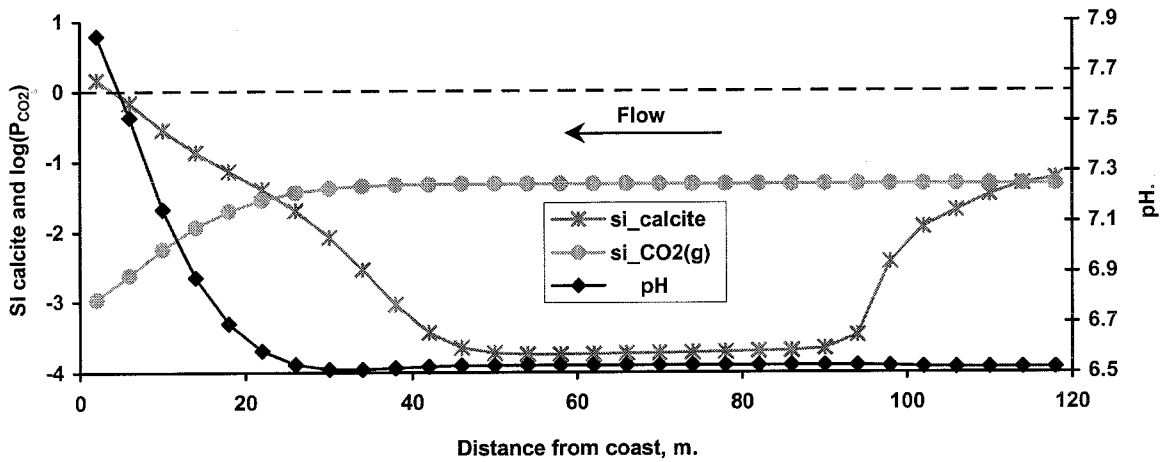

Figure 7.6: Calculated pH, calcite saturation index and log(P_{CO2}). Modelled PHREEQC results of ion exchange reactions (CEC = 24.6 meq/l pore water) in a column, initially containing seawater, flushed with freshwater from 120 m to 20 m from the coast (model Ia Table 7.6).

two redox-processes were found to be comparable in size but varying considerably in space. Average values in the order of 1 mM SO_4^{2-}/yr and 1 mM CH_4/yr were found (Nyvang, unpublished results). These rates are equivalent to an organic matter consumption of 2 mM CH_2O/yr as seen from the stoichiometry of equations (6.4) and (6.5). This value of 2 mM CH_2O/y is used as the initial rate constant (k) in the equation (7.8).

Results of flushing model: Ion exchange

Figure 7.4 shows the effects on the cation distribution of freshwater displacing seawater involving only ion exchange reactions (model Ia). The conservative front (Cl^-) has reached a position 20 m from the coast, defined by the model set-up. All the cations are also seen to decrease from zero to 40 m. Behind the front from 40 to 95 m is a plateau of constant concentrations. Here the concentrations of Ca^{2+} and Mg^{2+} are lower than found in both the seawater and the displacing freshwater. The plateau of low Ca^{2+} and Mg^{2+} concentrations is due to the decrease in salinity, which gives the dilution effect observed in the field studies by Valocchi et al. (1981a) and Bjerg et al. (1993) and described by Appelo (1996). The exchanger having a composition given by the seawater dictates the solution composition in this zone with low Ca^{2+} and Mg^{2+} concentrations and increased concentrations of Na^+ and K^+. In the zone from 95 to 120 m the marine cations are being displaced from the exchanger by Ca^{2+} in the inflowing freshwater giving rise to a chromatographic sequence (right side of Fig. 7.4). In this sequence (seen from the left) first Na^+ is being displaced by K^+ and Mg^{2+}. Then K^+ is displaced by Mg^{2+}. And finally Ca^{2+} displaces Mg^{2+}. This is in accordance with the sequence observed in the Aquia aquifer (Chapelle and Knobel, 1983, Appelo, 1994a).

The effects of the exchange are more clearly seen if the depletion or enrichment of the cations (compared to a conservative mix between freshwater and seawater, as calculated by equations (6.1) to (6.3)) is plotted (Fig. 7.5). From this Figure it is clear that there is less Ca^{2+} along the whole column, than predicted from a model without ion exchange. Close to the salinity front the Ca^{2+}-deficit is caused by the salinity decrease. In the plateau zone the Ca^{2+}-deficit is due to the exchanger having a seawater composition and dictating the solution composition. Further inland Ca^{2+} displaces the remaining seawater cations on the exchanger. The same pattern is seen for Mg^{2+}, but Δm_{Mg} is positive between 95 m and 120 m were Ca^{2+} is displacing Mg^{2+}. The monovalent cations have positive Δm_i-values in the whole model domain, close to the coast again due to the decreasing salinity forcing them of the exchanger, in the plateau zone due to the exchanger composition

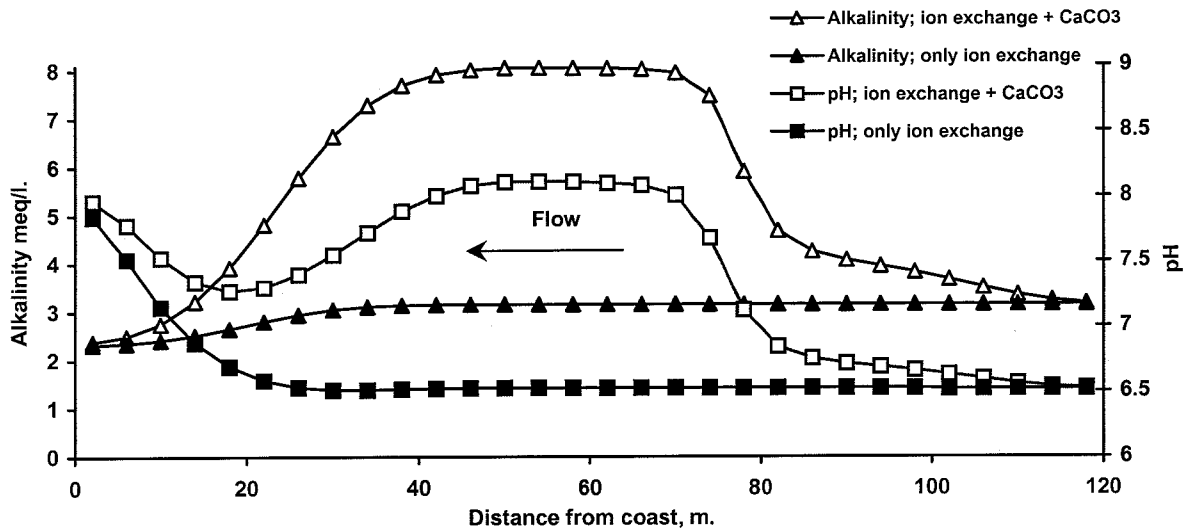

Figure 7.7: pH and alkalinity (meq/l) with and without calcite equilibrium ($SI_{calcite}$ = -1.2). Modelled PHREEQC results of ion exchange reactions (CEC = 24.6 meq/l pore water) in a column, initially containing seawater, flushed with freshwater from 120 m to 20 m from the coast (model Ia and Ib Table 7.6).

dictating the solution composition, and finally inland due to the exchanger attaining a composition in equilibrium with the displacing freshwater.

The loss of aqueous Ca^{2+} caused by the cation exchange lowers the calcite saturation index from an SI in the freshwater of –1.2 to a low SI of –3.7, as seen in Figure 7.6. Clearly this could lead to enhanced calcite dissolution provided that calcite is present. If the dispersivity coefficient is increased it will diminish the zone of subsaturation since dispersion will smear out the ion exchange reactions and bring Ca^{2+} further downstream in the column and thereby increasing the SI.

Calcite equilibrium is then imposed on the model allowing calcite to dissolve if the SI drops below the value observed in the freshwater (SI = -1.2). This will probably result in a conservative estimate of the extent of calcite dissolution. In this model calcite is not allowed to precipitate. The effects of the calcite dissolution in the model can most clearly be seen by the change in pH and the alkalinity (Fig. 7.7), because the changes in the Ca^{2+} concentration (Δm_{Ca}) are partly obscured by the large changes due to the ion exchange reactions. Due to the calcite dissolution, the pH increases from 6.5 in the freshwater to a value of about 8.2 and alkalinity increases from 3.1 to 8 meq/l, while the $\log(P_{CO2})$ is reduced from –1.3 to –2.5. In the transect, zones of elevated pH (7.6) and alkalinity (> 10 meq/l) are seen from around 50 m and towards the coast. About 2.5 mM of calcite is being dissolved in the model as a consequence of the coupling of ion exchange and calcite equilibrium during freshwater displacing seawater. This dissolution will be enhanced with a larger CEC and by allowing for a higher equilibrium SI for calcite.

Lefèvre et al. (1993) demonstrated the dynamic coupling of ion exchange reactions and carbonate mineral equilibrium by the migration of strontium in a column experiment, where both ion exchange and the degree of precipitation of Strontianite ($SrCO_3$) control the retardation of strontium. This type of coupling is apparently more difficult to discern in the field. Although calcite reactions where not described in the field experiment by Valocchi et al. (1981a), Appelo (1996) speculated on the effects of calcite reactions in this particular experiment. In this experiment freshwater was injected into a brackish aquifer giving a cation distribution pattern similar to that of Fig. 7.4. By including calcite dissolution triggered by the low Ca^{2+} concentration caused by the salinity effect Appelo (1996) showed that including calcite dissolution would accelerate the exchange sequence and equilibrium between the exchanger and the injected solution will be reached

faster. Dissolution of calcite in relation to ion exchange processes where possibly observed in the field experiment of Bjerg and Christensen (1993), where a saline pulse was injected into a fresh aquifer. They observed a small increase in the pH and the alkalinity occurring behind the pulse simultaneously with a decreasing saturation index for calcite due to the Ca^{2+} decreasing below the background level as dictated by the exchanger composition. This behavior of the involved species was attributed to calcite dissolution. However, the effects of calcite dissolution were small compared to the effects of the ion exchange reactions. On a regional scale the combination of cation exchange and calcite dissolution in relation to flushing of sea- or brackish water is believed to cause the occurrence of water enriched in Na^+ and HCO_3^- (Back, 1966, Chapelle, 1983, Appelo and Geirnaert, 1991, Melo et al., 1999, Logan et al., 1999 and Xue et al., 2000). The enrichment of HCO_3^- and the increase of Na^+ at the expense of Ca^{2+} strongly suggest the involvement of calcite dissolution.

Results of flushing model: Redox-processes

At the Skansehage field site sulfate depletion relative to seawater is substantial in the mixing zone (Fig. 6.5b), presumably due reduction by organic matter. Many investigators have found depletion of sulfate in coastal mixing zones with the most frequent explanation being sulfate reduction Nadler et al. (1980), Magaritz and Luzier (1985), Hahn (1991), Barker et al. (1998) and Logan et al. (1999). Many of these studies were however, in coastal aquifer systems affected by recent seawater intrusion. Thorough studies of redox-processes in coastal mixing zones, not affected by seawater intrusion caused by human activities, are comparatively fewer (Magaritz and Luzier 1985, Smart et al., 1988, Stoessell et al., 1993, Stuyfzand, 1993). The studies by Smart et al. (1988) and Stoessell et al. (1993) are from sinkholes in carbonate aquifers, but the study by Margaritz and Luzier (1985) of the Coos Bay aquifer in California seems comparable to the Skansehage aquifer. They studied the geochemical processes in a natural occurring interface in a sandy aquifer. They also observed depletion of sulfate and enrichment of HCO_3^- in the mixing zone, which they attributed to sulfate reduction. They did not give any estimate of the sulfate reduction rate, unfortunately. However, their system differs from the Skansehage system in that they observed higher concentrations of ferrous iron (Fe^{2+}) up to 40-50 μM in their freshwater zone and up to a maximum of 500 μM in their mixing zone indicating that the dominating redox-process in the freshwater is reduction of iron oxides. Also they documented the formation of cement coatings of siderite ($FeCO_3$) and pyrite in the mixing zone (Margaritz and Luzier, 1985).

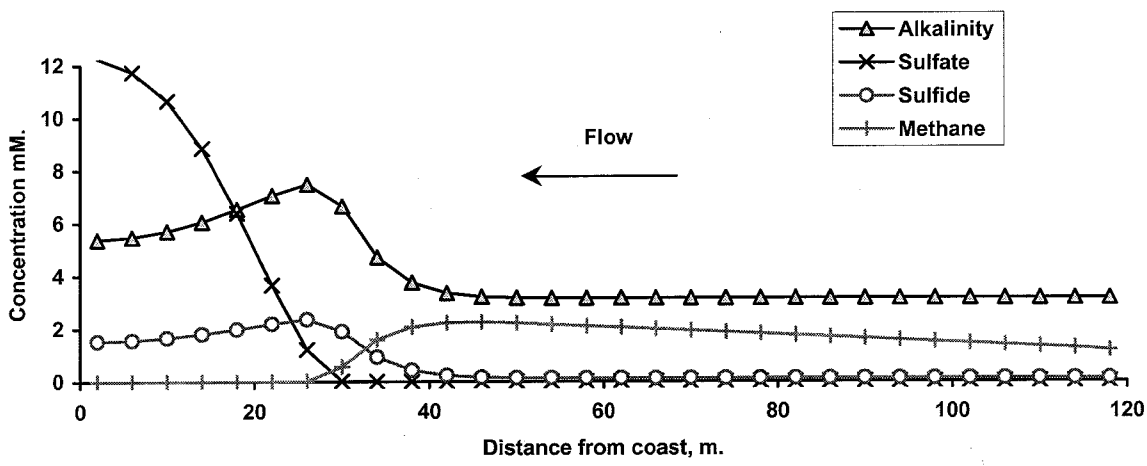

Figure 7.8: Distribution of alkalinity (meq/l), sulfate, sulfide and methane (mM). Modelled PHREEQC results of oxidation of organic matter with a rate of 2 mM CH_2O/yr, in a column, initially containing seawater, flushed with freshwater from 120 m to 20 m from the coast. The groundwater flow rate is 50 m/yr (model IIa, Table 7.6).

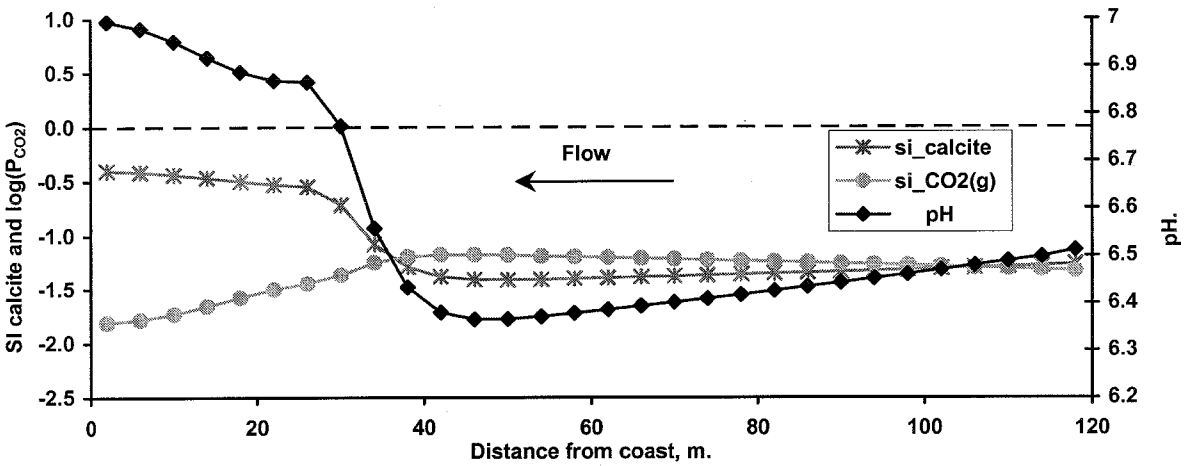

Figure 7.9: Calculated pH, SI calcite and log(P_{CO2}). Modelled PHREEQC results from the oxidation of organic matter (rate = 2 mM CH_2O/yr) in a column, initially containing seawater, flushed with freshwater from 120 m to 20 m from the coast (groundwater flow rate 50 m/yr) (model IIa, Table 7.6).

In contrast the dominating redox-process in the freshwater, at Skansehage, is methanogenesis leading to CH_4 concentrations up to 2 mM. Towards the coast and into the mixing zone the CH_4 concentrations decrease and disappear altogether when sulfate is present in higher concentrations. This indicates either a smaller CH_4 production in the presence of sulfate due to bacterial competition for substrate or perhaps some mechanism of CH_4 consumption. The reciprocal relationship between sulfate and methane is, however, not complete since some samples near the coast contain both methane and sulfate, which is probably due to the fact that methane is quite stable once formed (Appelo and Postma, 2001 in prep.) and that it by advective or diffusive transport has been mixed into the water containing sulfate. However, a number of studies (Iversen and Jørgensen, 1985, Hoehler et al. 1994) state that methane can readily be re-oxidised by sulfate in anoxic marine sediments (Hoehler et al., 1994), but has also been observed in fresh- or brackish environments (Whiticar, 1999). So the coexistence of methane and sulfate in the samples could be a consequence of sluggish reaction kinetics or perhaps a consequence of the sampling, where waters from adjacent sulfate reducing and methanogenic strata (or even sub grain- scale micro niches) are mixing in the monitoring well during sampling.

A simulation for seawater displaced by freshwater including only redox-reactions is shown in Fig. 7.8. In the seawater and on the seawater/freshwater front sulfate is being reduced producing both sulfide and inorganic carbon. In the freshwater methane formation is taking place producing methane, CO_2 and acidity. The effects on the carbonate system are less clear-cut than for ion exchange as reflected by the pH and the SI for calcite (Fig. 7.9). The pH and SI for calcite is decreasing in the freshwater due to the CO_2 production related to the methane formation. In the sulfate containing water from 10 to 30 m the sulfate reduction produces alkalinity and increases the SI for calcite as compared to a non-reactive model. But in the seaward portion (0 to 10 m) supersaturation for calcite is not attained and the pH is lower than for a model without reactions. This is partly because the sulfate reduction will have either an acidifying or bicarbonate producing effect depending on the pH of the solution. At pH above 6.8, sulfate reduction will have an acidifying effect because the formed H_2S is a weak acid. Below a pH of 6.8 the HCO_3^- will act as a base. This explains how the sulfate reduction process can both enhance and counteract calcite dissolution depending on the pH. Similar effects were observed by Stoessell et al. (1993). The increase in alkalinity and sulfide (Fig. 7.8) seen just behind the front (20 to 40 m) is caused by the dispersive mixing bringing sulfate containing and methane containing waters into contact with each

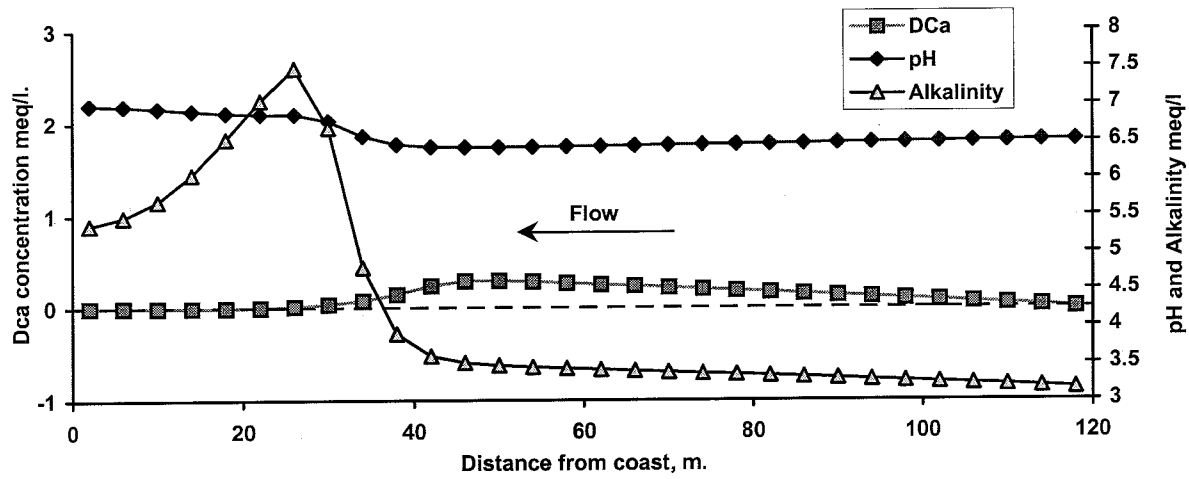

Figure 7.10: pH, alkalinity (meq/l) and Ca^{2+} concentration change (meq/l) relative to conservative mixing of seawater and freshwater (Δm_i-value). Modelled PHREEQC results of organic matter oxidation (rate = 2 mM CH_2O/yr) and calcite equilibrium ($SI_{calcite}$ = -1.2), in a column, initially containing seawater, flushed with freshwater from 120 m to 20 m from the coast (model IIb, Table 7.6).

other leading to oxidation of the methane by the sulfate according to equation (7.4). This leads to additional alkalinity because two moles of alkalinity are produced for each mole of sulfate being reduced and each mol of methane being oxidized. In the model the reaction between sulfate and methane is not kinetically controlled, as it would be in nature (Hoehler et al., 1994).

The model with redox-processes is re-run with imposed calcite equilibrium of SI = -1.2 and only allowing for dissolution. Again this is a conservative estimate. In figure 7.10 the resulting pH, alkalinity and increase in Ca^{2+} concentration relative to a conservative mix is shown. In the freshwater from 40 to 120 m the decreasing pH (and increasing P_{CO2}) associated with the methane formation leads to a minor dissolution of calcite of about 0.15 mM (Fig. 7.10), much less dramatic than in the ion exchange case (Fig. 7.7). However, the production of alkalinity by sulfate reduction and the high Ca^{2+} concentration in the seawater do increase the calcite saturation index on the sea-/freshwater front (from 10 to 40 m) potentially leading towards calcite saturation.

The production of CO_2 by organic matter degradation as the driving force of calcite dissolution is a well established phenomenon in groundwater geochemistry (Appelo and Postma, 1993). In the mixing zones of coastal carbonate aquifers redox-reactions involving sulfate has also been believed to lead to calcite dissolution in addition to the calcite dissolution caused by mixing of seawater and freshwater (Smart et al., 1988, Stoessell et al, 1993). Stoessell et al., (1993) attributed some of the calcite dissolution in the halocline of a carbonate aquifer in the Yucatan peninsula to the acid production associated with minor to moderate sulfate reduction. They calculated how even small amounts of sulfate reduction in the saline part of a mixing zone will lead to substantial subsaturation for calcite of saltwater previously supersaturated for calcite. However, in both the study by Smart et al., (1988) and Stoessell et al, (1993) the major part of the calcite dissolution was linked to a process of re-oxidation of the sulfide to sulfuric acid. This re-oxidation was thought to be instigated by the upward migration of the H_2S to oxic zones in the upper part of the halocline. Such a re-oxidation is not included in the model of Fig. 7.8, nor is it relevant for the Skansehage field site, because of the anoxic state of the overlying freshwater.

Results of flushing model: combing ion exchange and redox-processes

A model combining ion exchange and redox-reactions was run. Without including calcite equilibrium there are no parameters coupling the processes of ion exchange and redox-reactions,

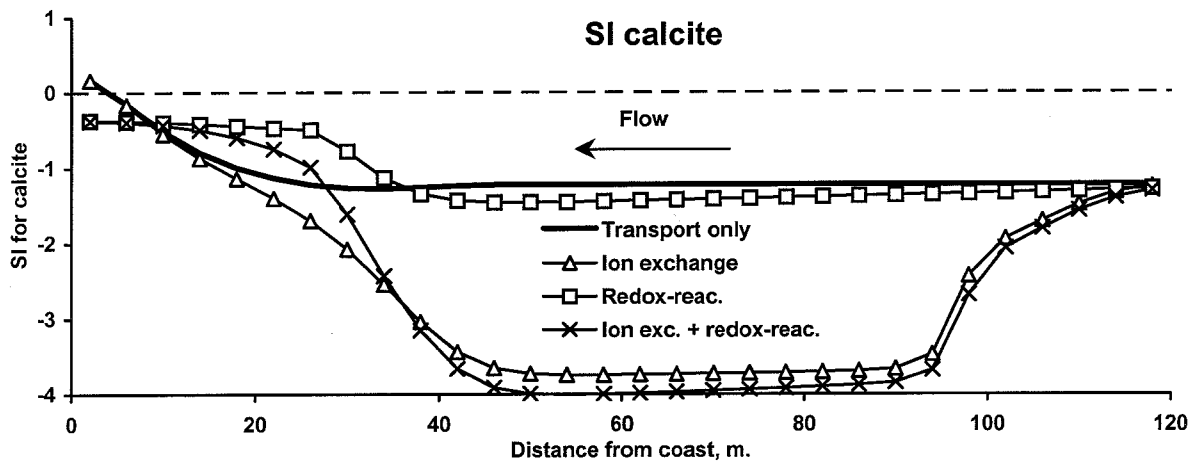

Figure 7.11: Calcite saturation index calculated for the four PHREEQC scenarios of freshwater displacing seawater. The scenarios are: Non- reactive transport, ion exchange (CEC = 24.6 mmol/l), redox-reactions (2 mM CH_2O/yr) and a combination of ion exchange and redox-reactions.

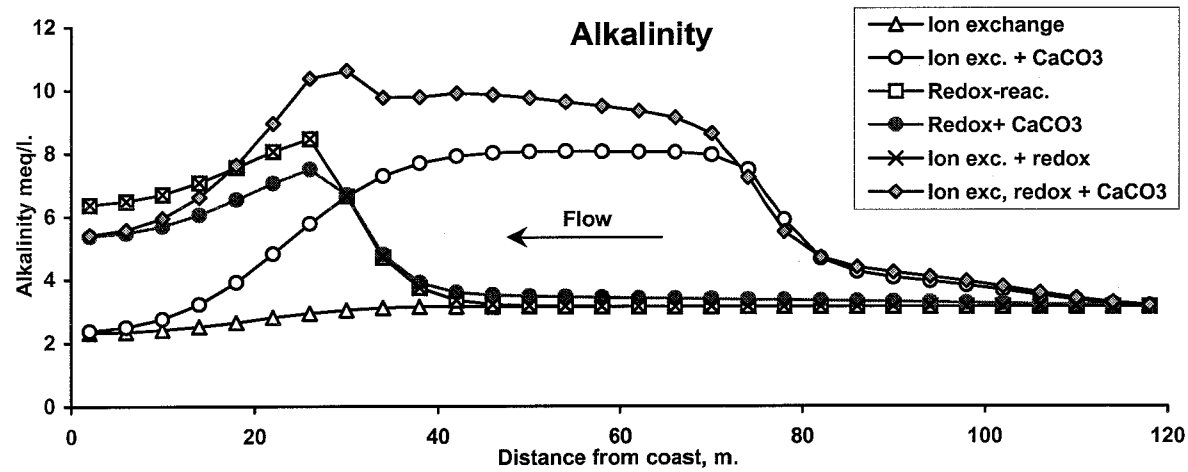

Figure 7.12: Alkalinity (meq/l) for six PHREEQC scenarios of freshwater displacing seawater in a column from 120 m to 20 m from the coast (groundwater flow rate 50 m/yr). The scenarios are: Ion exchange (CEC = 24.6 mmol/l), redox-reactions (2 mM CH_2O/yr) and a combination of ion exchange and redox-reactions, all carried out with and without imposed calcite equilibrium.

except for minor a release of ammonium from the organic matter, which will react with the cation exchanger and perhaps minor changes in the formation of complexes. Therefore the results will largely be identical to Figs. 7.4 and 7.8 respectively, with the cation distribution controlled by the ion exchange and the redox-species controlled by the organic matter degradation. Both processes however, do have an impact on the calculated SI for calcite as previously explained and the combined effect on the SI can be seen in Fig. 7.11, which also includes the SI calculations from the previous runs. With the organic carbon oxidation rate of 2 mmol CH_2O/yr and the CEC of 0.5 meq/100g used in the PHREEQC simulations, the effects of redox- and ion exchange reactions on the SI for calcite are clearly dominated by the ion exchange reactions. From the sea-/freshwater front and landward (35 to 120 m) the methane formation lowers the SI only slightly. On the seaward side of the sea-/freshwater front (10 to 35 m) the SI is however increased due to the sulfate reduction and methane oxidation and resulting in a production of alkalinity.

Calcite equilibrium with an SI = -1.2 (no precipitation allowed) is included in the model with both ion exchange and redox-reactions. Figure 7.12 show the resulting alkalinity together with the alkalinity of the previous models. It can be seen from the alkalinity in Figure 7.12 that the influence of the redox-reactions will increase the amount of calcite being dissolved by less than 1 mM on the landward side (40 to 80 m) of the sea-/freshwater front compared to the simulations with only ion exchange and calcite equilibrium. The pH increase of coupling all three processes will be smaller than pH for the simulation with only ion exchange and calcite equilibrium (Fig. 7.13), due to the redox-reactions. The coupled effects are spatially separated and calcite precipitation could theoretically occur between the sea-freshwater front and the coast as a result of the sulfate reduction, whereas dissolution will take place behind the front, due to a combined effect of cation exchange and methanogenesis.

In the light of the modelling above where a substantial quantity of calcite is dissolved, the low content of sedimentary inorganic carbon, 0 and 14 mmol IC/kg, measured in sediment samples in the transect (Fig. 6.18) is perhaps not surprising despite the marine origin of the aquifer material and the young age of the aquifer. Enhanced calcite dissolution due to repetitive seaward flushing of brackish water brought into the aquifer by inundation events seems to be an effective mechanism explaining the calcite depletion.

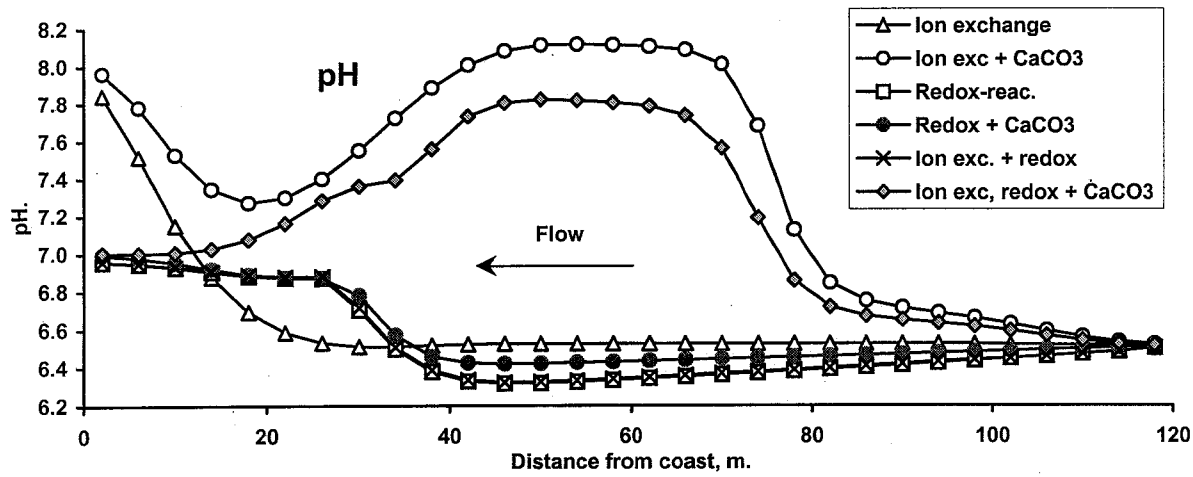

Figure 7.13: pH for six PHREEQC scenarios of freshwater displacing seawater in a column from 120 m to 20 m from the coast (groundwater flow rate 50 m/yr). The scenarios are: Ion exchange (CEC = 24.6 mmol/l), redox-reactions (2 mM CH_2O/yr) and a combination of ion exchange and redox-reactions, all carried out with and without imposed calcite equilibrium.

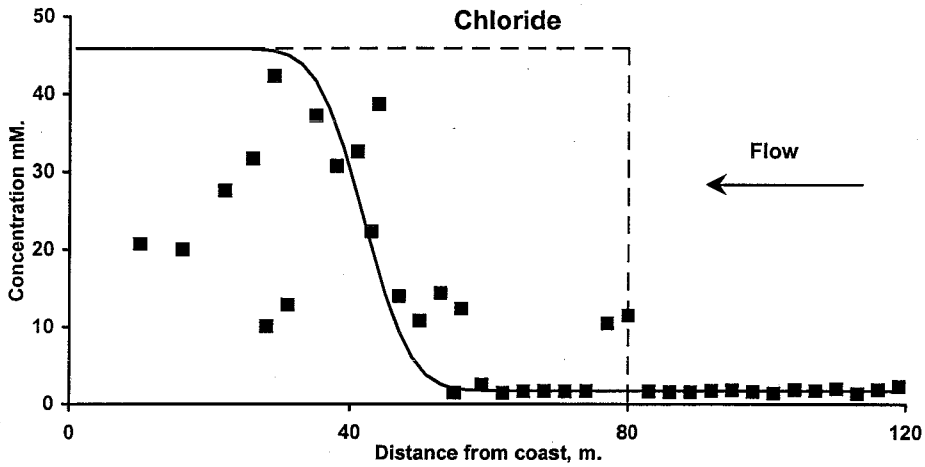

Figure 7.14: Observed chloride distribution (symbols) in a streamline (see Fig. 7.3) in the transect, August 1999. Compared with a chloride distribution modelled using PHREEQC (solid line) of percolated seawater being displaced with freshwater. Dashed line indicates the initial Cl^- distribution.

Some general features from the models described above can qualitatively be recognized in the field data. The Ca^{2+} depletion of Figure 7.4 and 7.5 is seen in the field in a zone from 40 to 80 m (Fig. 6.10c, 6.11a). This Ca^{2+} depletion should according to Figure 7.4 and 7.5 be matched by an increase in Na^{+} and K^{+}, indeed seen in the field at about 20- 60 m (Figs. 6.11a, 6.11d). The expected behavior of Mg^{2+} is more complex, because it is predicted to decrease below the freshwater Mg^{2+} concentration due to the salinity effect behind the decreasing salinity front. Further upstream it should increase due to the exchange with the freshwater Ca^{2+}. In the field data (Fig. 6.11b) only the upstream increase in Δm_{Mg} can convincingly be seen. The redox-parameters of Figure 7.8 compare reasonably with the field data. Where sulfate is depleted (Fig. 6.5b) sulfide concentrations are elevated (Fig. 6.5c), but the observed sulfate concentration are generally lower than in Fig. 7.8. High methane concentrations are mainly present in the fresher part of the transect upstream from 40 m and decreasing towards the coast (Fig. 6.6). The combined effects of ion exchange, calcite dissolution and to some extend also redox-reactions predicts an increase in the alkalinity to about 10 meq/l (Fig. 7.12) and pH to 7.8 (Fig. 7.13) at 20 and 80 m. In the field the increase in alkalinity (Fig. 6.8b) and pH (Fig. 6.8a) is found further towards the coast at around 60 m but with comparable levels for both pH and alkalinity.

Final flushing model

A final model is set up with the purpose of matching the observed water compositions in the upper part of the transect for the field data of August 1999. The assumption behind this model is that the chemical picture in the upper part of the transect of August can be explained by the flushing of a previous (but not recorded) inundation event. Instead of pure seawater the column is initialised with a water composition corresponding to an average composition in the density plume at St80 measured in March 2000 (see section 6.3). This water contains 15 % seawater. Initially the first 80 meters of the model column (from the coast) contain this dilute salt water to mimic the time after an inundation event where seawater has reached 80 m inland and percolated down through the aquifer. The model simulation is presumed to start at the time when the vertical plume migration ceases and the groundwater transport again becomes horizontal and directed towards the coast. The water in the column is transported 36 m towards the coast (as determined by the chloride distribution, Fig. 7.14) with a velocity of 50 m/yr, thus modelling a little less than a year of transport (0.72 yr). A dispersivity of 0.4 m was used. The size of the CEC is 24.6 meq/l (0.5 meq/100g) and the organic matter decomposition rate is again 2 mM CH_2O/yr. Calcite is only allowed to dissolve if the SI

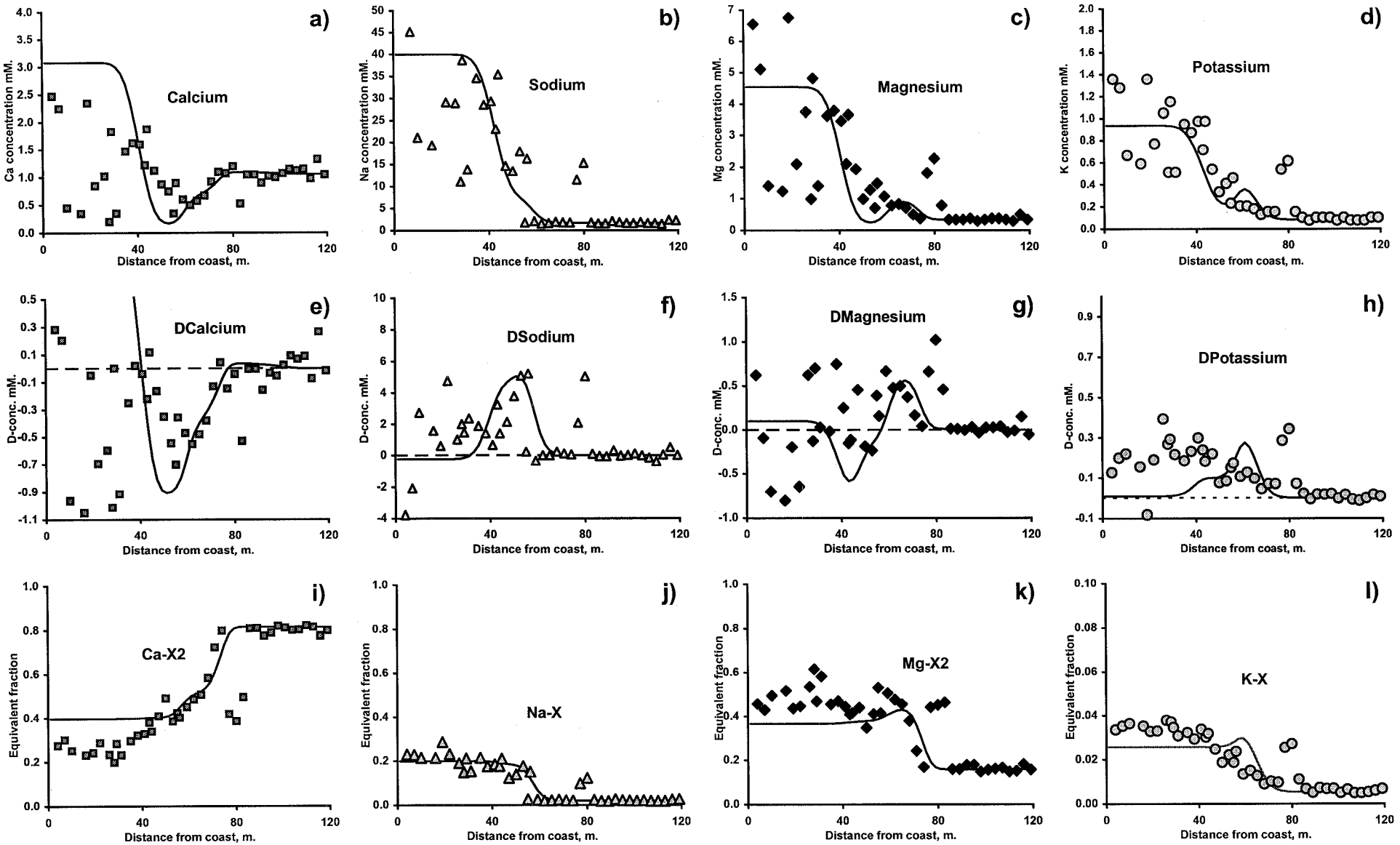

Figure 7.15: Observed distributions (symbols) of a) Ca^{2+}, b) Na^{+}, c) Mg^{2+}, d) K^{+}, e) Δm_{Ca}, f) Δm_{Na}, g) Δm_{Mg}, h) Δm_{K} (all in mM), i) Ca-X_2, j) Na-X, k) Mg-X_2 l) K-X (all as equivalent fractions), in a streamline (see Fig. 7.3) in the transect, August 1999. Compared with modelled distribution using PHREEQC (solid line) of percolated seawater being displaced with freshwater.

drops below -1.2, the SI of the freshwater. The model results are compared with water compositions of the August 1999 data, which are vertically roughly within ±1.5 meter from the inferred flow line indicated in Figure 7.3.

In Figure 7.14 the modelled distribution of chloride is compared with the observed distribution in the modelled streamline of Fig. 7.3. The spreading in the observed Cl^- is larger than the modelled, which partly can be explained by the dispersivity of 0.4 m employed, but most likely also by the fact that in reality the initial conditions are far from homogeneous as indicated by the chloride distribution in Figure 6.20a after the inundation.

In Figure 7.15 (a to d) the modelled distribution of Ca^{2+}, Mg^{2+}, Na^+ and K^+ are compared with the observed distributions in the modelled streamline (Figure 7.3). The cations generally decrease from the coast to 50 m following the decrease in Cl^- (Fig. 7.14). The field data show considerable scatter in the cation concentrations from 40 m towards the coast and with somewhat lower concentrations of Ca^{2+}. This probably reflects the inhomogeneous chemical conditions after the percolation of the density plumes with alternating zones of freshwater and dilute seawater as depicted in the figures 6.20 to 6.23. Behind the front of displaced saline water (40 to 60 m) the effect of the salinity decrease can be observed as decreasing concentrations of Ca^{2+} (Fig. 7.15a) and to a lesser extent Mg^{2+} (Fig. 7.15b) below the concentrations in the displacing freshwater, and increasing the concentrations of Na^+ and K^+. From about 60 to 80 m Ca^{2+} is gradually displacing the seawater derived cations Mg^{2+}, Na^+ and K^+ from the exchanger indicated by the lesser peaks of these cations in Fig. 7.15b-d. This is more easily seen from the modelled cation concentration changes relative to a conservative mix of freshwater and seawater (Δm_i-values) (Fig. 7.15e-h). But considerable scatter is seen in the observed Δm_i-values especially for Mg^{2+} and K^+. There is a reasonable agreement between the modelled distribution of exchangeable cations and the exchanger cation distribution calculated from the observed water compositions using the PHREEQC database (Fig. 7.15i-l). Near the coast however the model underestimates the equivalent fraction of Mg^{2+} on the exchanger and overestimates the Ca^{2+} equivalent fraction.

The redox-parameters sulfate, sulfide and CH_4 are plotted in Figure 7.16 a-c. The modelled sulfate concentration increases from near 0 mM in the fresh groundwater at 40 m to around 1 mM, whereas the observed sulfate seem to increase further towards the coast at 20 m (Fig. 7.16a). The sulfide

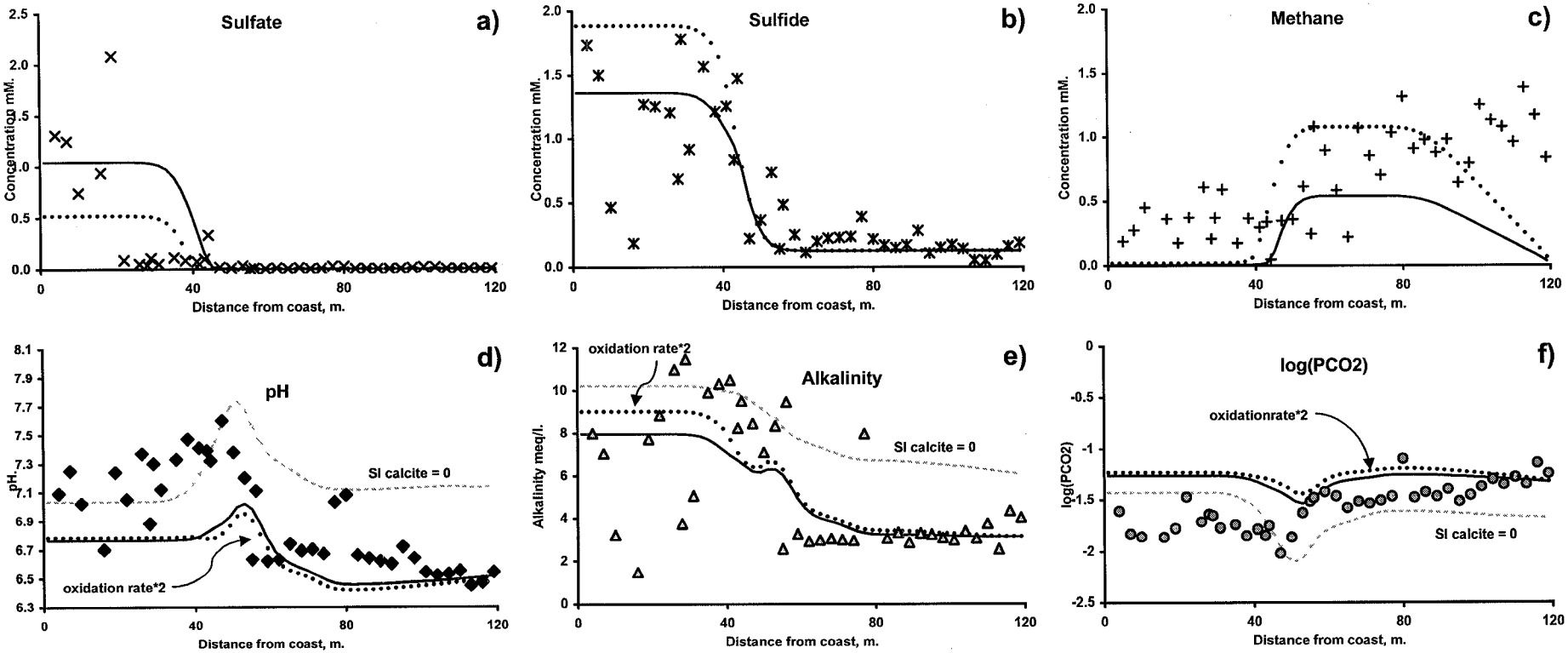

Figure 7.16: Observed distributions (symbols) of a) Sulfate (mM), b) Sulfide (mM), c) Methane (mM), d) pH, e) Alkalinity (meq/l), f) log(P_{CO_2}), in a streamline (see Fig. 7.3) in the transect, August 1999. Compared with modelled distribution using PHREEQC (lines) of percolated seawater being displaced with freshwater. Black solid line represents a rate of 2 mM CH_2O/yr, black dots represents a rate of 4 mM CH_2O/yr and grey broken line represents a rate of 2 mM CH_2O/yr and calcite equilibrium.

both observed and modelled increase around 50 to 60 m from 0.25 mM to about 1.5 mM from 40 m and to the coast (Fig. 7.16b). Both the observed sulfate and sulfide show considerable scatter towards the coast, probably caused by spatial fluctuation in the rate of organic matter degradation or it could reflect some degree of mixing with waters of a different composition from below or above. The observed methane distribution (Fig. 7.16c) is not simulated too well by the model. Observed methane concentrations decrease towards the coast, indicating CH_4-consumption towards the coast rather than a production. Possibly methane is re-oxidised by sulfate (7.4) as proposed by Iversen and Jørgensen (1985). This could perhaps also explain the low observed concentration of sulfate from 40 to 20 m (Fig 7.16a).

Better agreement between the model and the observed values are seen for pH, alkalinity and the $\log(P_{CO2})$ (Fig. 7.16d-f). The modelled increase in alkalinity (Fig. 7.16d) at 50 m from around 3 meq/l to about 8 meq/l at the coast is partly a result of the calcite dissolution caused by the decrease in the calcium concentration due to the ion exchange (3.5 meq/l) and partly caused by the sulfate reduction (1.5 meq/l). However, the highest observed alkalinities (of almost 12 meq/l) are not explained by this model. The dissolution of calcite and the sulfate reduction is also reflected in the pH (Fig. 7.16e) with an increase in the model from 6.5 to 7, again the model does not explain the higher observed pH values of up to 7.6, but the model does mimic the general distribution of pH. The same can be said for the $\log(P_{CO2})$ (Fig. 7.16f) where the modelled $\log(P_{CO2})$ has the same overall shape as the observed values, but generally too high. Increasing the equilibrium SI for calcite in the model from –1.2 to 0 (as observed for the zone from 30 to 50 m in Fig. 6.17a) leads to a much better fit for pH and alkalinity from 60 m and towards the coast, as indicated by the grey broken line in Fig. 7.16d-f. By using an SI of 0 the high observed pH of 7.6 at 50 m is reached and a higher alkalinity of 10 meq/l is obtained, towards the measure maximum of 12 meq/l. Also the low observed $\log(P_{CO2})$ from 50 to 30 m is described better by this increased SI. But the parameters in the landward part of the transect (upstream from 60 m) is fitted rather poorly by this model, showing that this increased calcite dissolution is not taking place in the fresh part of the transect.

As an alternative explanation the organic matter oxidation rate could possibly be higher. A rate twice as high (4 mM CH_2O/yr) is represented by the black dotted line in Figure 7.16a-f. Although increasing the alkalinity in the zone near the coast of about 1 mM, it does not improve the fits for

pH and CO_2. Another possibility could be that a part of the high alkalinity, pH and sulfide observed from 20 to 50 m are caused by in-mixing of groundwater from the wedge, rich in these components.

In conclusion the model gives a reasonable description of the distribution of the chemical parameters in the fresh part of the aquifer and to some extent in the upper part of the mixing zone. The flushing of inundating seawater leads to an alkalinity production of about 1.5 meq/l by sulfate reduction. Additional alkalinity of 3.5-6.5 mM (depending on the degree of calcite dissolution) is caused by calcite dissolution related to the Ca^{2+}-depletion associated with Ca^{2+} displacing of seawater-derived cations from the exchanger. The 1-D model cannot incorporate the influx of saline ground water with high sulfide, alkalinity and cation concentrations from the seawater wedge. Some of the alkalinity can therefore be attributed to in-mixing of saltwater from the wedge.

7.4.3 Natural intrusion

In the deeper part of the transect near the coast a natural circulation of seawater is to be expected in the wedge as generally hypothesized by Cooper (1964) and documented by Kohout (1964) to take place in the Biscayne aquifer in Florida, USA. In brief, the mechanism is that part of the salts in the seawater wedge by dispersion is mixed up in the discharging freshwater and lost. This loss in turn reduces the density of the water in the wedge and the mixing zone and induces a density driven landward transport of seawater. In this way a circulation of seawater with a net landward transport in the wedge can be maintained. It is possible that such a circulation is also taking place at the Skansehage field site. A 3-D density dependent flow and transport model with the geometry and physical parameters of the field site clearly renders the existence of the wedge circulation (Christensen unpublished data). At the field site hydraulic measurements documenting this circulation of seawater via the saline wedge have not been obtained. However, some chemical patterns may be used as evidence for the circulation. Close to the coast at an elevation of –4 to –6 m reaching 20 m into the aquifer is a zone with depletion of the seawater-derived cations Na^+, Mg^{2+} and K^+ relative to a conservative mixture of sea- and freshwater (negative Δm_i-values Fig. 6.11). The depletion of Na^+, Mg^{2+} and K^+ form a coherent area (less so for Mg^{2+}) and these areas for the different cations also roughly coincide. The zone of negative Δm_{Mg} seems to be smaller relative to the zones for Na^+ and K^+. This pattern of depletion indicates an ongoing seawater intrusion. Assuming intrusion occurs, the mechanism is that the cations in the seawater (Na^+, Mg^{2+} and K^+)

exchange with calcium on the exchanger and become depleted in the solution. The solution is correspondingly enriched in calcium, which is in fact is observed. However, the increase in Δm_{Ca} can be lessened somewhat by calcite precipitation, and in most of the area, saturation for calcite is also attained (Fig. 6.17a). Intrusion accompanied by ion exchange cannot continue perpetually because calcium will be depleted and the seawater cations will come into a steady state with the exchanger and exhibit Δm_i-values of zero. Steady state should be attained quickly, even with low flow velocities because of the high cation concentrations in the seawater compared to the CEC (Appelo and Postma, 1993). The ion exchange pattern observed must imply some mechanism of calcium replenishment. A probable mechanism could be changes in the direction of flow in the deeper saline part of the wedge caused by the changes in seasonal discharge. At low discharge (i.e. summer), the net-transport is landward in the bottom of the saline wedge displacing the sea-/freshwater interface. During high discharge (i.e. winter), the interface is pushed seaward again. During the seaward transport freshwater containing calcium is brought in to the zone affected by the circulation. Another probable explanation for the calcium replenishment is that calcium produced by calcite dissolution in the peat layer is transported up into the aquifer by diffusion.

The hypothesis of intrusion in the seawater wedge is further supported by the presence of sulfate in the same zone, which under stagnant conditions would be completely depleted. It therefore seems reasonable to attribute much of the alkalinity observed in the proposed intrusion zone (up to 36 meq/l) to reduction of sulfate brought in to the aquifer by the circulation. Since the reduction of the 15 mM SO_4^{2-} in the seawater should give an alkalinity of about 30 meq/l.

The natural intrusion of seawater due to the wedge circulation will not be modelled in this section because the chemical mechanisms are believed to be essentially the same as in the intrusion experiment (see section 10).

Similar cation distribution patterns as the ones described above are seen at the bottom of the aquifer (–7 to –9 m) 35 to 70 m from the coastline (Fig. 6.11). Here is a zone showing negative Δm_i-values for Na^+, Mg^{2+} and K^+ and positive increased values for Δm_{Ca}. But, here the zone of Mg^{2+} depletion is closer to the coast (35-45 m) and does not coincide with the depleted zones for Na^+ (50-70 m) and K^+ (50-65 m). It is difficult to establish whether this zone is somehow connected to or part of the intrusive zone near the coast or caused by upwards leakage through the bottom. Again the

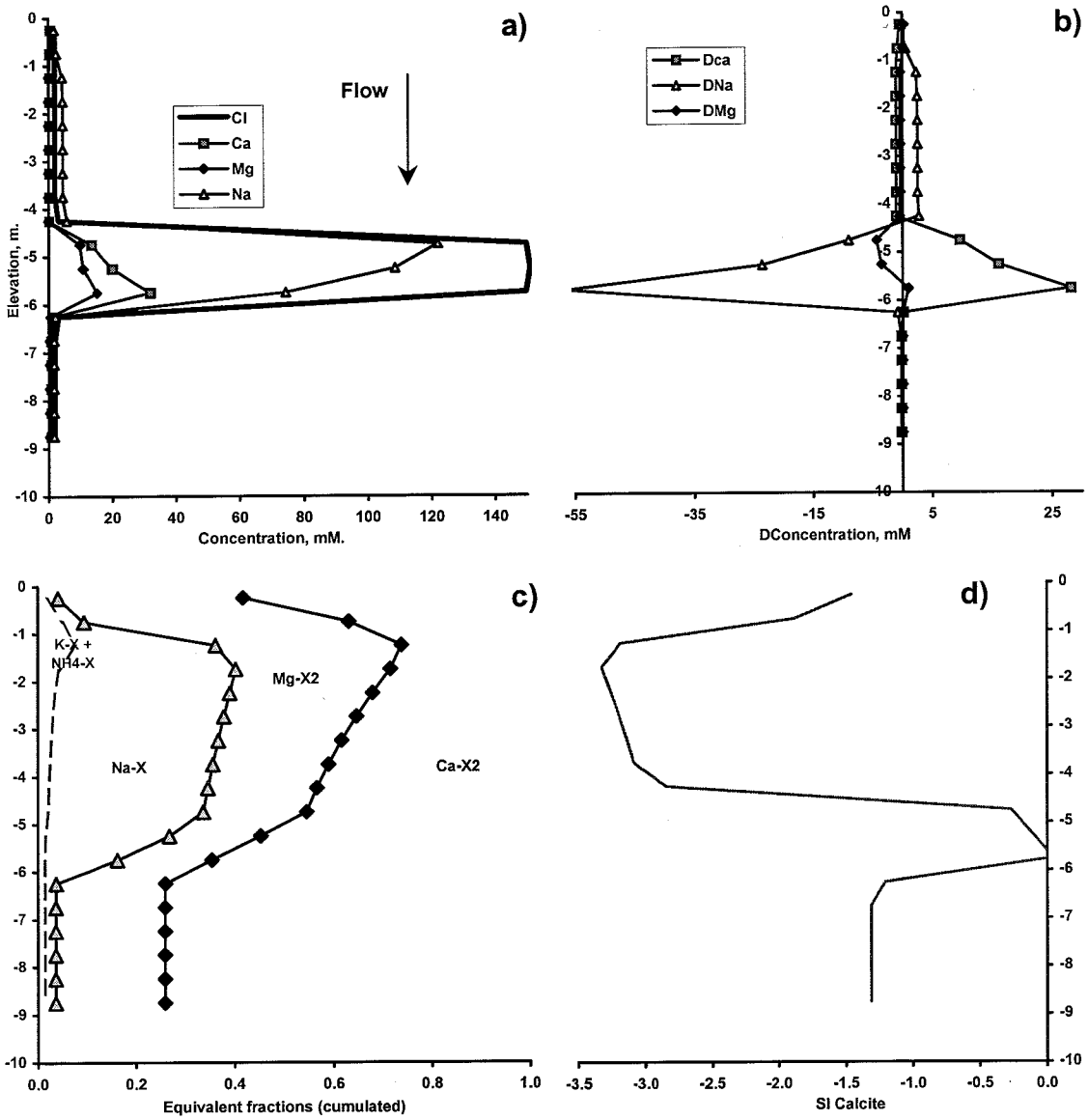

Figure 7.17: PHREEQC model of a vertical pulse of diluted seawater (50%) migrating down through a column initially containing fresh groundwater and a CEC of 0.5 meq/100g. The pulse is transported down by 12 shifts. a) Distribution of Cl^-, Na^+, Mg^{2+} and Ca^{2+} (mM) b) Concentration changes of Na^+, Mg^{2+} and Ca^{2+} (mM) relative to a conservative mix of sea- and freshwater c) Exchanger composition as cumulated equivalent fractions d) calculated calcite saturation index.

presence of sulfate (from 55 to 65 m) indicates a recent marine origin. If there is a connection all the way from the coast to this zone then the flow must take place in a very narrow layer, avoiding the filters from 20 to 35 m from the coast. Alternatively the flow is sideways in to the transect. Disregarding the actual flow path the result is a chromatographic sequence resembling saltwater intrusion, with Na^+ exchanging for Ca^{2+} on the exchanger, followed by K^+ and finally by Mg^{2+}. This water could alternatively also stem from a previous inundation and subsequent density plume percolation.

7.5 Modelling of the density driven plume percolation

The complexity of the downward migration of the seawater plumes renders modelling with the purpose of matching the field data difficult, without a very detailed description of the permeability distribution. Even with a detailed description of the permeability distribution the stochastic nature of the onset of density flow, caused by an unstable density distribution, will make the outcome of the modelling doubtful (Schincariol, 1998 and Simmons et al., 2001). Therefore, focus will first be put on a conceptual model of the chemical processes occurring in such a plume. Further more, PHREEQC, the model used in this work, cannot describe the downward motion of a density plume where flow ceases after the density plume has passed and aquifer water moves back in to the portion of the aquifer left by the plume. The plume will leave a low-density tail of seawater mixed up with freshwater behind, and in time the direction of flow will change and the tail will slowly be transported towards the coast (see Fig. 5.21). In spite of these inherent problems, valuable information can still be obtained from a conceptual model. In the following only cation exchange processes will be modelled, because little effect of sulfate reduction is observed in the short time modelled. However the real system is more complex as data indicate oxidation of sulfide minerals in the early stage of the density plume percolation.

First a simple conceptual model is constructed in order to understand the basic exchange effects related to the plume migration. A vertical homogeneous column of 10.5 m, representing the thickness of the aquifer and unsaturated zone, is divided into 21 cells each of 0.5 m, and is given a cation exchange capacity of 24.6 meq/l (equal to 0.5 meq/100g). The column is subdivided into two sections where the lower 18 cells are initialised with fresh groundwater. The upper 3 cells, representing the unsaturated zone, are initialised with seawater diluted with freshwater to a Cl^-

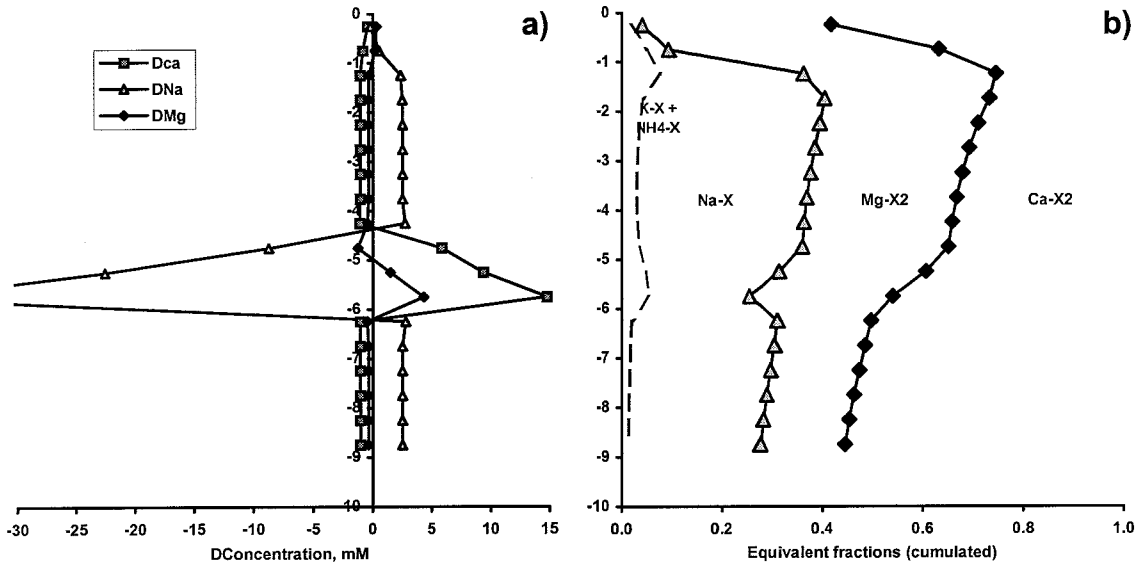

Figure 7.18: PHREEQC model of the successive migration of two vertical pulses of diluted seawater (50%), separated by 30 shifts of fresh groundwater, down through a column initially containing fresh groundwater and a CEC of 0.5 meq/100g. The second pulse is transported down by 12 shifts (42 shifts in total). a) Concentration changes of Na^+, Mg^{2+} and Ca^{2+} (mM) relative to a conservative mix of sea- and freshwater b) Exchanger composition as cumulated equivalent fractions.

concentration corresponding to 50% seawater. The seawater pulse is transported down through the column followed by fresh groundwater. To keep the model simple a dispersivity of 0 is used.

Figure 7.17a show the chloride and the major cation (Na^+, Ca^{2+} and Mg^{2+}) distribution over depth after 12 shifts (6 m). The sodium peak is depleted compared to chloride, especially at the front side (down side) of the seawater pulse. This Na^+ depletion is mirrored by an increase in the Ca^{2+} concentration at the front side, reflecting that Ca^{2+} on the exchanger is displaced into the solution by sodium in the pulse. In Figure 7.17b the cation concentration changes relative to a conservative mix of sea- and freshwater are showing that Mg^{2+} is also depleted in the seawater pulse and also part taking in displacing Ca^{2+} from the exchanger (from –4.5 to –6 m). Behind the seawater pulse is a plateau zone (from –1 to –4.5 m) where the exchanger has a cation composition dictated by the seawater pulse as shown in Fig. 7.17c. Here Ca^{2+} and Mg^{2+} are forced from the freshwater on to the exchanger at the expense of Na^+. At 0 to –1.5 m the exchanger is slowly restored to its original freshwater composition. If vertical transport, hypothetically, where to continue in the column after the passage of the seawater plume more than 10 pore volumes are needed to restore the original freshwater cation composition on the exchanger in the entire column (including the flushing of Mg^{2+}).

The effect on the calculated SI for calcite is shown in Figure 7.17d. An increase in the SI from –1.26 in the freshwater to saturation (SI = 0.05) is seen at the depth of the pulse due to the displaced Ca^{2+}. For comparison the initial SI in the 50% seawater pulse is –0.8. The supersaturation will increase as the pulse migrates further down. But more important is the zone of decreased SI to –3.4 behind the seawater pulse, where the depletion of Ca^{2+} is creating a substantial potential for calcite dissolution as also discussed in section 7.4.2. Such effects caused by coupling of ion exchange and calcite dissolution as related to salinity pulses were also observed in the injection experiments by Bjerg et al. (1993). However as here, it was difficult to discern the amount of calcite dissolution in that case.

A more complex cation exchange pattern is observed if a second seawater pulse is passed down trough the column before the exchanger cation composition has restored its original freshwater composition. This is illustrated in Figure 7.18a where a second seawater pulse identical to the one above is transported down by 12 shifts (to –6 m). 30 shifts of freshwater separate the two pulses.

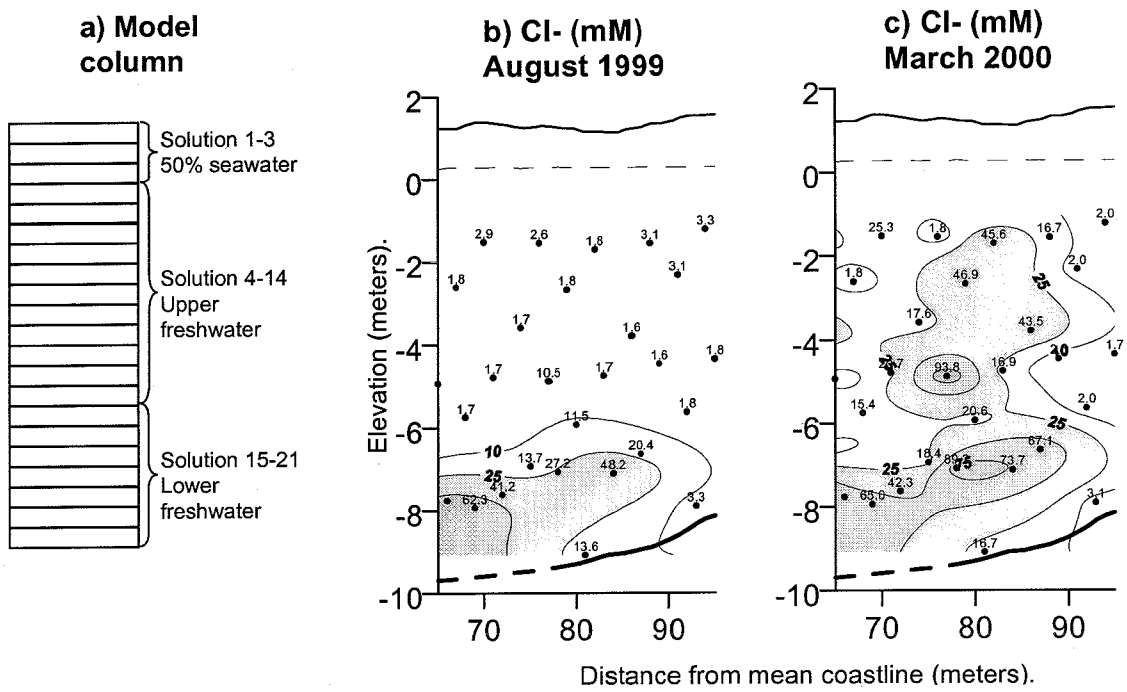

Figure 7.19: a) Model representing the initial situation a few days after the inundation event ±15 m around transect well St80 b) The chloride distribution prior to the inundation (August 1999) and c) The chloride distribution 50 days after the inundation event (March 2000).

The changes in cation concentrations relative to a conservative mix of seawater and freshwater are not as pronounced as during the passage of the first pulse. The major difference is that now also Mg^{2+} is displaced from the exchanger in the seawater pulse as seen from the Δm_{Mg} in Figure 7.18b. This is due to the salinity increase according to equation 3.2 forcing divalent cations of the exchanger, which this time contains a significant fraction of Mg^{2+} from the passage of the first pulse. This enrichment of Mg^{2+} in the front of the density pulse also seems to occur in the field (Fig. 6.24b).

Finally the model is now expanded to mimic the field data a little better. The density plume at 80 m is chosen as an example. Figure 7.19a shows a model column at about 80 m from the coast. The column has the same characteristics as the column employed above, apart from the fact that the lower part of the column is divided into two sections, at an elevation of –5.5 m. The division is based on the change in water chemistry, especially the chloride concentration, as shown in Fig 7.19. The two sections in the model from 0 m down to –5.5 m (cells 4-14) and from –5.5 m and down to –9 m (cells 15- 21) are initialised with a water composition equal to the average measured compositions of the August 1999 data in these intervals. The water compositions were averaged over a section of the transect from 75 to 85 meters from the coast. The solution flushing the column after the passage of the seawater plume is identical to the freshwater from 0 to –5.5 m. This solution represents an approximation for the freshwater filling in after the passing of the plume. A shortcoming of this infilling of freshwater is that it does not allow for the observed diluted plume tail. In the model, the seawater was transported down to –5.5 m by 11 shifts, a depth corresponding to the maximum chloride concentration in the main plume 50 days after the inundation. A dispersivity of 0.04 m was used (equal to 1% of the flow length).

Model results of Na^{+}, Mg^{2+} and Ca^{2+}, and calculated depletion/enrichment of these parameters compared to conservative mixing are shown together with the observed parameters in the Figures 7.20, 7.21 and 7.23. The model does not attempt to fit the high concentrations observed deeper (-7 m) in the aquifer, perhaps reflecting a fast flow path or the passage of a previous plume.

The model output is quite similar to the result obtained by the conceptual model of two seawater plumes descending in succession (Fig. 7.18). The lower section in the model set-up of Fig. 7.19, initialised with the observed water composition containing more Na^{+} and Mg^{2+}, creates the same

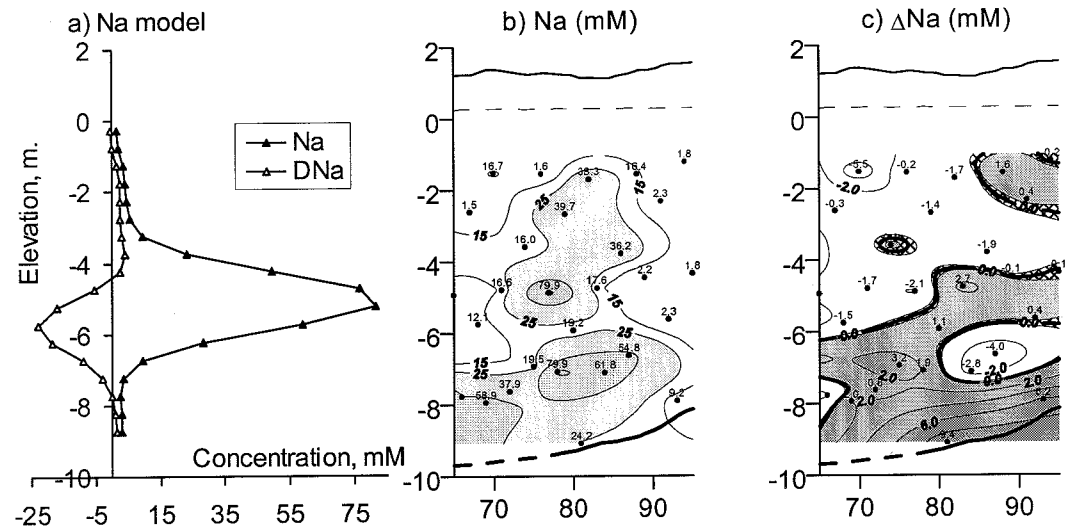

Figure 7.20: PHREEQC model of a vertical migrating seawater plume a) model output Na, ΔNa (mM), b) Observed Na (mM), c) Observed ΔNa (mM) Cross-hatching ± 0.2 mM.

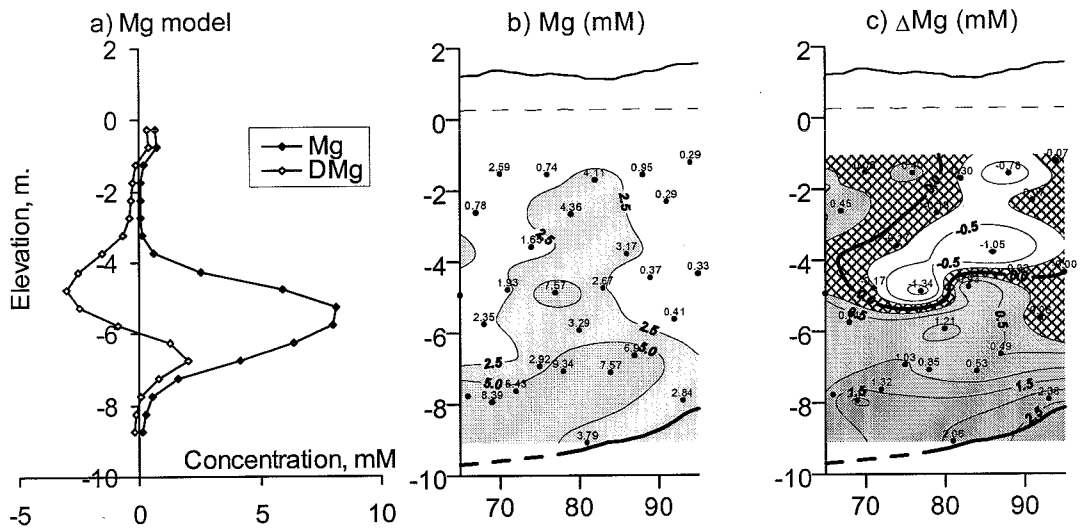

Figure 7.21: PHREEQC model of vertical migrating seawater plume a) model output Mg, ΔMg (mM), b) Observed Mg (mM), c) Observed ΔMg (mM) Cross-hatching ± 0.2 mM.

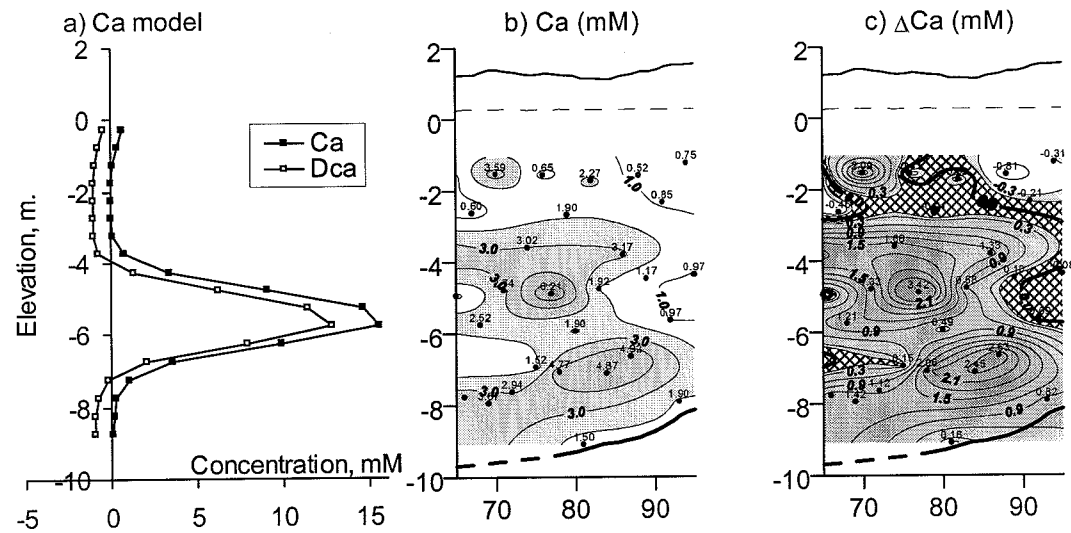

Figure 7.22: PHREEQC model of vertical migrating seawater plume a) model output Ca, ΔCa (mM), b) Observed Ca (mM), c) Observed ΔCa (mM) Cross-hatching ± 0.2 mM.

effect as when two seawater plumes descends in succession, by also displacing Mg^{2+} at the forefront of the seawater plume.

The modelled maximum values of Na^+ and Mg^{2+} at about –5 m agree well with the observed peak values of 80 mM and 7.6 mM, respectively (Figs. 7.20 and 7.21). But the modelled Ca^{2+} peak is twice as high (15 mM) as the observed of about 6 mM (Fig. 7.22). A reason for this could be that the Ca^{2+} released from the exchanger is precipitated as calcite, but this is not likely because slight subsaturation for calcite (SI<-0.1) is observed. Alternatively the explanation is that in reality the exchangeable Ca^{2+} is smaller than in the model, either because of a smaller average CEC or a smaller β_{Ca}.

Generally the observed enrichment or depletion compared to a conservative mix between seawater and freshwater (Δm_i-values of Figs. 7.20 to 7.22) of the cations are substantially smaller than the modelled. But the general pattern is that the modelled Δm_i-values agrees reasonably well with the observed depletion or enrichment for Ca^{2+} and Mg^{2+}. In the top part the observed Ca^{2+} is depleted to –2 m and the observed Mg^{2+} is depleted down to –4 m. In the central part the observed Ca^{2+} is enriched and Mg^{2+} is enriched in the lower part from –4 m. The observed Na^+ is not fitted too well with depletion in the top section (down to –5 m) where the model predicts a small enrichment. In the lower section enrichment of Na^+ is observed where the model predicts depletion.

The modelled calcite saturation index (not shown) overestimate the observed saturation index in the upper part of the transect (0 to –1 m) and underestimate it in the middle part (–1 to –4 m). The discrepancy in the top could be due to the oxidation of sulfide minerals having an acidifying effect. In the middle part the discrepancy could perhaps be due to some dissolution of calcite or mixing with water being closer to saturation for calcite.

The observed peaks of the cations (and Δm_i-values) of Figs. 7.20, 7.21 and 7.22 are generally more smeared out than in the model. This could largely be a result of the formation of the stagnant plume tail, or because the natural plume descend is much more complex than the 1-D model and therefore the discrepancies described above are to be expected. First of all the high degree of heterogeneity in the flow pattern, with preferential flow paths and stagnant zones, will create not one front of seawater but multiple fronts at different depths in the aquifer. Second the flow velocity in the

density plumes might be so high that the assumption of local equilibrium for the exchange reactions is not maintained. Appelo and Postma (1993) state that the local equilibrium assumption for ion exchange may not be valid for velocities above 100 m/yr. Both the heterogeneous flow and the possible chemical non-equilibrium will have a tendency to smear out the effects of the chemical reactions.

The dominating chemical reaction in the descending plume seem to be the ion exchange displacement of calcium by the seawater derived cations Na^{+} and Mg^{2+}. This affects the exchanger for a considerable time and flushes a substantial amount of calcium from the exchanger.

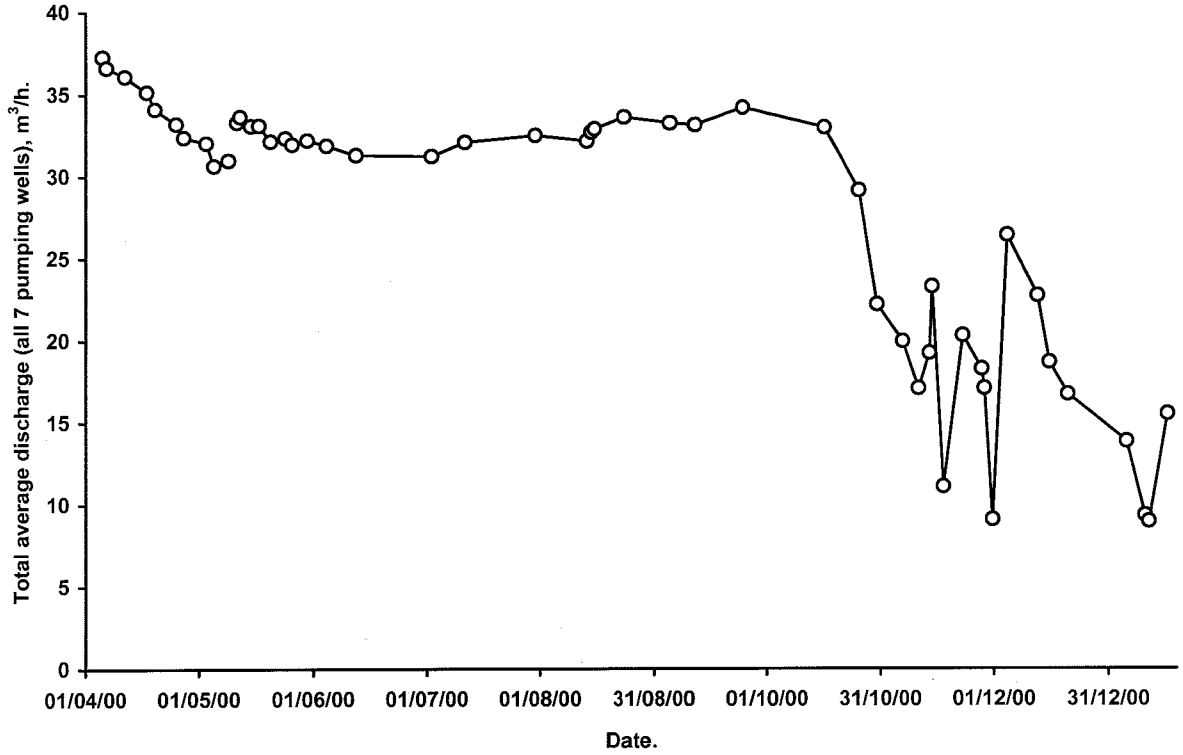

Figure 8.1: Total average discharge in m³/h from all 7 pumps at the pumping well field.

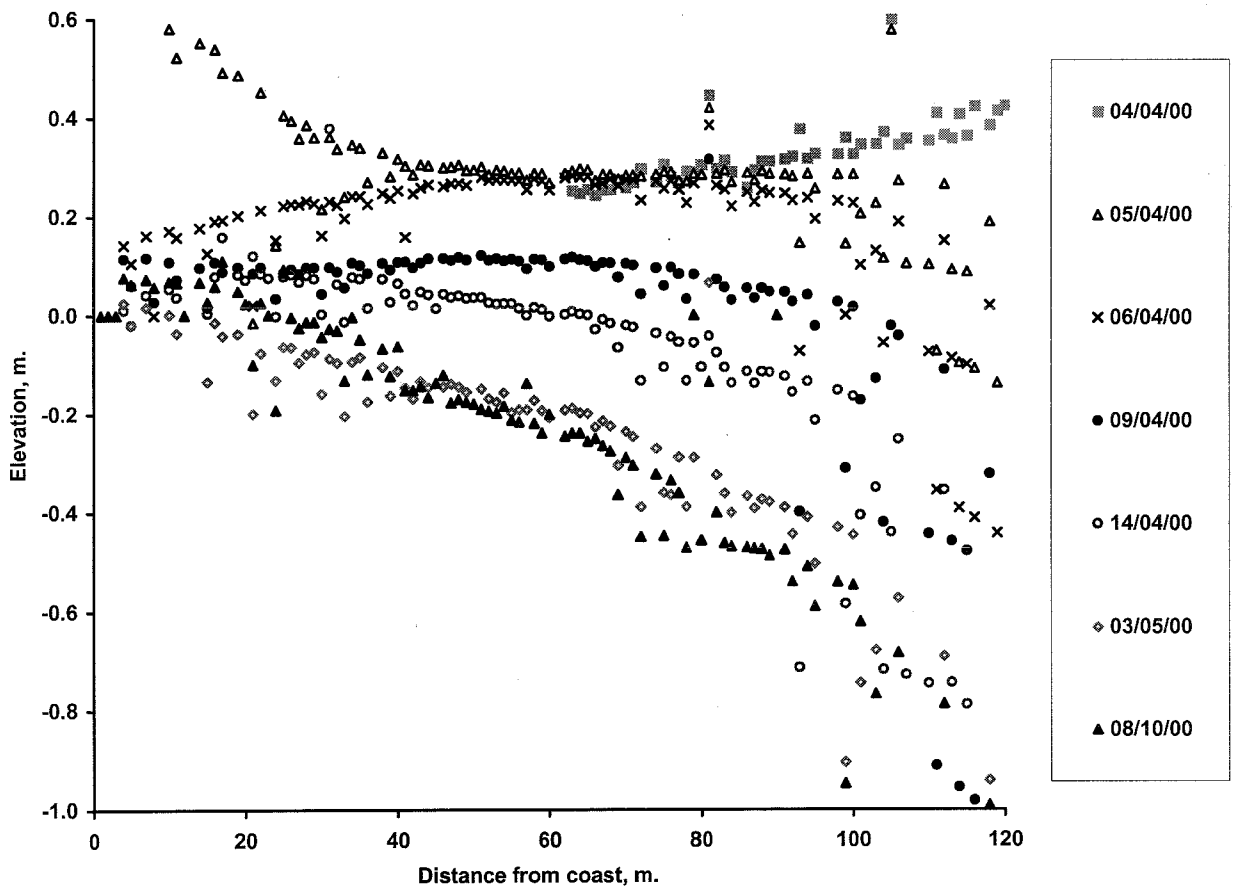

Figure 8.2: Water levels measured in the transect wells before and during the pumping.

8. THE SEAWATER INTRUSION EXPERIMENT: HYDROGEOLOGY

8.1 Discharge from pumping well field

The seawater intrusion experiment commenced the 4th of April 2000 by pumping fresh groundwater from the 7 pumping wells in Figure 4.1b. Initially the total average pump discharge from the 7 pumps was 37 m^3/h (Fig. 8.1). Within the first 23 days this decreased to a constant level of about 32 m^3/h, probably due to the development of a quasi-stationary cone of depression (Fig. 8.2). The discharge of 32 m^3/h was maintained for about 5½ month where after the discharge decreased to about 17 m^3/h. The decrease is caused by bio clogging of the pumps and the well screens when groundwater rich in hydrogen sulfide, reaches the pumping wells and comes in contact with atmospheric O_2. Probably mediated by bacteria, the oxidation of H_2S causes precipitation of elemental sulfur, which clogs the system. Several attempts were made in order to clean the pumps and well screens, but for the last three months the pumps were fluctuating erratically in performance and the average total discharge decreased to about 10 m^3/h towards the end of the experiment. The pumping field was operating for almost 10 months and a total of 193.900 m^3 of groundwater was pumped.

8.2 Development in the hydraulic head response

Figure 8.2 shows the development of the drawdown in the transect wells. A landward hydraulic gradient all the way from the coast towards the pumping well field was attained sometime between the 14th and 21st of April (not shown), after 10 to 17 days of pumping (Fig. 8.2). Between 21st of April and 3rd of May after 17 to 29 days of pumping a stationary drawdown was established along the monitoring transect as indicated by the nearly constant water level measurements (in Figure 8.2) Small fluctuations remain because variations in the seawater level continually change the potential gradients in the near coastal area. Figure 8.3a&b show the contoured groundwater potential for the field site from the 23rd of May and 10th of August 2000. The maximum drawdown in the pumping

a) 23'th of May 2000

b) 10'th of August 2000

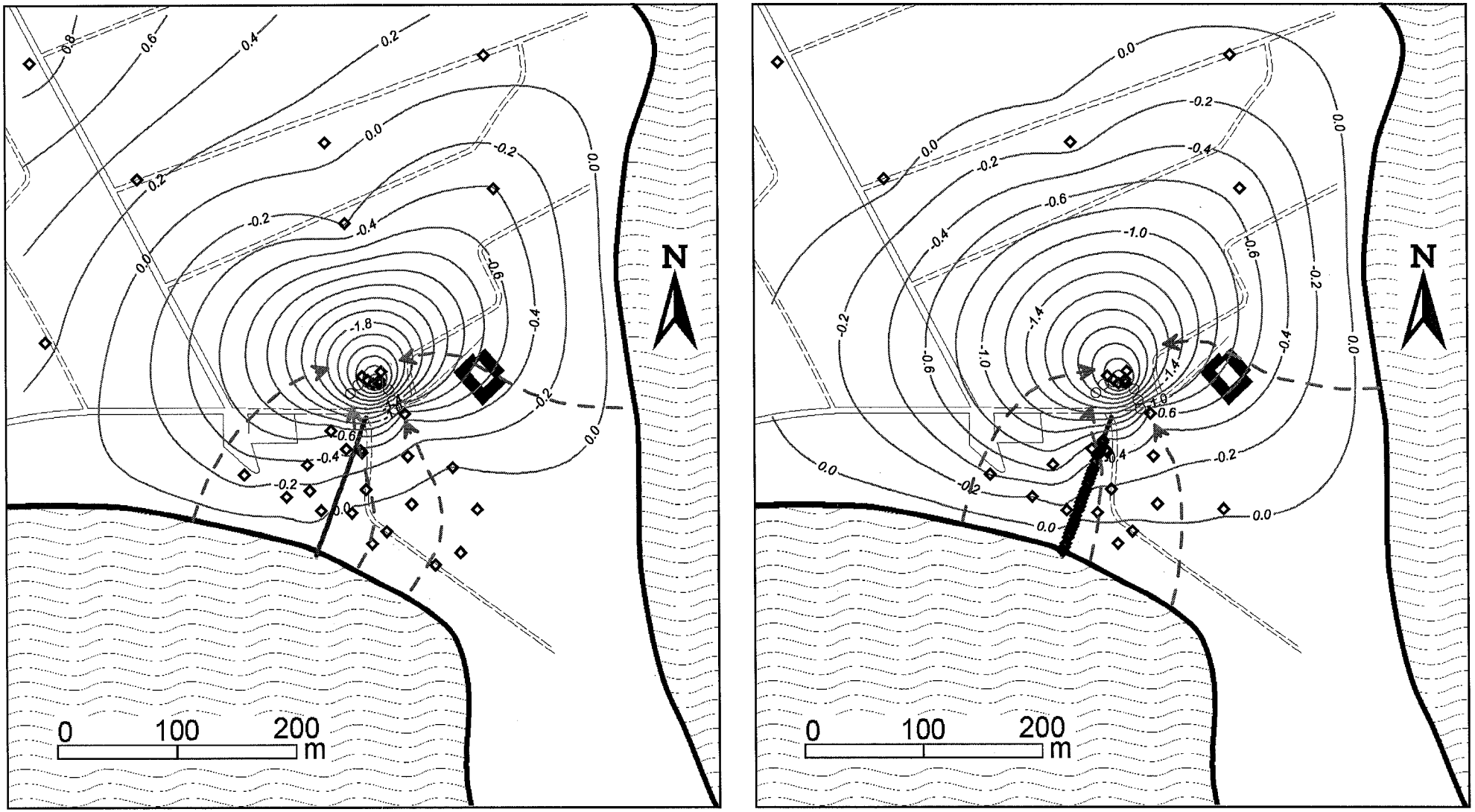

Figure 8.3: Groundwater potential maps during pumping (elevation, m). Conture intervals 0.2 m. Measured a) 23'th of May 2000 and b) 10'th of August 2000. Conturing si done in Surfer by Kriging.

well field is about –3 m. On the landward side of the pumping field the drawdown cone seems to expand further during the summer months, due to the low infiltration (Fig. 8.3b).

In the transect wells from 100 m and landward the water levels varies with up to 0.8 m between neighbouring wells. This indicates the presence of considerable geological heterogeneity in the aquifer (Fig. 8.2). It becomes even clearer when the heads are density corrected according to section 4.1.7 and plotted and contoured in the transect as shown for the 8th of October 2000 in Figure 8.4. In most of the transect (0 to 80 m) the lines of equal head are vertical indicating predominantly horizontal flow from the coast towards the pumping well field. In this part of the transect the gradient is 8‰ in October. At around 80/90 m from the coast the gradient in the freshwater head is steepening considerably towards the pumps. Furthermore the lines of equal freshwater head are no longer vertical from 80 m and landward, but oblique indicating a decreasing freshwater head with depth. The steepening gradient could be caused by low permeable layers as indicated by the el-logs Fig. 5.7. The peak at –4 m observed in the el-log boring St105 (Fig. 5.7a) at the landward end of the transect could be a hydraulic barrier causing this vertical head gradient during the intrusion experiment. The layer may be dipping toward the coast as indicated by the Ground Penetrating Radar profile (Fig. 5.5). It could be one or several of the thin peat layers less than 10 cm in thickness observed in some of the sediment core samples. Part of the explanation is also that the groundwater must have a downward component as indicated by the water table.

A zone with a low head at –6 to –8 m depth from 70 to 120 m on the other hand could imply the existence a high permeability zone. Indeed the hydraulic conductivity distribution (Fig. 5.8) seems to indicate the presence of such a zone. Near the coast at B in Fig. 8.4 varying heads show the influence of sea level fluctuations.

8.3 Intrusion of seawater (EC-plots)

In Figure 8.5 a) to i) the advancement of the intruding seawater is monitored using electrical conductivity (EC). On average, the seawater advances as a vertical front. Zones where the front is retarded and accelerated must be controlled by zones of low and high permeability respectively. This can be exemplified by comparing the hydraulic conductivity distribution of Fig. 5.8 with the

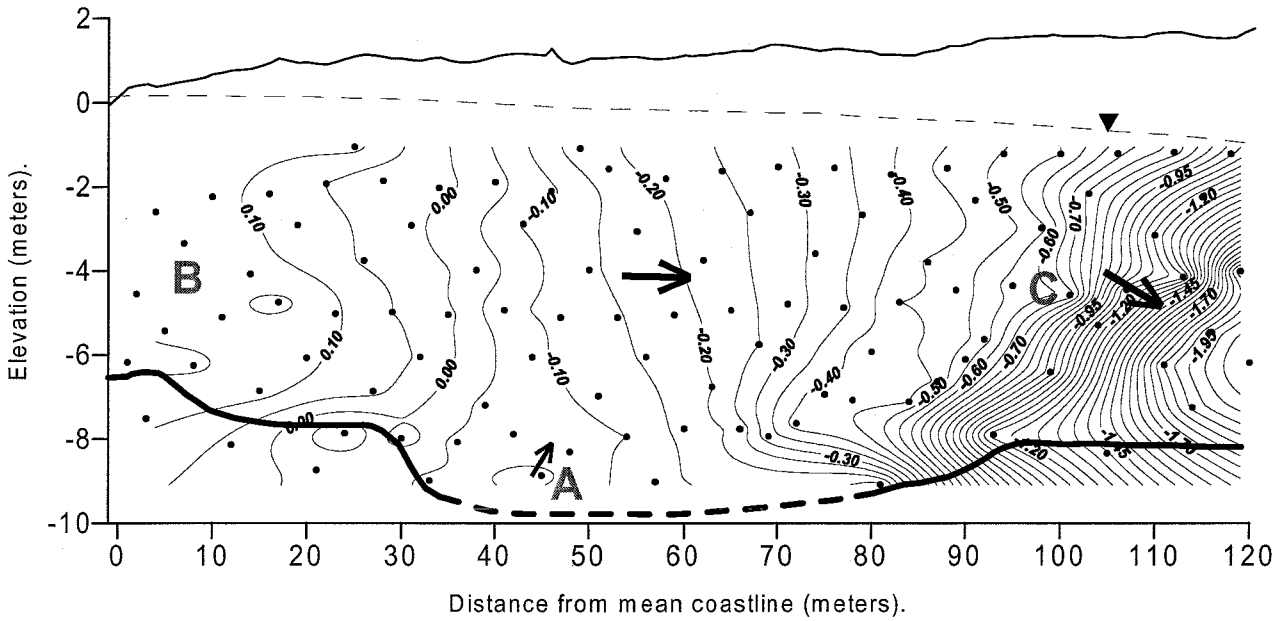

Figure 8.4: Contoured values of density corrected hydraulic freshwater heads in the monitoring transect 8th of October 2000. Contour intervals are 5 cm. At A near the bottom of the aquifer upward leakage may be occurring. Varying heads at B indicate influence of sea-level fluctuations.

EC 95 days after the start of the pumping (Fig. 8.5d). There is a zone with low EC indicating retarded transport at 15 to 30 m from the coast at –4 to –6 m corresponding to a zone of lower hydraulic conductivity of $1 10^{-4}$ m/s (Fig. 5.8). Also the zone of high hydraulic conductivity (up to $7 10^{-4}$ m/s) at –6 to –7 m depth seems to correlate with a zone where the EC is advancing ahead of the main front at 40 to 90 m from the coast. In the beginning of the experiment the remainder of percolated inundating seawater from 30 to 80 m (in Figure 5.18e) is pushed through the aquifer ahead of the advancing seawater front (Fig. 8.5a to c) with EC values ranging from 3000 to 9000 µS/cm. Between 33 and 46 days of pumping a zone of high EC is seen to develop at –6 m depth, 110 to 120 m from the coast in the lower high permeable zone. Most likely percolated inundating seawater flowing east of the transect is intersecting the transect. The groundwater potentials in Figure 8.3 a&b show that the flow from the coast and towards the pumps is not completely parallel with the transect. The overall flow direction seems to cross the transect at an angel of 20° from the east. Also the high pore water EC of up to 26300 µS/cm measured in the El-log (fig 5.19) 8 m east of St80 prior to the intrusion experiment supports this explanation. An alternative explanation is that the zone of elevated EC is caused by a narrow high permeability layer running all the way from the coast at a depth of –6 to –8 m, though it is improbable that this high EC water should completely avoid being sampled by any filters over the 60 to 80 m of the aquifer from the sea-/freshwater interface to the high EC zone.

Some leakage through the bottom aquitard up into the aquifer seems to occur throughout the experiment. Initially (a to c in Fig. 8.5) a pocket of low EC groundwater (1000 to 3000 µS/cm) at –8 to –9 m, 50 to 60 m from the coast seems to move upward. From about 168 days and onward (e to i in Fig. 8.5) after the start of the pumping leakage up through the bottom at 30 to 40 m from the coast becomes visible with groundwater of an EC as low as 9000 µS/cm. This water is partly mixed into the intruding seawater and flows towards the pumping well field most clearly seen in Fig. 8.5b-e at –6 to –8 m from 40 to 80 m. Indications of leakage were also seen prior to the intrusion experiment, so the lowering of the hydraulic head in the upper aquifer will most likely enhance this leakage due to the increased gradient over the bottom aquitard. This leakage is possibly retarding the advancement of the toe of the seawater front and thereby falsely indicating an apparent lower intrusion velocity of the toe. The leakage is also important to keep in mind when interpreting the chemical data in the lower part of the transect.

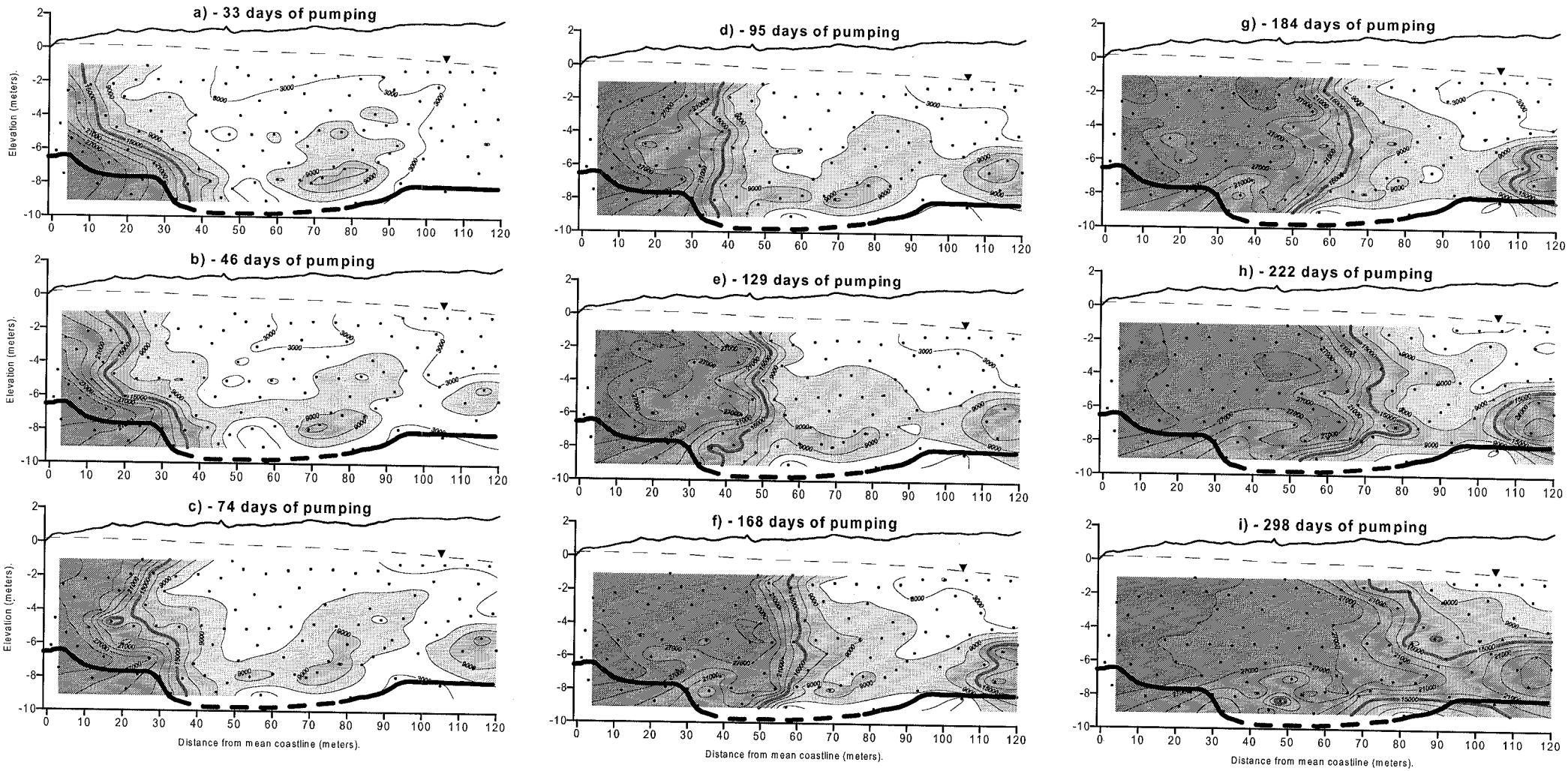

Figure 8.5: Electrical conductivity (EC) in µS/cm, measured in the transect during pumping. After: a) 33 days of pumping (07/05/00) b) 46 days of pumping (20/05/00) c) 74 days of pumping (17/06/00) d) 95 days of pumping (08/07/00) e) 129 days of pumping (11/08/00) f) 168 days of pumping (19/09/00) g) 184 days of pumping (05/10/00) h) 222 days of pumping (12/11/00) i) 298 days of pumping (18/01/01). Thick contour at 15000 µS/cm represents 50 % seawater at the begining of the experiment.

In the EC plots e to h in Fig. 8.5 a zone of elevated EC can be observed at about 40 to 50 m just behind the front. This elevated EC reflects the high winter EC in the surface seawater of the fjord (Fig. 6.2) in the initial stage of the experiment. Between this EC peak at 50 m and the coast lower EC values corresponds to the summer minima in the EC of the surface seawater of the fjord (Fig. 6.2). From 184 days to 298 days of pumping (Fig. 8.5 g to i) the EC minima is followed by increasing EC-values (at 0 to 30 m) corresponding to the higher winter EC in the surface seawater. This seasonal variation in the EC over the experiment are also recognised for the major ions (see section 9).

The flow pattern reflected by the EC plots in Figure 8.5 are summarised in Figure 8.6 where all the contoured curves of 50% seawater (15000 µS/cm) are plotted together. The seawater intrusion is basically advancing as a vertical front and penetrating to a maximum of about 80 to 90 m from the coast (ignoring the high permeable zone further inland).

The observed shift from a steady state wedge shaped sea-/freshwater interface into a vertical advancing seawater front (Figs. 8.5 and 8.6) is not what intuitively is to be expected. In a homogeneous aquifer it should be expected that the seawater front, during intrusion, will at least retain the wedge shape of the sea-/freshwater interface prior to the intrusion, or maybe even become more accentuated by density effects during the intrusion. In previous field- and modelling-studies intruding seawater fronts have often been shown to have a wedge shape (Bear et al., 1999). However, for an aquifer of small thickness affected by a large head gradient, the driving potential force due to density differences between the seawater and freshwater side of the front will be smaller than the potential energy related to the landward head gradient (Iribar et al., 1997). Christensen et al. (2001) simulated seawater intrusion into the Skansehage aquifer using a 3-D density dependent code PHASTD. They show that for a homogeneous case the wedge shaped sea-/freshwater interface observed prior to the intrusion will essentially be turned into a vertical front during intrusion, indicating that the density effects does not seem to be of any importance at the field site. But they use a relatively high transverse dispersivity of about 25% of the longitudinal dispersivity. According to Ataie-Ashtiani et al. (1999) a high transverse dispersivity will lead to a more vertical front whereas decreasing the transverse dispersivity will give a more wedge shaped front. At the field site a high transverse dispersivity is probably not the explanation for the vertical front. It is more likely that heterogeneities in the aquifer, such as permeability variations are

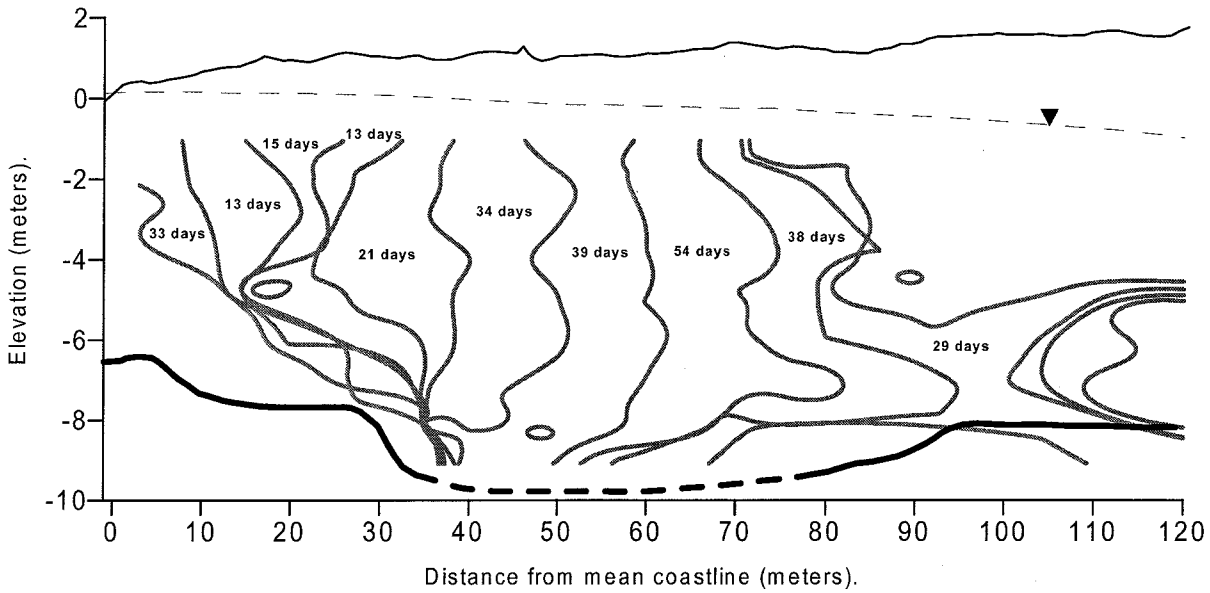

Figure 8.6: 50% seawater contours based on the 15000 µS/cm EC contour from measurements in the transect during pumping. Number of days between the curves represent time between measurements.

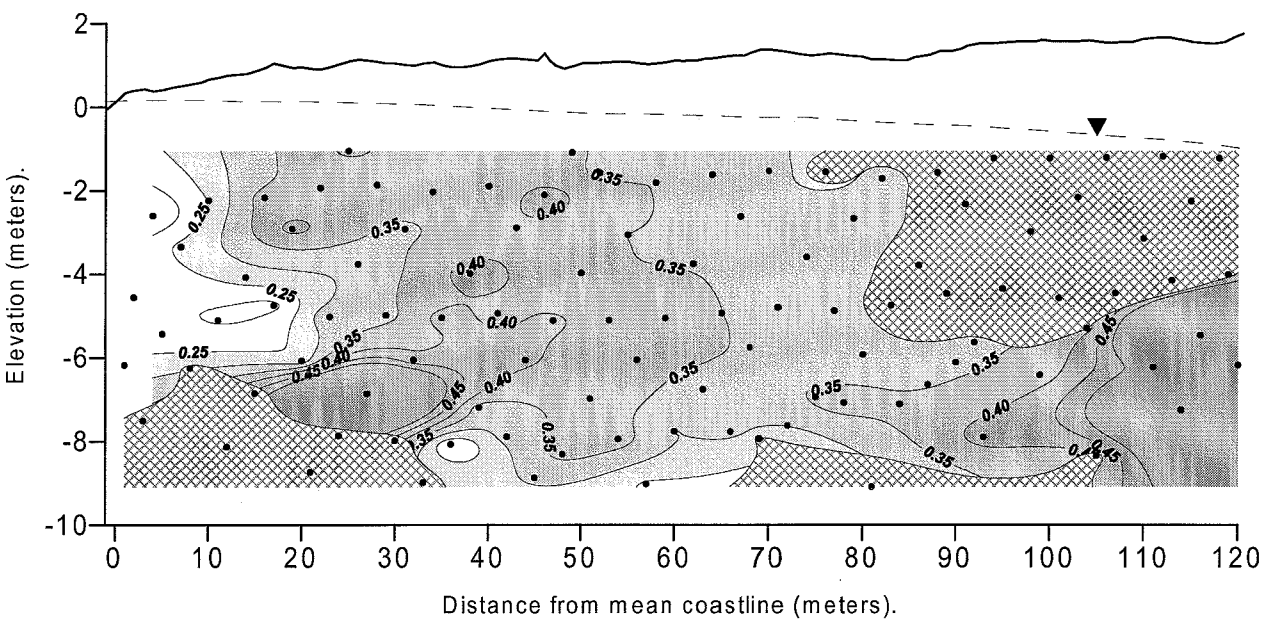

Figure 8.7: Average breakthrough velocities (v50) for the observation wells in the transect based on the time (t50) for arrival of the 50% seawater contour and the distance from the coast to a well (v50 = x/t50). No breakthrough was observed in the crosshatched areas. In the two lower crosshatched areas due to the low permeable peat layer and the upper landward crosshatched area was never reached by the intrusion.

controlling the front shape. And also as mentioned above the possible upward leakage from the aquifer below, could impede the advancement of the seawater toe by mixing are more likely to determine the shape of the seawater front.

Based on EC breakthrough curves from the measurements in Fig. 8.5 a mean travel time (t_{50}) for the arrival of the 50% seawater concentration can be estimated for each observation well. And by assuming the intrusion to begin at the coastline ($x = 0$), a mean velocity ($v_{50} = x/t_{50}$) for the arrival of the 50% seawater concentration can be calculated and plotted for every filter as done in Figure 8.7. The crosshatched areas in Figure 8.7 are areas with no breakthrough. The lack of breakthrough in the two lower cross-hatched areas is due to the low permeable peat layer. The upper cross-hatched area was never reached by the intrusion. Figure 8.7 shows the average flow velocity during the experiment to be around 0.33 m/d (10 m/month). The breakthrough velocity is low in the coastal part of the transect (0 to 20 m) reflecting the lag time for the development of the gradient in the beginning of the experiment. The zone with higher velocities up to 0.40 m/d (from 20 to 60 m) is identical with the period of high pump discharge (32 m^3/h) in Figure 8.1. The slightly lower velocity from 60 to 80 m reflects the deteriorating performance of the pumps from the end of October. Towards the end of the transect the high velocities of more than 0.5 m/d must be related to the sideward flow on to the transect of percolated inundation seawater from the eastern side and are therefore false. The derivations from the overall pattern must reflect the variation in the hydraulic conductivity.

In summary, the seawater front advanced about 80 m inland during the 10 months of pumping. The intruding seawater front is essentially vertical and advancing with an average velocity of about 0.33 m/d. The change from a wedge shape interface at steady state to a vertical advancing seawater front is believed to be mainly due to heterogeneities in the aquifer, but also because the density gradient over the front is negligible compared to the large head gradient over the front. Temporal and spatial variations in the shape of the advancing front is largely caused by variations in the hydraulic conductivity, flow crossing the transect line and leakage through the bottom of the aquifer. In the following sections the flow and transport related to the main seawater front will generally be assumed as being parallel to the transect.

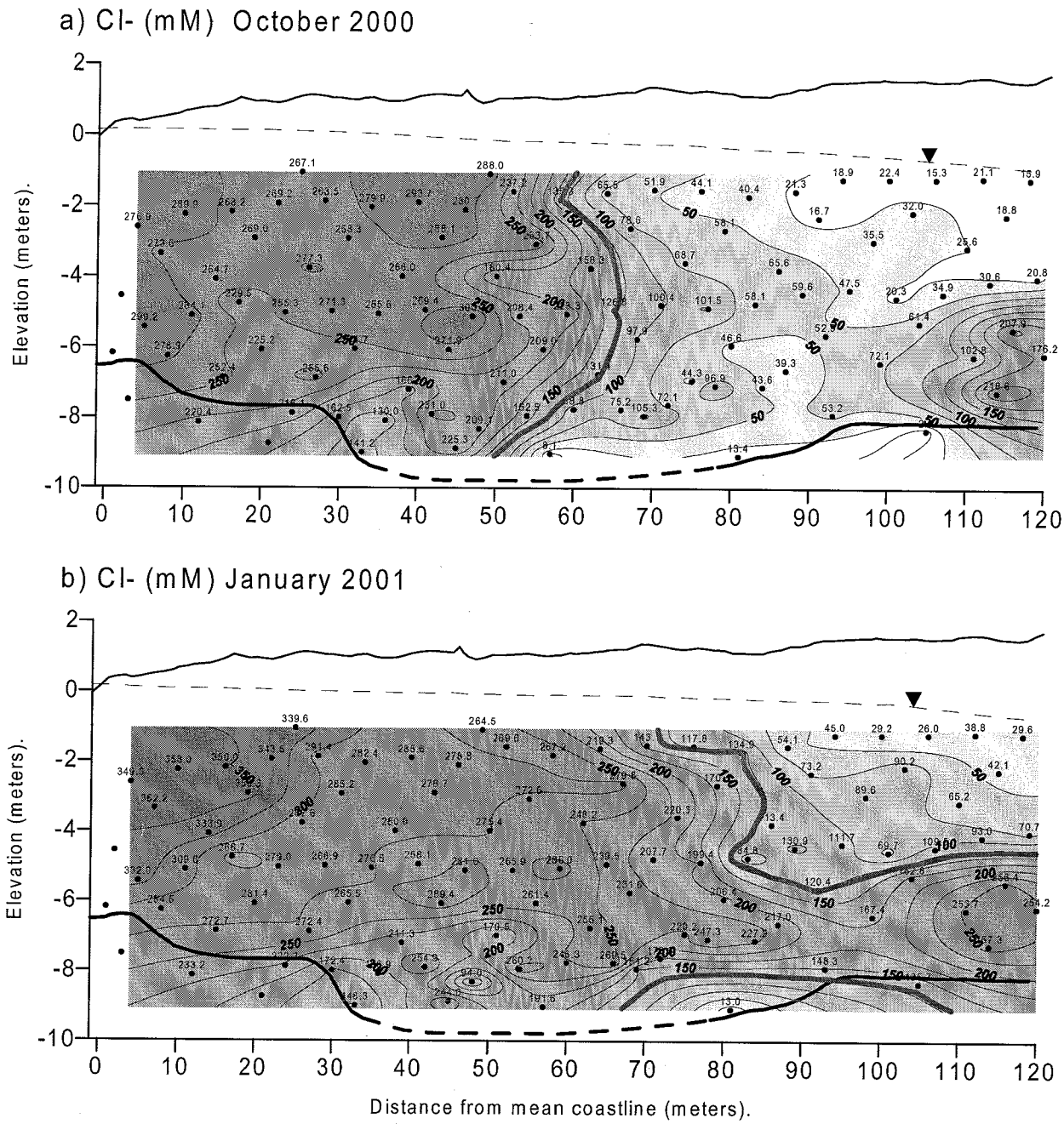

Figure 9.1: Chloride distribution (mM) in the transect, a) October 2000. b) January 2001. The thick grey line represents 50% seawater.

9. CHEMISTRY: INTRUSION EXPERIMENT

While the advancement of the seawater front was monitored by EC measurements at regular intervals the transect was sampled for full hydro-chemical analysis in October 2000 and in January 2001. Sediment cores were taken in October 2000 (Profile 2, Fig. 4.4b) parallel to groundwater sampling. In the following data presentation, focus will be on the October 2000 data where both water and sediment analysis exists. The data from January 2001 will only be introduced to the extent that they add dimensions to the findings of the October data.

9.1 Groundwater chemistry: intrusion

The landward head gradients not only forces fresh surface seawater into the aquifer, but also transports the pre-existing mixing zone, with its chemical characteristics, into the aquifer ahead of the surface seawater front. This zone can be characterised by a high alkalinity, a high concentration of sulfide, high pH-values and depletion of sulfate relative to chloride.

9.1.1 Chloride

In October 2000 the main chloride front, roughly representing the intruding seawater (50% seawater contour), is located about 65 m from the coast (Fig. 9.1a). The concentration profile across this front is skewed with a steep concentration increase from the 50% seawater contour to the 90% seawater contour over a distance of 10 to 20 m. The change in concentration from 50% to 10% seawater is more gradual over a distance of 30 to 50 m reflecting the pre-existing mixture of inundating seawater and freshwater being transported inland ahead of main front. All parts of the transect is therefore to some extent affected by seawater at this time. An anomalous zone of high chloride concentrations (100 to 200 mM) is located at 100 to 120 m, ahead of the main seawater front at an elevation –4 to –8 m. Upward leakage of less saline water from the aquifer beneath can be seen in zones from 30 to about 60 m from the coast. Except at 40 to 50 m where, near the bottom (–7 to –9 m), surface seawater seem to have moved downward.

In January 2001 the seawater front had advanced additional 15-20 meters, as compared to October 2000, to a position about 85 m from the coast (Fig. 9.1b). The main front and the high conductivity

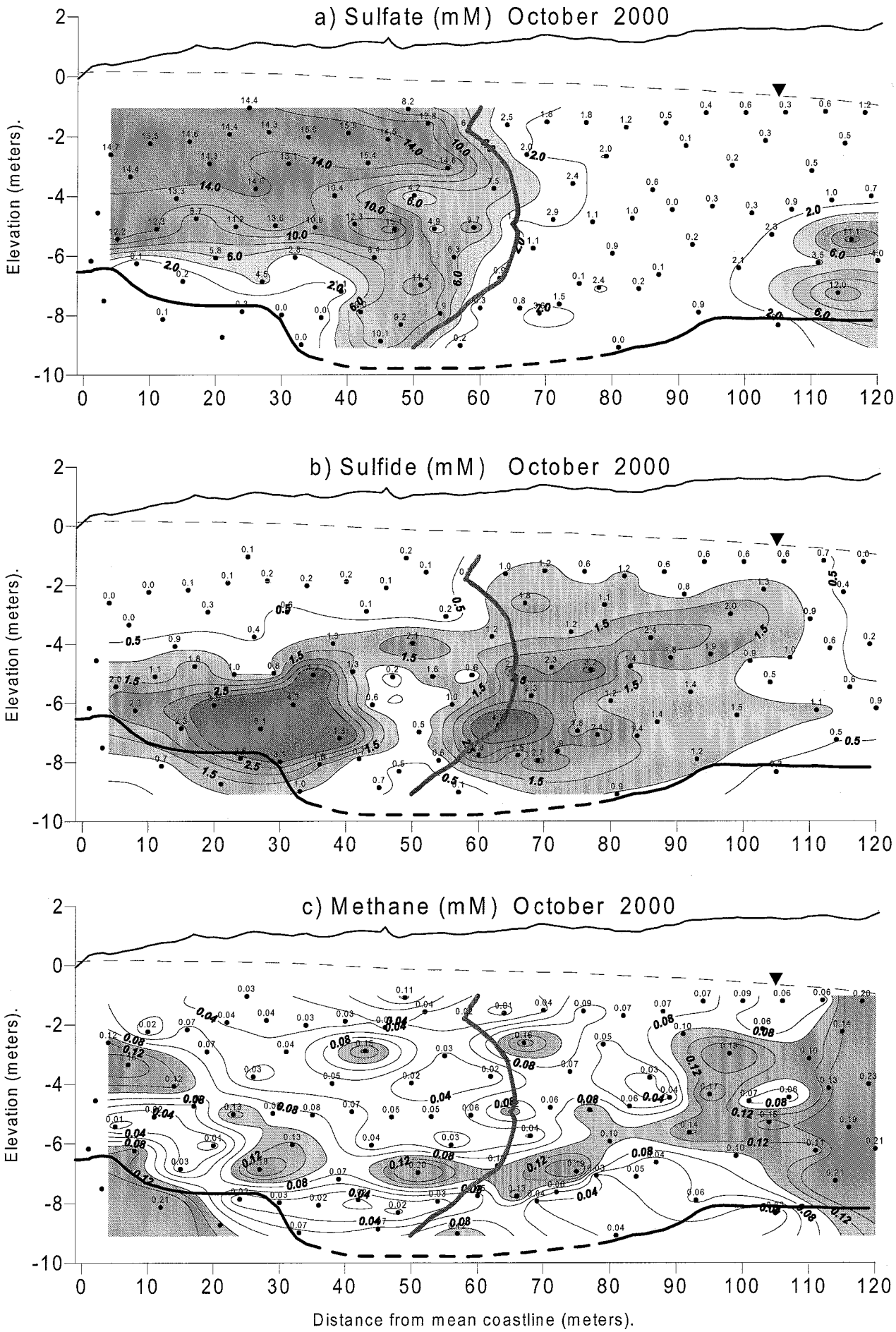

Figure 9.2: a) Sulfate (mM) b) sulfide (mM) and c) methane (mM) distribution in the transect October 2000.

zone (from 100 to 120 m) are now connected by high chloride concentrations. At 0 to 25 m from the coast an increased chloride concentration between 300 to 360 mM are now observed reflecting the appearance of the high salinity winter surface seawater seen in Figure 6.2. In the January 2001 chloride distribution the upward leakage of less saline water from the aquifer beneath from 30 to about 60 m is particular clear and seem to affect the transect groundwater chemistry in a zone up to an elevation of at least –6 m.

9.1.2 Redox-conditions

Sulfate

The sulfate distribution of October is shown in Fig. 9.2a. A sulfate concentration higher than 1 mM and up to 15.5 mM is seen to cover the zone from the coast and inland to 60 - 80 m. In the remaining brackish parts of the transect inland from 60 to 80 m sulfate is also present although in low concentrations from 0.2 to 1 mM. From 100 to 120 m at an elevation of –4 to –8 m there is a zone with high sulfate concentrations, up to 12 mM, clearly indicating a recent surface seawater origin of the salt groundwater in this zone. In association with the peat layer near the coast from 0 to 35 m, below –6 m, the sulfate concentration is low. The intruding seawater apparently only slowly penetrates the low permeable peat. But also a zone of 1 to 2 m in thickness above the peat layer has lower sulfate concentrations (1 to 13 mM) than the intruding seawater above –5 m. The low sulfate concentration may be due to one of or a combination of several conditions: Lower hydraulic conductivity (and thereby intrusion velocity) towards the peat layer (Fig. 5.8); Longer travel distance for the intrusion of fresh seawater due to the geometry of the off shore portion of the aquifer. Mixing with sulfate depleted groundwater leaking up from the aquifer below (especially at the zone from 30 to 40 m) (Figs. 8.4 and 8.5); Increased organic matter reactivity towards the peat layer and thus increased sulfate reduction rate. A high sulfate reduction rate as the sole explanation is improbable, because it would imply a reduction rate in the order of 25 to 30 mM SO_4^{2-}/yr.

A low sulfide concentration (0 to 0.2 mM) observed from the coast and landward to 50 m and above an elevation of –4 m must reflect the presence of freshly intruded surface seawater (Fig. 9.2b). Apart from this, two distinct zones dominate the sulfide distribution with a high concentration up to 4 to 6 mM. The zone with the highest concentration (6 mM) is situated from 0 to 40 m below –4 m. The other zone with somewhat lower concentrations is more diffuse and located from 60 m to about

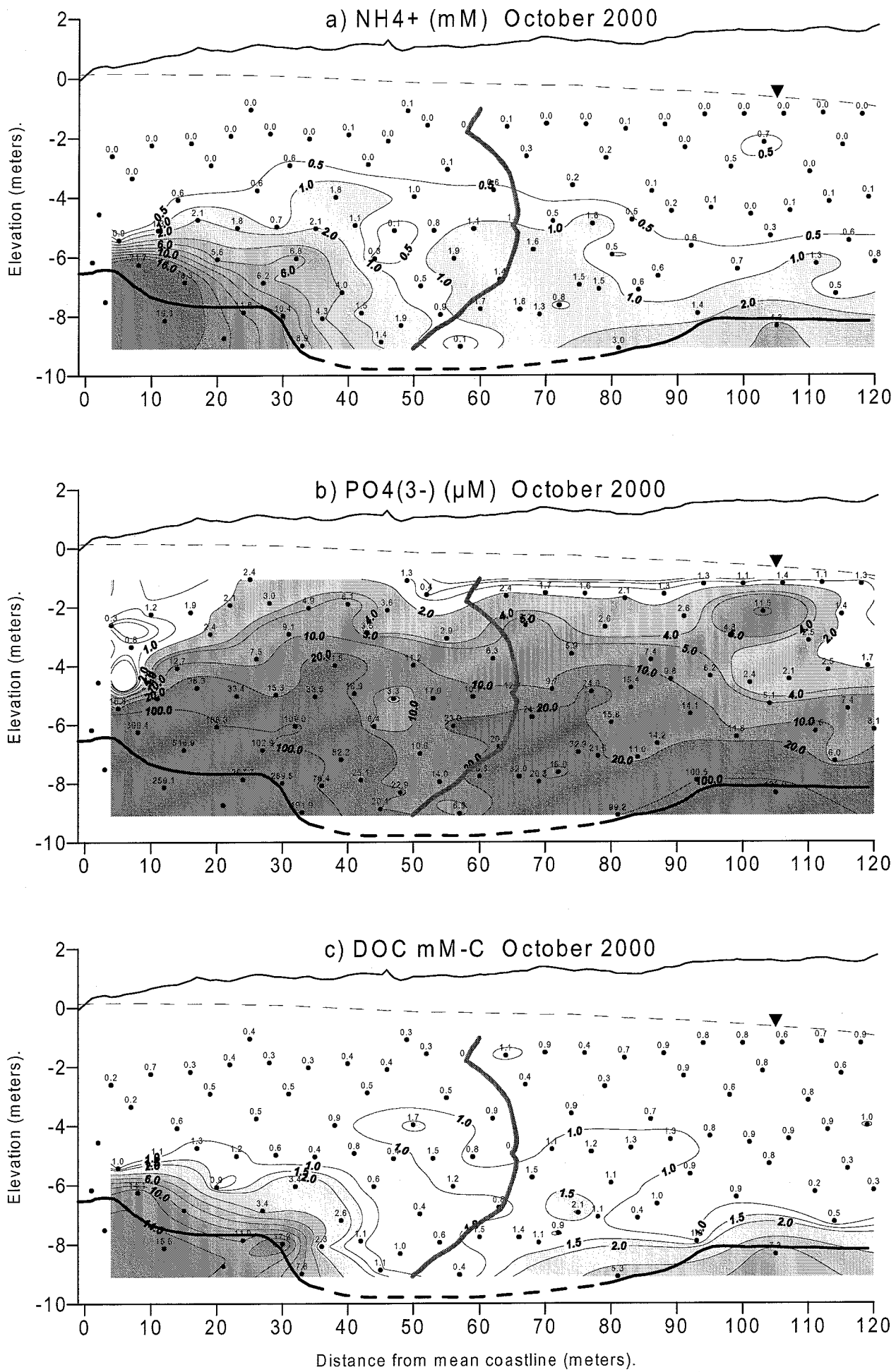

Figure 9.3: a) Ammonium concentrations (mM), b) Phosphate concentrations (µM) and c) DOC (mM-C) in the transect, October 2000.

110 m slightly in front of the 50% seawater contour and covering the full depth of the aquifer. In the later zone the major part of the sulfide is probably related to sulfide formed in the original mixing zone (see Fig. 6.5c) and is transported into the aquifer ahead of the intruding surface seawater. The sulfide in the former zone close to the coast could have the same origin but just being transported more slowly. The separation/break between the two zones from 45 to 55 m must be due to intrusion surface seawater low in sulfide percolating downward as indicated by the high chloride (Fig. 9.1a) and high sulfate (Fig. 9.2a) concentrations. It is difficult to accurately determine how much of the sulfide originates from sulfate reduction of the freshly intruded seawater sulfate. The total sulfide mass in October 2000 seems to be larger than in August 1999 (Fig. 6.5c) and to cover a larger area, but the peak concentrations of October are smaller than in the August data. The $\Delta m_{sulfate}$ values of October 2000 (not shown) basically mimic the sulfide distribution with large sulfate depletion correlating with high sulfide concentrations. The loss of sulfate is not completely balanced by the sulfide measured and deficits in the sulfur balance of more than 50% are observed.

Methane

In October there is very little methane (Fig. 9.2c) left in the transect, generally below 0.2 mM showing that it has been flushed from the transect and perhaps to some extent methane has been re-oxidised by the intruding sulfate (according to equation 7.4).

Ferrous iron

Fe^{2+} concentrations (not shown) are slightly elevated (up to 30 μM) in the upper and landward part of the transect (above –2 m), in particular from 100 m and landward. This is most likely due to the drawdown in the water table exposing sulfidic minerals to partial oxidation with atmospheric oxygen. The effect seems largest near the pumping well field where the drawdown is largest (Fig. 8.2).

The redox-parameters of the January dataset does not ad much to the findings of October apart from the continual advective landward transport and the redox-parameters of January are therefore not shown. In conclusion sulfate brought in with the surface seawater seem to have become the prevailing dissolved electron acceptor. Dissolved oxygen could not be detected and must have been oxidised in the seafloor. The low concentrations of methane suggests that methanogenesis is of no importance.

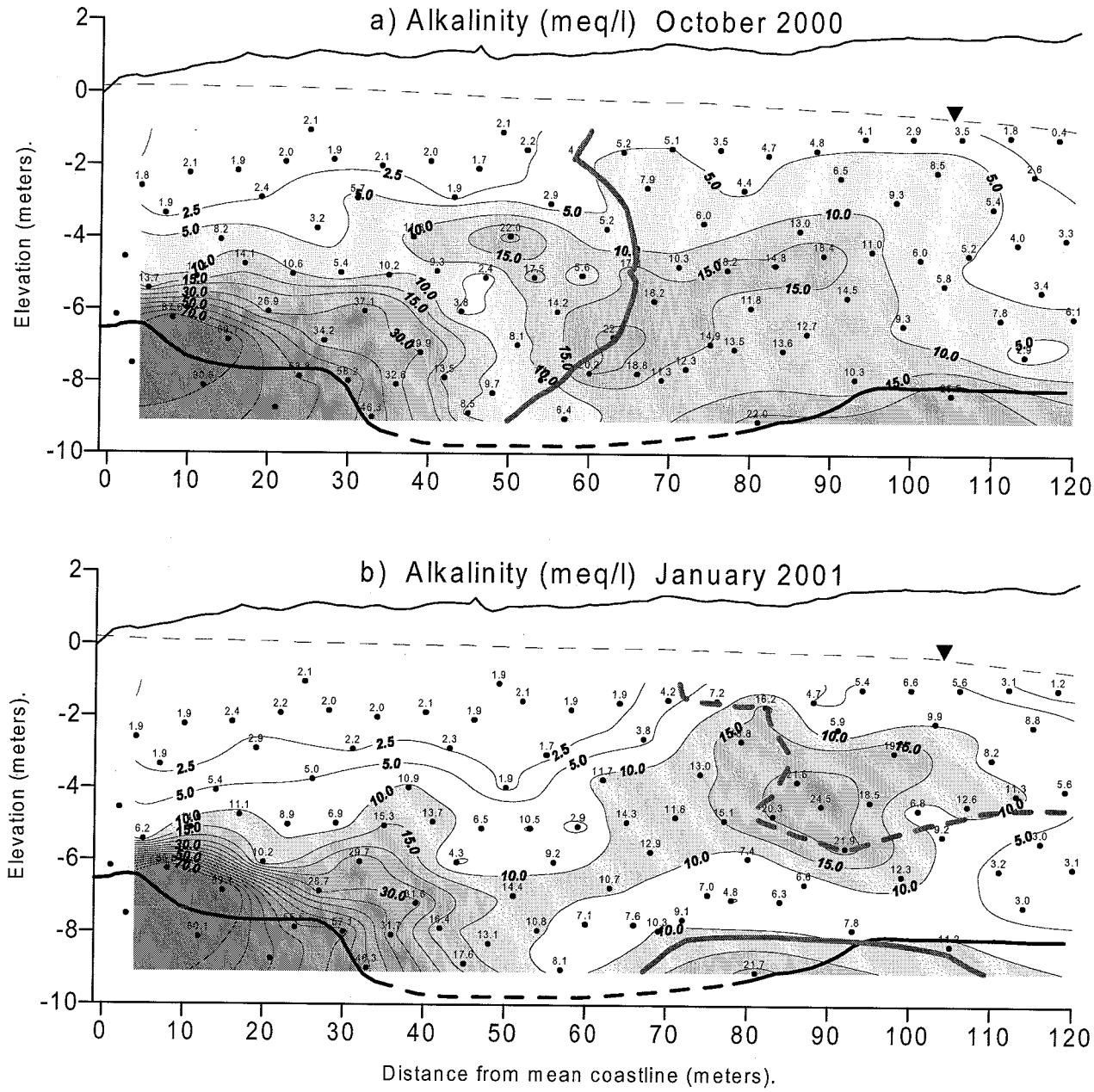

Figure 9.4: Measured alkalinity (meq/l) in the transect, a) October 2000, b) January 2001.

9.1.3 Decomposition of organic matter

It is hard to estimate the extent of organic matter decomposition occurred during the course of the intrusion experiment as superimposed on the organic matter decomposition which took place prior to the experiment. Considering the short duration of the intrusion experiment the additional decomposition occurring during the experiment is probably small. The distributions of ammonium, phosphate and DOC in October (Fig. 9.3) seem largely a consequence of the advective landward transport of the pre-existing distribution. Ammonium and DOC follow the distribution pattern described for sulfide, with a landward transport of ammonium and DOC from the lower part of the original mixing zone, perhaps with minor retardation of the ammonium due to ion exchange. However, phosphate (Fig. 9.3b) show an increase in concentration relative to the August 1999 (Fig. 6.7b), from ~ 2-5 μM and up to a general level of 10-30 μM, indicating some phosphate release, perhaps related to the change in salinity.

9.1.4 Alkalinity and pH

The alkalinity distribution of October 2000 (Fig. 9.4a) largely resembles the sulfide distribution (Fig. 9.2b). In October 2000 a low alkalinity of 2 mM is observed from the coast to 50 m inland and down to an elevation of –4 m reflecting surface seawater values. Apart from this two zones of high alkalinity are observed roughly in the same locations as the high sulfide zones. One zone is near and above the bottom peat layer, with an alkalinity up to 40 meq/l, and the other, with an alkalinity up to 20 meq/l, is located from 55 to 100 m and below –4 m. Again this distribution can probably largely be attributed to the original alkalinity distribution being transported into the aquifer ahead of the intruding seawater. The splitting of the zone into two parts is again caused by a combination of slower transport near the peat layer and the downward percolation of low alkalinity intruding surface seawater at the zone from 45 to 55 m, as also indicated by the chloride distribution (Fig. 9.1a). The alkalinity distribution of January 2001 (Fig. 9.4b) is basically as in October with a low alkalinity in the upper part of the transect (> –4 m) near the coast inland to 65 m. The high alkalinity zone near the coast (0 – 40 m) associated with the bottom peat layer is has not changed or moved. The high alkalinity zone at the seawater front has been displaced landward to around 80 - 100 m and apparently also upward. This upward motion is not easily recognisable from the chloride distribution (Fig. 9.1b).

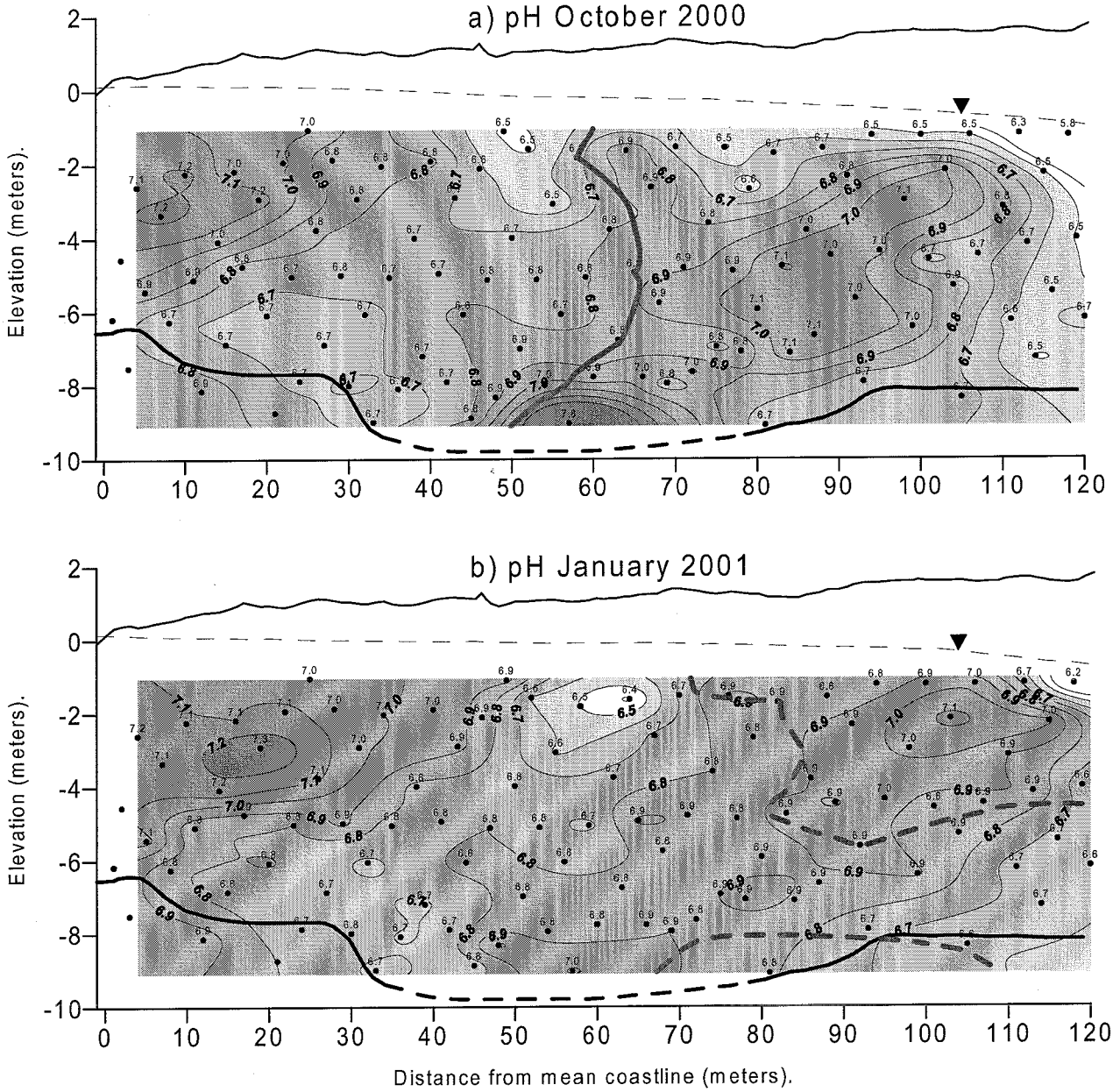

Figure 9.5: Measured pH in the transect a) October 2000, b) January 2001.

From the coast and 20 m into the transect the pH of October (Fig. 9.5a) has increased (to a maximum of 7.23) compared to the situation prior to pumping, especially in the upper part (> -4 m). This elevated pH reflects the influence of the higher pH in surface seawater. Between 20 and 60 m from the coast there is a zone with lower pH values ranging from 6.5 to 7. The zone with low pH values to some extent reflects the landward transport of the aquifer saltwater with comparable pH-values in the lower seaward part of the original mixing zone (Fig. 6.8a). In the upper parts of this zone, where the presence of fresh sulfate indicate a recent seawater origin, the low pH must rather reflect the effects created by mixing of aquifer groundwater with surface seawater as illustrated in Figure 7.1a or some reaction buffering pH. A zone with an elevated pH (~7) is seen ahead of the 50% seawater contour partially coinciding with the zone of high alkalinity, but 10-20 m further landward. Also prior to the intrusion experiment the high pH zone was situated further landward than the high alkalinity zone. However, the pH is on average half a unit lower than in the mixing zone of August 1999 (Fig. 6.8a).

In the January data the zone of high pH being pulled ahead of the seawater front has moved landward to 90 – 110 m (Fig. 9.5b). The pH for this zone may have decreased slightly compared to October. The upward motion as observed for alkalinity is particularly clear for pH (Fig. 9.5b). The upward flow component inferred from the pH and alkalinity could be due to the seaward dipping layers of lower permeability indicated by the GPR-profile (Fig. 5.5), the peat layers in the el-logs (Fig. 5.7) and the steep head gradient of the same zone during the intrusion experiment (Fig. 8.4). The landward flow is therefore forced up along these layers.

9.1.5 Distribution of major cations October

The October 2000 distribution of the major cations Ca^{2+}, Na^{+}, Mg^{2+} (Fig. 9.6) and K^{+} (not shown) follow on first inspection generally the distribution of chloride (Fig. 9.1a). There is a somewhat higher concentration of Ca^{2+} at the 50% seawater contour (from 50 to 70 m) at –4 to –7 m, which could be due to displacement of Ca^{2+} from the cation exchanger by the intruding seawater cations Na^{+} and Mg^{2+}. However, the excess Ca^{2+} could also be caused by advective transport of Ca^{2+} from a zone with a high Ca^{2+} concentration originally present above the peat layer from 0 to 20 m around an elevation of –6 m (Fig. 6.10c). It is also hard to detect the expected decrease in the concentrations of Na^{+} and Mg^{2+} by the proposed displacement by just looking at the concentration

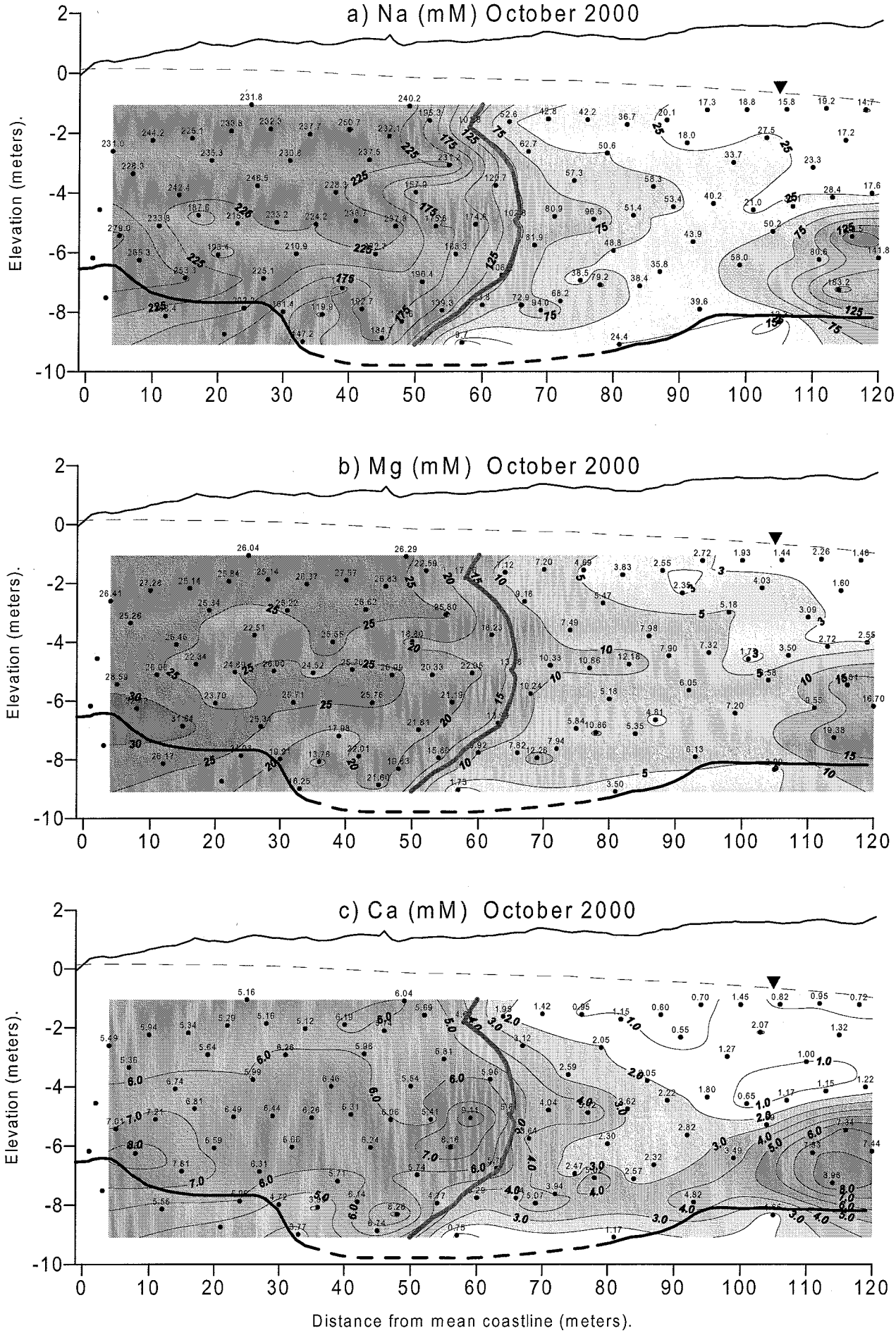

Figure 9.6: Concentrations of a) Na+, b) Mg2+ and c) Ca2+ (mM) in October 2000.

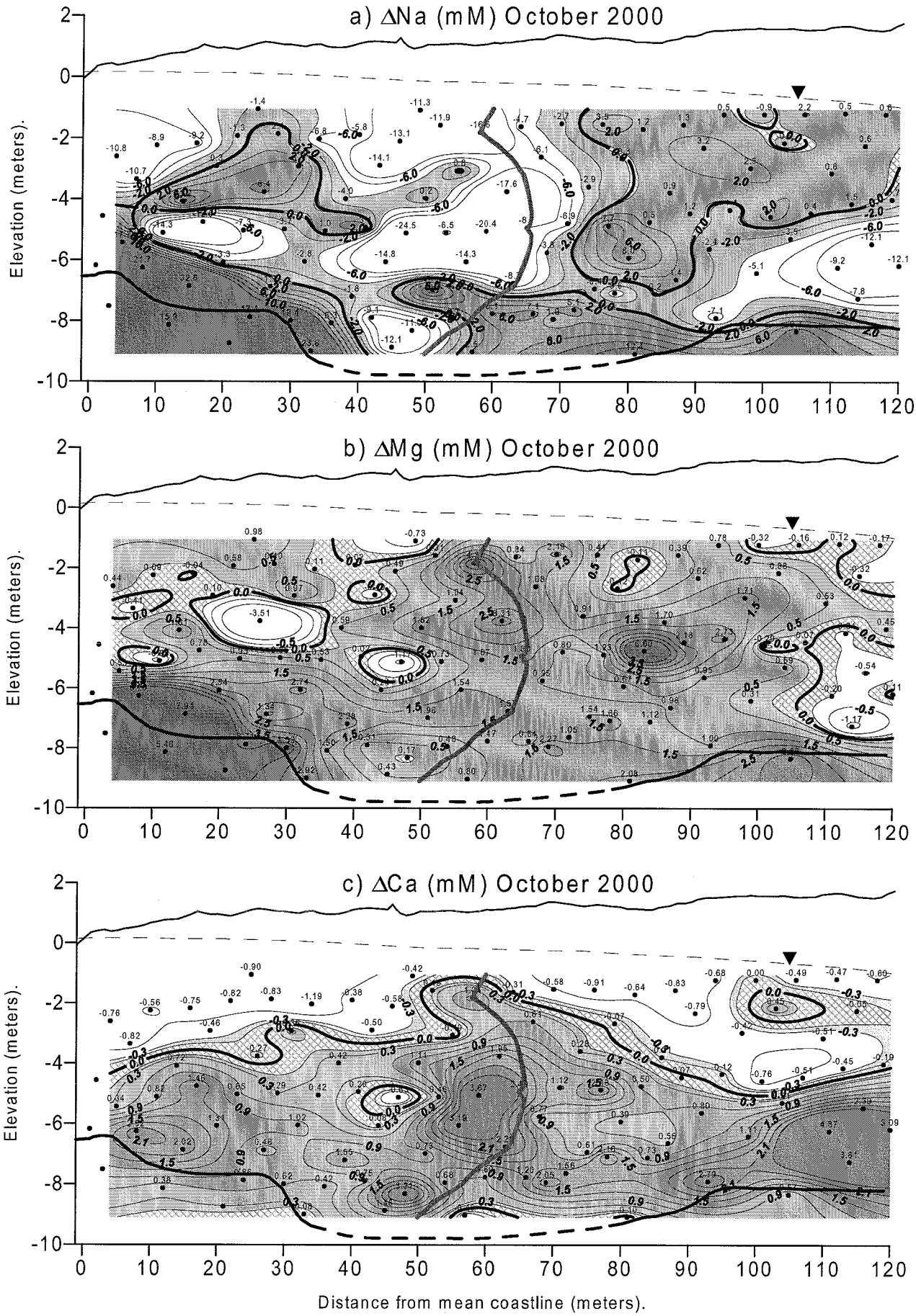

Figure 9.7: Enrichment or depletion compared to conservative mixing of a) ΔmNa, b) ΔmMg and c) ΔmCa (mM) in October 2000. The crosshatched areas represent a Δmi of 0 + 0.2 mM (i.e. essentially little or no depletion or enrichment).

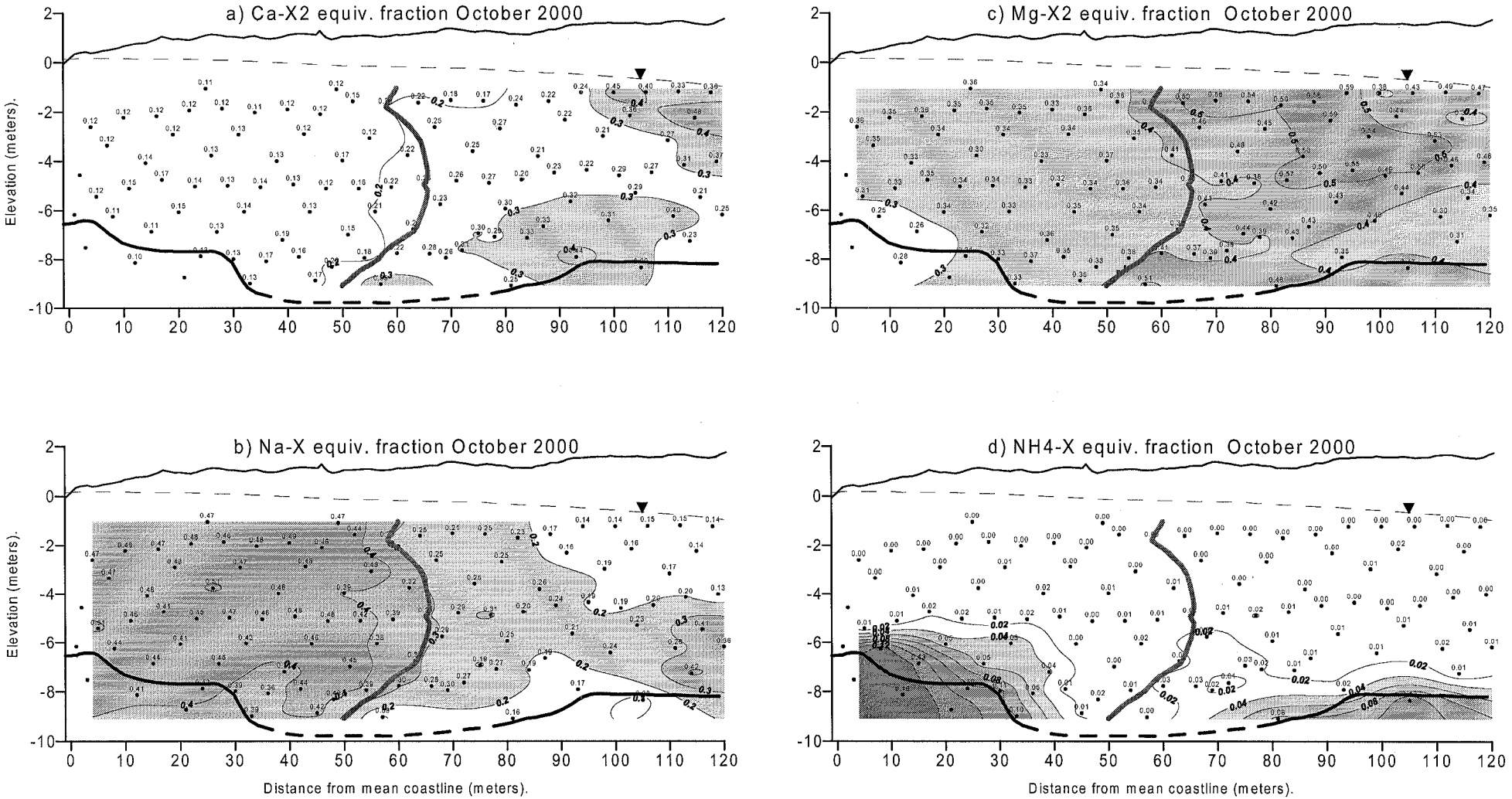

Figure 9.8: Equivalent fractions of a) Ca2+ b) Mg2+ c) Na+ and d) NH4+ (October 2000) on the exchanger calculated from the groundwater composition using PHREEQC and the standard selectivity coefficients in the PHREEQC database.

distributions (Fig. 9.6a and b). The seawater concentrations of Na^+ and Mg^{2+} are high compared to the changes expected by the ion exchange reactions. The plots of cation depletion or enrichment compared to conservative mixing (Δm_i-values) give more convincing evidence for the proposed ion exchange processes (Fig. 9.7). The Δm_{Ca} (Fig. 9.7c) is generally positive below –4 m with a relatively high Ca^{2+} enrichment of about 4 mM at 50 to 60 m corresponding to the Ca^{2+} peak in Figure 9.6c. In the zone from 50 to 70 m and above –4 m enrichment for Mg^{2+} of 3-4 mM is seen. This can be explained by the original distribution of cations on the exchanger (fig 6.17 and 6.25). In the upper zone, between 25 and 65 m (Fig. 6.25), the exchanger is heavily dominated by Mg^{2+} (with $\beta_{Mg} \sim 0.5$ to 0.7) prior to the experiment. Here the intruding seawater Na^+ displaces Mg^{2+} instead of Ca^{2+}. Part of the explanation is the salinity increase, favouring monovalent cations on the exchanger over divalent cations. From 70 m and towards the coast negative values for Δm_{Na} (down to a minimum of – 20 mM) is generally found to correlate with the zones enriched in Ca^{2+}. A discontinuous zone depleted in Mg^{2+} is also observed in the intruding seawater with negative Δm_{Mg}-values down to –3.5 mM. This zone of negative Δm_{Mg} is closer to the coast, restricted to a zone from 0 to 50 m and above –5 m. The depletion of Mg^{2+} is retarded relative to the depletion of Na^+.

Much of the disturbed pattern of the Δm_i-values in the transect is inherited from the disorderly cation distribution following the percolation of inundation seawater (Fig. 6.23). As the result ion exchange fronts develop at the same time at different places in the aquifer, when the seawater intrusion proceeds. Also the spatial variation in the hydraulic conductivity and variation in the size of the CEC could contribute to the messy distribution of Δm_i-values. In the zone of high hydraulic conductivity (and salinity) from 100 to 120 m at –4 to –7 m the pattern of Ca^{2+} enrichment ($\Delta m_{Ca} \sim$ 5 mM) and depletion of Na^+ ($\Delta m_{Na} \sim$ -12 mM) and Mg^{2+} ($\Delta m_{Mg} \sim$ -1 mM) is particularly clear (Fig. 9.7). The large enrichment of Ca^{2+} in this zone probably reflects a high original Ca^{2+}- equivalent fraction on the cation exchanger ($\beta_{Ca} \sim 0.7$ to 0.8, Fig. 6.17 and 6.25).

9.1.6 Calculated cation composition on the cation exchanger October

The exchanger equivalent fractions are calculated for all sampling points in the transect for the October data (Fig 9.8) broadly confirming the findings of Figure 9.6. Na^+ is dominating the exchanger in the saline zone from the coast to 50 m with β_{Na} of 0.4 to 0.5. In the landward part of the transect β_{Ca} is only over 0.3 in the upper landward corner, from 100 to 120 m above –4 m and in

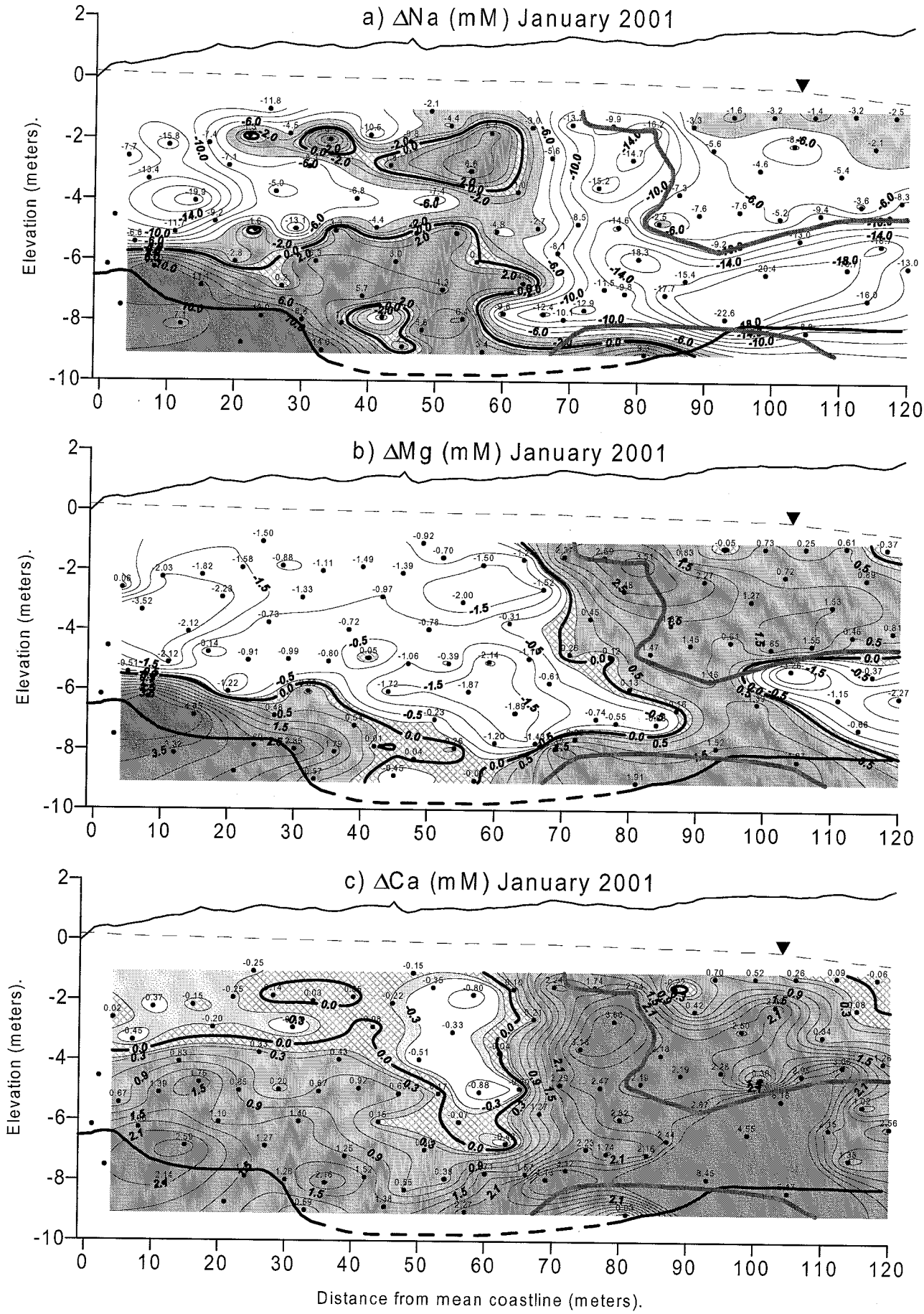

Figure 9.10: Enrichment or depletion of a) ΔmNa, b) ΔmMg and c) ΔmCa (mM) in January 2000. The crosshatched areas represent a Δmi of 0 + 0.2 mM (i.e. essentially little or no depletion or enrichment).

a lower zone (–6 to –9 m) from 75 to 110 m. The upper corner corresponds to the least seawater affected part of the transect with a seawater fraction of 0.10. Mg^{2+} dominates the exchanger in a zone from 60 to 110 m above –5 m with β_{Mg} of 0.5 to 0.6. The vertical division of the transect at –5 m from roughly 60 to 110 m with Mg^{2+} dominating the upper zone and Ca^{2+} the lower must be caused by a combination of the presumed depletion of carbonate minerals in the upper zone and the recent loading of the exchanger in the upper part with seawater derived Mg^{2+} from the inundation event in March. During the same inundation event the lower zone was enriched with Ca^{2+} by ion exchange processes related to the density plume migration. During the intrusion, Na^{+} in the seawater is therefore displacing Mg^{2+} in the upper part of the transect and Ca^{2+} in the lower part.

9.1.7 Distribution of major cations January

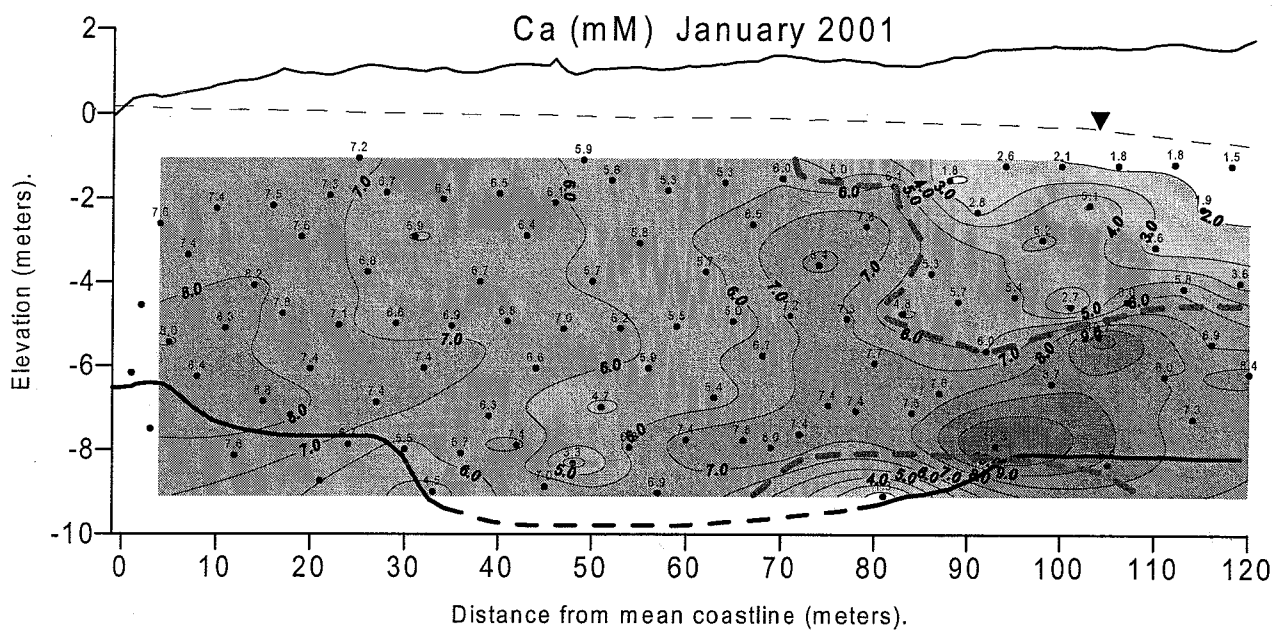

Figure 9.9: Concentrations of Ca2+ (mM) in January 2001.

In January the Ca^{2+} peak (Fig. 9.9) has become larger and more pronounced than in the October data. A zone with Ca^{2+} of about 7 to 8 mM from 70 to 80 m is now almost covering the full depth of the transect reflecting that the intruding seawater is now entering a part of the aquifer previously less affected by seawater and with an exchanger dominated by Ca^{2+}. The increased Ca^{2+} also reflects the accumulating effect of the landward progression. Once more it is hard to see the

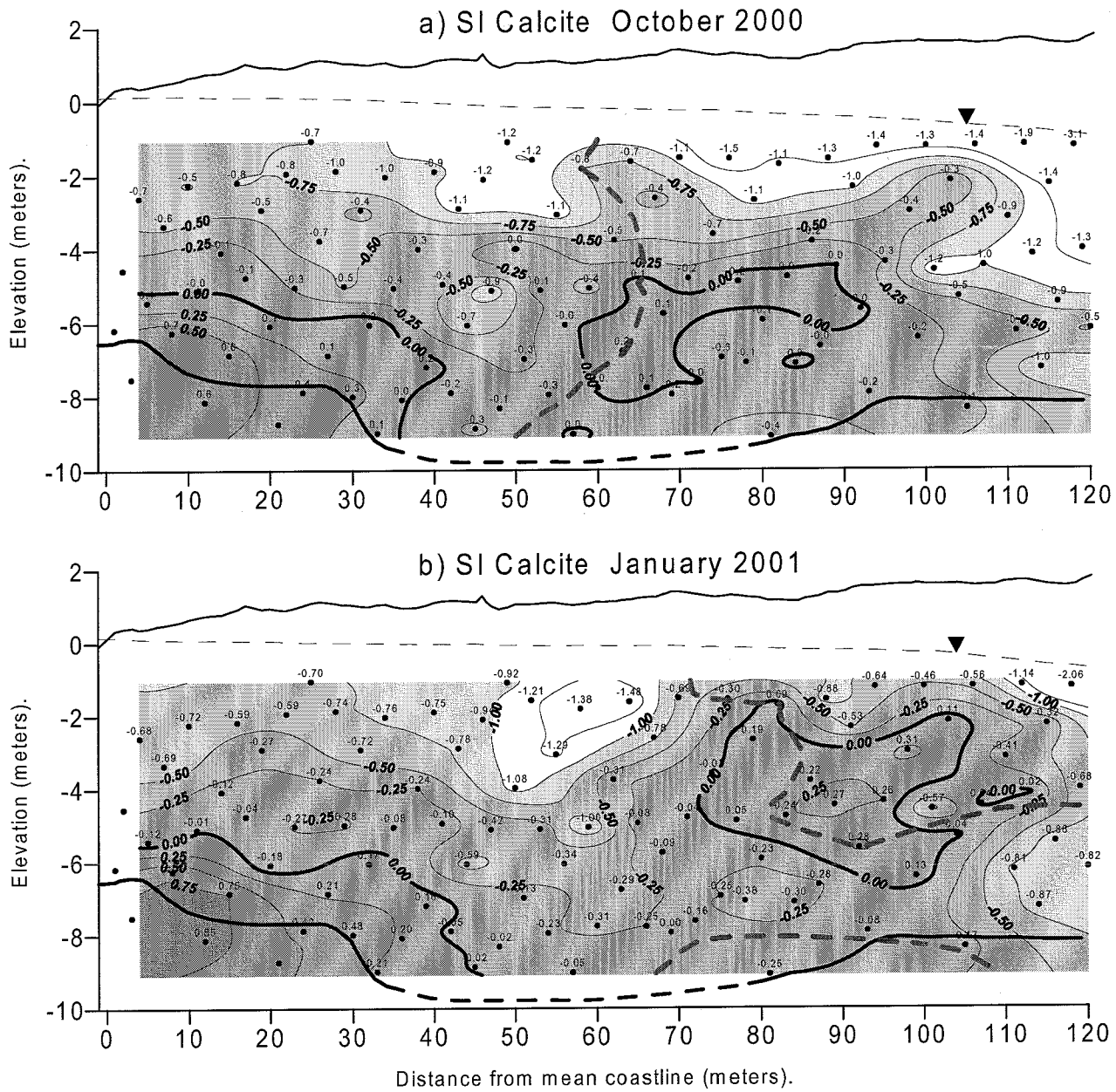

Figure 9.11: Saturation state (SI) for calcite calculated using PHREEQC, a) October 2000. b) January 2001.

expected concurrent changes in the measured Na^+ and Mg^{2+} (not shown) and these parameters at first inspection seem to follow the distribution of Cl^-. The plots of enrichment or depletion compared to conservative mixing (Fig. 9.10) are on the other hand clearer and more pronounced than for the October data (Fig. 9.7). The zone of positive Δm_{Ca} with values up 8.5 mM from 70 to 110 m (Fig. 9.10c) correlates nicely with the zone of negative Δm_{Na} (Fig. 9.10a) with values as low as –22 mM. In a zone from the coast to 70 m inland and above –6 to –7 m Δm_{Mg} is now negative with values around 0 to –3 mM, indicating that Mg^{2+} is going on to the exchanger possibly displacing Na^+. This is partly supported by the fact that, from 40 to 60 m, a zone with surplus of Na^+ up to 6 mM is now observed. This zone also partly correlates with a zone of slight depletion of Ca^{2+} of –1 mM and a zone of enhanced Mg^{2+} depletion down to –2 mM. The observed pattern could be caused by a slight salinity decrease corresponding to the summer surface seawater. Such a decrease would cause a salinity effect favouring Ca^{2+} and Mg^{2+} on the exchanger and displacing the monovalent Na^+ however there is not a very convincing drop in the chloride concentration.

9.1.8 Saturation states for solid phases

For calcite ($CaCO_3$) (Fig. 9.11a) the saturation index for October was generally negative although increasing with depth to SI > –0.4 below –4 m. Two zones of saturation to slight supersaturation are observed. One zone is related to the bottom peat layer near the coast, as was also observed in the August 1999 data (Fig. 6.26). The other zone is situated on the intruding seawater front, and corresponds to the zone of high alkalinity (Fig. 9.4b). The calcite saturation of this later zone seems therefore related to alkalinities above 15 meq/l. The existence of this zone of calcite saturation must largely be caused by the landward transport of the high alkalinity zone.

Compared to the October 2000 SI for calcite (Fig. 9.11b) the zone of supersaturation for calcite, related to the seawater intrusion front, has in January 2001 increased in both value (SI up to 0.3) and size (Fig. 9.16). This increase in SI for calcite is probably related to the increased Ca^{2+} concentration of the same zone caused by the ion exchange reactions. It is thus likely that calcite may precipitate in this zone. A zone of increased calcite subsaturation (–0.25 > SI > –1.4) has now developed behind the seawater front, 45 to 65 m from the coast. It seem as if this zone is related to both the low pH (Fig. 9.5b), the low alkalinity (Fig. 9.4b) and to the Ca^{2+} depletion (Fig. 9.9).

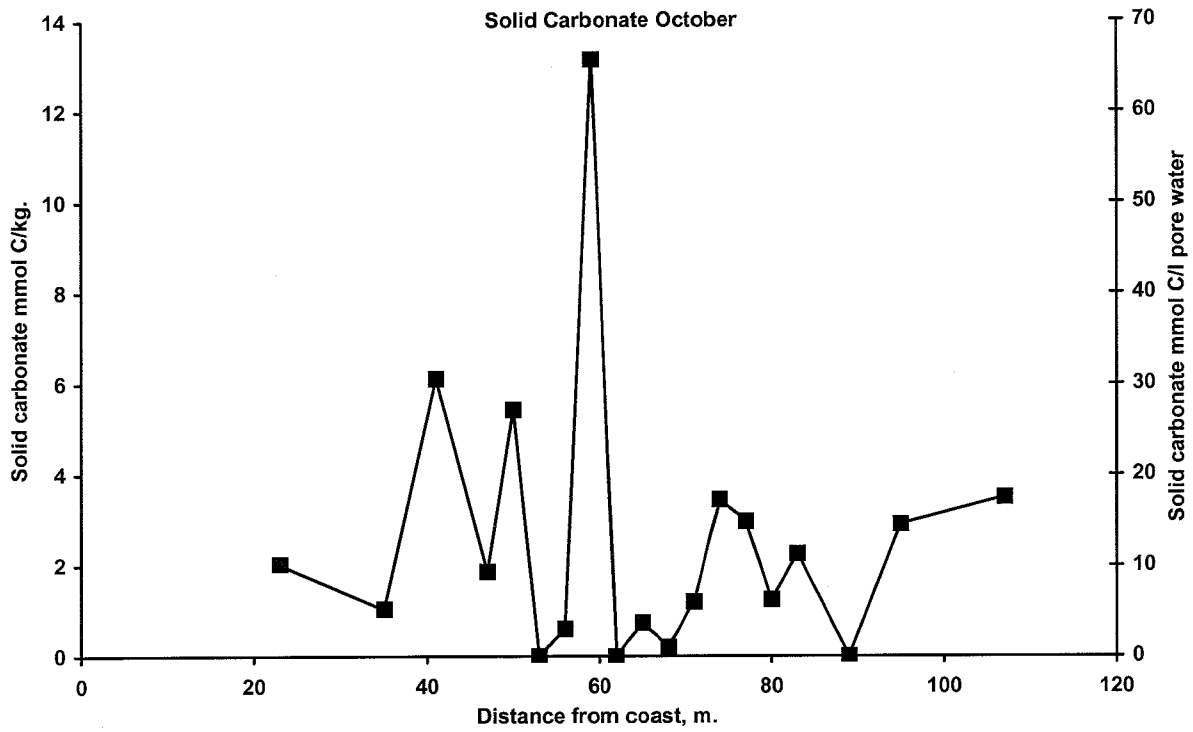

Figure 9.12: Sediment inorganic carbon content in mmol IC/kg (left axis) and mmol IC/l pore water (right axis) for sand samples. Samples are from the profile line 2 (October) Figure 4.4b.

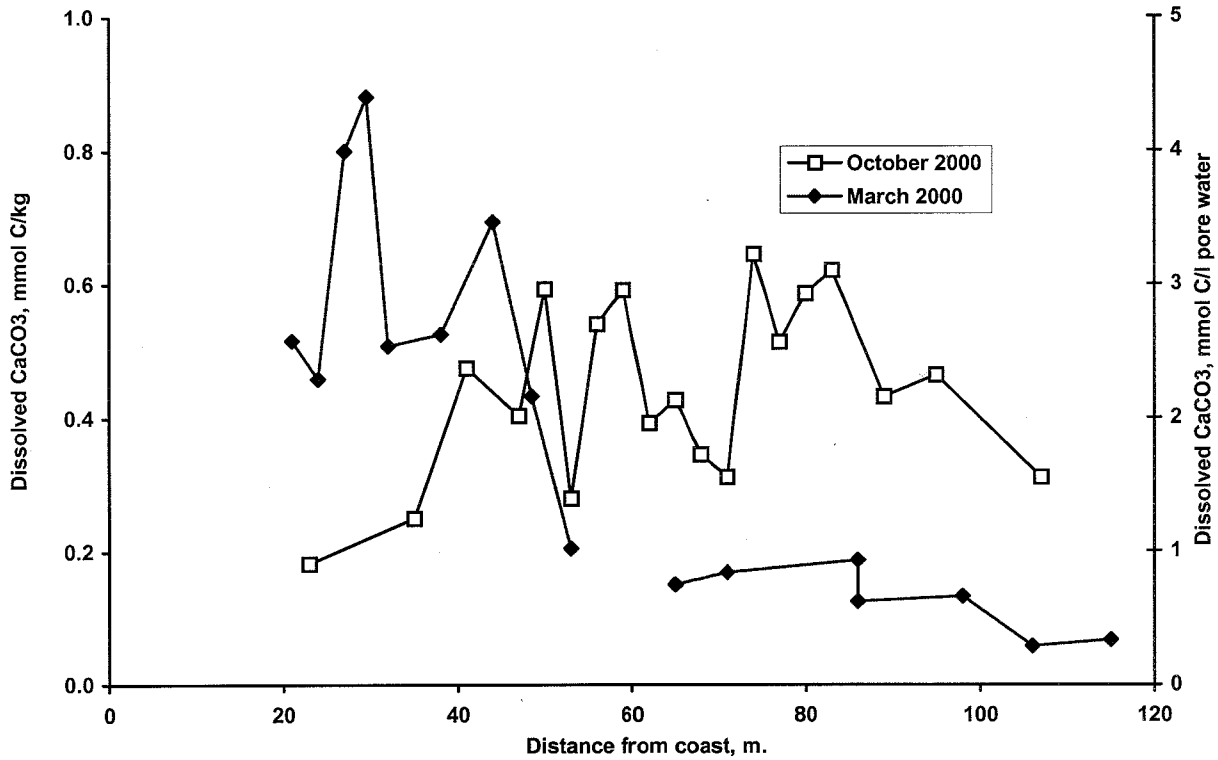

Figure 9.13: Amount of dissolved inorganic carbon (IC) in mmol IC/Kg (left axis) and mmol IC/l pore water (right axis), in NH_4Cl-supernatants for the sand core samples of March and October 2000 (peat sample are omitted).

The calculated saturation index for other minerals, in October, generally exhibits the same patterns as for the original situation. The SI for aragonite and dolomite mimics that of calcite, with a slightly lower SI for aragonite and a somewhat larger field of supersaturation for dolomite than that for calcite. In the whole transect subsaturation was still found for gypsum ($CaSO_4 \cdot 2H_2O$), siderite ($FeCO_3$), rhodochrosite ($MnCO_3$), vivianite ($Fe_3(PO_4)_2$) and amorphous FeS. For hydroxyapatite ($Ca_5(PO_4)_3(OH)$) supersaturation is still restricted to the bottom peat layer. The saturation indices for other minerals have, in January, not changed significantly compared to the October indices.

9.1.9 Dissolution or precipitation of calcium carbonate

Sedimentary carbonate

The sediment inorganic carbon (SIC) content of 20 core samples in the October profile (profile 2, Fig. 4.4b) is shown in Figure 9.12. The content varies between 0 and 7 mmol IC/kg (with an outlier of 13.3 mmol IC/kg). The sandy parts have an average content of 2.8 mmol IC/kg (or 13.3 mmol IC/l pore water), which is slightly lower than for the March data, but not significant considering the large fluctuations (Fig. 6.18). For the peat sample St11 (value not shown) the carbonate content is high, 103 mmol IC/kg, and here shell fragments have been identified. Figure 9.12 shows that small amounts of carbonate minerals are present in the transect, at least along the sampling line in Figure 4.4b.

The content of readily dissolvable inorganic carbon, obtained from the NH_4Cl exchange supernatants, could maybe represent a calcite pool of finely disseminated calcite crystals. For October 2000 (Fig. 9.13) the readily dissolvable inorganic carbon shows a somewhat different pattern compared to the data from March 2000 (Fig. 6.19), which are included in Figure 9.13 for comparison. In a broad zone from 40 to 90 m from the coast 2-3 mmol IC/l pore water was measured in October. This is 1-2 mM more than in the March data for roughly the same zone. The zone of elevated dissolvable IC coincides with the zone exhibiting calcite saturation to supersaturation in the October water chemistry data (Fig. 9.11a). This could perhaps indicate that about 1-2 mM of calcite has precipitated with the passing of the intruding seawater front.

At the zone from 20 to 40 m from the coast there was more than 2-4 mmol IC/l pore water observed in March and somewhat less 1-2 mmol IC/l pore water in October. Here dissolution of calcite may

possibly have occurred perhaps due to acidifying processes such as sulfate reduction, proton buffering or effects mixing of seawater and freshwater as the reduced pH-values may indicate. However, these interpretations should not be given too much emphasis because the method for determination of the readily dissolvable inorganic carbon is rather non-specific and rudimentary. The findings on the basis of Fig. 9.13 are therefore more a suggestion of calcite precipitation/dissolution than direct evidence.

Furthermore the observed variations in the readily dissolvable inorganic carbon are not recognisable in the total amounts of sedimentary carbonate (Fig. 6.18 and Fig 9.12). But the total sedimentary inorganic carbon content is an order of magnitude higher than the content of readily dissolvable inorganic carbon, reflecting that the dissolution or precipitation of a finely dispersed carbonate mineral phase ($CaCO_3$), as possibly seen here, is not weighting much in the total pool of sedimentary carbonate.

In conclusion

After 6 months and 10 months of pumping in October and January the main surface seawater front has moved 60 m and 80 m, respectively, into the aquifer as indicated by the distributions of chloride and sulfate.

Zones of high concentrations for some chemical species, such as alkalinity, sulfide, and high pH values, can to some extent be explained by the landward conservative transport of the original mixing zone ahead of the intruding surface seawater. The redox-conditions have changed from predominantly methanogenic to sulfate reducing with no or little methane present in the transect and most of the transect containing sulfate. But the accumulated impact of the sulfate reduction after 6 months is probably relatively small and difficult to assess and not readily distinguishable from the previous sulfate reduction in the mixing zone of the natural situation. The distribution of cations, especially Ca^{2+}, seems to be somewhat more affected and deviate some from this conservative advective transport. Ca^{2+} is accumulating on the front possibly displaced by the seawater derived cations Na^{+} and Mg^{2+}. This accumulation of Ca^{2+} together with the landward transport of alkalinity from the former mixing zone lead to a zone of calcite saturation and therefore possibly also a precipitation of calcite as indicated by Figure 9.13. However, this zone seems to be followed by a zone of subsaturation and decreasing pH values.

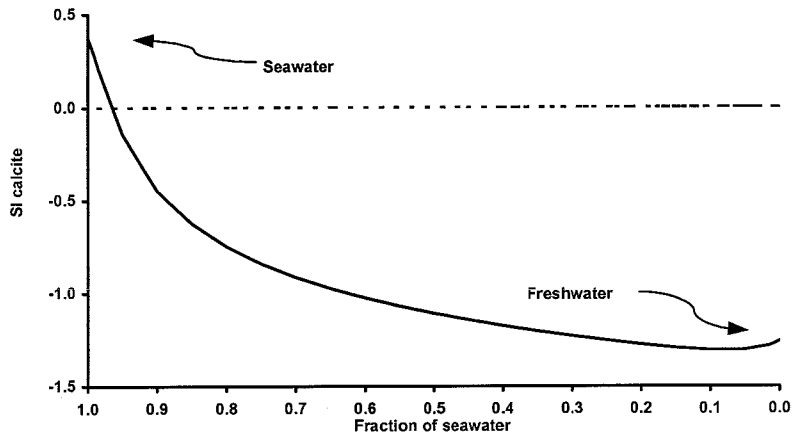

Figure 10.1: Calcite saturation index (SI) as a function of seawater fraction for surface seawater and freshwater mixed by using PHREEQC. The water compositions employed were: Surface seawater with an average composition as given in Table 6.1 and a fresh groundwater composition which is an average of 4 freshwater samples from August 1999 (St101, St107, St113 and St119). The seawater is supersaturated with SI = 0.4 and the freshwater is subsaturated with SI = -1.2.

10. DISCUSSION II: THE INTRUSION EXPERIMENT

In this chapter the results of the seawater intrusion experiment will be discussed. The relative influences of ion exchange-processes, redox-processes and calcite equilibria during the seawater intrusion experiment are assessed in a series of PHREEQC simulations. First the effects of mixing seawater and freshwater on the carbonate system and the saturation index for calcite, is analysed on an advancing seawater front. Then the processes of ion exchange and redox-reactions during seawater intrusion are analysed separately and in combination. Finally a model is set up aiming at describing the observed field data of October 2000 and January 2001.

10.1 Effect on carbonate equilibria by dispersive mixing

In this section dispersive mixing at an advancing sea-/freshwater front and its effects on the carbonate system will be addressed. Direct evidence of such mixing effects is hard to observe isolated in the field, because it is often masked by redox-processes, ion exchange reactions and precipitation/dissolution of minerals. But the mixing effect is probably always to some degree present as an underlying process. Such effects of mixing on the calcite saturation state was discussed in section 7.3. The question in the context of this investigation is how mixing at a migrating sea-/freshwater front will affect the carbonate system and the calcite saturation state. Figure 10.1 shows the non-linear effect of mixing surface seawater with freshwater on the SI for calcite. The figure is identical to Fig. 7.1b and corresponds to the general results obtained by Plummer (1975). For end-members comparable to the ones used in Fig. 10.1 Plummer (1975) and Wigley and Plummer (1976) show that the higher P_{CO2} of the freshwater end-member is causing a redistribution of the carbonate species in the mixed water, which leads to increased subsaturation for calcite. In the following the term "mixing effect" will refer to this increased subsaturation for calcite.

In a flow system mixing results from dispersive processes during advective transport, as an extension of the simple batch mixing of section 7.3. The resulting effect of dispersive mixing in a flow system on the SI for calcite will be the same as in Fig. 10.1 when plotted as a function of seawater fraction. The mixing effect in Figure 10.1, is therefore simply transformed on to the advective migrating front. The volumes of sea- and freshwater being mixed along the flow path will

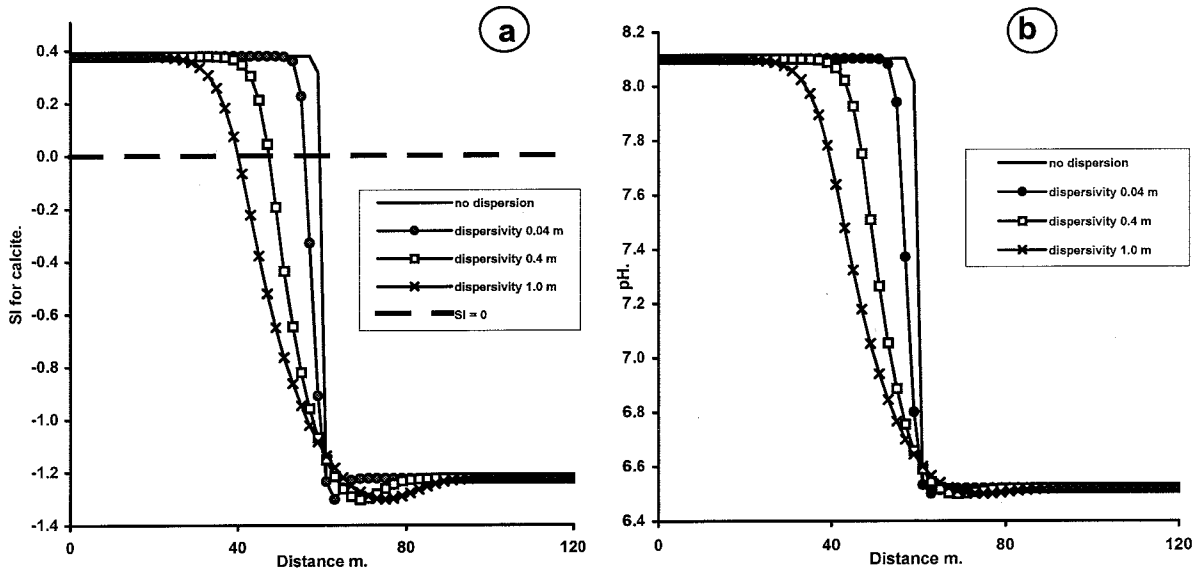

Figure 10.2: a) Calcite saturation index (SI) and b) pH as a function of distance in a column where surface seawater is displacing freshwater for PHREEQC simulations with varying dispersivity of 0, 0.04, 0.4 and 1.0 m.

be dependent on the amount of mixing or the dispersivity. For the hypothetical case of plug flow, without any dispersion, no water will be mixed and the effect will therefore be zero. So the mixing effect seems to increase with increased dispersivity.

This can be illustrated by a series of PHREEQC transport models with varying dispersivity to see the effects of dispersive mixing on the calcite saturation state and pH. The model is a column where surface seawater is displacing freshwater initially in the column. A column of 120 m (equivalent to the transect) is divided into 60 cells of 2 meter in length. The water compositions employed were: Surface seawater with an average composition as given in Table 6.1 and a fresh groundwater composition which is an average of 4 freshwater samples from August 1999 (St101, St107, St113 and St119). The surface seawater is supersaturated for calcite with SI = 0.4 and the freshwater is subsaturated with SI = -1.2. The column was initialised with freshwater and subsequently displaced by surface seawater, as during an intrusion. The surface seawater was transported half way (60 m) into the column by 30 shifts. The model was run with a varying dispersivity: 0 m, 0.04 m, 0.4 m and 1.0 m corresponding to 0%, 0.067%, 0.67% and 1.67% of the average flow length. These values roughly enclose the dispersivity determined in the field.

The PHREEQC database had to be slightly altered to avoid unwanted effects of redox-reactions on the pH. The sulfide system was defined separately with no redox link to sulfate, in the same manner, as ammonium is already defined separately from nitrate in the standard database. Methane was omitted from the water compositions to avoid unintentional re-oxidation affecting the carbonate system.

In Figure 10.2a the effect of varying dispersivity on the SI for calcite at an advancing sea-/freshwater front can be seen. Increasing the dispersivity gives a decreasing SI for calcite on the saline side of the front as compared to the simulation with no dispersion. A small decrease in the SI, below that of the freshwater, can also be seen ahead of the front in the freshwater. The same overall pattern can be observed for pH (Fig. 10.2b), where the pH decreases markedly on the saline side of the front for increasing dispersivity. Again a small decrease in pH, below that of the freshwater, can be seen ahead of the front on the freshwater side.

The rapid decrease in the SI for calcite for even small fractions of freshwater mixed into the surface seawater as seen in Fig. 10.1 is responsible for the diminishing SI for calcite on the seawater side of the non-dispersive $SI_{calcite}$ front as seen in Fig. 10.2a. For increasing dispersivity small fractions of freshwater are mixed further back in the column (towards the coast) as compared to the simulation without dispersion. The main factors causing the increased subsaturation in the mixed water, in this case, seem to be 1) the abundant CO_2 (H_2CO_3) in the fresh water compared with the surface seawater, and 2) the higher pH of the seawater causing a relative abundance of CO_3^{2-} in the seawater, compared to the freshwater. The CO_2 of the freshwater reacts with the CO_3^{2-} in the seawater to form HCO_3^-. The abundance of CO_2 in the freshwater relative to the CO_3^{2-} in the seawater causes the CO_2 concentration in the reacted water to be almost unchanged whereas the relative change in CO_3^{2-} concentration is huge. This change in CO_3^{2-} explains the decrease in the saturation index for calcite as can be seen in Fig. 10.2a.

This mixing induced subsaturation may always be present when the effects of ion exchange, redox- and other processes are studied in systems affected by considerable dispersion. But as the analysis of mixing aquifer saltwater and freshwater in section 7.3 showed, this does not need to be the case if the saltwater end-member of the mix has a lower pH and thus a higher relative concentration of H_2CO_3. However, it is clear that repeated mixing of freshwater and seawater (especially surface seawater) can lead to enhanced or accelerated calcite dissolution and eventually to an aquifer depleted in calcite, as is observed for the field site. The mixing can be caused by repeated fluctuations in the sea-/freshwater interface or by seawater inundation and subsequent development of density plumes described in section 7.5.

The new aspect here as compared to the work of Plummer (1975) and others is that the dispersivity at an advancing sea-/freshwater front will determine the impact of the mixing effect on the carbonate system and the saturation state for calcite. The heterogeneity or macro-dispersivity in an aquifer will thus determine the volumes of surface seawater and freshwater being mixed and in turn the amount of calcite that potentially can be dissolved as a result. A higher dispersion will therefore give a larger reduction in the SI for calcite and potentially lead to more calcite dissolution in the mixing zone.

10.2 Intrusion considering only ion exchange

For many years the occurrence of Ca-Cl_2 water type in coastal aquifers has been linked to intrusion of saltwater. The development of a Ca-Cl_2 water type has been attributed to ion exchange processes, where cations in the saltwater, mainly Na^+, exchanges with Ca^{2+} on the exchanger (Appelo and Willemsen, 1987, Appelo and Greirnaert, 1991, Stuyfzand, 1993). Very few detailed chemical field studies of seawater intrusion with a good control of the pre-intrusion conditions seem to so far have been conducted (Appelo and Postma, 1993). This is partly because the high ratio of solute cations over exchangeable cations is causing the exchange fronts to be coinciding with the general increase in salinity and therefore makes the exchange reactions difficult to discern in the field. However, the processes of water with higher salinity displacing fresh groundwater have been studied extensively in laboratory column experiments (Beekman, 1991, Gomis-Yagües et al., 1997, Cernik et al., 1994) and also in field injection experiments (Dance and Reardon, 1983, Ceazan et al., 1989, Bjerg et al., 1993, Van Breukelen et al., 1998) and in studies of landfill percolate (Engesgaard and Traberg, 1996, Brun, 1996). So the ion exchange processes that can be expected during a seawater intrusion experiment are quite well understood and documented.

The column experiment of Beekman and Appelo (1990) where freshwater is displaced by one time diluted seawater illustrate the ion exchange processes to be expected in a seawater intrusion event. Concentrations of all the cations are seen to increase when the seawater (Cl^-) arrives at the column outlet. But Ca^{2+} increases to a concentration more than 3 times higher than in the seawater, reflecting that it is being displaced from the exchanger complex. Also Mg^{2+} increases rapidly in the initial stage of the front arrival, an increase, which partly can be attributed to the high Ca^{2+} concentrations and partly by the increased salinity forcing ions of higher valence of the exchanger due to the salinity change according to equation (3.2). After the salinity front the concentrations of Ca^{2+} and Mg^{2+} decreases. Ca^{2+} slowly decreases to the level in the seawater whereas the Mg^{2+} concentration increases after 2 pore volumes to the level in seawater. The slow attainment of the seawater concentrations for Mg^{2+} and Ca^{2+} is due to the fact that they are displaced by Na^+ having a smaller affinity to the exchanger (a cation exchange front known as a broadening front).

In order to see the anticipated effects of ion exchange reactions during seawater intrusion a PHREEQC reactive transport model was established. The column used in the previous section 10.1

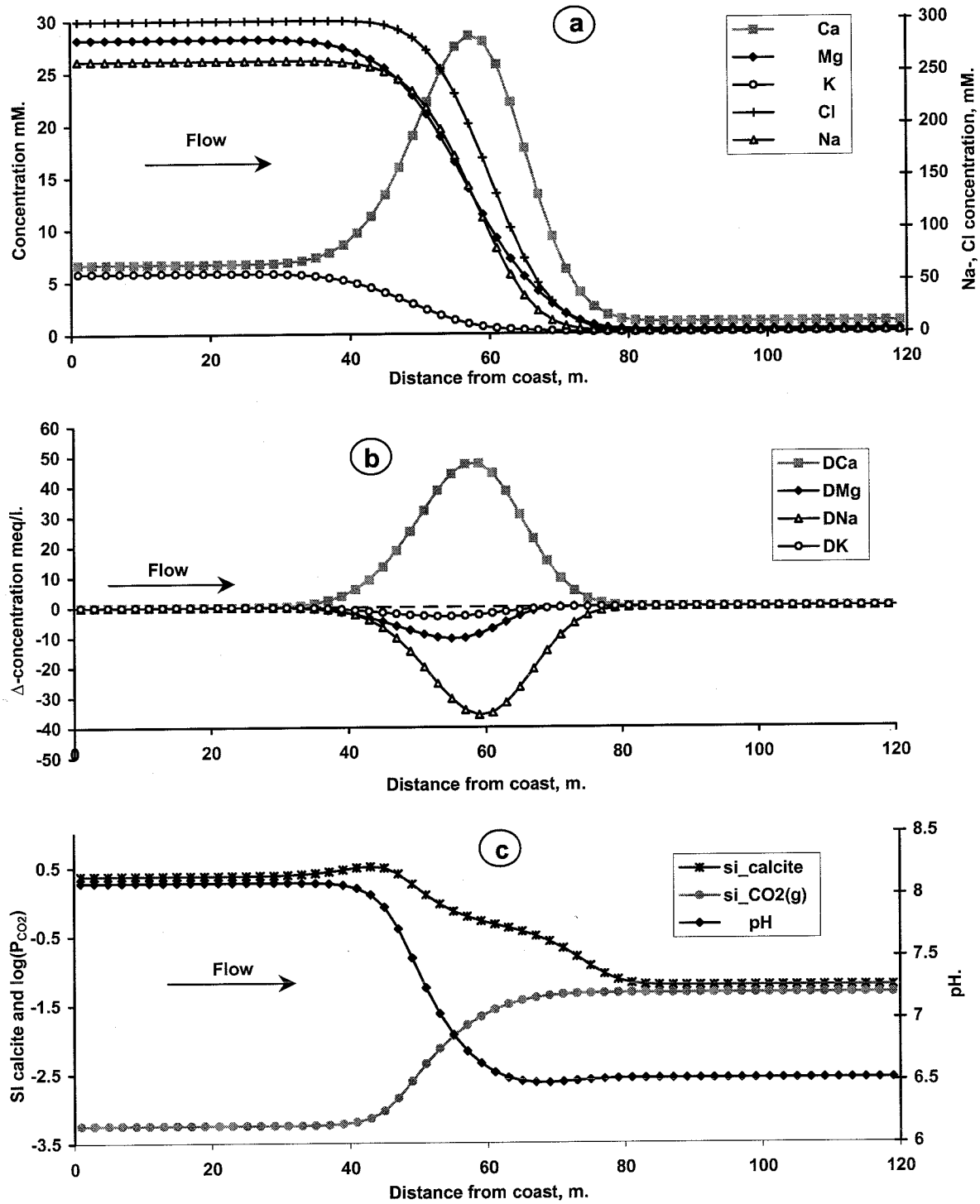

Figure 10.3: Modelled PHREEQC results of ion exchange reactions with a CEC of 24.6 meq/l pore water, in a column, initially containing freshwater, flushed with seawater from 0 m to 60 m. a) Distribution of Na^+, Cl^-, Ca^{2+}, Mg^{2+}, and K^+ (mM). b) Concentrations changes relative to conservative mixing of seawater and freshwater (Δm_i-values) for Na^+, Ca^{2+}, Mg^{2+}, and K^+ (meq/l). c) Calculated pH, calcite saturation index and log(P_{CO2}).

with identical fresh- and seawater compositions was given a cation exchange capacity (CEC) of 0.5 meq/100g, equivalent to 24.6 meq/l pore water (given a porosity of 0.35, see section 7.4.2). This exchanger was initially equilibrated with fresh groundwater in the column. Seawater was again transported 60 m into the column this time with a dispersivity of 0.4 m. Figure 10.3a show the resulting cation distribution with a calcium peak of about 25 mM at the sea- freshwater interface. The Ca^{2+}-peak is a result of ion exchange reactions where Na^{+}, Mg^{2+} and K^{+} in the intruding seawater displace the Ca^{2+} from the exchanger. In Figure 10.3b the depletion or enrichment of the different cations have been calculated and it becomes visible how the solution peak in Ca^{2+} is balanced by a depletion of Na^{+}, Mg^{2+} and K^{+}. Very little chromatographic separation of Na^{+}, Mg^{2+} and K^{+} is seen, because the exchangeable equivalents on the exchanger is relatively small compared to their amount in the intruding seawater (Appelo, 1996). The cation exchanger therefore quickly obtains a composition in equilibrium with the seawater. The peak in Mg^{2+} observed in the column experiment by Beekman and Appelo (1990) are not visible in this model due to the low β_{Mg} on the exchanger. On the contrary Mg^{2+} and K^{+} (Fig. 10.7b) are slightly retarded compared to Na^{+}. The calculated calcite saturation index for the simulation with ion exchange (Fig. 10.3c) is higher than for the previous PHREEQC simulations only considering transport and dispersion (Fig. 10.2a), due to the calcium peak. At about 40 to 50 m the mixed water becomes even more supersaturated than seawater is (SI = 0.51). The Ca^{2+} peak and thus the calcite saturation index increase with the distance that the front travels into the aquifer. The increased calcite saturation may be prevented by calcite precipitation, which seem possible because Ca^{2+} travels in front of Mg^{2+}, which potentially inhibits calcite precipitation in seawater (Berner, 1975)

10.3 Intrusion considering only redox-reactions

As also noted in section 7.4.2 many investigators have found depletion of sulfate in seawater intrusion zones. The most frequently given explanation is sulfate reduction (Nadler et al., 1980, Magaritz and Luzier, 1985, Hahn, 1991, Barker et al., 1998 and Logan et al., 1999). Gomis-Yagües et al. (2000) hypothesize that the depletion of sulfate during seawater intrusion could also be due to the precipitation of gypsum. Supersaturation for gypsum is attributed to a combination of landward transport of sulfate and the release of calcium due to ion exchange. This can be ruled out for Skansehage because subsaturation for gypsum was calculated for all data. Conversely Wicks and

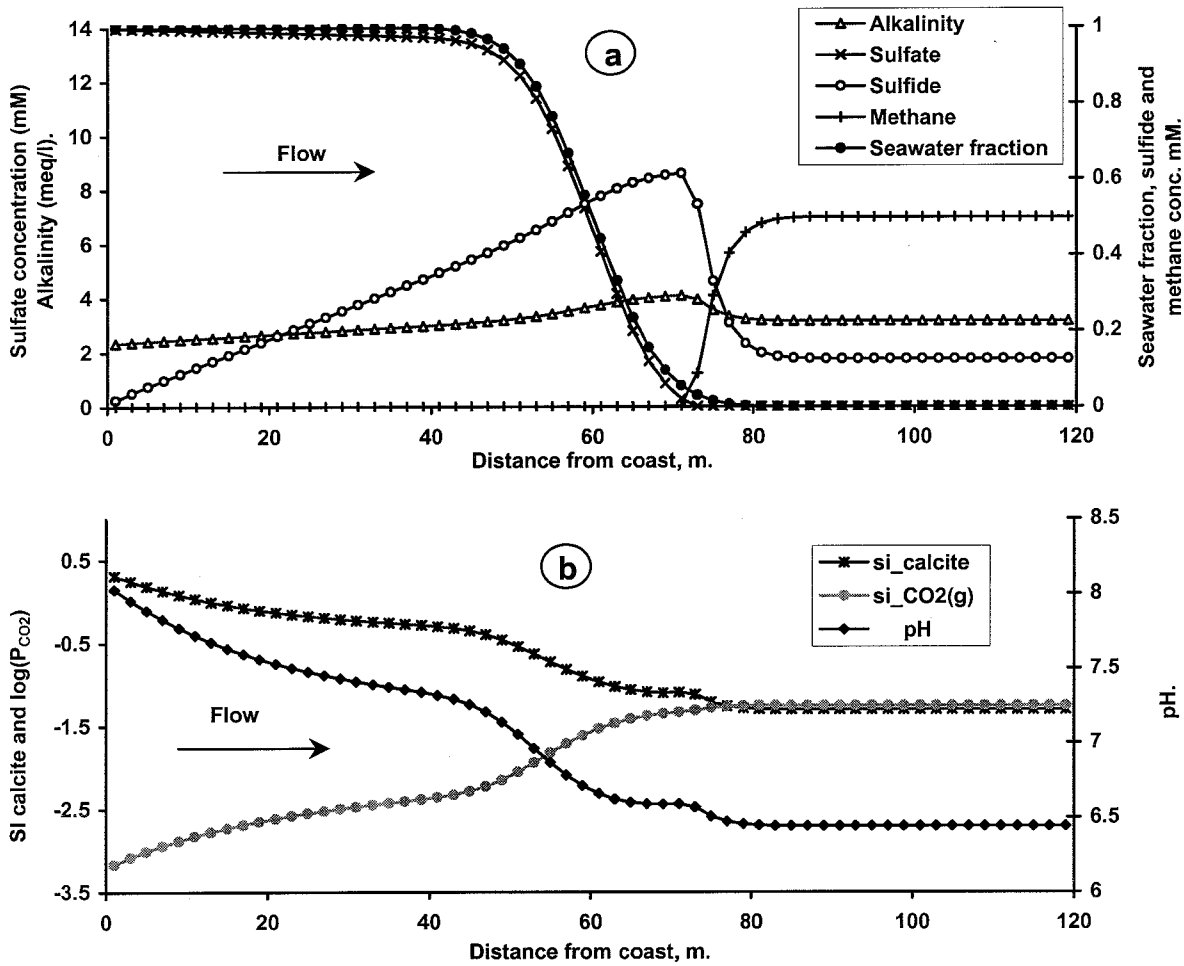

Figure 10.4: Modelled PHREEQC results of oxidation of organic matter with a rate of 2 mM CH_2O/yr, in a column, initially containing freshwater, flushed with seawater from 0 m to 60 m. The groundwater flow rate is 120 m/yr. a) Distribution of alkalinity (meq/l), sulfate, sulfide and methane (mM). b) Calculated pH, SI calcite and log(P_{CO2}).

Herman (1996) show that intruding seawater can become enriched in sulfate due to dissolution of gypsum thereby obscuring sulfate reduction.

A PHREEQC model was made with the purpose of illustrating the effects of seawater intrusion of sulfate containing seawater into an aquifer dominated by methanogenisis. In this simulation redox-processes during seawater intrusion where modelled with kinetically controlled degradation of organic matter. The same rate expression (7.8) as in section 7.4.2 is used and for simplicity CH_2O is again chosen as representing organic matter. The initial degradation rate is 2 mM CH_2O/yr (Nyvang, unpublished data). An initial amount of organic matter of 0.2 moles was used. Given a total modelling time of ½ yr the rate is practically constant during the modelling time. 30 shifts were used representing a total length of 60 m and giving a time step of 6.1 d.

Figure 10.4a shows the resulting redox-parameters of the simulation. The results are very similar to the results obtained from the redox-model of freshwater displacing seawater (Fig. 7.8 section 7.4.2). In the fresh part of the column no methane was initially present and about 0.5 mM of methane is produced during the ½ yr of modelling, corresponding to the stoichiometry of equation (6.5). The sulfate transported into the aquifer with the intruding seawater is being reduced by the organic matter as reflected by the production of sulfide and the loss of sulfate compared to the fraction of seawater (Cl^-). Sulfate is also being consumed by methane in the mixing zone according to equation (7.4) producing additional sulfide and alkalinity. This explains why the sulfide peak of 0.6 mM is larger than the 0.5 mM expected from the rate expression and the stoichiometry of equation (6.4). The SI for calcite (Fig. 10.4b) has decreased in the seawater intruded part of the column due to the acidifying effect of the sulfate reduction at a pH above 6.8 (which is slightly lower than the pK_1 of ~7 for the sulfide system). Stoessell et al. (1993) also observed this effect. Also in the fresh part of the column (80-120m) the SI for calcite is reduced, compared to the SI in the initial freshwater, due to the methanogenesis and the production of CO_2. In part of the mixing zone from 55 to 80 m the SI for calcite is increased compared to the SI of the simulation with only transport (Fig. 10.2a). The reason for this is the additional alkalinity production associated with the reaction between sulfate and methane where two moles of alkalinity is produced for every mol of sulfate and methane consumed, see (7.4).

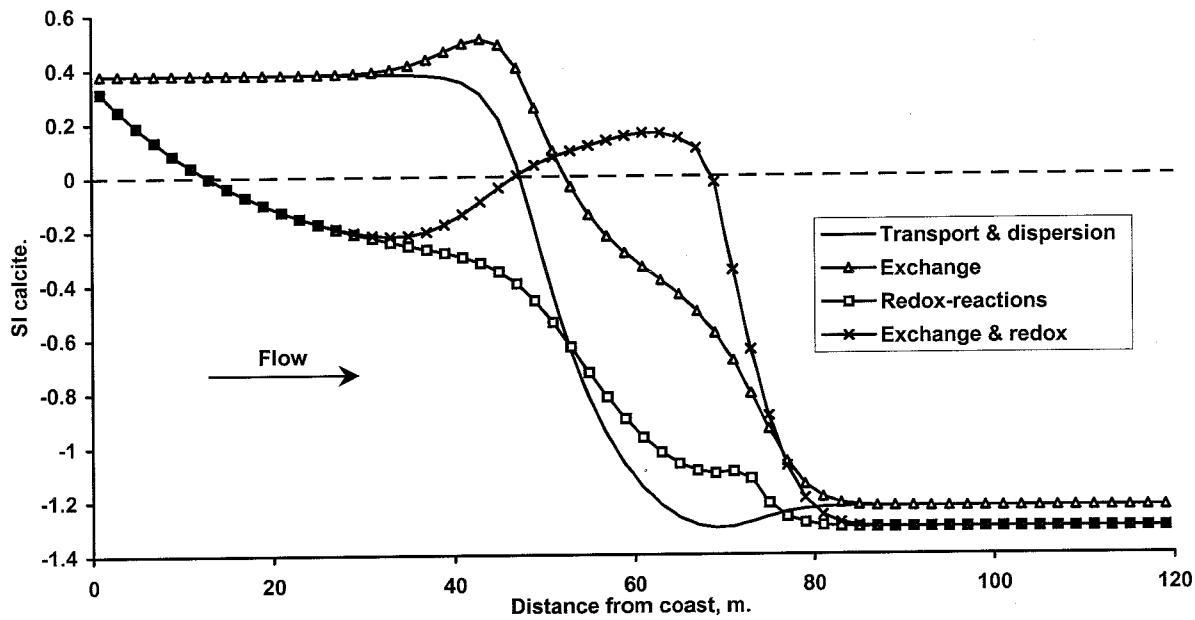

Figure 10.5: Calcite saturation index calculated for the four PHREEQC scenarios of seawater displacing freshwater. The scenarios are: Non- reactive transport, ion exchange (CEC = 24.6 mmol/l), redox-reactions (2 mM CH_2O/yr) and a combination of ion exchange and redox-reactions.

10.4 Intrusion combining ion exchange and redox-reactions

A PHREEQC simulation combining ion exchange and redox reactions were conducted, as mentioned previously the resulting distribution of cations and redox-parameters will be as seen in the Figures 10.3a and 10.4a respectively, because no parameter links the two processes. However, both processes have an impact on the calculated SI for calcite as seen from Figure 10.5, where the effects on the calcite saturation index is summarized for the different PHREEQC simulations of the Figures 10.2a, 10.3 and 10.4. The SI-curve for the combined effects of ion exchange and redox-processes decreases in the seawater part of the column from the coast and to 35 m due to the sulfate reduction. From 35 m the SI increases due to the displacement of calcium from the exchanger and the alkalinity production from the reaction between sulfate and methane to reach a supersaturation with a maximum of SI ~0.2 from 50 to 70 m.

It is difficult to include calcite equilibrium in this combined model because 1) the supersaturated seawater (0-10 m in Fig. 10.5) will probably retain its supersaturation due to the Mg^{2+} inhibition (Berner, 1975) and no calcite will precipitate in this zone. 2) It is unlikely to expect calcite dissolution in the freshwater to attain equilibrium (SI = 0), since the freshwater has previously been subsaturated. This leaves the zone with slight supersaturation from 50 to 70 m and the zone with subsaturation from 10 to 50 m. However, in these zones the deviations from equilibrium are small (SI = ±0.2). The reactions kinetics would therefore probably be slow (Appelo and Postma, 1993) and any effects of dissolution/precipitation reactions within this SI range will be minimal.

10.5 Reactive transport modelling of intrusion field data

The processes described in the previous section were used as a basis for modelling and understanding the observed seawater intrusion data of October 2000 and January 2001. Again the transect is represented by a 120 m horizontal column sectioned into 60 cells of 2 m in length. Representing the seawater intrusion into of the transect by a horizontal column can be justified in most of the transect (at least in the upper part, > –6 m, and from 0 to 100 m) by the predominantly vertical intrusion front as seen from the EC-plots (Fig. 8.5) and the near vertical lines of equal head (Fig. 8.4). The intrusion seawater used in the model is the average surface seawater of Table 6.1, but with the sulfate concentration adjusted upward from 14.1 to 15 mM to better fit the observed

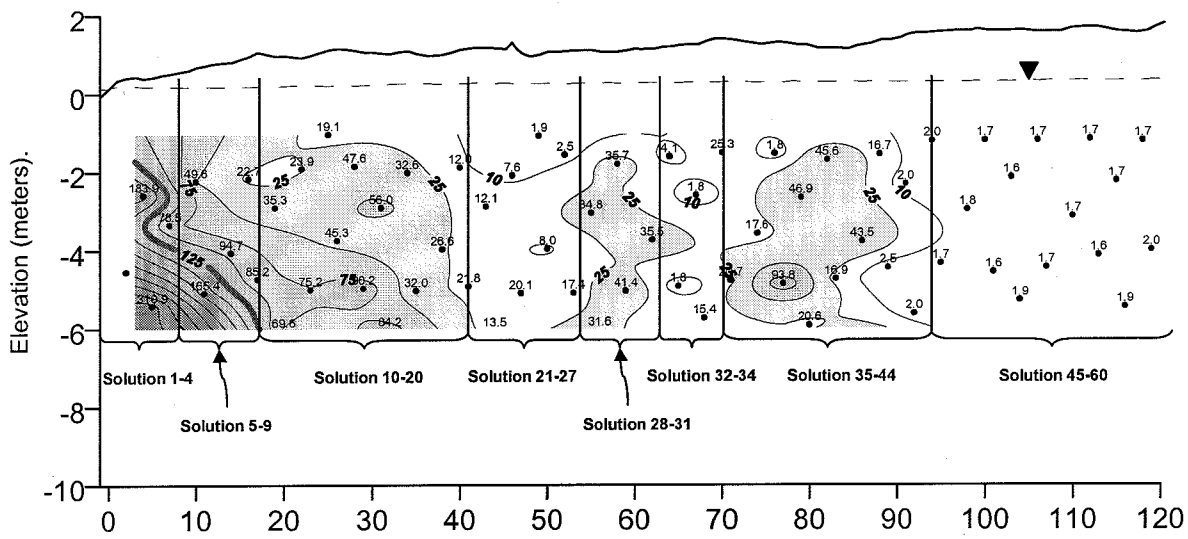

Figure 10.6: Chloride distribution (mM) in the upper part of the transect in March 2000, divided into 8 different zones. For each zone an average solution composition was calculated as initial solution for a PHREEQC model of the intrusion data of October 2000 and January 2001.

seawater concentrations. The transect data of March 2000 measured just prior to the commencement of the intrusion experiment is used as the initial chemical condition as shown in Fig. 10.6. The column is subdivided into 8 zones with different initial average solutions. The subdivision is based mainly on the chloride distribution of the pre-intrusion March data. Only data above an elevation of –6 m were used. In this way the water samples affected by the upward leakage of fresher water from the aquifer below (see Fig. 8.5) are avoided. And also this avoids the stagnant water compositions associated with the low permeable peat layer.

A uniform average CEC of 0.5 meq/100g (24.6 mmol/l) is employed and equilibrated with the initial 8 water compositions. The decomposition of organic matter is again modelled with the partial equilibrium approach (see section 7.4.2, eq. (7.8)), this time with two different initial rates of 2 and 10 mM CH_2O/yr for the purpose of seeing the effect of varying rates. An initial organic matter mass of 0.2 moles was used. The seawater is shifted landward by 27 shifts (= 54 m) for the October data and by 36 shifts (= 72 m) for the January data. Different time steps are used for October and January of 163 and 200 hours respectively, in order to match the period between the start of the experiment and the time of sampling. This is necessary because of the decreasing intrusion velocity towards the end of the experiment. Five different simulations were conducted: 1) A model with CEC = 24.6 mmol/l, organic matter degradation rate of 2 mM CH_2O/yr and no calcite equilibrium; 2) same model but with higher organic matter degradation rate of 10 mM CH_2O/yr; 3) as the first model but this time with calcite equilibrium 4) a model without redox-processes and calcite equilibrium, only ion exchange and 5) a conservative model without any reactions.

10.5.1 Chloride distribution

A dispersivity of 0.4 m was estimated by trial an error, fitting the model to the observed chloride concentration distribution of the October data set as shown in Fig. 10.7a. A part of the spreading in the Cl^- field data of Fig. 10.7a is caused by the spreading present in the mixing zone of the natural situation and the inundation event prior to the intrusion experiment (Fig. 6.20a). Part of this pre-intrusion spreading is initially incorporated into the model by the different initial water compositions along the column having a gradual landward decrease of the chloride concentration as in the mixing zone from 0 to 40 m (Fig. 10.6).

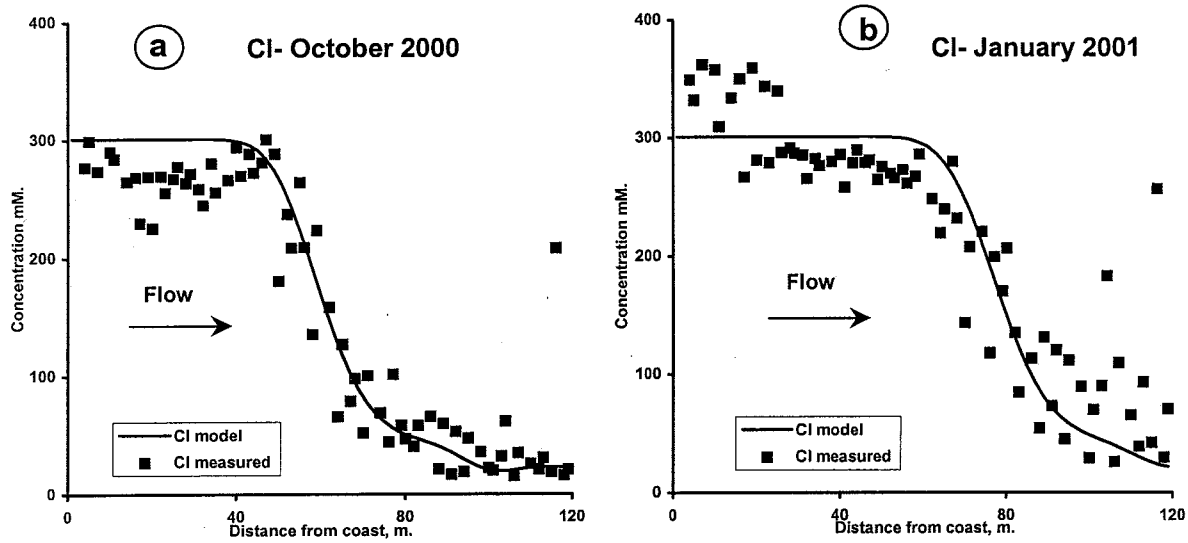

Figure 10.7: Modelled and measured (of upper 6 m in the transect) chloride distributions (mM) as a function of distance from the coast a) October 2000 and b) January 2001.

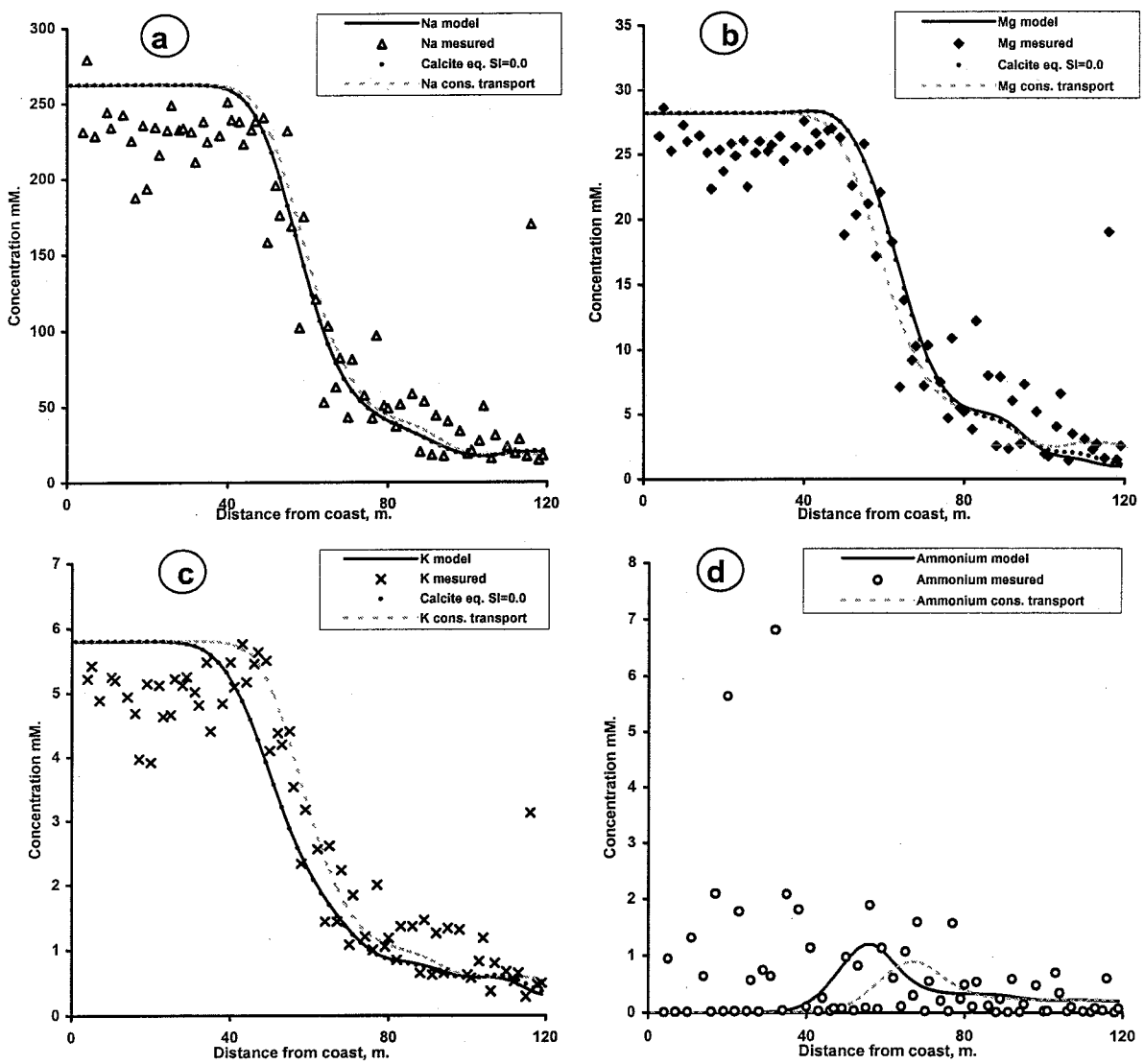

Figure 10.8: Modelled and measured (of upper 6 m in the transect) cation distributions (mM) of October 2000 as a function of distance from the coast a) Na^+, b) Mg^{2+}, c) K^+ and d) NH_4^+. Black solid line: Ion exchange (CEC = 24.4 mM). Grey broken line: Conservative transport. Black

The modelled Cl^-- concentration for October 2000 (Fig. 10.7a) describes the observed Cl^- data quite well with a steep breakthrough of surface seawater at 50 to 70 m. Landwards from 70 m the gradual decrease in the Cl^- concentration reflects part of the old interface/mixing zone and the density plumes. A local minimum in the observed intrusion seawater Cl^- concentration is seen at about 20 m, representing the summer salinity minima in the bay surface seawater seen in Figure 6.2. This minimum also shows for other seawater species such as Mg^{2+} and K^+ (Fig. 10.8a and c). Ideally the intrusion seawater of the model should have been varied accordingly, but that would probably not give much additional information. The modelled Cl^- distribution for January 2001 (Fig. 10.7b), also simulated using a dispersivity of 0.4 m, is somewhat steeper than the measured Cl^- distribution, indicating that the dispersion is larger in this part of the transect. This is supported by the observed increased heterogeneous flow pattern (Fig 8.5). Therefore the data of the two situations cannot in principle be modelled with a constant dispersivity due to the increased macro-dispersion. The chloride distribution of January 2001 (Fig.10.7b) show the appearance of the high salinity winter surface seawater in the first 20 m of the transect with Cl^- values up to 360 mM. This increase is also clearly reflected by the distributions of cations exemplified by Ca^{2+} (Fig. 10.9b) and the sulfate, which increases to 18 mM (not shown).

10.5.2 Ion exchange

The solute concentrations of the cations Na^+, Mg^{2+} and K^+ of October broadly follow the general trends of the chloride concentration in both the field data and in the model including ion exchange reactions (solid black line in Fig. 10.8 a, b and c). The effects of ion exchange reactions on the distributions of Na^+, Mg^{2+} and K^+ are small compared to conservative transport without ion exchange (grey broken line in Fig. 10.8 a, b and c). Na^+ is only very slightly retarded by the ion exchange. The modelled Mg^{2+}, including ion exchange, is slightly ahead of the conservatively transported Mg^{2+} (grey broken line) showing that Mg^{2+} initially on the exchanger is being displaced, mainly by Na^+. A similar effect was observed by Stuyfzand (1993) for intrusion data in Holland. For K^+ the conservative model seems to describe the field data better than the model with ion exchange, which retards the K^+ distribution too much. The modelled Ca^{2+} distribution of October (Fig. 10.9a) shows considerable difference between the conservative model and the model with ion exchange. The conservative transport of Ca^{2+} (grey broken line) seems to describe the bulk of the field data better than the modelled Ca^{2+} including ion exchange (solid black line), which

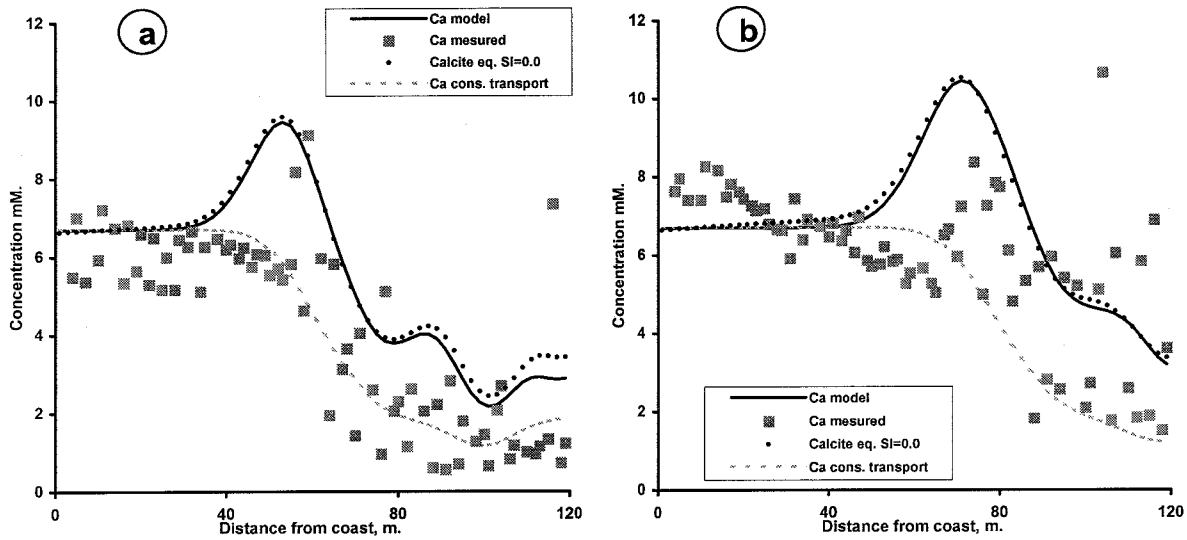

Figure 10.9: Modelled and measured (of upper 6 m in the transect) Ca^{2+} distributions (mM) as a function of distance from the coast a) October 2000 and b) January 2001. Black solid line: Ion exchange (CEC = 24.4 mM). Grey broken line: Conservative transport. Black broken line: Calcite equilibrium (SI = 0).

generally lies higher than the Ca^{2+} field data. The Ca^{2+} peak up to 10 mM at about 40 to 70 m, in the model including ion exchange, is due to Ca^{2+} being displaced from the exchanger mainly by Na^{+}. This peak is much smaller than the peak in the conceptual model (Fig. 10.4a) because the actual fraction of Ca^{2+} on the cation exchanger in the seaward portion of the transect (0 to 60 m) is quite small at the start of the experiment (see Fig. 6.25). This is partly accounted for in the model by using the March data as the initial condition. In the field data only two data points support the modelled Ca^{2+} peak. The few field data in the Ca^{2+} peak are partly due to the presence of Mg^{2+} instead of Ca^{2+} on the exchanger in the upper part of the transect prior to the experiment (Fig. 6.25). Therefore it is mainly Mg^{2+} that is displaced by Na^{+} in the upper 4 m of the transect. This is not obvious from Fig. 10.8b, but can be seen from the Δm_{Mg} data (Figure 9.10b). In the Ca^{2+} distribution for January (Fig. 10.9b) there is a more convincing agreement between the field data and the model including ion exchange than in October (Fig. 10.9a) This is a consequence of the landward progression of the seawater front into sediments containing a higher equivalent fraction of Ca^{2+} (Fig. 6.25). Still the observed Ca^{2+} peak is located further landward and is about 1-2 mM smaller than the modelled peak. A group of field data with a low Ca^{2+} concentration (~2 mM) observed at 80 to 120 m is still better described by the modelled conservative Ca^{2+} distribution. Probably this is caused by vertical variation in the size of the CEC or exchanger composition over the 6 m depth of the transect. Apart from the advective landward displacement only minor changes are seen in the distributions of Na^{+}, Mg^{2+} and K^{+} for the January data. Inclusion of calcite equilibrium in the model (grey line in Fig. 10.9) does not significantly change the modelled Ca^{2+} concentration at the peak.

The observed solute concentration of K^{+} (Fig. 10.8c) is somewhat ahead of the modelled K^{+}-concentration and indicate that K^{+} is being more easily released in reality than expected from the selectivity coefficients in the PHREEQC database. The cation exchanger in these sediments is mainly dominated by organic matter (Fig. 6.13), which does not have the same specific affinity for K^{+} as illitic clay (Appelo, 1996).

10.5.3 Redox-processes

Figure 10.10a shows the surface seawater sulfate being transported into the aquifer with a concentration of 15 mM. The conservative model without redox-processes, represented by the grey

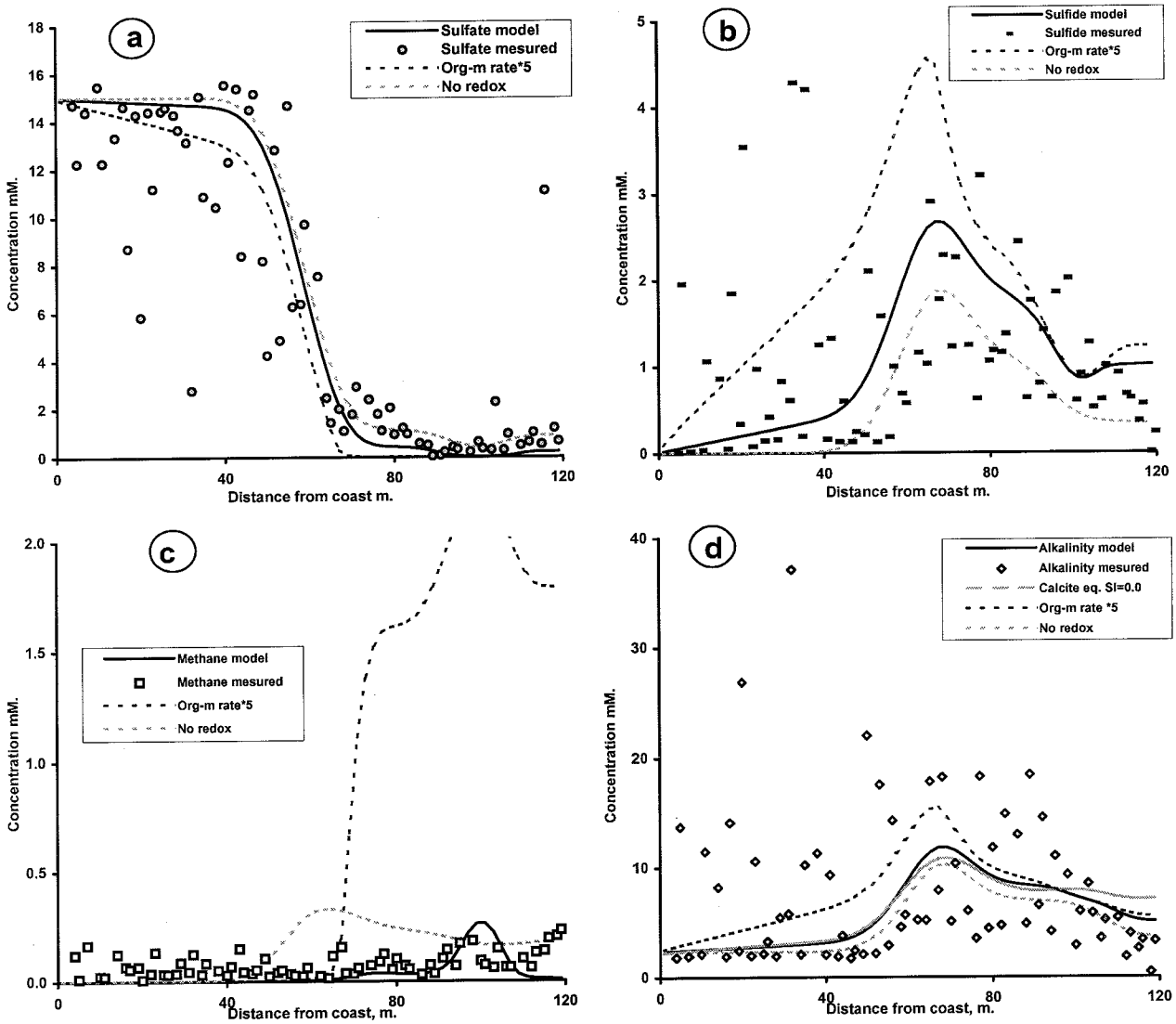

Figure 10.10: Modelled and measured (of upper 6 m in the transect) Redox-parameter distributions of October 2000 as a function of distance from the coast a) Sulfate (mM), b) Sulfide (mM), c) Methane (mM) and d) Alkalinity (meq/l). Black solid line: CEC = 24.6 mM and organic matter degradation rate = 2 mMCH_2O/yr. Grey solid line: As black solid and also calcite equilibrium (SI = 0). Grey broken line: Conservative transport. Black broken line: As black solid but with organic matter degradation rate = 10 mMCH_2O/yr.

broken line in Figure 10.10a describe the measured sulfate concentrations and the position of the sulfate front quite well. Landward from the front the modelled sulfate decreases to less than 1 mM. The modelled methane concentration without redox-processes (grey broken line in Fig. 10.10c) is a bit higher than the field measurements. The pre-existing mixing zone with its high concentration of alkalinity and sulfide and its sulfate depletion is being pulled ahead of the intruding surface seawater. This is evident form the sulfide and alkalinity plots (Fig. 10.10b and d) where the field data show diffuse peaks of sulfide (3 mM) and alkalinity (20 meq/l), from roughly 40 to 100 m. The model without redox-processes (grey broken line) predicts a maximum concentration of 2 mM for sulfide and 10 meq/l for alkalinity. The observed alkalinity and sulfide values, in the zone from 40 to 100 m, situated above the conservative model (grey broken line) can to some extent be explained by the averaging of the initial solutions (the March 2000 data) and thereby a levelling of the extreme values in the model. One option is to model the intrusion field data conservatively without organic matter degradation. But the model omitting the redox-processes does not fit the observed pH and the log(P_{CO2}) data at all, as will be discussed below, indicating that the redox-processes in fact do play a significant role.

The model with an organic matter degradation rate of 2 mM CH_2O/yr (shown by the solid black line), reasonably well fits the sulfate in the intruded part of the transect (0 - 50 m) and the front in the field data from 50 to 70 m. Landward from the front the modelled sulfate decreases to less than 1 mM and becomes totally depleted between 90 and 110 m. This depletion fits poorly with the field sulfate concentration being generally higher (0.2 – 1 mM). The discrepancy could be explained by the fact that the sulfate reduction rate, in other studies, have been found to change from zero to first order dependence on the sulfate concentration below a concentration of 1 mM (Boudreau and Westrich, 1984), leading to a lowering of the field rate at low concentrations. In the seawater part of the transect (< 50 m) behind the sea-/freshwater front some scattering in the measured sulfate concentrations from 2 to 14 mM is observed. The lower sulfate values are associated with a zone from –4 to –6 m where also the sulfide concentration (Fig. 10.10b) and the alkalinity (Fig. 10.10b) are high. This water composition must to a large extent be attributed to sulfate reduction occurred prior to the experiment. Perhaps a part of the sulfate-depleted saltwater intrudes from the offshore portions of the aquifer. The observed alkalinity and sulfide is still fitted well by the organic matter degradation rate of 2 mM CH_2O/yr (shown by the solid black line), with the maximum alkalinity of about 12 meq/l and sulfide of 2.5 mM.

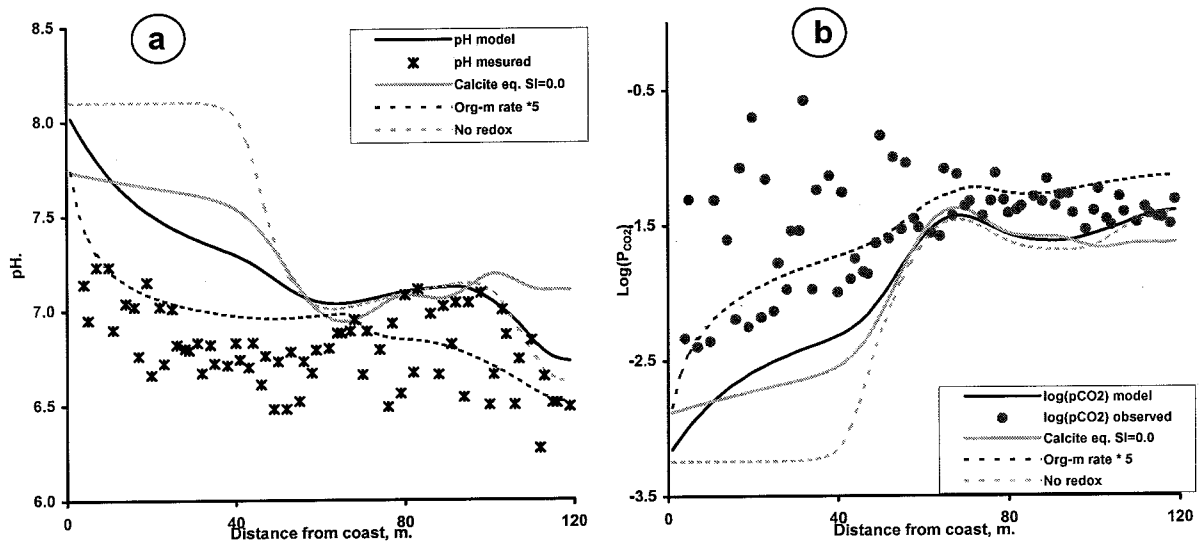

Figure 10.11: Modelled and measured (of upper 6 m in the transect) a) pH and b) log(P_{CO2}) of October 2000 as a function of distance from the coast. Black solid line: CEC = 24.6 mM and organic matter degradation rate = 2 mMCH_2O/yr. Grey solid line: As black solid and also calcite equilibrium (SI = 0). Grey broken line: Only ion exchange. Black broken line: As black solid but with organic matter degradation rate = 10 mMCH_2O/yr.

The pH of the model without organic matter degradation is shown as a grey broken line in Fig. 10.11a. It retains the seawater pH all the way to 40 m where it drops to about 7 and decreasing again from around 100 m to about 6.7. The field pH is generally lying much lower and not well described by this model. At the coast the field pH decreases from around 7-7.2 to a minimum of 6.5 at 50 m. From here the spreading increases with some samples retaining the low value of 6.5 and some increasing to about 7. From around 100 m the field pH falls below 6.7. The $\log(P_{CO2})$ of the model without organic matter degradation is shown as a grey broken line in Fig. 10.11b is generally far below the $\log(P_{CO2})$ calculated from the field data.

The pH of the model with an organic matter degradation rate of 2 mM CH_2O/yr (black solid line in Fig. 10.11a) gives a better fit decreasing from the seawater pH of 8.1 to about pH = 7 at 50 m. At around 80 to 100 m there is a small maximum in the pH of 7.2 corresponding to the high pH zone of the pre-existing mixing zone (Fig. 6.8a). The field data is generally following this trend but at about 0.5 to 1 pH units lower than in the model. The discrepancy is largest at the coast, possibly the intruding seawater must pass through the fjord bottom and a section of the off shore part of the aquifer before entering the transect. The intruding seawater has therefore already been influenced by some degree of organic matter oxidation. The model with 2 mM CH_2O/yr still underestimate the amount of CO_2 in most of the transect with a model $\log(P_{CO2})$ consistently below the field data (black solid line in Fig. 10.11b).

A better overall fit to pH and $\log(P_{CO2})$ can be obtained if the organic matter degradation rate is increased to about 10 to 20 mM CH_2O/yr. A rate of 10 mM CH_2O/yr gives model results for pH and $\log(P_{CO2})$ more comparable with the field data (black broken line in Fig. 10.11). Still even with this elevated rate the modelled pH and $\log(P_{CO2})$ are only within the upper and lower limits, respectively, of the observed field data.

The high organic matter degradation rate of 10 mM CH_2O/yr still gives an acceptable fit to all four redox-parameters in the seawater affected part of the transect (black broken line in Fig. 10.10). The maximum sulfide and alkalinity (black broken line in Fig. 10.10b and d) increases to 4.5 mM and 15 mM, respectively. A seriously deviation between the model and the observed data is seen in the freshwater part of the transect (70 to 120 m) for methane where the modelled concentration of ~2

mM becomes much higher than the measured (Fig. 10.10c). The explanation is that the modelled sulfate at this high rate becomes totally depleted from 50 m and landward thus triggering methane formation. Clearly this does not agree with the observed lack of methane and the presence of sulfate in concentration of about 0.2- 1 mM (Fig. 10.10a) The high organic matter degradation rate (10 mM CH_2O/yr) therefore does not seem applicable in the fresher part of the transect. Perhaps the organic matter degradation rate somehow is dependent on the salinity or a parameter correlating with the salinity. In fact radiotracer sulfate reduction rate measurements show rates up to 5 mM SO_4^{2-}/yr, in the seawater intruded part of the transect (Nyvang, unpublished data). The exact mechanism behind the increase in rate is not known. But as a consequence of the decoupling of the sulfate reduction rate and the methane formation rate the partial equilibrium model (Postma and Jakobsen, 1996) - where organic matter degradation is the rate controlling step and the TEAP's are controlled by equilibrium - seem to be an inadequate description of the redox-processes in this system.

Judging from the model, the sulfate reduction rate seem to be in the upper part of the range of 1 - 5 mM SO_4^{2-}/yr in the seawater influenced part of the transect, whereas the methane formation rate remains low in the whole transect with the methane concentrations in Fig. 10.10c being close to the detection limit. Alternatively the methane formation could in reality be continuing in sulfate depleted micro-zones with the same rate as before the intrusion experiment and the inundation event, but with the produced methane being re-oxidised as coming into contact with the seawater sulfate. This process is known from marine sediments (Barnes and Goldberg, 1976, and Iversen and Jørgensen, 1985, Hoehler et al., 1994)).

The redox-parameters sulfate, sulfide and methane of January 2001 basically show the same as for the October data apart for the additional landward transport and are therefore not shown.

10.5.4 Calcite precipitation/dissolution

Calcite precipitation/dissolution seems to play a minor role during the intrusion experiment. The field data of October and January generally exhibit slight subsaturation for calcite in the upper part of the transect (>–6 m) in spite of the presence of surface seawater (Fig. 9.11a,b and Fig. 10.12a,b). In the permeable part of the transect, supersaturation is only observed in a small zone. In October the zone of supersaturation is located from 60-90 m with an $0<SI<0.2$. In January the zone located

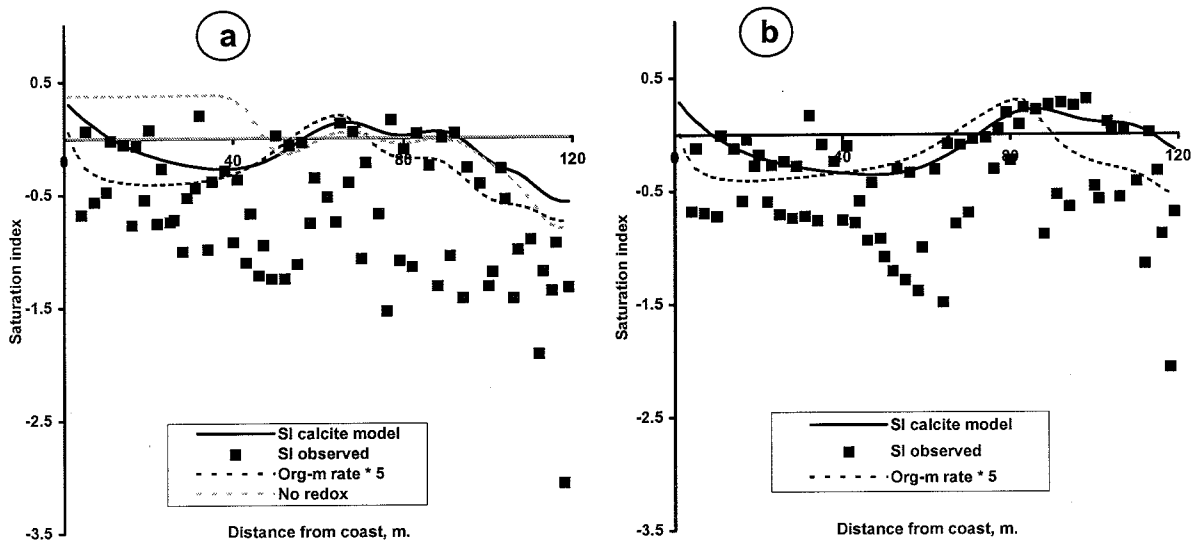

Figure 10.12: Modelled and measured (of upper 6 m in the transect) saturation index (SI) for calcite (mM) as a function of distance from the coast a) October 2000 and b) January 2001. Black solid line: CEC = 24.6 mM and organic matter degradation rate = 2 mMCH_2O/yr. Grey broken line: Only ion exchange. Black broken line: CEC = 24.6 mM and organic matter degradation rate = 10 mMCH_2O/yr.

at 75-110 m and seem to have increased in both extention and supersaturation with SI ~ 0.3. Part of this supersaturation is related to the landward transport of the pre-existing mixing zone and largely related to the high alkalinity. However, the increase in the supersaturation from October to January indicates that part of the increase is related to processes occurring during the intrusion. This could either be the displacement of Ca^{2+} from the exchanger, the alkalinity production from the sulfate reduction or a combination of both. The modelled saturation index for calcite of October with ion exchange and an organic matter degradation rate of 2 mM CH_2O/yr remain close to zero ($-0.5<SI<0.5$). From the seawater and 40 m into the transect the modelled SI for calcite decrease from the supersaturation in the seawater to a subsaturation of –0.4 due to the acid production associated with the sulfate reduction. At 40 m the modelled SI increases again, to become supersaturated at 55 m, due to a combination of several processes: 1) The Ca^{2+} released by the ion exchange reactions, 2) The landward transport of alkalinity from the pre-existing mixing zone and 3) the reaction between sulfate and methane producing alkalinity according to equation (7.4). The modelled supersaturation also increases in magnitude from October (SI = 0.2) to January (SI = 0.3) as observed for the field data.

The agreement in the size of the observed and modelled supersaturation suggests that the amount of calcite precipitated is probably small. A slight decrease in the pH of January in the supersaturated zone (Fig. 9.5b) compared to the October data (Fig. 9.5a) could support a small amount of calcite precipitation. However, if the front where to move further landward the supersaturation would increase as a consequence of the ion exchange and subsequently calcite precipitation would probably increase. Precipitation of calcite would only be temporary because a zone with subsaturation trails the zone of supersaturation. In January the modelled subsaturation for calcite (of –0.3) has increased, compared to October in both magnitude and extent stretching almost from the coast and to 70 m. It's caused by the additional sulfate reduction occurred between October and January. The observed subsaturation is somewhat larger than the modelled pointing towards either a larger sulfate reduction rate or other processes decreasing the pH. This decrease in saturation of the intruding seawater as compared to the surface seawater will tend to re-dissolve any calcite precipitated at the seawater front further landward.

Including equilibrium for calcite in the model has only minor effects on the alkalinity (Fig. 10.10d) and the calcium distribution as indicated by the dotted line in Fig. 10.9a,b. The effect is slightly

larger in January compared to October with a little calcite precipitation at the Ca^{2+} peak (80 - 90 m), and some calcite dissolution behind the peak 20 to 80 m).

The low pH of 6.5 – 7.2 (Fig. 9.5) of the intruded part of the transect (< 50 m) compared to surface seawater, does not seem to be entirely explained by the redox-processes described so far and other buffering processes may have to be considered. First of all, effects caused by processes in the sea floor have to be considered. Here organic matter degradation rates can be very high due to the young and more reactive organic matter (Troelsen and Jørgensen, 1982). Jakobsen and Postma (1994) documented rates of sulfate reduction in aquifers to be 3-4 magnitudes lower than in marine environments. Also oxygen dissolved in the surface seawater will part take in the oxidation of organic matter, lowering the pH. Secondly proton buffering in the fresher part of the transect could be lowering the pH as documented by Sayles and Mangelsdorf (1977). Appelo (1994a) also successfully explained by proton buffering the pH variations in the refreshening data of the Aquia aquifer by Chapelle and Knobel (1983). At Skansehage this is most likely taking place in the upper and more calcite depleted part of the transect and this is also where the lowest pH values are found (see Fig. 9.5a,b). However, pH measurements in the NaCl- and NH_4Cl-supernatants of the batch determinations of exchangeable cations and CEC (see section 4.4.2) of this study generally do not indicate any significant proton buffering. The pH of the supernatants after reaction with the sediment samples remained equal to or above the pH of the pure NaCl- and NH_4Cl-supernatant as seen from Figure 4.11. This was also the case for samples without any calcite dissolution.

11. CONCLUSIONS

- The traditional notion of the dynamics in a sea-/freshwater interface is that of a slow seawater convection within the seawater wedge being driven by the loss of sea-salt to the discharging freshwater due to dispersive mixing of seawater and freshwater across the interface. This process only partly explains the interface dynamics in the Skansehage aquifer. The low topography of the field site makes this aquifer prone to frequent inundations of surface seawater during winter storms. These inundations are causing density driven seawater plumes to migrate down into fresh regions of the aquifer and thereby constitute an important additional mechanism for the transport of seawater into the aquifer.

- The repeated inundation with seawater and subsequent downward migration of density plumes into the fresher parts of the aquifer (up to 80 m from the coast) apparently leads to a decalcification of the aquifer despite the surface seawater being supersaturated for calcite. The chemical processes responsible for a lowering of the calcite saturation state and possible dissolution of calcite are 1) Non-linear effects on the carbonate system by mixing of sea- and freshwater. 2) Ion exchange processes related to the seaward flushing of the density plumes, where Ca^{2+} in the fresh groundwater displaces the cations Na^{+}, Mg^{2+} and K^{+} and become depleted in the solution. The seawater plumes caused by inundation, also changes the prevailing redox-condition from methanogenic to sulfate reducing.

- The sea-/freshwater interface did not retain its landward dipping shape during the seawater intrusion experiment, but essentially advanced as a vertical front contrary to the common belief of a wedge shaped seawater intrusion caused by density driven flow. It seems that the shape of the migrating interface is mainly controlled by a heterogeneous permeability distribution in the aquifer and by leakage up through the aquifer bottom. An important part of the explanation is also that the density contrast between the sea- and freshwater in the current case has a much smaller effect than the landward head gradients caused by the pumping.

- In many previous studies of the geochemical effects of seawater intrusion the focus has mainly been on the cation exchange reactions and the resulting development of a $CaCl_2$ water composition. This study, however, shows that the composition of the pre-existing mixing zone and its landward transport may have a significant effect on the processes during the intrusion. In this case the high alkalinity in the pre-existing mixing zone advanced landward while Ca^{2+} is released by the ion exchange reactions with the seawater-derived Na^{+}, Mg^{2+} and K^{+}. The accumulation of Ca^{2+} as the front travels landward leads to an increasing calcite supersaturation with travelled distance and possibly to the precipitation of calcite. However, a zone of subsaturation believed to be caused by the acid production related to sulfate reduction follows the zone of calcite supersaturation, potentially re-dissolving calcite and diminishing the effect of calcite precipitated at the front.

12. REFERENCES

Appelo, C.A.J. (1994a): Cation and proton exchange, pH variations, and carbonate reactions in a freshening aquifer. *Water Resour. Res.*, vol. 30, no. 10, p. 2793-2805.

Appelo, C.A.J. (1994b): Some calculations on multicomponent transport with cation exchange in aquifers. *Ground Water*, vol. 32, no. 6, p. 968-975.

Appelo, C.A.J. (1996): Multicomponent ion exchange and chromatography in natural systems. In: Lichtner, P.C., Steefel, C.I. and Oelkers, E.H. (Eds.). (1996): *Reactive Transport in porous media.* Reviews in Mineralogy 34. Mineral. Soc. Am., Washington D.C.,USA, p. 193-227.

Appelo, C.A.J. and Geirnaert, W. (1991): Processes accompanying the intrusion of salt water. In: de Breuk (Ed.) (1991): *Hydrology of salt water intrusion. A selection of SWIM Papers*, IAH, vol. 11, Heise, Hannover.

Appelo, C.A.J and Postma, D. (1993): *Geochemistry, groundwater and pollution,* A.A. Balkema, Rotterdam.

Appelo, C.A.J. and Willemsen, A. (1987): Geochemical calculations and observations on salt water intrusions, I. A combined geochemical/mixing cell model. *J. Hydrol.*, 94, p. 313-330.

Appelo, C.A.J., Willemsen, A., Beekman, H.E. and Griffioen, J. (1990): Geochemical calculations and observations on salt water intrusions. II. Validation of a geochemical model with laboratory experiments. . *J. Hydrol.*, 120, p. 225-250.

Archie, G.E. (1942): The electrical resistivity log as an aid in determining some reservoir characteristics. *Trans. A.I.M.E.*, 146, 54-64.

Arps, J.J. (1953): The effects of temperature on the density and electrical resistivity of sodium chloride solutions. *J. Petroleum Technology.* Technical note 195. p. 17-20.

Ataie-Ashtiani, B.,Volker, R.E., Lockington, D.A. (1999): Tidal effects on sea water intrusion in unconfined aquifers. *J. Hydrol.* Vol. 216, 17-31.

Back, W. (1966): Hydrochemical facies and groundwater flow patterns in northern part of Atlantic coastal plain. *US Geol. Surv. Prof. Paper 498-A*, 42 pp.

Back, W., Hanshaw, B.B., Herman, J.S., Van Driel, J.N., (1986): Differential dissolution of a Pleistocene reef in the ground-water mixing zone of coastal Yucatan, Mexico. *Geology*, vol. 14, p. 137-140.

Back, W., Hanshaw, B.B., Pyle, T.E., Plummer, L.N. and Weidie, A.E. (1979): Geochemical significance of groundwater discharge and carbonate solution to the formation of Caleta Xel Ha, Quintana Roo, Mexico. *Water Resour. Res.*, vol. 15, no. 6, p. 1521-1535.

Barker, A.P., Newton, R.J., Bottrell, S.H. and Tellam, J.H. (1998): Processes affecting groundwater chemistry in a zone of saline intrusion into an urban sandstone aquifer. *Applied Geochemistry*, vol. 13, no 6, p. 735-749.

Barnes, R.O. and Goldberg, E.D. (1976): Methane production and consumption in anoxic marine sediments. *Geology*, v. 4, p. 297-300.

Bear, J. (1972): *Dynamics of fluids in porous media.* Elsevier, Amsterdam, 764 pp.

Bear, J., Cheng, A.H.D., Sorek, S., Ouazar, D. and Herrera, I. (Eds). (1999). *Seawater intrusion in coastal aquifers: Concepts, methods and practices, theory and application of transport in porous media*, vol.14, Kluwer Acad., Norwell, Mass.

Beekman, H.E. (1991): *Ion chromatography of fresh and salt water intrusions.* Ph.D. thesis, Free University, Amsterdam, 198 pp.

Beekman, H.E. and Appelo, C.A.J. (1990): Ion chromatography of fresh- and salt-water displacement: Laboratory experiments and multicomponent transport modelling. *J. Contam. Hydrol.*, 7, p. 21-37.

Berner, R.A. (1975): The role of magnesium in the crystal growth of calcite and aragonite from sea water. *Geochim. Cosmohim. Acta*, vol. 39, p. 489-504.

Berner, R.A. (1981): Authigenic mineral formation resulting from organic matter decomposition in modern sediments, *Fortschr. Miner.*, 59, 1, 117-135

Berner, R.A., Westrich, J.T., Graber, R., Smith, J. and Martens, C.S. (1978): Inhibition of aragonite precipitation from supersaturated seawater: A laboratory and field study. *Am. J. Sci.*, 278, p. 816-837.

Bjerg, P.L., Ammentorp, H.C. and Christensen, T.H. (1993): Model simulations of a field experiment on cation exchange-affected multicomponent solute transport in a sandy aquifer. *J. Contam. Hydrol.*, 12, p. 291-311.

Bjerg, P.L. and Christensen, T.H. (1993): A field experiment on cation exchange-affected multicomponent solute transport in a sandy aquifer. *J. Contam. Hydrol.*, 12, p. 269-290.

Bjerg, P.L., Jakobsen, R., Bay, H., Rasmussen, M., Albrechtsen, H.-J. and Christensen, T.H. (1997): Effects of sampling well construction on H_2 measurements made for characterization of redox conditions in a contaminated aquifer, *Environ. Sci. Technol.*, vol. 31, p. 3029-3031.

Bögli, A. (1978): *Karsthydrographie und physische Speläologie*. Springer Verlag, Berlin, 292 pp.

Bolt, G.H. (ed.) (1982). *Soil Chemistry, B. Physico-chemical models*. Elsevier, Amsterdam.

Boudreau, B.P. and Ruddick, B.R. (1991): On a reactive continuum representation of organic matter diagenesis. *Am. J. Sci.*, vol. 291, p. 507-538.

Boudreau, B.P. and Westrich, J.T. (1984): The dependence of bacterical sulfate reduction on sulfate concentration in marine sediments. *Geochim. Cosmohim. Acta*, vol. 48, p. 2503-2516.

Braithwaite, F. (1855): On the infiltration of salt water into the springs of wells under London and Liverpool. *Proc. Inst. Civil Engrs.*, vol. 14, p. 507-523.

Bruggenwert, M.G.M. and Kamphorst, A. (1982): Survey of experimental information on cation exchange in soil systems. In Bolt, G.H. (ed.) (1982). *Soil Chemistry, B. Physico-chemical models*. Elsevier, Amsterdam, p. 141-203.

Brun, A. (1996*): Reactive transport modelling of coupled inorganic organic processes in groundwater*. Ph.D. Thesis, Technical University of Denmark, Lyngby.

Calvache, M.L. and Pulido-Bosch, A. (1997): Effects of geology and human activity on the dynamics of salt-water intrusion in three coastal aquifers in southern Spain. *Environ. Geol.*, 30 (3/4), p. 215-223.

Ceazan, M.L., Thurman, E.M. and Smith, R.L. (1989): Retardation of ammonium and potassium transport through a contaminated sand and gravel aquifer: The role of cation exchange. *Environ. Sci. Technol.*, vol. 23, p. 1402-1408.

Cerník, M. Barmettler, K., Grolimund, D., Rohr, W., Borkovec, M. and Sticher, H. (1994): Cation transport in natural porous media on laboratory scale: multicomponent effects. *J. Cont. Hydrol.*, vol. 16, p. 319-337.

Champ, D.R., Gulens, J. and Jackson, R.E. (1979): Oxidation-reduction sequences in ground water flow systems. *Can. J. Earth Sci.*, 16, p. 12-23.

Chapelle, F.H. (1983): Groundwater geochemistry and calcite cementation of the Aquia Aquifer in Southern Maryland. *Water Resour. Res.*, vol. 19, no. 2, p. 545-558.

Chapelle, F.H. and Knobel, L.L. (1983): Aqueous geochemistry and the exchangeable cation composition of glauconite in the Aquia Aquifer, Maryland. *Ground Water*, vol. 21, no. 3, p. 343-352.

Chapelle, F.H. and Lovley, D.R. (1992): Competitive exclusion of sulfate reduction by Fe (III)-reducing bacteria: A mechanism for producing discrete zones of high-iron ground water. *Ground Water*, vol. 30, p. 29-36.

Chapelle, F.H. and McMahon, P.B. (1991): Geochemistry of dissolved inorganic carbon in a Coastal Plain aquifer. 1. Sulfate from confining beds as an oxidant in microbial CO_2 production. *J. Hydrol.*, 127, p. 85-108.

Cheng, A.H.D. and Ouazar, D. (1999) analytical solutions. In: Bear, J., Cheng, A.H.D., Sorek, S., Ouazar, D. and Herrera, I. (Eds). (1999). *Seawater intrusion in coastal aquifers: Concepts, methods and practices, theory and application of transport in porous media*, vol.14, Kluwer Acad., Norwell, Mass.

Christensen, F.D., Engesgaard, P. and Kipp, K.L. (2001): A reactive transport investigation of a seawater intrusion experiment in a shallow aquifer, Skansehage, Denmark. In proceeding of *First international conference on saltwater intrusion and coastal aquifers – Monitoring, modelling, and management. Essaouira, Morocco, April 23-25, 2001.*

Cline, J.D. (1967): Spectrophotometric dertermination of hydrogen sulfide in natural waters. *Limnol. Oceanogr.* 14, p. 454-458.

Conrad, R. (1999): Contribution of hydrogen to methane production and control of hydrogen concentrations in methanogenic soils and sediments. *FEMS Microbiol. Ecol.*, vol. 28, p. 193-202.

Cooper, H.H. (1964): A hypothesis concerning the dynamic balance of fresh water and salt water in a coastal aquifer. In: Sea water in coastal aquifers. *US Geological Survey Water-Supply Paper,* 1613-C p. 1-11.

Dance, J.T. and Reardon, E.J. (1983): Migration of contaminants in groundwater at a landfill: a case study, 5. Cation migration in the dispersion test. *J. Hydrol.*, vol. 63, p. 109-130.

Danish Forest and Nature Agency (1987): *Geofysik og råstofkortlægning.* Miljøministeriet, Skov- og Naturstyrelsen.

Edmunds, W.M. and Walton, N.R.G. (1983): The Lincolnshire limestone – Hydrogeochemical evolution over a ten-year period. *J. Hydrol.*, 61, p. 201-211.

EN 1189 (1996): Water quality – Determination of phosphorus – Ammonium molybdate spectrometric method. *European Standard*, CEN.

Engesgaard, P. and Traberg, R. (1996): Contaminant transport at a waste residue deposit, 2. Geochemical transport modeling. *Water Resour. Res.*, vol. 32, p. 939-951.

Fetter, C.W. (1993): *Contaminant Hydrogeology*, Macmillan Publishing Company, New York.

Fetter, C.W. (1994): *Applied Hydrogeology*, 3rd ed., Prentice-Hall, Inc. Englewood Cliffs, New Jersey.

Foster, M.D. (1950): The origin of high sodium bicarbonate waters in the Atlantic and Gulf coastal plains. *Geochim. Cosmohim. Acta*, vol. 1, p. 33-48.

Gaines, G.L. and Thomas, H.C. (1953): Adsorption studies on clay minerals. II. A formulation of the thermodynamics of exchange adsorption. *J. Chem. Phys.*, 21, p. 714-718.

Gapon, E.N. (1933): Theory of exchange adsorption. V. *(in Russian). J. Gen. Chem. (USSR),* 3, p. 667-669. (*Chem. Abstr.* 28, 4516, 1934).

Giménez, E. and Morell, I. (1997): Hydrogeochemical analysis of salinization processes in the coastal aquifer of Oropesa (Castellón, Spain). *Environ. Geol.*, 29 (1/2), p. 118-131.

Glover, R.E., (1964): The pattern of fresh-water flow in a coastal aquifer. In: Sea water in coastal aquifers. *US Geological Survey Water-Supply Paper,* 1613-C. p. 32-34.

Goldenberg, L.C. (1985): Decrease of hydraulic conductivity in sand at the interface between seawater and dilute clay suspensions. *J. Hydrol.*, vol. 78, p. 183-199.

Goldenberg, L.C., Magaritz, M. and Mandel, S. (1983): Experimental investigation on irreversible changes of hydraulic conductivity on the seawater-freshwater interface in coastal aquifers. *Water Resour. Res.*, vol. 19, no. 1, p. 77-85.

Gomis-Yagües, V., Boluda-Botella, N. and Ruiz-Beviá, F. (1997): Column displacement experiments to validate hydrogeochemical models of seawater intrusions. *J. Contam. Hydrol.*, 29, p. 81-91.

Gomis-Yagües, V., Boluda-Botella, N. and Ruiz-Beviá, F. (2000): Gypsum precipitation/dissolution as an explanation of the decrease of sulphate concentration during seawater intrusion. *J. Hydrol.*, 228, p. 48-55.

Griffioen, J. (1992): *Cation-exchange and carbonate chemistry in aquifers following groundwater flow*. Ph.D. Thesis, Free University, Amsterdam, 182 pp.

Hahn, J. (1991): Aspects of groundwater salinization in the Wittmund (East Friesland) coastal area. In: de Breuk (Ed.) (1991): *Hydrology of salt water intrusion. A selection of SWIM Papers*, IAH, vol. 11, Heise, Hannover.

Hansen, B.K. and Postma, D. (1995): Acidification, buffering, and salt effects in the unsaturated zone of a sandy aquifer, Klosterhede, Denmark. *Water Resour. Res.*, vol. 31, p. 2795-2809.

Hansen, E. (1980): *Lecture notes in course 8862 Hydrology*, ISVA, Technical University of Denmark.

Hansen, L.K., Jakobsen, R. and Postma, D. (2001): Methanogenesis in a shallow sandy aquifer, Rømø, Denmark. *Geochim. Cosmohim. Acta*, vol. 65, p. 2925-2936.

Hinsby, K., Bjerg, P.L., Andersen, L.J., Skov, B. and Clausen, E.V. (1992): A mini slug test method for determination of a local hydraulic conductivity of an unconfined sandy aquifer. *J. Hydrol.*, 136, p. 87-106.

Hoehler, T.M., Alperin, M.J., Albert, D.B. and Martens, C.S. (1994): Field and laboratory studies of methane oxidation in an anoxic marine sediment: Evidence for a methanogen-sulfate reducer consortium. *Global Biogeochem. Cycles*, vol. 8, no. 4, p. 451-463.

Howard, K.W.F. and Mullings, E. (1996): Hydrochemical analysis of ground-water flow and saline incursion in the Clarendon Basin, Jamaica. *Ground Water*, vol. 34, no. 5, p. 801-810.

Hvorslev, J.M. (1951): Time lag and soil permeability in ground-water observations, *Bull. 36*, 50 pp., U.S. Corps of Eng., Waterways Exp. Sta., Vicksburg, Miss.

Iribar, V., Carrera, J., Custodio, E. and Medina, A. (1997): Inverse modelling of seawater intrusion in the Llobregat delta deep aquifer. *J. Hydrol.*, 198, p. 226-244.

Iversen, N. and Jørgensen, B.B. (1985): Anaerobic methane oxidation rates at the sulfate-methane transition in marine sediments from Kattegat and Skagerrak (Denmark). *Limnol. Oceanogr.* 30, p. 944-955.

Jakobsen, R., (1995): *Sulfate reduction, Fe-reduction and methanogenesis in groundwater*, Ph.D. dissertation, Institute of Geology and Geotechnical Engineering, Technical of Denmark.

Jakobsen, R. and Postma, D. (1994): In situ rates of sulfate reduction in an aquifer (Rømø, Denmark) and implications for the reactivity of organic matter. *Geology*, vol. 22, p. 1103-1106.

Jakobsen, R. and Postma, D. (1999): Redox zoning, rates of sulfate reduction and interactions with Fe-redution and methanogenesis in a shallow sandy aquifer, Rømø, Denmark. *Geochim. Cosmohim. Acta*, vol. 63, p. 137-151.

Jankowski, J. and Jacobsen, G. (1991): Hydrochemistry of a groundwater-seawater mixing zone, Nauru Island, central Pacific Ocean. *BMR Journal of Australian Geology & Geophysics*, vol. 12, p. 51-64.

Kipp, K.L. (1987): HST3D: A computer code for simulation of heat and solute tranport in three-dimensional ground-water flow systems. *U.S. Geol. Surv., Water-Resources Investigations Report*, 86-4095.

Kohout, F.A., (1964): The flow of fresh water and salt water in the Biscayne aquifer of the Miami area, Florida. *US Geological Survey Water-Supply Paper* 1613-C. p. 12-32.

Konikow, L.F., August, L.L. and Voss, C.I. (2001): Effects of clay dispersion on aquifer storage and recovery in coastal aquifers. In proceeding of *First international conference on saltwater intrusion and coastal aquifers – Monitoring, modelling, and management. Essaouira, Morocco, April 23-25, 2001.*

Kooi, H. and Groen, J. (2001): Offshore continuation of coastal groundwater systems; predictions using sharp-interface approximations and variable-density flow modelling. *J. Hydrol.*, 246, p. 19-35.

Kooi, H., Groen, J. and Leijnse, A., (2000): Modes of seawater intrusion during transgressions. *Water Resour. Res.*, vol. 36, no. 12, p. 3581-3589.

Kruseman, G.P. and de Ridder, N.A., (1983): *Analysis and evaluation of pumping test data*, 3rd edition, Bulletin 11 ILRI, Wargeningen, The Nederland's.

Laverty, F.B. and van der Goot, H.A. (1955): Development of a fresh-water barrier in southern California for the prevention of sea water intrusion, *Jour. Amer. Water Works Assoc.*, vol. 47, p. 886-908.

Lefèvre, F., Sardin, M. and Schweich, D. (1993): Migration of strontium in clayey and calcareous sandy soil: Precipitation and ion exchange. *J. Contam. Hydrol.*, 13, p. 215-229.

Logan, W.S., Auge, M.P. and Panarello, H.O. (1999): Bicarbonate, sulfate, and chloride water in a shallow, clastic-dominated coastal flow system, Argentina. *Ground Water*, vol. 37, no. 2, p. 287-295.

Lovley, D.R. and Chapelle, F.H. (1995): Deep subsurface microbial processes. *Rev. Geophys.*,vol. 33, no. 3, p. 365-381.

Lusczynski, N.J., (1961): Head and flow of ground water of variable density. *J. Geophys. Res.*, vol. 66, p. 4247-4256.

Lusczynski, N.J. and Swarzenski, W.V. (1966): Salt-water encroachment in Southern Nassau and Southeastern Queens Counties, Long Island, New York, *U.S. Geological Survey Water-Supply Paper*, 1613-F, 76 pp.

Magaritz, M. and Luzier, J.E. (1985): Water-rock interactions and seawater-freshwater mixing effects in the coastal dunes aquifer, Coos Bay, Oregon. *Geochim. Cosmohim. Acta*, vol. 49, p. 2515-2525.

Martens, C.S. and Berner, R.A. (1977): Interstitial water chemistry of anoxic Long Island Sound sediments. 1. Dissolved gases. *Limnol. Oceanogr.* 22(1), p. 10-25.

Martens, C.S. and Klump, J.V. (1980): Biogeochemical cycling in an organic-rich coastal marine basin - I. Methane sediment-water exchange processes. *Geochim. Cosmohim. Acta*, vol. 44, p. 471-490.

Melo, M.T.C., Marques da Silva, M.A. and Edmunds, W.M. (1999): Hydrochemistry and flow modelling of the Aveiro Multilayer Cretaceous Aquifer. *Phys. Chem. Earth (B)*, vol. 24, no. 4, p. 331-336.

Mertz, E.L. (1924): Oversigt over de sen- og postglaciale niveauforandringer i Danmark. *Danmarks geologiske Undersøgelse*, II. Række, nr. 41.

Nadler, A., Magaritz, M. and Mazor, E. (1980): Chemical reactions of seawater with rocks and freshwater: experimental and field observations on brackish waters in Israel. *Geochim. Cosmohim. Acta*, vol. 44, p. 879-886.

Parkes, R.J., Cragg, B.A., Fry, J.C., Herbert, R.A. and Wimpenny, J.W.T. (1990): Bacterial biomass and activity in deep sediment layers from the Peru margin. *Phil. Trans. R. Soc. Lond.* A331, p. 139-153.

Parkhurst, D.L. and Appelo, C.A.J. (1999): *User's guide to PHREEQC (version 2) – A computer program for speciation, reaction-path, 1D-transport, and inverse geochemical calculations.* U.S. Geol. Surv., Water Resour. Inv. Rep., 99-4259.

Plummer, L.N., (1975): Mixing of seawater with calcium carbonate ground water. *Geol. Soc. Am. Mem.* 42, p. 219-236.

Post, V.E.A., Kooi, H., Groen, J. and de Vries, J.J. (2001): Modelling the influence of sea level change and geological processes on the distribution of fresh and salt water in the Netherlands coastal areas. In proceeding of *First international conference on saltwater intrusion and coastal aquifers – Monitoring, modelling, and management. Essaouira, Morocco, April 23-25, 2001.*

Postma, D. (1993): The reactivity of iron oxides in sediments: a kinetic approach, *Geochim. Cosmohim. Acta*, vol. 57, p. 5027-5034.

Postma, D. and Jakobsen, R. (1996): Redox zonation: Equilibrium constraints on Fe(III)/SO_4-reduction interface. *Geochim. Cosmohim. Acta*, vol. 60, p. 3169-3175.

Redfield, A.C., Ketchum, B.J. and Richards, F.A. (1963): The influence of organisms on the composition of seawater. In Hill, M.N. (ed.). (1963): *The sea*, v.2. Interscience.

Reeburgh, W.S. (1980): Anaerobic methane oxidation: Rate depth distributions in Skan Bay sediments. *Earth Planet. Sci. Lett.*, 47, p. 345-352.

Reilly, T.E. (1993): Analysis of ground-water systems in freshwater-saltwater environments. In: Alley, W.M. (ed.) (1993): *Regional Groundwater Quality*, Van Nostrand Reinhold, Ny, Chap. 18, p. 443-469.

Reilly, T.E. and Goodman, A.S. (1985): Quantitative analysis of saltwater-freshwater relationships in groundwater systems – a historical perspective. *J. Hydrol.*, vol. 80, p. 125-160.

Sanford, W.E. and Konikow, L.F, (1989): Simulation of calcite dissolution and porosity changes in saltwater mixing zones in coastal aquifers. *Water Resour. Res.*, vol. 25, p. 655-667.

Sayles, F.L. and Mangelsdorf, JR., P.C. (1977): The equilibration of clay minerals with seawater: exchange reactions. *Geochim. Cosmohim. Acta*, vol. 41, p. 951-960.

Scheffer, F. and Schachtschabel, P. (1970): *Lehrbuch der Bodenkunde.* Enke, Stuttgart, 448 pp.

Schincariol, R.A. (1998): Dispersive mixing dynamics of dense miscible plumes: natural perturbation initiation by local-scale heterogeneities. *J. Contam. Hydrol.*, vol. 34, p. 247-271.

Schou, A. (1945): *Det marine forland.* H. Hagerup's Forlag, København. p. 112-114 & p 183.

Simmons, C.T., Fenstemaker, T.R. and Sharp Jr., J.M. (2001): Variable-density groundwater flow and solute transport in heterogeneous porous media: approaches, resolutions and future challenges.
J. Contam. Hydrol., vol. 52, p. 245-275.

Smart, P.L., Dawans, J.M. and Whitaker, F., (1988): Carbonate dissolution in modern mixing zone. *Nature*, vol. 335, p. 811-813.

Steinich, B., Escolero, O. and Marín, L.E. (1998): Salt-water intrusion and nitrate contamination in the Valley of Hermosillo and El Sahuaral coastal aquifers, Sonora, Mexico. *Hydrogeol. J.*, 6, p. 51-526.

Stoessell, R.K., Moore, Y.H. and Coke, J.G. (1993): The occurrence and effect of sulfate reduction and sulfide oxidation on coastal limestone dissolution in Yucatan Cenotes. *Ground Water*, vol. 31, no. 4, p. 566-575.

Stookey. L.L. (1970): Ferrozine – A new spectrophotometric reagent for iron. *Anal. Chem.* 42(7), p. 779-781.

Stumm, W. and Morgan, J.J. (1981): *Aquatic chemistry.* 2nd ed. Wiley & Sons, New York, 780 pp.

Stuyfzand, P.J. (1989): An accurate, relatively simple calculation of the saturation index of calcite for fresh to salt water. *J. Hydrol.*, vol. 105. p. 95-107.

Stuyfzand, P.J. (1993): *Hydrochemistry and hydrology of the coastal dune area of the western Netherlands*. Ph.D-thesis, Nieuwegein, KIWA.

Telford, W.M., Geldart, L.P. and Sheriff, R.E., (1990): *Applied Geophysics*, 2nd edition, Cambridge.

Todd, D.K. (1980): *Groundwater hydrology*, 2nd ed., Wiley, New York, N.Y., p. 494-520.

Troelsen, H. and Jørgensen, B.B. (1982): Seasonal dynamics of elemental sulfur in two coastal sediments. *Estuarine, Coastal and Shelf Science*, v. 15, p. 255-266.

Valocchi, A.J., Street, R.L. and Roberts, P.V. (1981a): Transport of ion-exchanging solutes in groundwater: Chromatographic theory and field simulation. *Water Resour. Res.*, vol. 17, no. 5, p. 1517-1527.

Valocchi, A.J., Street, R.L., Parks, G.A. and Roberts, P.V. (1981b): Simulation of the transport of ion-exchanging solutes using laboratory-determined chemical parameter values. *Ground Water,* vol. 19, no. 6, p. 600-607.

Van Breukelen, B.M., Appelo, C.A.J. and Olsthoorn, T.N. (1998): Hydrogeochemical transport modeling of 24 years of Rhine water infiltration in the dunes of the Amsterdam Water Supply. *J. Hydrol.*, vol. 209. p. 281-296.

Van der Molen, W.H. (1958): *The exchangeable cations in soils flooded with seawater*. Staatsdrukkerij, Den Haag, 167 p.

Vanselow, A.P. (1932):Equilibria of the base-exchange reactions of bentonites, permutites, soil colloids and zeolites. *Soil Sci.* 33, p. 95-113.

Voss, C.I. (1984): SUTRA: A finite-element simulation model for saturated-unsaturated fluid-density-dependent ground-water flow with energy transport or chemically-reactive single-species solute transport. *U.S. Geol. Surv. Water Resour. Invest. Rep.* 84-4369.

Walter, L.M. and Hanor, J.S. (1979): Effect of orthophosphate on the dissolution kinetics of biogenic magnesian calcites. *Geochim. Cosmohim. Acta*, vol. 43, p. 1377-1385.

Whiticar, M.J. (1999): Carbon and hydrogen isotope systematics of bacterial formation and oxidation of methane. *Chem. Geol.*, 161, p. 291-314.

Wicks, C.M. and Herman, J.S. (1995): The effect of zones of high porosity and permeability on the configuration of the saline-freshwater mixing zone. *Ground Water*, vol. 33, no. 5, p. 733-740.

Wicks, C.M. and Herman, J.S. (1996): Regional hydrogeochemistry of a modern coastal mixing zone. *Water Resour. Res.*, vol. 32, no. 2, p. 401-407.

Wigley, T.M.L. and Plummer, L.N. (1976): Mixing of carbonate waters. *Geochim. Cosmohim. Acta*, vol. 40, p. 989-995.

Worthington, A.E.P., Hedges, J.H. and Pallatt, N. (1990): SCA Guidelines for sample preparation and porosity measurement of electrical resistivity samples. Part I-Guidelines for preparation of brine and determination of brine resistivity for use in electrical resistivity measurements. *The Log Analyst.* Jan.-Feb. p. 20-28.

Xue, Y., Wu, J. Ye, S. and Zhang, Y. (2000): Hydrogeology and hydrogeochemical studies for salt water intrusion on the south coast of Laizhou Bay, China. *Ground Water*, Jan-Feb, vol. 38, no. 1, p. 38-45.

ISBN 87-89220-89-7